CRANFIELD UNIVERSITY

RODRIGO FÉLIX MORENO

SITUATIONAL AWARENESS-BASED ENERGY MANAGEMENT
FOR UNMANNED ELECTRIC SURVEILLANCE PLATFORMS

CRANFIELD DEFENCE AND SECURITY

THESIS SUBMISSION FOR THE DEGREE OF PHILOSOPHY
DOCTOR
Academic Year: 2014

Supervisor: Dr. John T. Economou
January 2015

CRANFIELD UNIVERSITY

CRANFIELD DEFENCE AND SECURITY

THESIS SUBMISSION FOR THE DEGREE OF PhD

Academic Year 2011 - 2014

RODRIGO FÉLIX MORENO

SITUATIONAL AWARENESS-BASED ENERGY MANAGEMENT
FOR UNMANNED ELECTRIC SURVEILLANCE PLATFORMS

Supervisor: John T. Economou
January 2015

ABSTRACT

In the present day fossil fuel availability, cost, security and the pollutant emissions resulting from its use have driven industry into looking for alternative ways of powering vehicles. The aim of this research is to synthesize/design and develop a framework of novel control architectures which can result in complex powered vehicle subsystems to perform better with reduced exogeneuous information.

This research looks into the area of energy management by proposing an intelligent based system which not only looks at the beaten path of where energy comes from and how much of it to use, but it goes further by taking into consideration the world around it. By operating without GPS, it realies on data such as usage, average consumption, system loads and even other surrounding vehicles are considered when making the difficult decisions of where to direct the energy into, how much of it, and even when to cut systems off in benefit of others. All this is achieved in an integrated way by working within the limitations of non-fossil fuelled energy sources like fuel cells, ultracapacitors and battery banks using driver-provided information or by crafting an artificial usage profile from historicaly learnt data. By using an organic computing philosophy based on artificial intelligence this alternative approach to energy supply systems presents a different perspective beginning by accepting the fact that when hardware is set energy can be optimized only so much and takes a step further by answering the question of how to best manage it when refuelling might not be an option. The result is a situationally aware system concept that is portable to any type of electrically powered platform be it ground, aerial or marine since it operates on the fact that all operate within three dimensional space. The system´s capabilities are then verified in a virtual reality environment which can be tailored to the meet reseach needs including allowing for different altitudes, environmental temperature and humidity profiles. This VR system is coupled with a chassis dynamometer to allow for testing of real physical prototype unmanned ground vehicles where the intelligent system will benefit by learning from real platform data. The Thesis contributions and objectives are summarised next:

- The control system proposed includes an awareness of the surroundings within which the vehicle is operating without relying on GPS position information.
- The system proposed is portable and could be used to control other systems.

- The test platform developed within the Thesis is flexible and could be used for other systems.
- The control system for the fuel cell system described within the work has included an allowance for altitude and humidity. These factors would appear to be significant for such systems.
- The structure of the control system and its hierarchy is novel.
- The ability of the system to be applied to a UAV and as such control a 'vehicle' in 3 dimensions, and yet be also applied to a ground vehicle, where roll and pitch are largely a function of the ground over which it travels (so the UGV only uses a subset of the control functionality).
- The mission awareness of the control structure appears to be the heart of the potential contribution to knowledge, and that this also includes the ability to create an estimated, artificial mission profile should one not be input by the operators. This learnt / adaptive input could be expanded on to highlight this aspect.

ACKNOWLEDGEMENTS

TABLE OF CONTENTS

LIST OF FIGURES

LIST OF TABLES

LIST OF EQUATIONS

LIST OF ABBREVIATIONS

B	Low Level Layer – Battery Only Operating Mode
BESS	Battery Energy Storage System
BEV	Battery Electric Vehicle
CW	Curb Weight
DBO	Distance Between Objects [m]
DoD	Department of Defense
Emf	Electromotive Force
FB	Low Level Layer - Fuel Cell/Battery Operating Mode
FC	Low Level Layer - Fuel Cell Only Operating Mode
FCEV	Fuel Cell Electric Vehicle
FTP-75	Federal Test Procedure 75
GVW	Gross Vehicle Weight
GVWR	Gross Vehicle Weight Rating
HEV	Hybrid Electric Vehicle
HVB	Home Vector Bias
HWFET	Hightway Fuel Economy Test
ICS	Intelligent Control Structure
ISAF	International Security Assistance Force
LFF	Look-forward Forecast
LMTD	Log Mean Temperature Difference Method
LPM	Litre Per Minute
m.a.s.l.	Meters Above Sea Level
Mt	Metric Ton
MXN	Mexican Peso
NTE	Not-To-Exceed
OCDE	Organisation for Economic Co-operation and Development
PEM	Proton Exchange Membrane
PM	Permanent Magnet
PMSM	Permanent Magnet Synchronous Machine
PM_x	Particulate Matter
PTO	Power-Take-Off

rms	Root Mean Square
SOC	State of Charge
SUV	Sport Utility Vehicle
TTV	Threat-To-Vehicle distance [m]
USD	U.S.A. Dollar
Wb	Weber
UGV	Unmanned Ground Vehicle
UAV	Unmanned Aerial Vehicle

LIST OF SYMBOLS

A	Road Slope Angle
A	UAV Propeller Angle of Attack
A	Pipe Cross-Section
A	Vehicle Acceleration
A_a	Fuel Cell Radiator Air Side Total Heat Transfer Area
A_c	Fuel Cell Radiator Coolant Side Total Heat Transfer Area
A_{exp}	Battery Voltage Drop Along Exponential Zone
A_f	Fuel Cell Radiator Fin Total Heat Transfer Area
A_f	Vehicle Frontal Area
$A_{fr,f}$	Fuel Cell Radiator Fin Frontal Heat Transfer Area
$A_{fr,r}$	Fuel Cell Radiator Core Frontal Area
$A_{fr,t}$	Fuel Cell Radiator Coolant Tube Frontal Area
$A_{p,a}$	Fuel Cell Radiator Total Air Pass Area
$A_{p,c}$	Fuel Cell Radiator Total Coolant Pass Area
A_{tf}	Trailer Frontal Area
A_x	UAV Propeller Area on X Axis
A_y	UAV Propeller Area on Y Axis
A_{yaw}	Propeller Shadow Projection on Yaw Plane
$\hat{A}_{yaw}$	Propeller Shadow Projection on Yaw Plane Vector
A_z	UAV Propeller Area on Z Axis
B_0	Magnet No Load Flux Density
B_{exp}	Battery Charge at the End of the Exponential Zone
B_m	Magnet Total Flux Density
B_{ml}	Peak Fundamental Flux Density
$\dot{C}_a$	Radiator Air Heat Capacity Rate
$\dot{C}_c$	Radiator Coolant Heat Capacity Rate
C_d	Vehicle Drag Coefficient
Cd_{uav}	UAV Aerodynamic Drag Coefficient
$\dot{C}_{max}$	Radiator Maximum Heat Capacity Rate

$\dot{C}_{min}$	Radiator Minimum Heat Capacity Rate
$\dot{C}_r$	Radiator Heat Capacity Index
C_{td}	Trailer Drag Coefficient
D_e	Equivalent Diameter for an Elliptical Pipe
D_h	Hydraulic Diameter
$D_{h,c}$	Hydraulic Diameter of the Coolant Pipes
E	Fuel Cell Open Circuit Voltage
E_0	Fuel Cell Ideal Voltage
E_{exp}	Battery Exponential Zone Limit Voltage
E_{full}	Battery Fully Charged Voltage
E_m	Peak Induced emf
$E_{o,batt}$	Battery Polarization Voltage
F	Friction Factor for isothermal flows inside tubes
F	Tyre Friction Coefficient
F_e	External Source mmf
F_i	Skid Steering force on the "inner" side of the vehicle during the maneuver
F_l	Fuel Cell Radiator Fin Length
F_o	Skid Steering force on the "outer" side of the vehicle during the maneuver
f_s	Stator Supply Frequency
f_t	Trailer Tyre Friction Coefficient
G	Maximum Mass Flow Rate Flux
G	Acceleration Due to Gravity
h_a	Convective Heat Transfer Coefficient
H_e	External Field Intensity
I	Battery Current
I	Driveline Gear Ratio
i_{as}, i_{bs}, i_{cs}	Machine Three Phase Currents in the Stator
I_{nom}	Battery Nominal Current
i_o	Q and D Axes imbalance current
i_s	Source Current
i_{ds}^r, i_{qs}^r	Q and D Axes currents in the stator frame of reference

J	Coulburn Modulus for Louvered Fin Surfaces or Fuel Cell Radiator Air Heat Transfer Coefficient
Kc	Thermal Conductivity
Kf	Water Ethylene Glycol 50% Thermal Conductivity
K_{pol}	Battery Polarization Voltage Constant
k_{w}	Winding Factor
L	Effective Fin Length
L_{d}	Direct Axes Inductance
L_{q}	Quadrature Axes Inductance
M	Fin Efficiency Parameter
M	Vehicle Mass
M_{r}	Moment of Lateral Resistance
$\dot{m}_a$	Final Airflow for Cooling System
$\dot{m}_{fan}$	Fan Airflow
$\dot{m}_{grill}$	Mass Airflow Through Vehicle's Front Grill
m_{t}	Fuel Cell Exhaust Throttle Coefficient
m_{t}	Trailer Mass
n_{cell}	Number of Fuel Cells in the Stack
Nm	Newton-Metre
NO_x	Nitrogen Oxides
NTU	Number of Transfer Units
Nu	Nusselt's Number
P	Wetted Perimeter
P_{a}	Motor Air Gap Power
P_{r}	Prandtl Number
P_{sc}	Machine Winding Power Losses
P_{tot}	Fuel Cell Total Power Released by the Anode Chemical Reaction
p_{vehicle}	Atmospheric pressure at Vehicle Geopotential Altitude
$\dot{Q}_{actual}$	Radiator Actual Heat Transfer Rate
$\dot{Q}_{cool}$	Fuel Cell Heat Removal Rate
Q_{exp}	Battery Exponential Zone Limit Charge
$\dot{Q}_{hx}$	Fuel Cell System Heat Generation Rate

Q_{loss}	Fuel Cell Surface Heat Loss
$\dot{Q}_{max}$	Radiator Maximum Heat Transfer Rate
Q_{nom}	Battery Nominal Charge
$\dot{Q}_{stack}$	Fuel Cell Stack Heat Absorption Rate
R	Battery Internal Resistance
R	Skid Steering Turn Radius
R_{θ}	Gradient Resistance
R_{a}	Aerodynamic Resistance
R_{b}	Braking Force
r_{d}	Wheel Radius
Re	Reynolds Number
R_{I}	Inertia Resistance
R_{r}	Vehicle Rolling Resistance
R_{s}	Machine Resistive Losses
R_{t}	Trailer Resistance
R_{z}	Body Drag Effect
St	Stanton's Number
T_{air}	Fuel Cell Inlet Air Temperature
$T_{air,out}$	Radiator Outlet Air Temperature
$T_{coolant,out}$	Radiator Outlet Coolant Temperature
T_{e}	Electromagnetic Torque
U_1	UAV Vertical Force
U_2	UAV Body Roll Torque
U_3	UAV Pitch Torque
U_4	UAV Yaw Torque
$UA_{\mathrm{fr,r}}$	Radiator Heat Transfer
V	Wind Speed Relative to Vehicle Speed
V_{a}	Radiator Air Flow Speed
V_{act}	Fuel Cell Activation Voltage
v_{as}, v_{bs}, v_{cs}	Machine Three phase voltages
V_{batt}	Battery Total Voltage
V_{c}	Radiator Coolant Flow Speed
V_{conc}	Fuel Cell Concentration Voltage or losses

Veh_{Rot}	Vehicle Rotation
V_{m}	Peak Supply Voltage
V_{nom}	Battery Nominal Voltage
V_{ohm}	Fuel Cell Ohmic Voltage or losses
V_{spd}	Vehicle Speed
V_{st}	Fuel Cell Stack Voltage
V_{uav}	UAV Speed Vector
V_{wind}	Wind Speed
$\hat{V}_{UGV}$	UGV Velocity Vector Direction
v_{ds}^{r}	Direct Axes Voltage
v_{qs}^{r}	Quadrature Axes Voltage
W	Vehicle Normal Force on the Ground
$W_{v,inj}$	Fuel Cell Humidifier Injected Water Vapour Flow Rate
X_{drag}	Propeller Drag Force in the X Axis Direction
$\ddot{X}_{uav}$	UAV Inertial Acceleration Along X Axis
Y_{drag}	Propeller Drag Force in the Y Axis Direction
$\ddot{Y}_{uav}$	UAV Inertial Acceleration Along Y Axis
Z_{drag}	Propeller Drag Force in the Z Axis Direction
$\ddot{Z}_{uav}$	UAV Inertial Acceleration Along Z Axis
δ	Equivalent Rotational Mass Factor
η	Driveline Efficiency
ε	Effectiveness
μ	Dynamic Viscosity
ρ	Fuel Cell Radiator Inlet Air Density
λ_{af}	Armature Flux Linkage
ρ_{air}	Atmospheric Air Density
θ	Pitch Angle
$\ddot{\theta}$	Pitch Acceleration
ψ	Yaw Angle
$\ddot{\psi}$	Yaw Acceleration
ϕ	Roll Angle
ϕ_{ml}	Peak Fundamental Flux

$\ddot{\phi}$	Roll Acceleration
ε-NTU	Effectiveness-Number of Transfer Units Method
η_f	Fin Heat Transfer Efficiency
η_o	Fin Total Surface Efficiency
ρ_{atm}	Fuel Cell Inlet Air Density
γ_m	Inertia Mass Factor
Ω_z	Skid Steer Yaw Velocity

Vehicle 1: Surveillance Vehicle (SV) Simulation Parameters (Felix 2013)

Vehicle	
Curb Weight	15,867 kg.
Payload Weight	6,600 kg.
Frontal Area	7.2 m
Tyre Size	395/85R20
Fuel Capacity	492L H_2@70 MPa
Drive Power	4 x 75 kW PMSM
Payload Power (Search Mode)	19 kW
On-board Electrical Load Power	190 kW
Fuel Cell Module	
Brake Power	300 kW
Number of Fuel Cells per Module	2
Maximum Current	300 A
Environmental	
Ambient Air Temperature	43 °C
Elevation	Sea Level

Vehicle 2: Medium Duty Vehicle (MDV) Simulation Parameters

Parameter	Value	Unit
Machine Type	AC PMSM	
Motor Nominal Power	320	kW
Motor Nominal Current	492	A
Motor Nominal Voltage	650	V
Motor Nominal Speed	2000	RPM
Gear Reduction	3.97 : 1	
	2.32 : 1	
	1.52 : 1	
	1.15 : 1	
	0.86 : 1	
	0.67 : 1	
	3.13 : 1	
Tyre Diameter	810.3	Mm
Estimated GVW	8845	Kg

Vehicle 3: Unmanned Ground Vehicle (UGV) Simulation Parameters

Parameter	Value	Unit
Machine Type	DC PM	
Motor Nominal Power	750	W
Motor Nominal Current	40	A
Motor Nominal Voltage	24	V
Motor Nominal Speed	3300	RPM
Motor Nominal Torque	2.2	Nm
Gear Reduction	7.78:1	
Tyre Diameter	279.4	Mm
Estimated GVW	250	Kg

1 INTRODUCTION

The purpose of this brief introduction, the space between this line and the start of Section 1.1, is to introduce the reader into the background which triggered this research undertaking. There is enough space in this thesis to elaborate on literature, but the intention is to first "open up the floor" to discuss about the basic concepts and motivations which started this research down the path of vehicle electrification and the control systems inside them. So, with no further delays, let us begin.

Vehicle electrification has in recent years garnered many headlines and found a home in many universities and industrial laboratories. The topic has become popular in recent years as the dependence on fossil fuels has not only imposed economic strain on the world's security forces, but also logistical, political and environmental constraints on the way such forces can be deployed. On top of all this the environmental impact of the continued use of fossil fuels is also driving more and more governments to look for a replacement energy source. This research prompted many new technologies for the generation of energy to be used by an increasingly more technologically dependent society. In the automotive sector these efforts caused novel propulsion systems such as Battery Electric Vehicles (BEV), Petrol or Diesel Electric Hybrids (HEV) in Parallel or Series Configurations and many other derivatives to be looked at in greater detail. By introducing electric motors into the drivetrain each vehicle cuts its greenhouse emissions by burning less fuel therefore addressing some of the concerns cited before.Yet with all their benefits all of the previous options rely on heavy bulky batteries as the pillar of the energy supply architecture. This translates into longer resupply times, versus conventional fossil fuels, higher system costs and packaging problems when an existing platform is to be converted into any of these new architectures.

1

An option being considered in many countries by both armed forces and vehicle manufacturers is the use of Fuel Cells. In the case of this work where ground vehicles are approached the technology of interest is that of the Proton Exchange Membrane (PEM) fuel cell used to then create a Fuel Cell Electric Vehicle (FCEV). In these architectures the fuel cell promotes the reaction of diatomic Hydrogen (H_2) with the Oxygen content of atmospheric air to create an electric current and water vapour. This current in turn is used to power the vehicle powertrain and on-board systems. One of the many advantages of using these architectures is the obvious reduction in photochemical smog and greenhouse gases, but also the reduction of airborne noise and emission of particulate matter species (PM_x). Furthermore Hydrogen as a fuel can be fed into a bespoke vehicle storage tank on times similar to those taken to resupply liquid fossil fuels.

Although the technology presents some benefits many challenges still exist for the widespread adoption of FCEVs. System cost, vehicle range, refuelling infrastructure are the ones more frequently mentioned. Hydrogen is abundant in nature and can be refined from many sources such as fossil fuels, biomass or even the electrolysis of water. Unfortunately by being a gaseous fuel it has a lower energy density, J/m^3, than petrol or diesel therefore requires a larger volume to store the same amount of energy. In addition to this the first steps for the adoption of electric powertrains have involved the conversion of existing platforms, designed around the packaging requirements of liquid fossil fuels, to the new technologies. When adding both factors together the result is a vehicle platform which cannot store the same amount of energy in its fuel tank consequently suffering from a shorter autonomy range. Finally, early fuel cell stacks of equivalent power output took up larger quantities of space than the original power plant and could not be packed inside the existing space, so not only did the newly converted vehicle have a shorter range it also had less power.

Furthermore and as a result of the power reductions just mentioned FCEV prototypes have been mainly passenger vehicles. Though this sounds logical at first it is not when one looks at the context of national vehicle fleets and their pollutant emission inventory. As will be illustrated in following sections national emissions inventories are driven mainly not by passenger and private transportation, but by heavy less numerous commercial platforms. This is because their usage profile includes more hours and miles of travel per day whilst being powered by larger engines. Luckily recent advances in fuel cell technology have provided high power fuel cells which occupy the same volume as the equivalent internal combustion engines. This behoves the analysis of their introduction into heavier vehicles.

One way to tackle this challenge is to analyse what would be required to successfully electrify a vehicle whose gross vehicle weight rating (GVWR) is higher than that of a passenger vehicle. Also, it will be necessary to further dissect the existing energy supply and vehicle electrification technological contexts to properly select a target platform; once this is done a set of requirements and limitations can be drawn up which will guide any research work towards a viable and feasible solution.

In parallel to all of this, another technological sector has also become increasingly important as of late which is that of driverless platforms. At first sight these vehicles do not provide relief in ecological, political or even financial terms, with an easily overlooked improvement in occupant and pedestrian safety not gathering much comment. Yet it is quite the contrary. A driverless vehicle can be programmed to use its energy more efficiently potentially saving countless amounts of fuel, therefore money, and by doing so also reducing pollutant emissions. Also a driverless vehicle can use external data sources to plan and account for traffic and weather conditions potentially also saving travel time. Although incredible sophisticated driverless vehicles do require a person

to be on-board behind a back-up conventional driving system in case it meets an unforeseen condition or scenario.

On the other hand, driverless vehicles have a fellow technology: The unmanned vehicle. Very popular in the news thanks to its mainly military aerial versions, the unmanned vehicle can really exist in any environment be it aquatic, terrestrial or aerial. Also, as their name implies, and in contrast with their driverless brethren, these vehicles do not carry any passengers. They can operate by wireless communications or even autonomously under close supervision. When paired with electric drivetrains such vehicles can be both quiet and have a reduced thermal signature plus they can operate without placing an operator at risk. All of these give them a great advantage for their consideration in security and military environments.

When all of the discussed technologies are summed together the outcome is a highly sophisticated vehicle which has the following advantages:

- From fuel cells, at vehicle level:
    - Lower noise and thermal signature than HEV,
    - Lower pollutant emissions,
    - Zero PM_x emissions,
    - Short refill times,
    - Greater autonomy than BEVs.
- From driverless technologies:
    - Vision and navigation systems,
    - Automatic powertrain and vehicle systems control,
- From unmanned vehicle technologies:
    - Off board data links,
    - No risk to operator.

For all its advantages the unmanned electrified vehicle still has to overcome many barriers and one of them is the shorter range which stems from hydrogen storage. When used in a security or military context the vehicle cannot run out of fuel in the middle of a mission as that could then negate some of its benefits by having to put people in harm's way to recover it. Also, in some theatres of operation the refuelling infrastructure could be limited placing more emphasis on range. Using this as motivation this research has been conducted with the aim of providing an integrated software and hardware alternative for the implementation of FCEV technology on security platforms. The proposed solution looks at how to intelligently manage the vehicle´s energy taking into account not only component efficiency, but also more abstract considerations as the situational context around it. As such this thesis is structured as follows:

- o The following half of Chapter One will provide a detailed analysis on the overall environmental, technological and political setting of what has been discussed in this introduction; literature references will finally make their appearance.
- o Near its end Chapter One will look into the State of the Art regarding FCEVs power management and control systems. This analysis will then allow for the introduction of the research topic. Finally details for the criteria used to select surveillance platforms as the object of analysis for this research will be discussed.
- o Since the chosen energy supply system is that of an FCEV, Chapter Two will describe the numerical model for the PEM fuel cell.
- o Once a power system is established Chapter Three will describe the vehicle powertrain model and how it incorporates the Fuel Cell Stack system into it.
- o Chapter Four will provide a description of the control software concept.
- o Chapter Five will then provide a detailed explanation of the complete set of algorithms employed to create a novel intelligent energy management solution and how it fulfils the research objectives.

o Chapter Six describes the test platform used to validate the control system algorithms.

o Chapter Seven is dedicated to the discussion of the results obtained from simulation and physical testing.

o Chapter Eight will close with a discussion of the advantages, disadvantages, and further work. Finally, conclussions will be drawn and that will close this thesis.

Now, as promised the following section starts with the analysis of the overall context for this research. Since this research is only possible thanks to the support of the Mexican National Council for Science and Technology the contextual analysis will emphasise Mexico's specific situation.

1.1 World fossil fuel energy context

The 20th century saw the rise of the automobile as a feasible and commercially viable mean of transporting people and goods. Although some of the earliest prototypes where powered by electricity, the vehicles that finally made it into the market were powered by internal combustion engines. This was in no small part due the ease with which liquid fuels could be stored and transported on board. Unfortunately, with the growth of the global vehicle fleet, some problems have become clear:

A. Development became tied to fossil fuels from non-renewable sources.

B. Burning of these fuels results in the emission of chemical species that in turn can react with the surrounding environment to form "greenhouse gases" and photochemical smog.

C. Gasoline and diesel oil prices have risen gradually, forced by external conditions such as international conflicts, political manoeuvring or embargoes.

As already mentioned the inherent issue with depending on fossils fuels is that petroleum is a non-renewable energy source. In North America, between 1999 and 2009, proven oil reserves have fallen 25.12% to 73.3 million barrels (British Petroleum June 2014). Mexican oil reserves contribution to this figure fell from 53.11% to only 16% in the same period. Although exploration efforts between 2012 and 2014 have increased the reserves forecast for Canada and the U.S.A. in a combined 17%, Mexican reserves have fallen 1% in that same time period (British Petroleum June 2014). In global terms oil production increased 0.6% whilst consumption rose 1.4% (British Petroleum June 2014) putting pressure on exploration and development of new oil fields which as numbers show has not been successful for all countries.

Furthermore the economic impact of the unstable supply of petroleum in the 21st century has been negative. For example, in the U.S. during the summer of 2008 the price of a gallon of petrol reached USD$ 4.05. A considerable spike when compared to the price of the same commodity by the end of the same year of USD$ 1.59. In 2011 as a side effect of the Arab Spring, gasoline reached a price of USD$ 3.89 per gallon (E. I. Agency 2011). On 22 September 2014, average gasoline prices in the U.S.A. remained far above their 2008 levels at USD$ 3.353 per U.S gallon (U.S. Energy Information Administration 2014)

Closer to Europe, tensions in the Ukraine led to stockpiling of oil supplies by fuel vendors in anticipation of Western sanctions on Russia driving the price of crude oil higher (The Guardian 2014). In the U.K. as of September, 2014, JBC Energy, an independent oil & gas market research company, was cited by news

agency Reuters to believe that the coming winter together with continued tensions in the Ukraine could lead to a gas supply cut by Russia. Therefore many suppliers are also stockpiling gas to cope with potential supply disruptions (REUTERS 2014).

Another factor affecting the supply of fossil fuels is again the size of available exploitable reserves. As North African sources become embroiled in civil warfare, countries in other parts of the world have suddenly found themselves becoming big international players in the energy market. According to a report by the World Energy Council Venezuela's reserves jumped from 9,842 Mt (Metric Ton) of oil to 40,450 thereby surpassing Saudi Arabia as the country with the most abundant reserves. (World Energy Council 2013) This change in balance has brought about a new set of rules in South America as the leftist Venezuelan government has been using its new found wealth to influence the region's political agenda. (Noticias 24 2014), (El Universal 2012). Even the U.S.A. who advertises itself as "leader of the free world" is sacrificing this image by having Venezuela, whose government is frequently accused of installing a de facto dictatorship, become its third largest supplier of crude oil. (U.S. Energy Information Administration 2014).

Finally and to quickly cover the main topics related to fossil fuel use, the 2009 CO_2 emissions inventory linked to motor vehicles in the U.S. was of 1,718 million metric tons, an important increment of 16% over the previous decade (E. I. Agency 2011). In Mexico, according to information from the OCDE, CO_2 emissions from fossil fuel burning increased from 357 million tons of CO_2e, in 2000, to 438 million tons of CO_2e by 2007 (Organisation for Economic Co-operation and Development 2010).

1.2 Mexico fossil fuel energy context

Now that a global picture has been described it is time to ask what the situation is like in Mexico. A country where a considerable share of its government's income comes from oil exports (Banco de México 2010) and where fossil fuel pollution has caused its capital, Mexico City, to implement many programs to reduce airborne harmful emissions.

1.2.1 Government Income from Petroleum Sales

Mexico, even with its closed fuel market, has not remained unaffected by the increase in fuel prices. In 2008 a standard gallon of Premium fuel was sold at MXN$31.71, reaching MXN$ 38.63 in March of 2011 (Petróleos Mexicanos 2011) and MXN$ 48.61 in July of 2014 (Petroleos Mexicanos 2014) . On this same topic, Table 1-1 shows a breakdown of income sources for the Mexican federal government. This study, published by the central bank "Banco de México", established that in 2008 income from state-owned oil company PEMEX made up 43.72% of the Budget for that fiscal year. In 2009, the real income from the same source fell to 36.69%, a reduction of 7% in just one year (Banco de México 2010), (Banco de México 2011). International factors have helped increase the price of crude oil which has helped the government's budget, where income from oil rose to 41.10% in 2013, but it still has not reached its previous heights (Banco de México 2012) (Centro de Estudios de las Finanzas Públicas - Cámara de Diputados 2014).

Table 1-1 Public Balance Sheet for 2008 through to 2013 (with information from (Banco de México 2010), (Banco de México 2011), (Banco de México 2012), (Centro de Estudios de las Finanzas Públicas - Cámara de Diputados 2014))

Mexican Government Public Balance						
Year	2008	2009	2010	2011	2012	2013
Budgetable Income*						
Oil	1054.6	874.2	973	1101.9	1189.5	1290.1
Taxes	1207.7	1125.4	1314.3	1436.7	1517	1561.6
Other	150.1	382.8	178.1	176.9	214.7	287.44
% from oil	43.72%	36.69%	39.47%	40.58%	40.72%	41.10%

*Not considering income for state workers social security

1.2.2 Vehicle Emissions

At the time of the last emissions inventory in Mexico, 1999, medium to heavy trucks (GVWR >= 3859 kg) made up only 30.62% of the national fleet (Instituto Nacional de Ecología 2006) yet they made up an important part of the total pollutant emissions linked to automotive sources:

65.30 % of NO_x,

23.37 % of SO_x,

11.61% of CO, y

42.3 % of all Solid Particulate Matter (PM_{10}, $PM_{2.5}$ y PM_3).

Since then the vehicle fleet has doubled its size; whilst the share of it belonging to medium/heavy platforms has remained relatively constant (Instituto Nacional de Estadística y Geografía 2009). Although in relative terms this means that NO_x emissions remain near 65.30%, their magnitude has risen from 284,490 Mg/year, in 1999, to 617,003 Mg/year, in 2011 (assuming that average emissions per vehicle remain constant, a fair assumption as Mexican diesel specifications were not updated in this time period). Of the previous pollutant emissions figures, diesel engine exhaust accounts for 41% of PM_x and 62% of NO_x emissions in national fleet terms.

As discussed in previous sections Mexican oil reserves have fallen consistently in recent years, yet the country remains a G15 economy with a sizeable commercial vehicle fleet. To answer the inherent need of fuelling these vehicles, and the accompanying industry, local and federal governments are looking towards other sources of energy which can help reduce the country's internal fossil fuel requirements for production of electricity and vehicle propulsion (Comision Federal de Electricidad 2012), (Estados Unidos Mexicanos-Presidencia de la República 2008).

1.3 Military context of fuel usage and supply

Currently, military forces are the main consumers of fossil fuels. From light reconnaissance vehicles to main battle tanks and fighter jets all use some sort of petroleum derivate. Obviously armored vehicles are heavier than many private or commercial ones and do not operate of smooth paved roads. Instead they operate on rough steep trails which in turn increase fuel consumption. In the sea, navy frigates bet their survivability on their speed and acceleration which again can increase their fuel consumption over a civilian ship of equivalent length, beam and weight. In the air, military aircraft operate at high speeds and low altitudes which increases drag losses and drive fuel consumption up. It is therefore of paramount importance that fuel is available to a fighting force in enough quantities to support its mission. Unfortunately no army carries with it a portable oil refinery and drilling equipment, so fuel must be transported from the home front to the point of use. This requires in many cases dangerous treks through exposed territory, like the Afghanistan-Pakistani border crossings, where convoys and their highly flammable cargoes are open to enemy attack. Maj. David Thompson, U.S. Army, describes in a monograph for the United States Army Command and General Staff College that during operation Iraqi Freedom there were 279 recorded deaths of military or contracted civilian personnel during convoy operations (Thompson 2012). Using this information and with data from the American DoD Defense Casualty

Analysis System it can be calculated that 3.5% of military casualties during Operation Iraqi Freedom happened during convoy security operations. The figures do not contemplate the number of wounded personnel.

In Afghanistan in 2014 the Taliban insurgency has mounted a number of attacks which have cost ISAF at least 237 fuel tanker trucks (RT 2014), (PressTV 2014), (GBTimes 2014). A standard fuel tanker can carry 10,000 liter, so the losses inflicted amount to 2,370,000 liters of fuel at a minimum.

Looking at the previous information it is no surprise that the U.S. military is formally looking at increasing its energy efficiency and for new, more secure, sources with programs like "Great Green Fleet".

From what has been discussed so far it is clear that the international energy scenario is not proving to be simple therefore it is safe to argue that using fossil fuels for energy supply is consistently becoming a more complicated affair. It is therefore necessary to analyse other options. In efforts to approach the issue, worldwide discourse about replacement energy sources in the context of global warming usually drifts towards the renewable kind.

1.4 Renewable Energy Context

According to the World Energy Resources: 2013 Survey: Summary the global share of electricity produced by renewable sources has increased from 10% in 1993 to 16% in 2013; an important increase to consider especially when the extra share was taken from fossil fuels. (World Energy Council 2013). These numbers by themselves signal a shift not only in the market, but also in policy as many renewables, like solar, come with governmental subsidies. (The

Guardian 2014). In Mexico this comes in the shape of "green mortgages". Here the state's INFONAVIT, an institution whose purpose is to give out loans for lower to middle class housing, increases the amount available to loan when the property includes eco-friendly technologies like solar water heaters (INFONAVIT 2014).

Though as promising they may there is still no "renewable silver bullet". Many of these technologies have only started on their road to maturity. This has been possible in no small part to the money invested in them in the light of global warming. So, which one could be the one for motor vehicles? As already briefly mention in the introduction BEVs and FCEVs are the main contenders for the creation of a vehicle with little or no pollutant emissions. Yet, batteries are heavier and take longer to recharge which does not make for a versatile platform which could face small trips one day (where BEVs excel) or cover longer distances the next (where refuelling will be necessary and therefore is where FCEVs take the lead). Due to its eco-friendly emissions and shorter refuelling times FCEVs are seen as the most viable contender in the long run. It behoves then the discussion of where and how to obtain its fuel: Hydrogen.

1.4.1 The Case for Hydrogen

Amongst all the alternative fuels the most feared is hydrogen. Although biodiesel and ethanol are flammable the inferno of the Hindenburg is still present in popular culture. Hydrogen is a versatile chemical. It is present in almost everything around us bonded together with carbon or oxygen to create most organic compounds and as such it is rarely found in its diatomic stable form H_2. Yet it has many advantages versus other eco-friendly fuels. Its production does not drive food prices to increase (USA Today 2011) nor does its use spur an informal energy economy like biodiesel does by having people "brew" unknown quantities of fuel in their backyards. Another advantage for

hydrogen is that it already has a strong production infrastructure as it is commonly used for fossil fuel refinement. It is then safe to say that as the demand for fossil fuels has increased so has the demand for hydrogen. Unfortunately approximately 62% of hydrogen is currently obtained from natural gas or other hydrocarbon fuels with an additional 18% coming as a by-product of petrol fuel reforming (Meier 2014). Yet hydrogen can also be obtained from less pollutant sources like chemical electrolysis. The electricity for this process can be obtained from hydropower plants, Eolic generators or solar panels. Even if hydrogen were to be obtained from fossil fuels the fact that fuel cells are more efficient than IC engines would mean a reduction of greenhouse gas emissions. Moreover as clearly set out by Smith, from the University of St. Andrews, there are many infrastructural advantages for hydrogen For example, when a BEV is used for inner city transportation the vehicle might require at least two charging points to be installed; one at the owner's home and the second at his or her destination. Although the cost of a charging point might not be as high as the cost of a full-fledged hydrogen fuelling station a single station can service a greater number of vehicles just like existing petrol stations do. (Smith 2013).

Finally, hydrogen also could reduce the security concerns for all nations which today do not have their own oil reserves. Japan, the world's third largest oil importer (U.S. Energy Information Administration 2014), has been working since 1973 in developing a Hydrogen economy by having its government work closely with industry to drive costs down and develop the necessary technology (Manoj Pudukudy 2014). Not far from Japan, South Korea, the world's fifth largest importer of oil (U.S. Energy Information Administration 2014), in a similar manner to Japan has destined government funds to create the technology necessary to keep its industry green and growing by implementing initiatives like the High-Efficient Hydrogen Production Program and has coordinated with its industry to focus each sector in an individual technology. For example, Samsung Energy Enterprise is working on the fuel cells for mobile applications

whilst car manufacturer Hyundai has developed fuel cell Sonata prototype, amongst others. (Manoj Pudukudy 2014).,

Even in oil rich nations like Canada, home of the largest oil reserves in North America (British Petroleum June 2014), hydrogen is being looked at, but for different reasons. In Canada the interest in non-fossil fuels relies on ecological and social reasons (Ali Almansoori 2012). On this topic the Canadian government has published a report titled "Canada in a Changing Climate: Sector Perspectives on Impacts and Adaptation" where it outlines how it projects the country will be affected by global warming, what actions it is taking to combat greenhouse gases and adapt face extreme weather events. To combat greenhouse gas and particulate emissions, it funded in the year 2000 the Canadian Transportation Fuel Cell Alliance to demonstrate and evaluate fuelling infrastructure for FCEVs (Government of Canada 2013). More recently in 2008 the NSERC Hydrogen Canada alliance was created to bring together government and academia to develop the technology necessary for safe production, storage and deployment of hydrogen (NSERC Hydrogen Canada 2014). It is no surprise then why Ballard Energy Systems, a leading supplier of fuel cells which has an alliance with Ford and Daimler AG, is based in Burnaby, British Columbia.

1.5 Current Fuel Cell Vehicle Development

As already discussed, motivated by the existing situation many countries around the globe have begun working towards the development of new propulsion technologies with which to replace the internal combustion engine as the nucleus of private and commercial powertrains.

The E.U. has put together several initiatives which have resulted in a strategic development agenda oriented towards bringing fuel cell technology to the

market place as a commercially viable power generation option; this with the intent of not only implementing such systems within automobiles, but also as the power supply for portable devices (European Comission, Directorate-General for Research Cooperation | Energy 2008) and residential heating. Table 1-2 show the key assumptions for one such effort, the Joint Technology Initiative for Fuel Cells and Hydrogen.

Table 1-2 Key Assumptions on Hydrogen & Fuel Cell Applications for 2020 Scenario. Extract from (European Comission, Directorate-General for Research Cooperation | Energy 2008)

	Road Transport
EU Hydrogen (H2)/ FC units sold per year projection 2020	0.4 million to 1.8 million
EU cumulative sales projections until 2020	1-5 million
EU Expected 2020 Market Status	Mass market roll-out
Average power FC System	80 kW
FC system cost Target	< 100 €/kW (for 150,000 units per year)

More recently the E.U. launched in July 2014 the "Fuel Cells and Hydrogen 2 Joint Undertaking," under the Horizon 2020 framework. This initiative seeks to further stimulate fuel cell development in order to accelerate its commercial deployment by investing €1.33 billion. (European Comission 2014)

Meanwhile, General Motors Corp. has been testing a fleet of fuel cell vehicles globally and at its development centre in Mainz-Kastel, Germany. Representatives of the company stated in 2010 that they considered fuel cell technology ready, and that the next road block would be implementing the refuelling infrastructure (Just-Auto 2010). In 2014 and after having invested over USD$ 2.5 billion in fuel cell development General Motors stated that it had

achieved progress in cutting the overall cost of the fuel cell system by removing redundant system components and reducing the content of precious metals (Crothers, "With Toyota in its rearview mirro, GM talks fuel-cell cars" 2014). This latest technology was installed in a series of 119 Chevrolet Equinox sport-utility vehicles which were then given to real customers in California for them to drive and provide feedback on the vehicle's performance. Furthermore GM has partnered with Honda and the U.S. military to continue developing hydrogen fuel cell technology (McEachern 2014).

In Korea, the federal government has vowed to inject USD$ 2.7 billion into the automotive industry, from 2010 to 2015, to turn the country into a green growth powerhouse. These funds are to be aimed towards manufacturing of fuel cell, electric, hybrid electric, plug-in hybrid electric and clean diesel vehicles. The target is to market 1.2 million vehicles by 2015, of which 900,000 will be exported (Just-Auto 2010). Also, Hyundai has completed development of the new Tucson ix FCEV, a fuel cell version of its Tucson SUV. This vehicle has 95% of its components manufactured locally (Just-Auto 2010). As of 2014 the Tucson FCEV is available in Southern California for a 36 month lease. Hyundai will take care of maintenance and fuel costs (Hyundai Motor Company 2014).
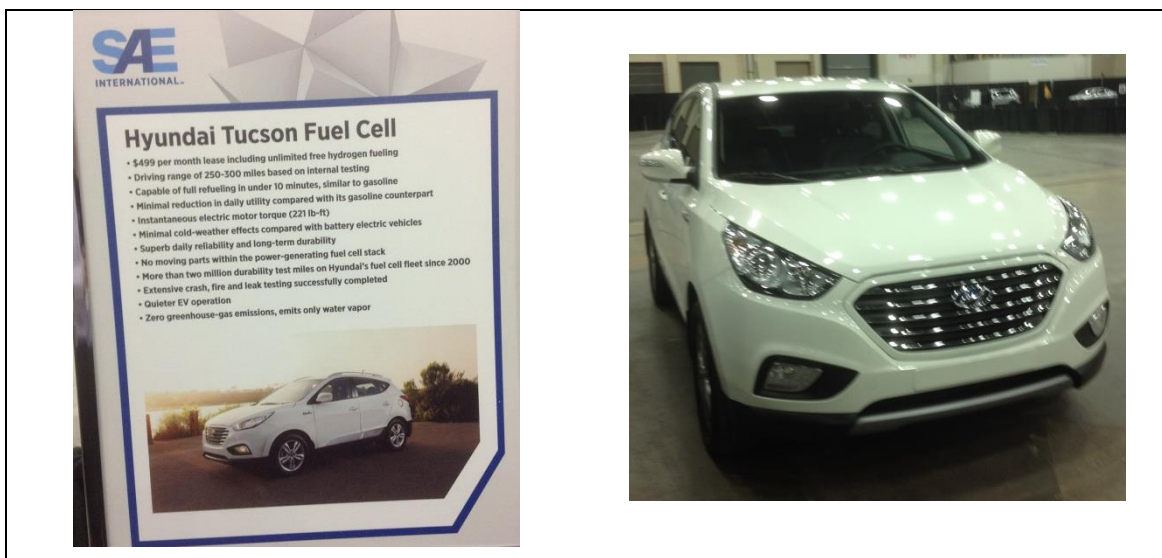
Figure 1-1 Hyundai Tucson FCEV at a test drive event during the SAE World Congress, April 2014

In this same context, in early March of 2011 Toyota Motor published a statement saying that by 2015 the company planned to start selling a fuel cell sedan. This contemplated cutting the cost of the fuel cell stack to one twentieth of what is was back in 2008. To achieve such a reduction Toyota planned to use less platinum in the fuel stack, simplify the design of the fuel cell and lower the cost of the carbon fibre reinforced hydrogen storage tanks (Greimel 2011). The successful outcome of this vehicle development programme was visible when Toyota announced, in June 2014, that it will start selling its first commercial fuel cell vehicle in April 2015 in Japan, and release it in the U.S. and Europe during the summer of the same year. (Crothers, Toyota to launch first hydrogen fuel-cell vehicle for about $70K 2014).

Lastly, in the security market there is already interest in the use of hydrogen fuel cells. In 2008, the U.S. fuel cell council, an organization made up private and public entities like Daimler, Nissan, Ford and Siemens, published a presentation about how hydrogen fuel cells can be used in different applications. More importantly how they could be used by military forces (Rose 2008). In it is mentioned that not only could fuel cells be used on armoured vehicles which are on silent watch operations, but also on unmanned ground and aerial platforms which already have an electric motor (Rose 2008).

If application in those areas is successful, then it could be possible that armoured electric vehicles, like the Russian Krymsk, could also receive a fuel cell to power its electric drivetrain. Krymsk is a remote controlled version of the BTR-90 Rostok which was tested in 2013. It uses a diesel-electric hybrid which can run on its main internal combustion engine for normal operation, or electric motor when on silent mode (Strategic Defence Intelligence 2013). The vehicle's silent operation range is limited by battery capacity. Currently the BTR-90 platform utilizes a 380 kW diesel engine (IHS Jane's 2014). To convert to fuel cell use the manufacturer could use a 340 kW fuel cell like the one developed by Green GT (Green GT 2012). In its original use the fuel cell system can run

for less than an hour due to the reduced fuel packaging space available. Yet inside or around the armoured cell of a heavy vehicle more fuel could be packaged to increase the range.

It is therefore a credible assumption that fuel cells can be used for military purposes.

1.6 Control Software State of the Art

Now that the case for the use of fuel cells and the need for alternative ways to fuel a vehicle has been made it is time to review the field of energy management systems for electrified vehicular platforms. In recent years this area of research has been the object of many efforts which attempt to tackle the problem from different perspectives.

A first approach, which is tied strongly to environmental concerns, is that of using less fuel; and by that it means using either less petrol/diesel, for the case of hybrid vehicles, or less hydrogen, in the case of fuel cell hybrids. In these plaforms the fuel-burning device is paired with a battery and the overall intention is to extract as much energy from the battery as possible to reduce the amount of vehicle gasesous emissions. This would be very simple, yet it has to be done whilst protecting the battery from deep discharges. Both objectives are contradictory and hence the need for intelligent systems arises. A first example is that of Qi *et al* (Qi Li 2012)*.* They propose a system which is fuzzy logic based for a fuel cell/battery/ultracapacitor hybrid where the target is to consume as little hydrogen as possible by using the battery. The system operates in one of four modes oriented at exploiting each component to support the others as best as possible. For example, the battery and fuel cell can work together to drive the vehicle, or the fuel cell can do it on its own whilst recharging the battery. On the other hand the ultracapacitor is employed to keep the battery

from discharging too deeply, which would shorten its life. How the vehicle´s power demand is met whilst the energy supplied arbitration is happening is the task of a Mamdani Fuzzy Logic Inference System (Mamdani 1981). This system splits the energy requirement between all the supplies and also selects their mode of operation. Another example of the classical approach is that of Hannan, Azidin and Mohamed (M.A. Hannan 2012). In their work the authors propose a control system for a fuel cell/battery/ultracapacitor hybrid which uses vehicle inputs like pedal offset, power duration load and battery capacity to choose one operational state amongst seven possible options. All energy supplies are connected to a common switching device. This device opens or closes a current flow path between the powertrain´s electrical machine and each supply depending on the actual operating mode. Once more the focus of the work is to use less hydrogen whilst keeping the battery as highly charged as possible during the drive cycle. A slightly different take on the classical approach is that taken by Dib *et al* (Wissam Dib 2014). The basis of their approach is that of getting the vehicle to use less energy to save energy, in other words their aim is to optimize the powetrain´s efficiency. To achieve this end they analyze three different energy usage assessment techniques dubbed Offline Assessment, Online Assessment and Online Assistance. In the first case a trip is evaluated in terms of the ratio between actual energy consumption and the ideal case. This ratio produces what is called an Eco-Driving score. If the score is equal to one, the vehicle used the minimum estimated energy. If it is less than one the consumption was too high. To obtain the ideal energy consumption figure the problem is stated as an optimal control problem where a controller estimates the best way to drive the vehicle along the specified route using as little energy as possible. If the calculation is done after the fact it is called *offline*. In the second case, the trip is subdivided into a group of smaller trip segments. At the end of each segment the eco-driving score is computed and the driver is given the result. Finally, in Online Assessment the optimization routine is run continuously in time. By using the same trip segments which were defined for the former method, online assessment uses GPS or similar geospatial systems to determine where the vehicle is. It then estimates the eco-

driving score for what remains of the segment based on the user driving style. The score is presented to the driver at every calculation time step. In essence then all of the previous research projects have used different intelligent systems to achieve the same goal of using less fuel. Yet the last case gave a slight cue of another major avenue of energy management research.

In this second avenue systems started using geospatial systems, such as GPS, to create a preview of the route ahead. For example, Zhang and Vahidi (Zhang March 2012) propose a multilayer system which uses long and short time horizons. For the long time horizon dynamic programming is once again used to create the optimum energy consumption benchmark for the whole trip, whilst in the second layer a shorter trip horizon is estimated by an equivalent consumption minimization strategy. This strategy can be computed fast enough to be used as an online solution. Once this figure is computed it is used in a control system which manages the power split between battery and internal combustion engine with the objective of minimizing fuel consumption. Another example of geospatial systems is that of Yu, Tseng and McGee (Yu 2012). In this case a machine learning algorithm, clustering, is used to estimate electric vehicle range by identifying driving patterns and grouping them together by high impact characteristics which include energy consumption data. To train this type of system the authors reject the notion of using only known driver data as they consider it incomplete and prone to leaving gaps in the system. To solve this off-board data sources are considered which provide trip related data such as road type, traffic levels and speed limits to create a driving pattern library which is then reused in future trips. The pattern library is then used to compute a highly accurate range estimation.

So far the evolution of energy management software has followed the route of going from simply making sure less fuel was used, be it hydrogen or otherwise, to employing more elaborate geospatially based techniques to predict how much energy will be spent and try to have the driver spend less of it. Yu, Tseng

and McGee (Yu 2012) took things a step further by starting to use machine learning to have the vehicle accurately predict how much energy would be spent. Machine learning is a relatively recent branch of artificial intelligence where the system is meant to deal with unknown future information and make forecasts based on known data, its training data set. Training a system of this kind requires that the training set be selected to be as representative as possible of what the vehicle will encounter out in the open road. In a series of papers Park, Chen, Kuang, Masrur *et al* (Park November 2009), (Murphey October 2012), (Y. L. Murphey January 2013) elaborate on how to train a machine learning predictor. In their first effort (Park November 2009) they propose a neural network for road and congestion prediction to be used by a HEV. This systems works more like a classifier than a continuous predictor. Its training data comes from eleven facility specific drive cycles. Each drive cycle represents a given type of road with an associated traffic congestion load. By capturing vehicle data a feature selection algorithm feeds the neural network which in turn selects a road type and traffic congestion profile from its training set. A vehicle trip is segmented into sliding time windows inside which the controller captures data and makes the road type and traffic congestion selection to then compute the optimal battery and engine torque control commands. To validate their system the optimal online parameters are compared against a dynamic programming offline result for the same drive cycle. Both online and offline results match with a margin of error lower than one percent. Unfortunately, this holds true for a drive cycle made up of training set profiles. The proposed controller is unprepared to face real world driving.

In their second effort, published as a series of two articles (Y. L. Murphey October 2012), (Y. L. Murphey January 2013), the authors tackle the real world driving issue by adding to their sliding time window analysis of a driving trend. This new concept aims to capture driver short-term actions and is used as an input to the neural network in charge of generating the power command for the battery. This augmented version of the algorithm presented (Park November

2009) has similar accuracy, but with the added benefit of including driver behaviour into the learning process. In the final paper of the series (Y. L. Murphey January 2013). The authors use their neural networks to once more classify their road type and congestion level and also return to the neural network for determining driving trends. The target is again to issue power split commands for the battery and engine. To build on previous results for versions of their control system are trained with different philosophies. By generating several dynamic programming optimum energy expenditure routes they train each power split controller with ever growing and more complex data sets. Going from single to multiple SOC point routes, which distinguish both road types and driving trends to finalize with a controller version which only takes into account the latter parameter. The results are interesting as the controller with the best fuel saving results was that where there are multiple initial battery SOC, but a single target ending SOC. This is somewhat predictable and more applicable to real life as it simulates a vehicle which can start a journey with any random battery conditions, but aims to finish it at a given point. This allows for stability in the controller as there is a fixed set point for the battery which in turn influences the power split commands for the engine.

In a few words the state of the art for energy management aims to accomplish the following:

- Minimize the amount of hydrogen or petrol fuel used for a given route.
- Employ geospatial data to better predict near and long term energy expenditure.
- Protect the battery by maintaining its state of charge above a certain level or within an optimal operating band.
- Use artificial intelligence to adapt to future unknown driving conditions using previously experienced training data.
- Obtain geospatial data from off-board sources as an option to using past training data.

By acknowledging the previous a gap can clearly be seen and takes the following form. No author has yet considered the effects on both internal combustion engines and fuel cell reactors of environmental conditions. Changes in altitude reduce atmospheric air density, and air is a vital actor in both fossil fuel and hydrogen power producing reactions. In the presence of less air both devices are less efficient. Also, environmental temperature can greatly increase the ancilliary losses of both power generation systems by requiring more energy for cooling purposes as heat rejection becomes more difficult in hotter environments. So, take for example the learning sets of (Y. L. Murphey January 2013) each of the eleven road type and traffic congestion profiles can require very different energy levels for a certain set of environmental conditions. Also even in the best of conditions in developed countries there is never a guarantee that off-board information sources will be available as network coverage not only depends on infrastructure, but is also weather and is line of sight dependant. Therefore energy management strategies which rely on such sources could very well be left lacking needed information half way through a trip. Finally, and this is very important for security related applications, no mention has been made of fuel supply availability. No author has mentioned who recharges the battery to a optimum state of charge after their strategy drained it to save fuel; that bill has to be paid by someone. In addition, what if the route is too long for the available on-board energy? No system has been proposed which tackles this possibility. In civiliandom there are always fuel stations not far away, yet in a security deployment that could not be the case, so what happens then?

The previous questions need answering, and that will be the foundation for this research undertaking.

1.7 Research Definition

Now that the surrounding context has been analysed and given all the facts discussed until now, the objective of this PhD project will be to create a design of an intelligent based power management system for a fuel cell converted vehicle for military use.

The universe of military applications and vehicles is vast, so to further define the scope of this work a single vehicular platform should be selected. From what was discussed in previous sections it can be established that an appropriate candidate for researching the incorporation of a fuel cell powertrain is the diesel medium duty platform weighing between 3859 kg and 8853 kg. Gross Vehicle Weight (GVW). This is because as mentioned before the common automobile has already been the subject of fuel cell power research, which in terms covers much of the problem in national fleet size terms. Yet, medium and heavy duty diesel platforms contribute with a large portion of polluting emissions; even exceeding what lighter more numerous vehicles emit in at least two harmful chemical species. Furthermore, vehicles of the weight class (8853 kg > GVW > 3859) are commonly used for delivery and frequent start-stop applications (school and public transport) within cities, which in turn means that idle operation is more frequent translating into higher fuel consumption. The versatility of these vehicles also means that no one option can be all encompassing, yet one stands out as a big power user: The surveillance vehicle.

1.7.1 Platform Definition

The selected type of vehicle was identified as one of the possible worst case scenarios. These platforms can include, amongst many things, extra lights, winch, PTO, rescue equipment which means that they operate closer to their

GVW limit more frequently than other configurations. It is important to mention that in terms of weight what sets these vehicles apart from a regular goods delivery truck are the excess electrical loads. Together, loads and weight create a higher demand for power than what is observed on a regular automobile or pick-up truck. The following sections list out the basic requirements the new FCEV architecture must meet.

1.7.1.1 Power and Torque

Existing diesel offering of the afore mentioned weight class can generate from 894 Nm to 1100 Nm, together with more than 230 kW of traction power.

1.7.1.2 Payload and Curb Weight

Curb weight (CW) is that of a vehicle ready to be used, it considers things such as the fuel and whatever equipment is permanently installed on it. In this case, the minimum CW is 3,100 kg. with a payload of up to 5,750 kg.

1.7.1.3 Electrical System

Whilst supplying power to the drivetrain the network must also feed up to 360 ampere of DC electrical current for the ancillary loads (lights, electrical equipment, etc.).

1.7.2 Power Supply Architecture

As mentioned in the introduction, in present time fuel cell vehicle work has been focused mainly in the light duty market (GVW < 3859 kg.) This is expanded by C.C. Chan in (C. Chan 2007) and (C. A. Chan 2010). Basically the fore runners of the electric architecture for long ranges are Battery Electric Vehicles (BEV) and Fuel Cell Electric Vehicles (FCEV). Veziroglu and Macario (Veziroglu 2011) make a very detailed analysis of all the societal and otherwise hidden costs in the technology chain for these new technologies.

From the previous sources key facts can be identified:

1. BEV and FCEVs will be commercially available by 2020.

2. Deep market penetration will happen by 2050.

3. In the present BEVs are better suited for start-stop urban applications, where FCEVs are best for long range extra-urban areas.

4. FCEVs have the lowest gaseous pollutant emissions, and depending on how hydrogen is supplied to them this technology is the most environmentally friendly of all electric powertrains.

5. In terms of hydrogen storage on board the vehicle liquid hydrogen is the best option as it is lightweight and takes less volume than high pressure gas storage systems.

6. Most importantly due to the slower reaction times of the fuel cell chemical reactor the best way forward for a vehicle that is competitive in performance against an IC engine powered one is a new type of Hybrid Electric Vehicle (HEV): Fuel Cell/Battery hybrid.

In this new approach, fuel cell reactors work hand in hand with a Battery Energy Storage System (BESS) to provide an electric drivetrain with the power and current required to meet driver torque requests. This new context requires a more complex and thorough integration of a growing number of systems. According to C.C. Chan (C. Chan 2007) depending on the level in the control structure where a given subsystem exists, the more detailed and complex is its function. As a controller works with more dynamic systems (i.e. motors, valves) the faster it must be, whereas the higher arbitration or intelligent management logic can be slower as it also takes decisions in the long run (i.e. battery State of Charge management).
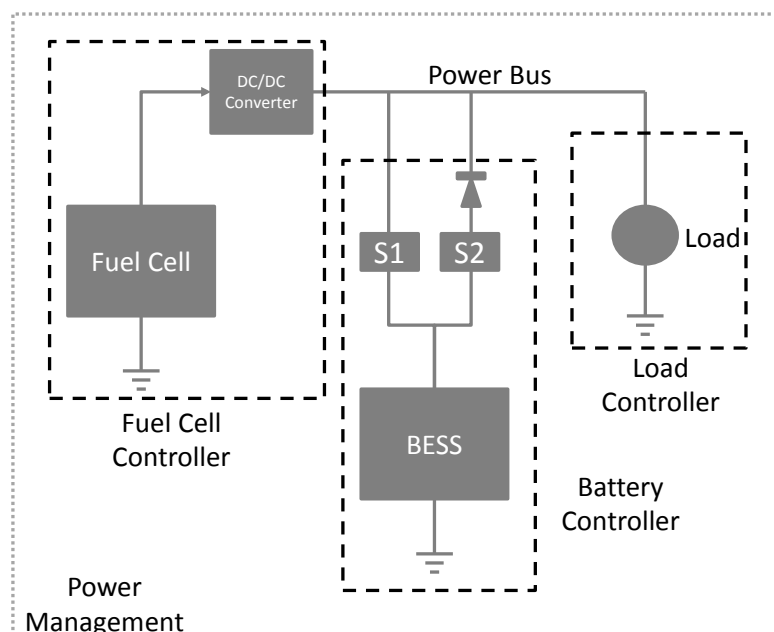
Figure 1-2 Dual Converter Power Architecture
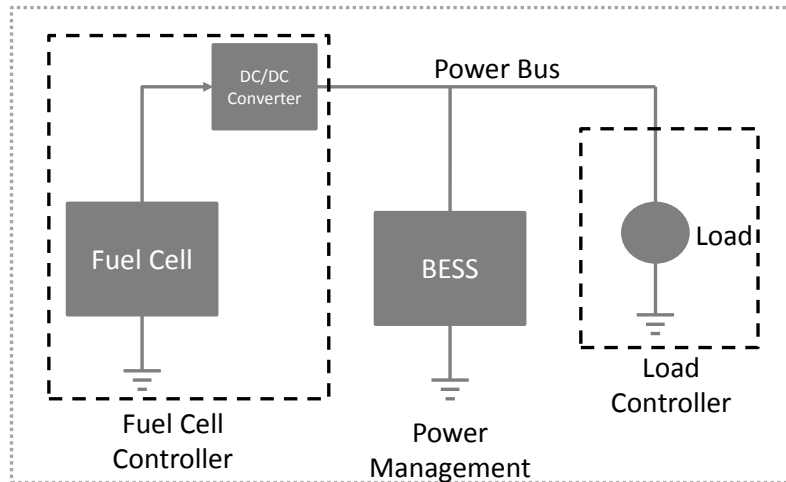
Figure 1-3 Single Converter Power Architecture

Figure 1-2 is a clear example of such systems; while the individual controllers operate at a quicker rate as needed by their individual systems, the higher level supervisory logic acts at a slower speed in part because it works on a wider horizon of time. This means that as the quicker controller is busy operating its own component, the supervisory power management system can be making decisions that will affect the vehicle on the long term, such as allowing the battery to discharge more or increasing the fuel cell load further depleting the hydrogen tank, etc. Figure 1-3 shows a more simple system where the battery is allowed to react freely to bus loading. In this case the power management supervisory logic is not as powerful as it only has control over the load and fuel cell. These two figures exemplify the main trends in research discussed in (Erdinc 2010). This work will focus on the former type where each component has its own converter.

1.7.3 Proposal

To properly assert whether a vehicle as described before can be powered by a fuel cell electric architecture and answer the questions possed in Section 1.6 (Control Software State of the Art) the aim of this research will be to:

   a. Develop a vehicle model for simulation which can reproduce real life dynamic results. This model will then be augmented to include the electrical drivetrain and its matching electricity supply system.

   b. Published information indicates that on-board hydrogen storage is still far from being able to match the energy per liter density of liquid fossil fuels. Because of this an important component of the control software will be a forecasting and management engine which will optimize how energy is used in the vehicle to maximize its range with a target to match the existing fossil fuel range levels. This software will be based on artificial intelligence. The design philosophy to be used is that just as the human brain has specialized sector for specific functions, this software will employ different algorithms in a manner where each works where it is best suited.

   The software will be divided into different layers which will have authority over specific calculations and/or subsystems in order to better manage and control each energy consumer, and self-configure the vehicle if needed. Because of the military nature of the proposal no GPS will be considered when crafting an energy forecast. The forecasts should be built around user provided mission information, and when absent the vehicle must be able to

create an artificial mission profile from historical usage data and update this profile as the mission progresses.

c. Because of the high cost of a full size prototype a scaled down working prototype of the vehicle architecture will be built to analyse the operation in real life of the electrical supply system and its control software.

d. Design a test bed for vehicle functional testing. To create repeatable set of tests a new bespoke chassis dynamometer will be built which can be used to test the vehicle under different road load conditions. This test bed will be built such as it is able to also accept vehicles of similar dimensions, but different energy supply systems.

The test bed will incorporate a virtual world environment where the artificial intelligence system will be tested to determine its capability to control other electrically powered platforms (aerial or otherwise) based on the concept that all vehicles move in three dimensional space, and as such, albeit considering certain restrictions, should be capable of being controlled by the same system. Finally the system should be portable so as to be taken to other research facilities.

e. To maximize the impact of this research the fuel cell supply and control system will be made such that it can operate on any type of electric vehicle and allow for changes in the operating environment such as humidity, temperature and altitude.

1.7.4 Benefits

There will be a number of benefits which will result from this work:

a. As fuel cells are chemical reactors the rate at which they produce usable power is limited by reaction dynamics. Furthermore the fuel cell considered for this work will employ a compressed air intake system which in itself also has its own dynamics such as compressor spool time. These two effects together with the higher power demands associated with a vehicle of the described weight class will impose heavy and sudden power transients on the supply system which need to be understood. Once this is complete the risks and implications of building such vehicles will be better known.

b. Military surveillance platforms incorporate another challenge and that is the use of armour plating. This necessary equipment makes dissipating any waste heat all the more difficult. Another benefit of this work will be a proposal of cooling system strategies and requirements.

c. Current FCEVs operate in parallel with at least two kinds of power supplies in parallel, be it a fuel cell/battery tandem or fuel cell/ultra-capacitor one. Some work has been done with all three, but again not on this kind of platforms, therefore another benefit will be the understanding of what a power management system must observe to fully control all three energy storage devices working together.

1.7.5 Contributions

a. Firstly, one contribution will be the creation of a novel test bed where the given vehicle can be tested in a repeatable fashion under different road conditions.

b. Secondly, it will demonstrate how different artificial intelligence methodologies or algorithms can interact with each other to create an integral system. This system will deviate from the norm by using energy and not power as the control parameter for managing the supply and storage components on board.

c. Finally, the requirements, risks and benefits for creating a medium duty armoured surveillance FCEV will be understood.

2 FUEL CELL MODEL

Chapter Summary:

At the heart of the power generation system for the target platform sits a PEM Fuel cell. This chapter will elaborate on the elemental physics and chemistry of PEM hydrogen fuel cells and the ancilliary components required to support its operation.

2.1 PEM Fuel Cells

Proton Exchange Membrane Fuel Cells (PEM Fuel cells) are widely used nowadays for vehicle applications. This is in part due to their low operating temperature (50-100 ^{O}C (Khalig 2010)) which matches the engine bay temperatures already experienced with IC engines.

Fuel cells are chemical reactors that create an electrical current from the reaction of hydrogen and oxygen inside a stack of polymer membranes (Gou 2010).

2.1.1 Fuel Cell Voltage / Current Relationship.

$$Anode: 2H_2 \rightarrow 4H^+ + 4e^-$$ **2-1**

$$Cathode: O_2 + 4H^+ + 4e^- \rightarrow 2H_2O$$ **2-2**
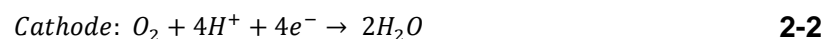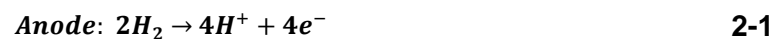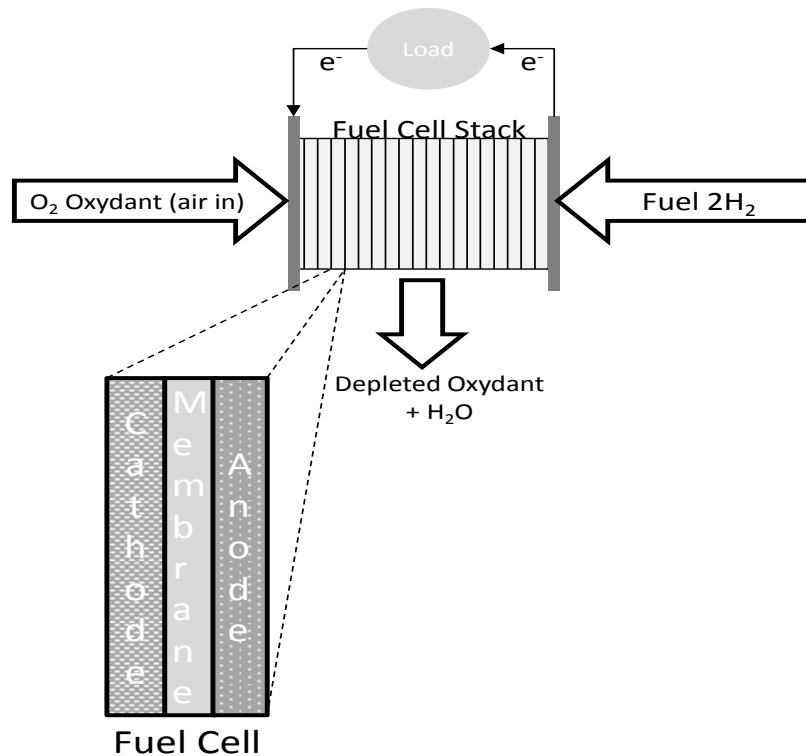
Figure 2-1 Fuel Cell Stack Diagram, from (R. J. Felix Moreno 2013)

Figure 2-1 shows a simplified diagram of a fuel cell stack. Each cell is made up of a cathode, anode and membrane or electrolyte. High pressure hydrogen gas enters the cell through the anode manifold and tries to go through the electrolyte. The membrane allows only positive ions, or protons, to pass while blocking negatively charged electrons. These electrons are collected and sent over an electric circuit creating a current which powers the load. Both protons and electrons reunite at the cathode where they react with oxygen in the pressurised atmospheric air to form water. The reaction at the anode is described by Equation 2-1, whilst the cathode process is described by Equation 2-2. The typical voltage of a Nafion 117 PEM fuel cell is 1.2 volts of direct current. To obtain higher voltages a string of such cells are connected together electrically and through manifold piping to create a stack.
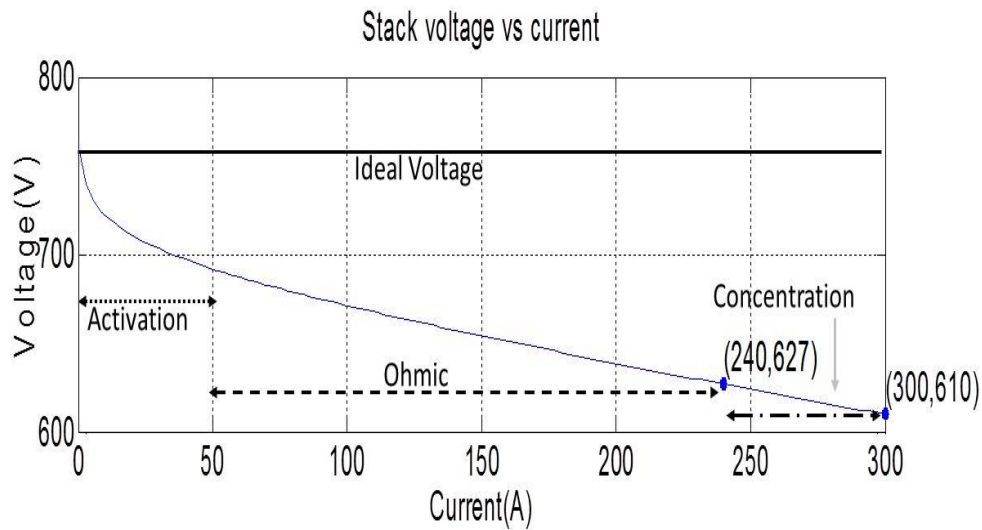
Figure 2-2 PEM Fuel Cell Polarization Curve

The real power that can be drawn from a fuel cell is far from ideal. Natural losses are dominated by three kinds (Gou 2010):

- Activation losses, v_{act}: Caused by the transportation of electrons and the creation and destruction of chemical bonds on the opposing sides of the fuel cell. Because the reaction at the cathode is more complex and slower the local conditions on this side dominate when calculating these losses.

$$v_{act} = N \frac{RT}{2\alpha F} \ln \left(\frac{I_{fc} + I_n}{I_o} \right) \text{ [V]} \qquad \textbf{2-3}$$

Where

N is the cell number in the stack,

R is the universal gas constant, in 8.3144 [J/(mol.^{o}K)],

T is the fuel cell temperature, in [°K],

α is the charge transfer coefficient,

F is Faraday`s constant, 96,485 in [C/mol],

I_{fc} is the output current density of the fuel cell, in [A/cm^2],

I_n is the internal current density, in [A/cm^2],

I_o is the exchange current density, in [A/cm^2].

These losses dominate the left-hand side of the curve as this is where electron flow is initiated to create an electrical current for the load.

- Ohmic losses, v_{ohm}: This resistance or loss arises from the polymer membrane´s reluctance to allow the transfer of protons and from the resistance of the electrode and collector plates to transfer the freed electrons (Pukrushpan 2004)

$$v_{ohm} = i\, R_{ohm} = i\left(\frac{t_m}{\sigma_m}\right) \text{[V]} \qquad \textbf{2-4}$$

Where

i is the fuel cell current density, in [A/cm^2],

R_{ohm} is the internal electrical resistance, in [Ω.cm^2],

t_m is the thickness of the membrane, in [cm],

σ_m is the membrane conductivity, in [1/ (Ω .cm)], which is a function of fuel cell temperature and water content.

This component comes to dominate the middle section of the polarization curve where electron flow has already been established. Its behaviour is nearly linear.

- Concentration losses, v_{conc}: Results from the shortage of reactants caused as they have been consumed by the reaction itself, hence its name. As there is no more material to subject to the reaction mechanism the voltage begins to drop rapidly due to the lack of available electrons to maintain the same power level. It dominates the right-hand side of the polarization curve (Pukrushpan 2004).

$$v_{conc} = i \left(c_2 \frac{i}{i_{max}} \right)^{c_3} \text{ [V]} \qquad \textbf{2-5}$$

Where

i is the fuel cell current density, in [A/cm^2],

C_2 and C_3 are constants obtained by experimental data regression,

i_{max} is the maximum current density for a Nafion 117 fuel cell, in [A/cm^2].

Fuel cell current density is defined by the stack current and the active area of the cell (Pukrushpan 2004).

$$i = \frac{I_{st}}{A_{fc}} \text{ [A/cm}^2\text{]} \qquad \textbf{2-6}$$

Where,

I_{st} is the stack current, in [A],

A_{fc} is the active area of the fuel cell, in [cm^2].

The ideal voltage of an individual cell is given by (Barbir 2005)

$$E_0 = \frac{-\Delta G}{nF} = \frac{237,340 \; [J/mol]}{2(96485)\left[C/_{mol}\right]} = 1.23 \qquad [V] \qquad \textbf{2-7}$$

Where

ΔG is the Gibbs free energy, in [J/mol],

n is the number of electrons in the hydrogen reaction,

F is Faraday´s constant with a value of 96,485 [C/mol]

Taking into account the effect of temperature and reactant pressure Equation 2-7 is expanded (Barbir 2005) to obtain the open circuit voltage, E.

$$E = E_0 - \frac{RT}{nF} ln \left(\frac{P_{H_2} P_{O_2}^{0.5}}{P_{H_2O}} \right) \qquad [V] \qquad \textbf{2-8}$$

Finally the stack voltage, V_{st}, is given taking in account all the losses and the number of cells involved.

$$V_{st} = n_{cell} \; (E_o - V_{act} - V_{ohm} - V_{conc}) \qquad [V] \qquad \textbf{2-9}$$

The only new term is n_{cell} which is the number of fuel cells in the stack.

It is clear now that the voltage and current relationship has been established how a higher load current will negatively affect the stack output voltage level. This is a factor that needs to be considered in the design of the fuel cell power generation system. Higher currents will need more cells in the stack to keep up with the power demands of the whole architecture which can in turn be offset by

a larger cell active area to in turn reduce the instantaneous current density which would also have an effect on the losses.

2.2 Fuel Cell Power Generation System

The previous section elaborated on how the internals of the stack worked to generate power for the overall system. Next a quick glance at the complete system will be taken to understand the complexity of what the individual fuel cell controller must include in order to interact with the rest of the vehicle in a harmonious manner.
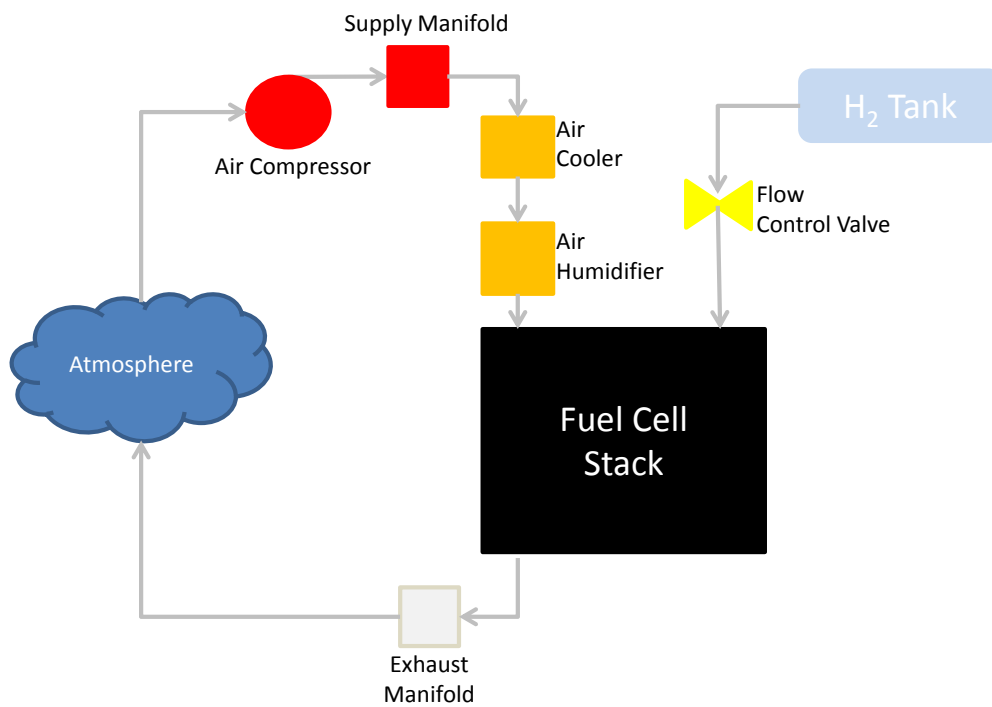
Figure 2-3 Fuel Cell Reactant Flow Subsystem
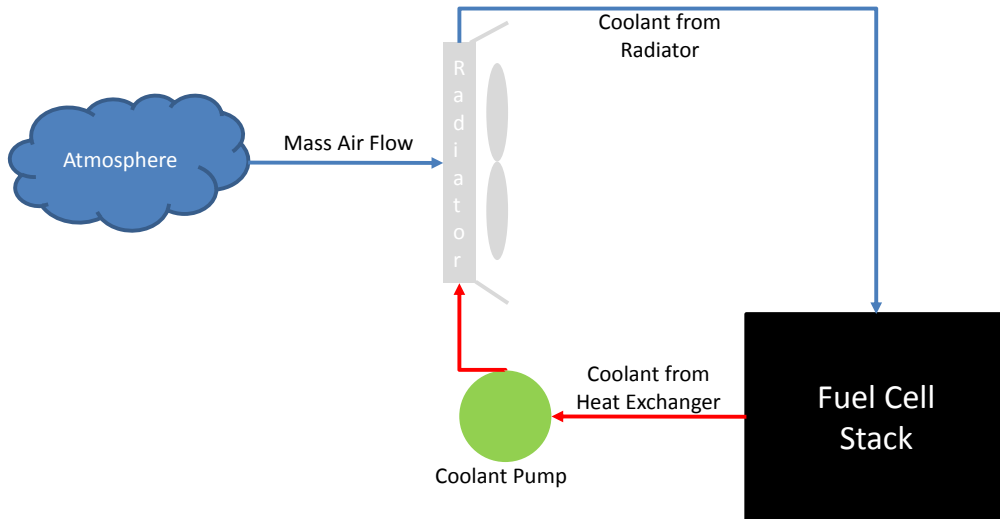
Figure 2-4 Fuel Cell Stack Cooling Subsystem
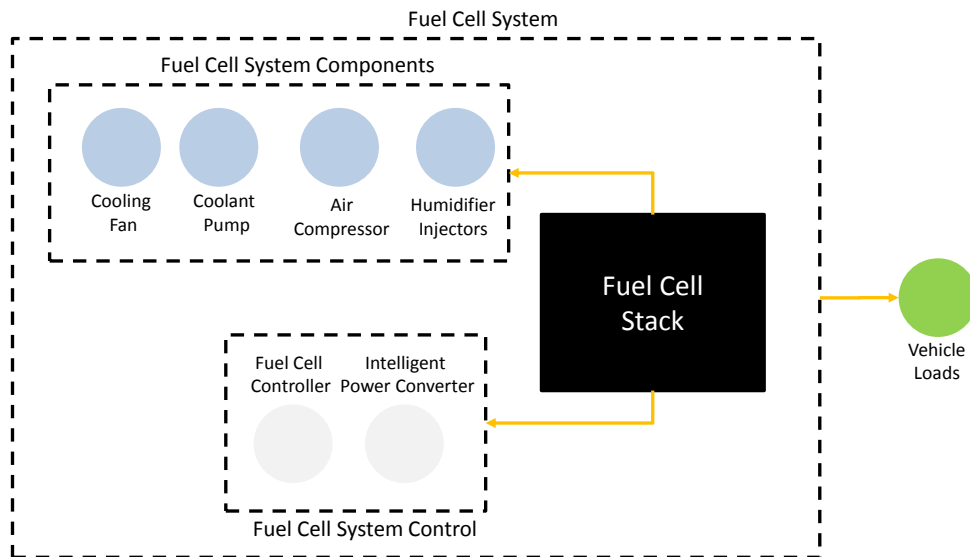
Figure 2-5 Fuel Cell Power Distribution

Figure 2-3 through Figure 2-5 exemplify the different subsystems that comprise the fuel cell system. There are multiple domains that need to be understood in order for the power generation to be successful as not only does the fuel cell need to supply the load, it also needs to make sure its own individual subsystems operate correctly and are fully supplied with power. This only adds more complexity, but also makes controlling the electric vehicle more interesting.

3 POWERTRAIN MODEL

Chapter Summary:

When an electrical power supply system is mounted in a ground vehicle it must be prepared to cope with random and varying energy demands. To attack this modern PEM fuel cell power supply systems can be enhanced by the addition of parallel supplies such as batteries. Furthermore, vehicles do not operate in ideal conditions which need to also be reproduced to fully assess and simulate a platforms operation. This chapter will then discuss how the vehicle model incorporates provisions for varying driving conditions, power demands and environmental conditions.

3.1 Li-Ion Battery Model

The architecture for Fuel Cell vehicles is best supported when additional means of energy storage are included in the power system. In this case a generic Li-Ion battery model has been included based on the works of Tremblay, *et al* (Tremblay May, 2009), and Spiegel (Spiegel 2008). In a first instance the authors of the aforementioned works derived a generic model considering similar dynamics for charging and discharging, but then progressed to a more detailed equation where dynamics are different for each current flow regime. Unfortunately, the later version of the model considered parameters that are not readily available (i.e. polarization resistance), so in order to move forward a hybrid model was created which uses polarization voltage, K, instead of resistance. Then, the open circuit battery voltage, E, is calculated as follows.

Discharge Model:

$$E_{Batt} = E_0 - K\frac{Q_{rated}}{Q_{rated} - \int_0^t i(t)dt} + A exp\left(-B\int_0^t i(t)dt\right) \qquad [V] \quad \textbf{3-1}$$

Charge Model:

$$E_{Batt} = E_0 - K\frac{Q_{rated}}{0.1Q_{rated} + \int_0^t i(t)dt} + A exp\left(-B\int_0^t i(t)dt\right) \qquad [V] \quad \textbf{3-2}$$

Where E_0 is the open circuit voltage, in [V], K is the polarization voltage, in [V], A is the exponential voltage component, in [V], B is the charge at the end of the exponential zone of the discharge curve, in [Ah], finally i is the battery current, in [A]. The 0.1 factor in the denominator of second term of the charge equation is there to model degrading over use as will be illustrated by Figure 3-4. Overall the main assumptions of the model are that internal resistance is considered constant, there is no Peukert effect, there is no sensitivity to temperature and no self- discharge is considered.

To understand and calculate the values of the different terms in Equations 3-1 and 3-2, please consider Figure 3-1. The figure shows how battery voltage output drops as current draw accumulates until the rated value is reached.

43
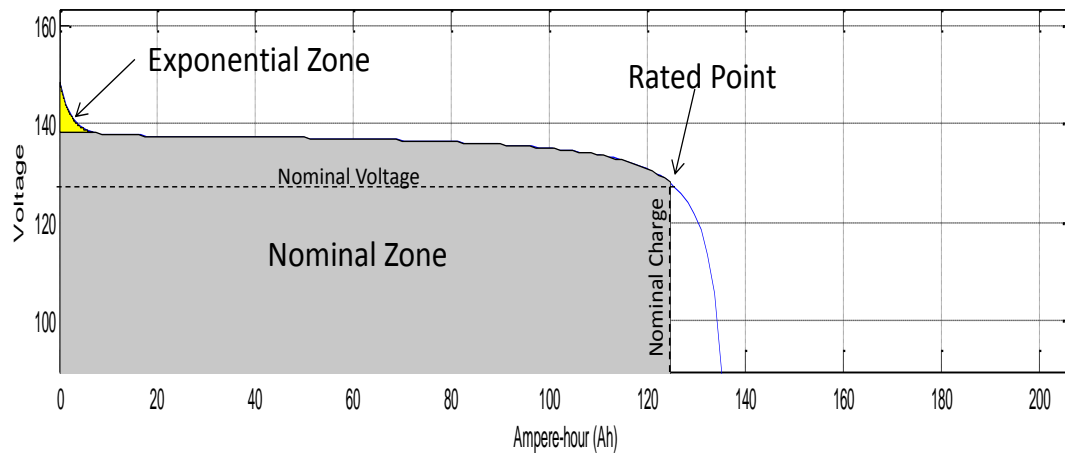
Figure 3-1 Typical Li-Ion battery discharge curve. Based on a 128 Vdc, 138 Ah battery pack

All parameters for the model are deduced from discharge characteristics and assumed to be the same for charging. Based on the previous graph the following estimations have been made in order to calculate the different parameters of Equations 3-1 and 3-2.

Nominal current	$I_{nom} = \dfrac{0.43}{1hr} Q_{rated}$	[A]	**3-3**
Nominal charge	$Q_{nom} = 0.904\, Q_{rated}$	[Ah]	**3-4**
Exponential zone charge	$Q_{exp} = 0.0491\, Q_{rated}$	[Ah]	**3-5**
Fully charged voltage	$E_{full} = 1.21\, E_{nom}$	[V]	**3-6**
Exponential zone voltage	$E_{exp} = 1.08\, E_{nom}$	[V]	**3-7**
Voltage drop along exponential zone	$A_{exp} = E_{full} - E_{exp}$	[V]	**3-8**
Charge at the end of the exponential zone	$B_{exp} = \dfrac{3}{Q_{exp}}$	[Ah]	**3-9**

44

Polarisation Voltage, derived per assumptions from Equation 3-1.

$$K_{pol} = \frac{\left(E_{full} - E_{nom} + A_{exp}\big(exp(-B_{exp}Q_{nom}) - 1\big)\right)(Q_{rated} - Q_{nom})}{Q_{nom}}$$ [V]   **3-10**

Voltage Constant,

$$E_{0,batt} = E_{full} + K_{pol} + Ri - A_{exp}$$ [V]   **3-11**

Parameters Nominal voltage, V_{nom}, Internal resistance, R, and Rated capacity, Q_{rated}, are inputs from manufacturer data. The battery current "i" is calculated in the power bus section of the model.
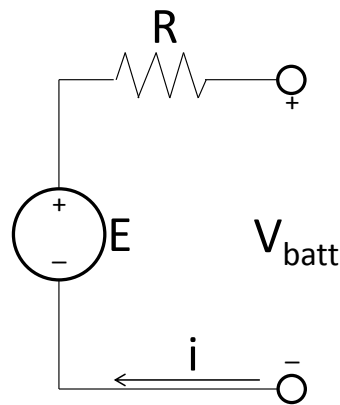
Figure 3-2 Battery Model Electrical Circuit Diagram

From the electrical circuit the equation for the total battery voltage, V_{batt}, can be derived.

$$V_{batt} = E + Ri$$ [V]   **3-12**
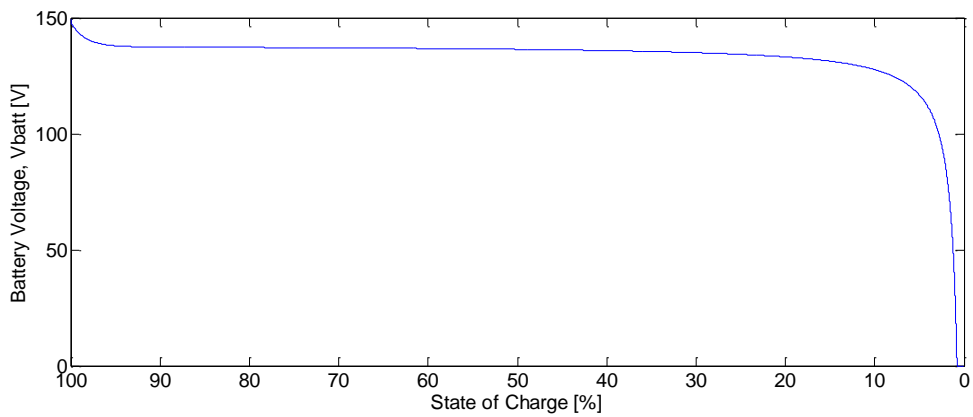
Figure 3-3 Discharge Curve Produced by Battery Model

The above figure shows the performance of the battery model. This plot was produced by running the model with 128V and 138 Ah nominal parameters with an internal resistance of 9.27mΩ. The discharge current was 138 A.
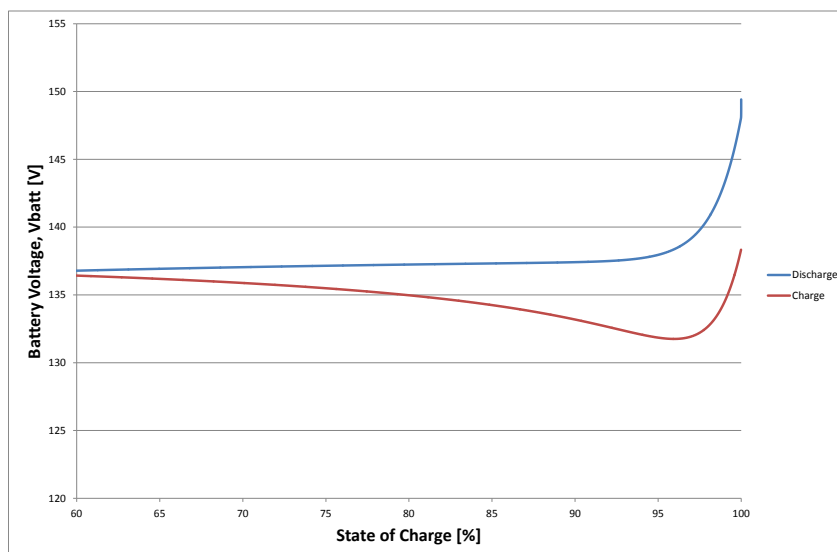
Figure 3-4 Effect of discharge on Final Recharge Battery Voltage

Analysis of the previous two figures shows how the model´s performance is acceptable. It exhibits exponential behaviour near full charge, followed by a near linear nominal region, finishing off at a drop off area right of the nominal point. Figure 3-4 helps visualize how the model degrades the battery not

46

allowing the fully charged voltage to return to the original value once the battery has been discharged. Battery degrading can be tuned to more closely mimic a given battery´s behaviour.

3.2 Application Specific Fuel Cell Model

At the heart of the power generation system sits the hydrogen fuel cell. In this case a PEM fuel cell has been considered due to its lower operating temperature (< 100 ^{o}C) when compared with other options such as Solid Oxide Fuel Cells (> 500 ^{o}C). The model is divided into two major blocks: Air Compressor and Fuel Cell Stack.

The model developed was built using inputs from (Pukrushpan 2004), (Spiegel 2008) and (Gou 2010) together with original contributions when either the proposed architectures or assumptions did not meet or match the model´s own assumptions or operational requirements.

3.2.1 Electric Compressor

At the air inlet of the fuel cell system is the compressor. This component is in charge of supplying an air mass flow adequate to at the same time keep oxygen partial pressure inside the cathode high enough whilst also making sure the available mass of oxygen needed for the chemical reaction meets the stoichiometric requirement. Pukrushpan, *et al* (Pukrushpan 2004) propose a model derived for one Allied Signal compressor first discussed in (Cunningham 1999).

The main derivation of the compressor model can be found in (Pukrushpan 2004). Constant pressure and ambient temperature are assumed in the execution of the model in (Pukrushpan 2004), yet that does not fit the purpose of the system described in this work. To solve this, a number of modifications where made.

3.2.1.1 Ambient Pressure and Temperature Dependencies

To account for changes in atmospheric conditions a dynamic estimation of the ambient pressure is done following road cycle inputs. Changes in altitude were considered via a look-up table included in every system that has either ambient pressure or air density as an input (i.e. cooling radiators). Each sub-model used the altitude above sea level to determine, through Internal Standard Atmosphere data, what values to use.

Table 3-1 ISA Temperature Lapse Rates for different altitudes

Geopotential Altitude Above Sea Level [m]	Temperature Lapse Rate [^{o}K/km]
0 – 10,999	-6.5
> 11,000	0.0

Inlet Air temperature was calculated as follows:

$$T_{air} = \left(T_{base} + T_{offset}\right) + a(H_{Vehicle} - H_{base}) \qquad [^{o}K] \qquad \textbf{3-13}$$

Where:

T_{air} is the inlet air temperature, in °K,

T_{base} is the base layer temperature per ISA standards, in °K,

T_{offset} is the temperature delta for the specific simulation run, in °K,

a is the layer temperature lapse rate, in °K/m,

$H_{Vehicle}$ is the geopotential altitude of the vehicle, in m,

H_{base} is the layer base geopotential altitude, in m.

Atmospheric air density was calculated then by assuming air as an ideal gas.

$$\rho_{atm} = \frac{p_{vehicle}}{RT_{air}} \qquad [kg/m^3] \qquad \textbf{3-14}$$

$p_{vehicle}$ is the atmospheric air pressure at the vehicle altitude, in m, which is calculated using Equation 3-15.

R is the gas constant for air with a value of 287.058 J/(kg.°K),

Finally, to be able to compute the air density in Equation 3-14, $p_{vehicle}$ needs to be computed beforehand as follows:

$$p_{vehicle} = p_{base} \left(\frac{T_{air}}{T_{base}}\right)^{-\frac{g}{aR}} \qquad [Pa] \qquad \textbf{3-15}$$

Where,

p_{base} is the base layer pressure, in Pa,

g is the acceleration due to gravity, taken constant at 9.81 m/s² as geopotential altitude is being considered.

In this manner all sub-models, including the fuel cell stack and compressor, which depend on atmospheric parameters can have updated data should the road cycle require it.

3.2.1.2 Results

Running the model with the previous modifications provided data on how each system is affected by variations in atmospheric conditions.

In the case of the fuel cell system a load ramp from 0 to 275 amperes was applied at different altitudes with ambient temperature of $33^{o}C$.

Figure 3-5 illustrates how as altitude increases the fuel cell compressor´s ability to feed the supply manifold with air decreases together with its density. Also, as the inlet air pressure decreases the pressure ratio across the compressor increases meaning higher power consumption and less overall system efficiency as the fuel cell uses more energy to drive its own auxiliary components.

In Figure 3-13 the air capacity rate diminishes with altitude. As the air becomes less dense the "cold side" of the radiator can accept less energy. This in turn drives results in a higher operating temperature for the stack which again impacts its efficiency.
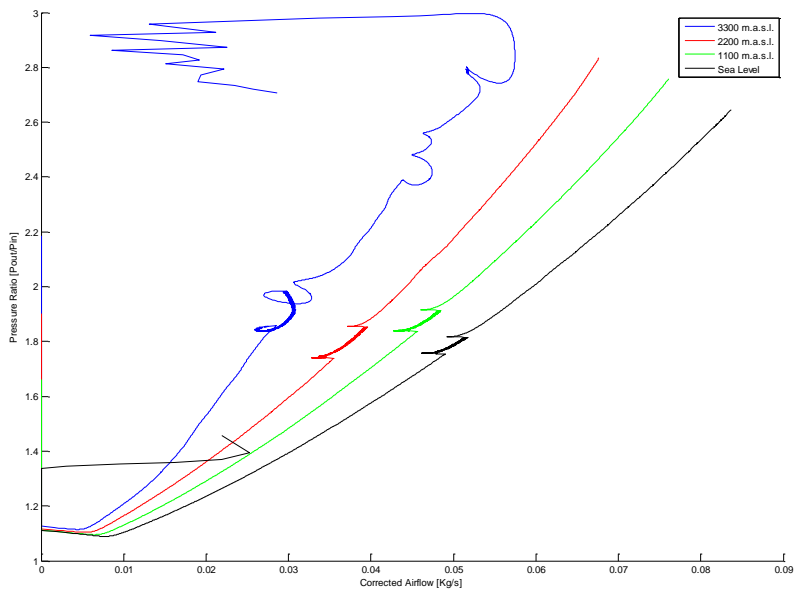
Figure 3-5 Compressor Operation from Sea Level to 3300 m.a.s.l.
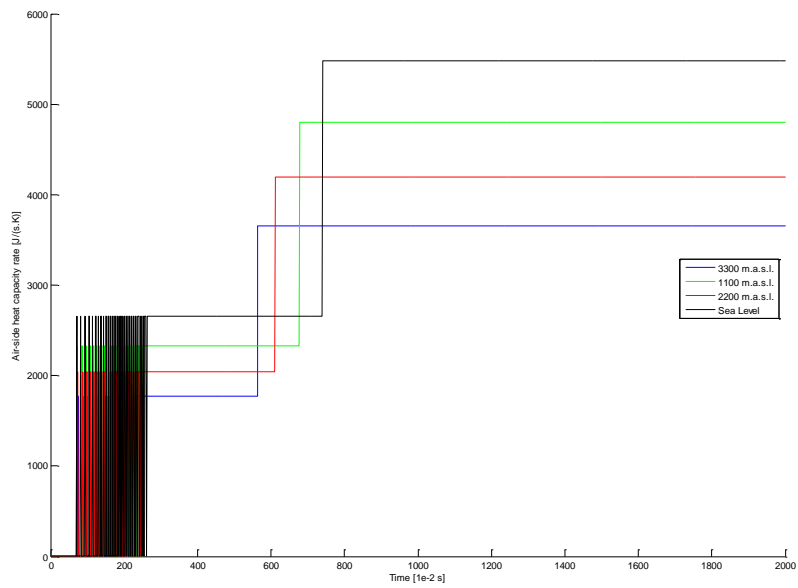
Figure 3-6 Main Cooling Radiator Air Side Heat Capacity Rate From Sea Level to 3300 m.a.s.l.

3.2.2 Fuel Cell Stack

The fuel cell stack model from (Pukrushpan 2004) was modified to accommodate other control mechanisms that will be used to explore new control algorithms.

3.2.2.1 Return Manifold Throttle

The return, or exhaust, manifold was modified to consider a throttle plate instead of a fixed orifice. This modification could be used to explore the effect the pressure inside this segment of pipe has on cathode pressure and how it can be exploited for pressure build up at start up, etc.

Aono and Kowatari (Aono 2006) developed a throttle model for an internal combustion engine control algorithm. This equation is used with the original discharge coefficient from (Pukrushpan 2004) as the open throttle coefficient and the original references where modified to reflect its placement at the exit versus the inlet.

$$\dot{m}_t = c_t \frac{\pi}{4} D^2 \frac{P_{rm}}{\sqrt{T_{prm}R}} \sqrt{\frac{2\gamma}{\gamma - 1}(1 - \cos\theta)} \sqrt{\left(\frac{p_{amb}}{p_{rm}}\right)^{2/\gamma} - \left(\frac{p_{amb}}{p_{rm}}\right)^{\gamma+1/\gamma}} \quad \text{[mol/s]} \quad \textbf{3-16}$$

Where

C_t is the discharge coefficient,

D is the throttle plate diameter, in [m],

P_{rm} is the return manifold pressure, in [Pa],

P_{amb} is the ambient pressure, in [Pa],

γ is the ratio of specific heats,

T_{prm} is the return manifold temperature, in [^{o}K]

R is the ideal gas constant with value of 8.3144 [J/(mol.^{o}K)].

The throttle flow rate is obtained by multiplying the result of Equation 3-16 by the molar mass of air, in [kg/mol].

3.2.2.2 Humidity Control

Originally, the humidifier was controlled by taking in mind only the inlet air humidity and estimating how much water vapour should be used to keep the cathode at 100% humidity. Spiegel (Spiegel 2008) suggests also taking into consideration whatever water is produced during the chemical reaction. One benefit comes from this latter proposal: The model is more sensitive to changes to outside humidity and humidifier injection. In its original configuration there was always enough water inside the cathode, so that changes in ambient humidity were almost neglected. The final equation is as follows.

$$W_{v,inj} = \frac{M_v}{M_a}\frac{\emptyset_{des}P_{sat}(T_{cl})}{p_{a,cl}}W_{a,cl} - W_{v,cl} - W_{v,gen} \qquad [\text{kg/s}] \qquad \textbf{3-17}$$

Where

$W_{v,inj}$ is the injected vapour flow rate, in [kg/s],

M_v is the molar mass of vapour, in [kg/mol],

M_a is the molar mass of air, in [kg/mol]

ϕ_{des} is the desired humidity,

$P_{sat}(T_{cl})$ is the saturation pressure at the temperature of the air cooler, in [$^{\circ}$K],

$p_{a,cl}$ is the partial pressure of air in the humidifier, in [Pa],

$W_{a,cl}$ is the air cooler mass flow rate of air, in [kg/s],

$W_{v,cl}$ is the air cooler mass flow rate of vapour, in [kg/s]

$W_{v,gen}$ is the mass flow rate of vapour generated in the cathode reaction, in [kg/s].

3.2.3 Dual Stack and Battery Assistance

To be able to drive all the associated loads in the power system it was decided that a single fuel cell, which is rated at 75 kW, would not be enough as just the electric motor exceeds this rating. Therefore two fuel cells are considered to be connected in series together to make up a 150 kW "module", backed up by a 128 V/138Ah Li-Ion battery pack. The fuel cell characteristic plot at sea level is shown in Figure 3-7.
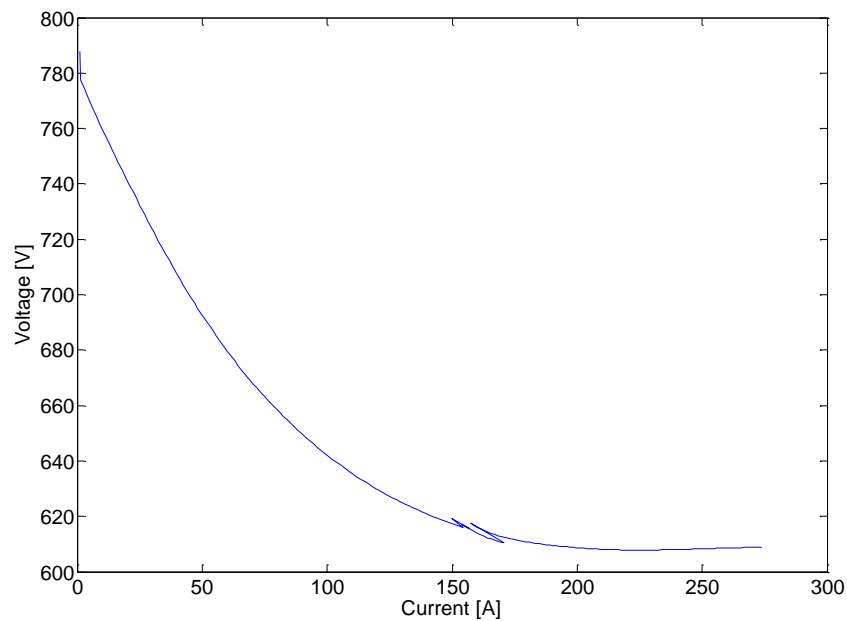
Figure 3-7 Combined Fuel Cell Module Characteristic Curve

3.2.4 Application Specific Parameters

Finally, the original model (Pukrushpan 2004) considers a stack made up from 381 cells with an active area of 280 cm^2. After initially testing the modelled vehicle using FTP-75 the power demand was such that higher voltage and current density was required, therefore the fuel cells which make up the module with the response shown in Figure 3-7 have 410 cells each, with an active area of 1024 cm^2, or 32 cm on a side.

3.3 Vehicle Model

The last section of the system is the vehicle longitudinal dynamics model. It is divided into six sections of what will become the road load (Genta 1997).
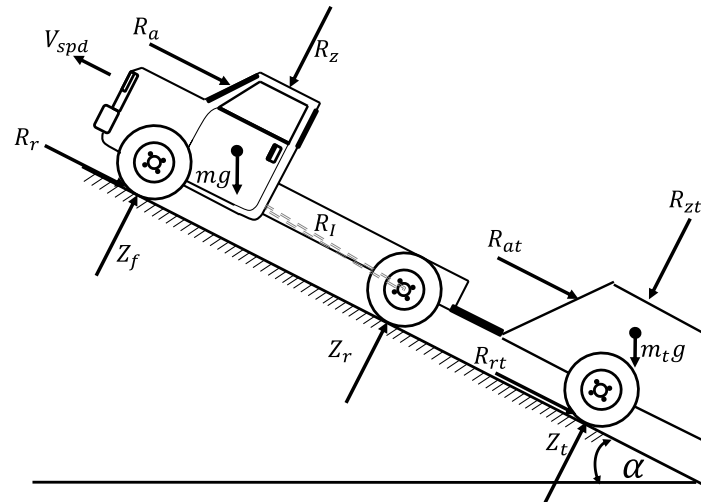
Figure 3-8 Longitudinal Forces Acting on the Vehicle

3.3.1 Rolling Resistance

Rolling resistance can be viewed as a way to describe how the weight of a vehicle impacts its motion. The equation also considers aerodynamic effects brought about by body components (Genta 1997).

$$R_r = f * (W + R_z) \qquad [N] \qquad \textbf{3-18}$$

Where,

f is the tyre friction coefficient (assumed $0.01+0.001*V_{spd}$),

W is the vehicle normal force on the ground, in [N],

R_z is the effect of body drag or lift (assumed zero for this model),

V_{spd} is the speed of the vehicle, [m/s],

$$W = mg \cos(\alpha) \qquad [N] \qquad \textbf{3-19}$$

Where

m is the vehicle mass, in [kg],

g is the acceleration due to gravity, [m/s^2],

α is the road slope angle, in [rad].

3.3.2 Aerodynamic Resistance

An important term for any road vehicle travelling at speeds where air, as a fluid, can be considered compressible is aerodynamic resistance to motion. In the case of the medium duty trucks considered it is of great significance as the frontal area is large compared to saloon or sports cars (Genta 1997).

$$R_a = C_d A_f \rho_{air}(V^2/2) \qquad [N] \qquad \textbf{3-20}$$

Where,

C_d is the drag coefficient,

A_f is the frontal area, in [m],

ρ_{air} is the atmospheric air density, in [kg/m^3],

V is the wind speed relative to vehicle speed, in [m/s],

$$V = V_{spd} + (V_{wind} * Wind\_Direction) \qquad [N] \qquad \textbf{3-21}$$

Where

V_{wind} is the wind speed, in [m/s],

Wind_Direction is the direction of the wind relative to vehicle motion. It takes values of zero for no wind, one for head wind and negative one for tail wind.

3.3.3 Inertia Resistance

As the vehicle accelerates or brakes it has to overcome its own inertia. This inertia must also consider that of all rotational components in the drivetrain, basically the equivalent rotational mass (Genta 1997).

$$R_I = \delta ma \qquad [N] \qquad \textbf{3-22}$$

Where

m is the vehicle mass, in [kg],

a is the vehicle acceleration, in [m/s^2],

δ is the equivalent rotational mass factor.

3.3.4 Gradient Resistance

Part of this work will be looking at how the proposed vehicle reacts to changes in road gradient. Also, some simulations will be performed to analyse take off from rest at a given slope angle (all components of Equation 3-23 have been introduced earlier) (Genta 1997).

$$R_\theta = mg\sin(\alpha) \qquad\qquad [N] \qquad\qquad \textbf{3-23}$$

3.3.5 Trailer Resistance

Perhaps the most complex of all loads, trailer resistance is that imposed on the powertrain by towing. It considers rolling, aerodynamic and gradient resistances in a single term (Genta 1997).

$$R_T = C_{td}A_{tf}\rho_{air}(V^2/2) \; + f_t m_t g\cos(\alpha) + m_t g\sin(\alpha) \qquad [N] \qquad \textbf{3-24}$$

Where

C_{td} is the trailer drag coefficient,

A_{tf} is the trailer frontal area, in [m^2],

m_t is the trailer mass, in [kg],

f_t is the trailer tyre friction coefficient (assumed to be 0.01+0.001*V_{spd}).

No dynamic weight transfer between trailer and vehicle is considered.

3.3.6 Vehicle Speed and Acceleration

Now that the forces acting on the vehicle have been defined it is possible to calculate its speed and acceleration.

$$a = \frac{\frac{(T_e i \eta)}{r_d} - R_B - \sum R_x}{m} \qquad [\text{m/s}^2] \qquad \textbf{3-25}$$

Where

T_e is the electrical machine torque, in [Nm], i is the gear ratio of the driveline,

η is the driveline efficiency, r_d is the wheel radius, in [m],

R_B is braking force, in [N], ΣR_x is the sum of all the resistance forces, in [N],

m is the vehicle mass, in [kg].

Vehicle speed is obtained by numerical integration of acceleration.

3.4 Summary of Assumptions

3.4.1 Permanent Magnet Synchronous Machine

- To calculate heat generation only copper losses are considered.
- The magnet remnant flux density, Br, does not deteriorate.

- Permeability of air does not change with altitude or ambient temperature.
- The rotor winding factor is 0.9.
- Stator core slots and teeth have the same width.
- Saturation is neglected.
- The back EMF is sinusoidal.
- Eddy currents and hysteresis losses are negligible.

3.4.2 Cooling System

- Air is treated as an ideal gas.
- ISA altitude factors assume 25 ^{o}C ambient temperature. Here it is assumed that any change driven by ambient conditions is negligible.
- Equation 5.27 estimates the temperature for a single fuel cell. It is assumed that both stacks work at the exact same temperature; hence any heat generated by one cell is doubled before being input into the radiator equation system. The result of the radiator model is then divided by two in order to calculate the stack temperature.
- The maximum input temperature for the main loop radiator is 80 ^{o}C, for the secondary loop is 100 ^{o}C.
- For purposes of air passage calculations the area formed by the fins is considered to be a perfect triangle.
- The coolant carries no bubbles.
- To calculate heat transfer resistance no fouling is considered, nor the resistance of the radiator materials.
- There are no air leaks around the radiators (all the air mass that passes through the grill makes it through the air paths).

3.4.3 Battery Model

- Internal resistance is considered constant.
- No Peukert effect.
- There is no sensitivity to temperature.
- No self-discharge is considered.
- All charging and discharging parameters are equal.
- The battery bank is made up of individual batteries connected in series. Each battery is described by Equation 3-12.

3.4.4 Fuel Cell Model

- All gases are considered ideal.
- The operating temperature of the stack is 80 ^{o}C.
- Cathode temperature is considered homogeneous all along its length.
- The return manifold temperature is considered constant and equal to the cathode outlet temperature.
- Hydrogen gas is considered to be 100% humid.
- The return manifold fully open throttle discharge coefficient is assumed to be the same as for the original exhaust pipe.
- For a full list of assumptions please refer to (Pukrushpan 2004).

3.4.5 Vehicle Model

- No tyre squash is considered.
- No dynamic weight transfer between trailer and vehicle is considered.
- There is no lift or down force from the body components.

3.5 Simulation Scenarios

Since the base vehicle for this work is based off a Ford Super Duty F-Series diesel truck, then the question of how to test the proposed system architecture model is not complicated, but not straight forward either. These trucks are sold in markets that require emissions homologation procedures which are similar to the U.S., EPA compliant markets, or Europe's, EURO compliant markets.

In the case of simulations run for vehicles similar to the F-250 pick-up, the cycle to be used would be the Federal Test Procedure 75 (FTP-75), for emissions, and Highway Fuel Economy cycle for city and extra urban fuel economy calculations (HWFET). For vehicles of the weight class above the latter, mainly above 9000 kg GVW, the heavy duty diesel transient cycle (HDDT), European Stationary (ESC) and Transient cycles (ETC) must be used for emissions and fuel economy calculations. Applicable legislation requires that all emissions homologation tests be run at either sea level or below 1,500 m.a.s.l. Although not required by all markets, but inevitably related to the surveillance vehicle scenario, cycle FTP-75 will be used to emulate a more aggressive high speed/acceleration driving. To validate the performance of each platform the following series of simulations will be performed:

Table 3-2 Simulation Scenarios

Weight Class	Emissions Cycle	Fuel Economy Cycle	Performance Testing
10,000 lbs > GVW =>8,353 lbs	FTP-75	HWFET	0-100 kph time, 10%, 20% and 30% gradient, US-06
19,500 lbs >= GVW >= 10,000 lbs	HDDT, ESC, ETC		0-100 kph time, 10%, 20% and 30% gradient, US-06

Since the ideal exhaust of a fuel cell power generation architecture is water, the target data to be provided by these test cycles, specifically the emissions ones, is how power is generated, managed and/or recovered during motoring or braking.

3.5.1 Emissions Cycles

The drive cycle plots or data tables are shown next.
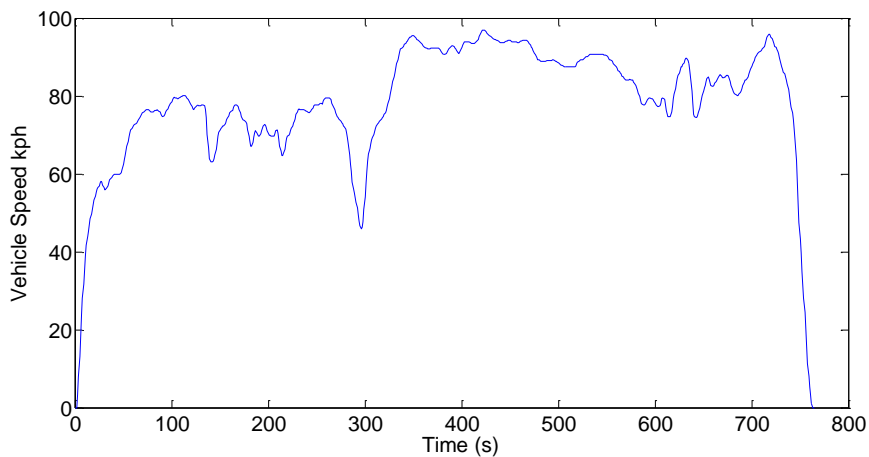
Figure 3-9 Highway Fuel Economy Test (HWFET) (E. P. Agency 2008)
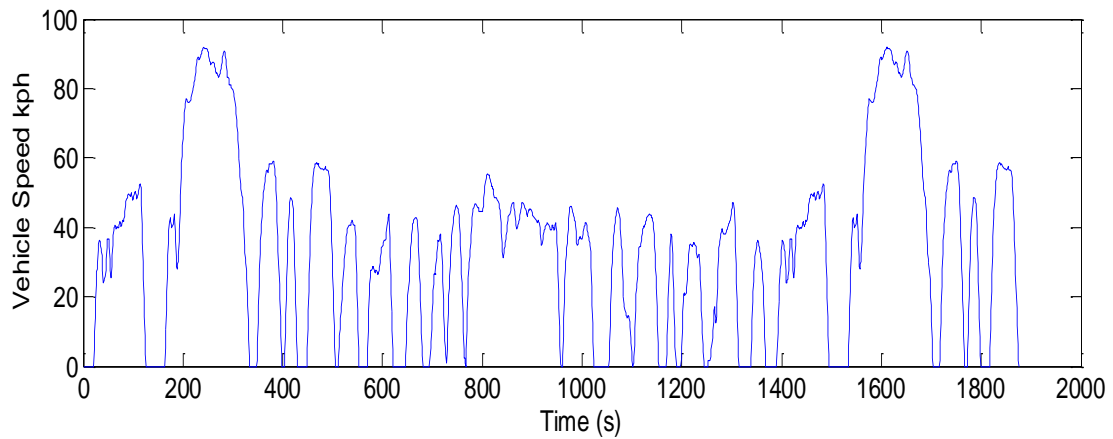
Figure 3-10 Federal Test Procedure 75 (E. P. Agency 2008)
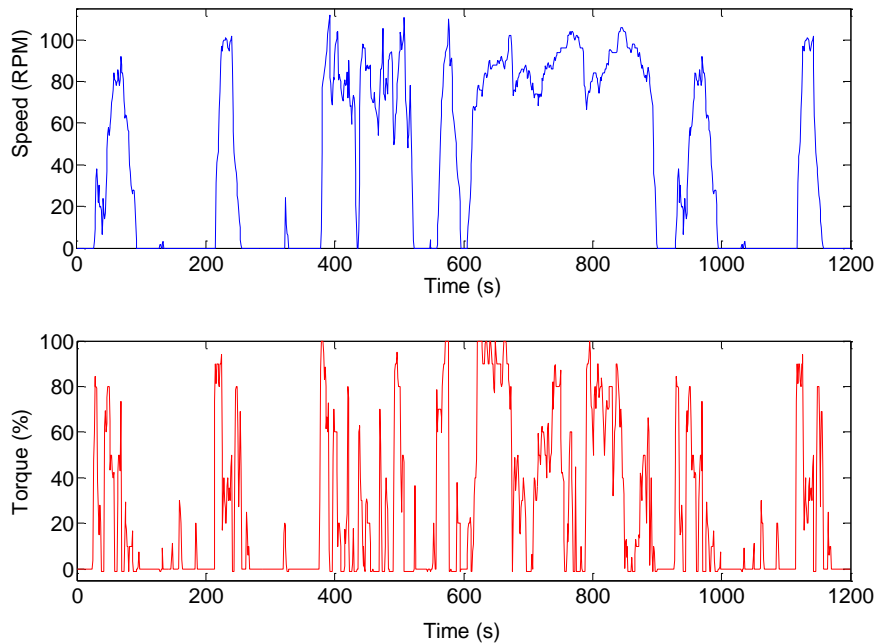
Figure 3-11 Engine Brake Dynamometer Heavy Duty Diesel Transient Cycle (normalized torque and speed plots) (U.S.A. Government 2014)

This last cycle is run twice, with a 20 minute soak period in between. Motor speed is normalized against the maximum speed where the full load of the machine limits motor torque to zero. Normalized torque is calculated as a percentage of the maximum torque at a given motor speed (U.S.A. Government 2014).

Table 3-3 European Stationary Cycle speed/load points and weight factors
(Diesel Net 2000)

ESC Test Modes				
Mode	Engine Speed	% Load	Weight factor, %	Duration
1	Low idle	0	15	4 minutes
2	A	100	8	2 minutes
3	B	50	10	2 minutes
4	B	75	10	2 minutes
5	A	50	5	2 minutes
6	A	75	5	2 minutes
7	A	25	5	2 minutes
8	B	100	9	2 minutes
9	B	25	10	2 minutes
10	C	100	8	2 minutes
11	C	25	5	2 minutes
12	C	75	5	2 minutes
13	C	50	5	2 minutes

The A, B and C engine speeds are defined as follows (Diesel Net 2000):

1. The high speed n_{hi} is determined by calculating 70% of the declared maximum net power. This is the highest engine speed where this power value occurs after the rated speed on the power curve.

2. The low speed n_{lo} is determined by calculating 50% of the declared maximum net power. This is the lowest engine speed where this power value occurs below the rated speed on the power curve.

3. The A, B, and C engine speeds to be used during the test are then calculated from the following formulae:

$$A = n_{lo} + 0.25(n_{hi} - n_{lo}) \qquad \text{[RPM]} \quad (6.1)$$

$$B = n_{lo} + 0.50(n_{hi} - n_{lo}) \qquad \text{[RPM]} \quad (6.2)$$

$$C = n_{lo} + 0.75(n_{hi} - n_{lo}) \qquad \text{[RPM]} \quad (6.3)$$

3.5.2 Performance Testing

Perhaps the most widely known performance test is the 0 – 100 kph launch test.
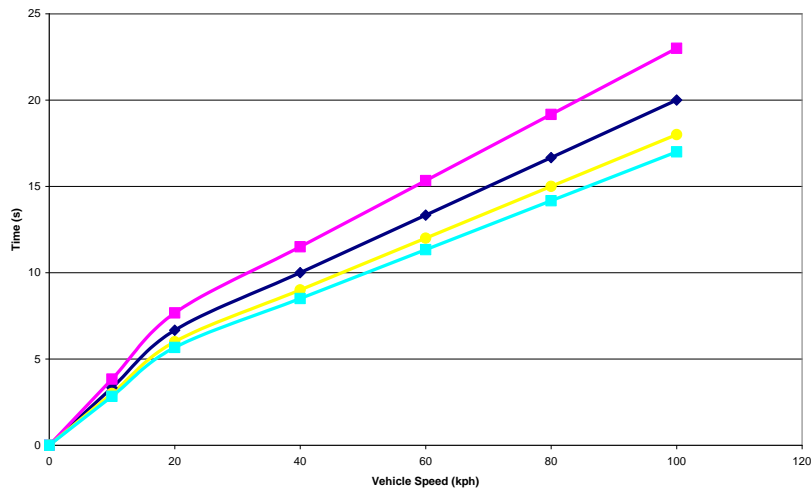
Figure 3-12 Typical 0-100 kph Launch Performance Plots

This test is used to compare, amongst many things, top vehicle performance and is used in part to determine the performance feel of a vehicle.

Another important performance indicator is the vehicle's capability to achieve longitudinal motion on an incline at gross vehicle weight. Per standards it should be able to start from rest on a 30% incline. The second factor that is evaluated on this test is the sustained maximum speed the vehicle can reach.

Once all the simulations are complete a thorough analysis of the resulting data can be made and conclusions can be drawn on the efficiency, operation and suitability of the different control system algorithms and power generation and control architectures.
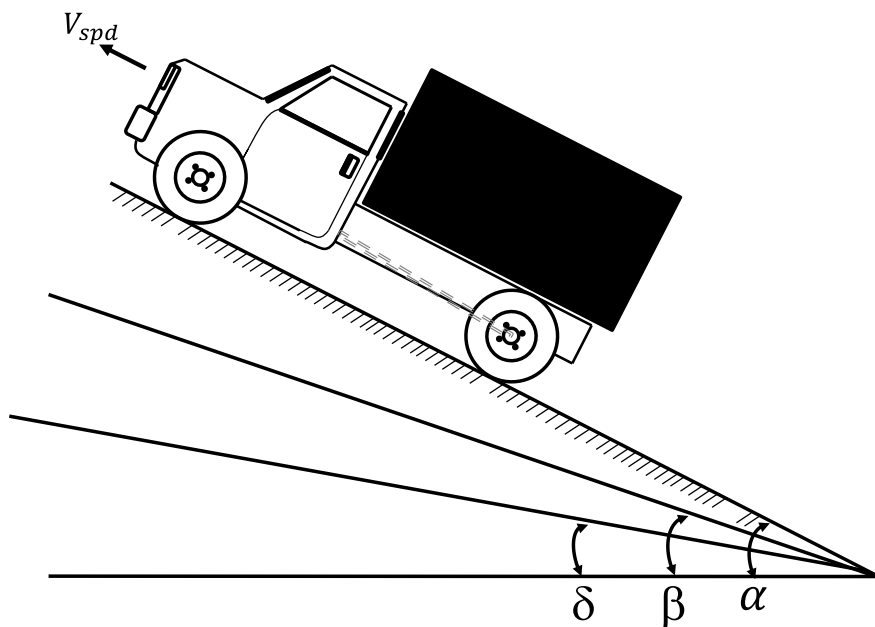
Figure 3-13 Diagram of Different Grade Slopes for Gradeability Testing

4 ENERGY CONTROL STRUCTURE

Chapter Summary:

This chapter will discuss the premise behind the conception of an intelligent energy management system. The concept will handle vehicle loads by dividing them into three different classes and based on vehicle inputs, such as driver demands, will decide how to optimally distribute vehicle energy to satisfy predetermined functional criteria.

4.1 Load Type Definition

As proposed in Chapter 1, the software architecture will be created considering two main driving philosophies. First, no single algorithm will be used as each one is best employed when it is used in a specific and specialized manner. For example, a PID controller is a powerful tool for automatic control systems, yet if the system is quite noisy one might be better off using a lesser PI controller to avoid the noise amplification effects brought about by the derivative component. Secondly inspiration for this approach also comes from the human mind itself. The human brain works by using specialist neurons for specific tasks. The frontal lobes are in charge of planning, organizing, problem solving and memory amongst other tasks. Elsewhere the hippocampus is in charge of memory creation and retention and it facilitates our ability to navigate our surroundings. (Dubin 2002). As such then each software feature will be structured in a way that it works on the most appropriate piece of information through the execution flow. This should then allow for greater flexibility versus the one algorithm adaption approach. In the latter approach one algorithm is used for everything and then research rests on the variation mechanisms to use this given procedure in different applications. This work aims to analyse a system of systems working together (cooling, fuel cell stack, battery, powertrain, etc.) to

optimize how energy is spent and distributed amongst the stakeholder functions. If one were to try and use a single methodology for every task it would undoubtedly work to some extent, yet the increased share of work destined for adaptation would take away from the overall scope, yet by applying a specialist algorithm per function then each one could more easily reach its potential. In this manner the focus would rightly lean more towards the overall scope and system interaction dynamics than making sure the selected methodology is capable of executing the task it was entrusted with.

Chapter 5 will elaborate on the specific algorithms used at different levels of the control system loop. Yet it is necessary to initially provide a general bird's eye view of how each system handles and transmits information.

The energy load structure is made up of three distinct blocks. First is the powertrain subsystem, then comes the vision subsystem and finally the lighting subsystem. It will be obvious to any reader that an ordinary vehicle has more equipment than is mentioned here, but these systems were chosen because they represent the three types of energy consuming loads around which one can group any other additional components. Each group is referred to as a "Port":

Port A.　　Continuous: This type of load cannot be interrupted because doing so might cause a catastrophic failure. They can be optimized to consume less energy, but cannot be turned off during a vehicle's deployment. One such load is the powertrain. The driver can choose a given driving style which can save or waste energy, but if the motors do not receive enough current the vehicle will not go anywhere.

Port B.   Interruptible: Lights are a good example of interruptible devices. Once a given technology is used to provide lighting for the vehicle (be it headlamps, interior lighting, etc.) no more can be done, but turn them on or off. The wattage of the bulb or LED cannot be changed. Even PWM control does this albeit at higher speeds. To optimize how much energy used on this loads then their usage profile (on time) needs to be controlled. This type of loads is also referred to as ON/OFF loads.

Port C.   Configurable: The telecommunications system is an example of a configurable load. Although at first sight it looks to be interruptible in nature, (it transmits or not) radio systems do have adjustable gains and are obviously attached to speaker whose audible volume can be adjusted. Therefore, in summary a configurable load is one which can be interrupted, but also has an adjustable factor. Due to test equipment limitations, which will be explained in Chapter 8, this research will use the vision system as representative of this group.

The following sections will go deeper into how each type of load is represented in the system of systems and how the control software manages it.

4.2 Conceptual Structure

In this work the word *control* is used not in the traditional automatic regulation sense of poles, zeros and overshoots, but in the general meaning of having influence on how things happen and their results. With that firmly in mind, lets then start the discussion about the conceptual picture of what will come to be known as the Intelligent Control Structure, or ICS. The control structure is divided into three different layers according to time horizon of action, speed of reaction and authority. The wider the time horizon the higher up the structure each feature is situated. At the highest level is the Behavioural layer, in charge

of monitoring driver and environmental inputs to determine if an overriding action over a lower layer is in order. The medium layer is a composite one. It includes a forecasting engine together with energy management and allocation logic. Based on historical and statistical information this layer assigns energy using appropriate parameters for each load type. Interruptible loads are assigned their allowed on-time. Configurable loads are given their operational parameters and continuous loads are given operational limits which must be observed. All this is done so that, in case of an energy shortage, each system can operate for as long as possible prioritizing powertrain energy allocation to ensure the vehicle does not fail in reaching its destination. Figure 4-1 shows the complete conceptual diagram for the control structure.
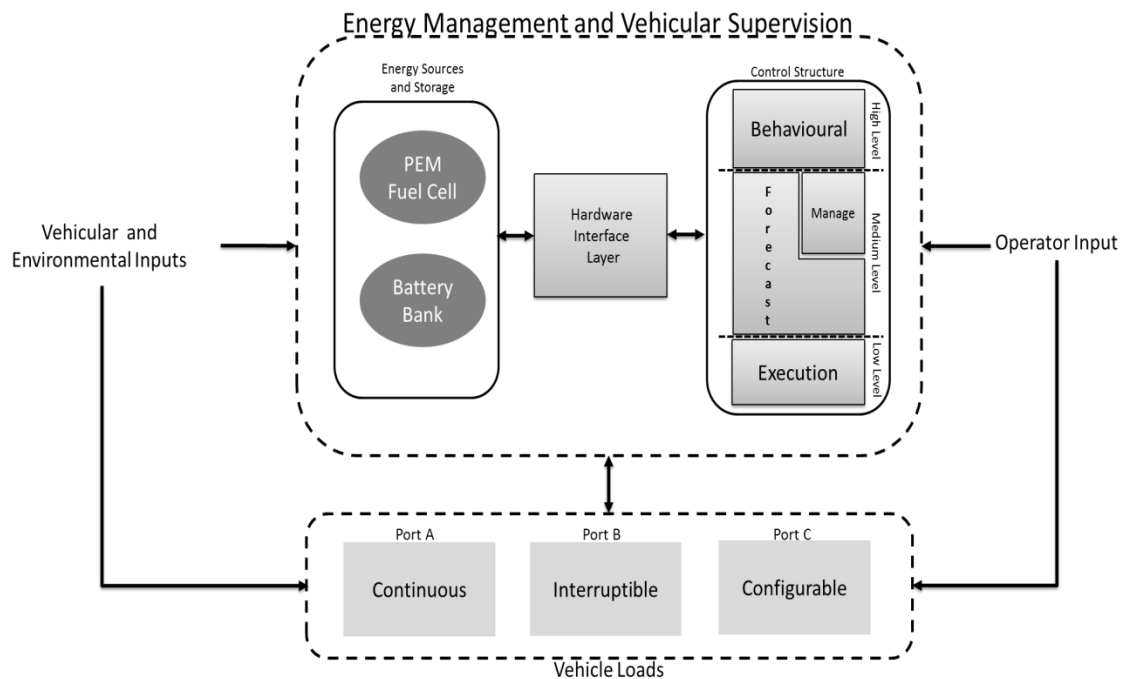
Figure 4-1 Energy Control Structure Flow of Information

4.3 Input Handling

Driver input information is received by both loads and control system. What this means in real life is that as the operator drives the vehicles, activates or

configures a specific system the central supervision system receives this information from the loads for its own computations. Vehicular and environmental inputs mean data coming from the vehicle sensors and other health monitoring systems like diagnostics. Available sensor information includes location, roll, pitch and yaw angle, heading and load current sensing.

Current sensing is communicated back to each load driving device, so that in the case of overcurrent the load can be deactivated locally to protect it and the overall health of the system. This way energy can be kept from being wasted by a faulty load. The supervisory system also receives the same information for updating usage profile data for forecasting purposes.

The behavioural layer receives a special piece of data which is that of the position of possible threats. This information is used to calculate an escape route for the vehicle which does attempt to keep it away from the threat, but progressing towards its target as much as possible.

4.4 Power Request Handling

Power requests are grouped per load type and dubbed Port A for Powertrain, Port B for Interruptible loads and Port C for Configurable. It is done in this manner to keep the logic in the central system as generic as possible; that way should a simulation be needed where the interruptible loads are different then nothing needs to be changed in the software, but the list of initial load nominal parameters.

The medium layer keeps track of the energy expenditure by each "Port" and uses it to participate in arbitration in case of energy shortage. The forecasting

engine uses actual consumption data from load current sensing to create look-back and look-forward forecast of vehicular energy consumption over its surveillance deployment or mission.

The lower layer includes a fuzzy logic feature used to split an existing power request between the two power supplies based on reaction time limitations of the fuel cell and battery state of charge (SOC). Furthermore this layer monitors how much energy is left in each source, and what sources are available to set a specific mode of operation for the whole system. The energy split commands issued by the lower layer are then translated by the hardware interface layer for their implementation by the dc/dc converter belonging to each layer. Figure 3-3 shows how the hardware interacts with the supervisory system. This is a more detailed schematic of the system shown in Figure 2-1(a).

4.5 Control Structure Internal Information Flow and Authority Levels

As a complex system the control structure of the supervisory logic receives information from different outside sources. This data is then shared amongst the different individual layers or components in its raw or processed form. How data is transmitted is illustrated in Figure 4-2.
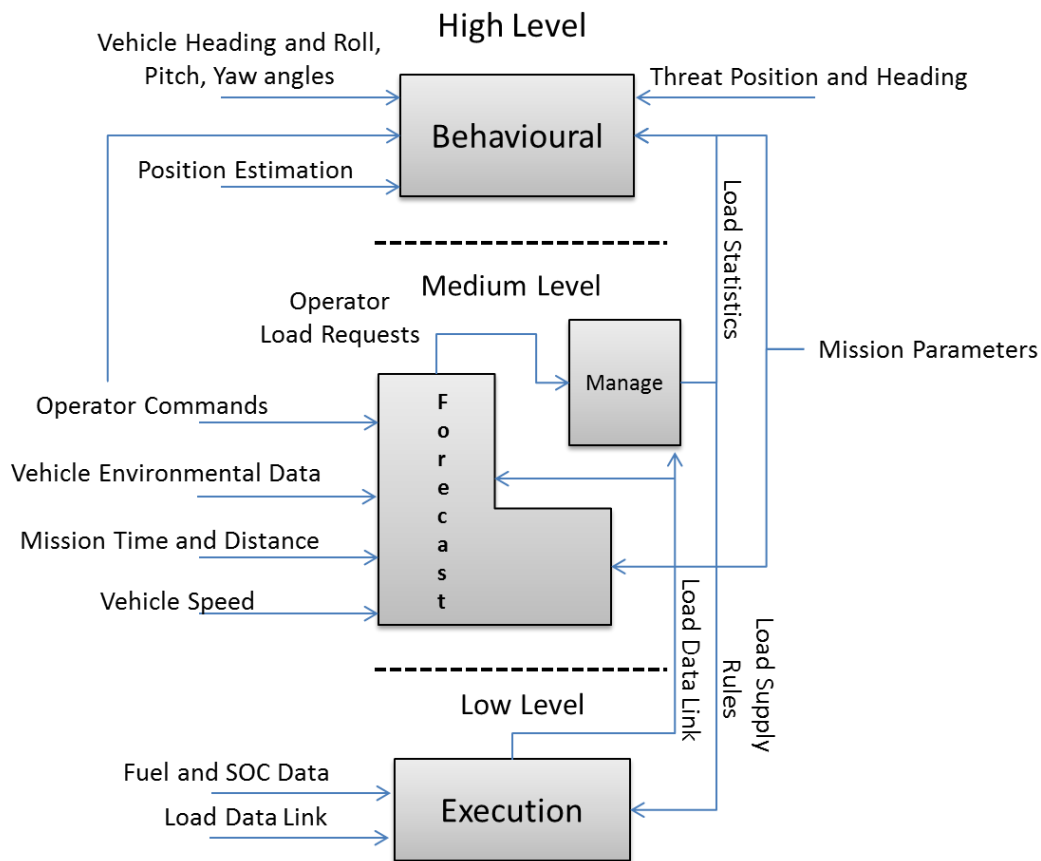
Figure 4-2 Internal Flow of Foreign Information

The way information is passed and transformed along its way to trigger different software features creates an effect akin to organic computing. This lies in the following facts:

- Self-configuration: By being able to dialog with the load drivers, the central supervisory logic can and, if allowed by the operator, will configure the vehicle's loads on its own.
- Context Awareness: Thanks to the external vehicle sensors and on-board databases which store mission data and other system historical usage information the structure can be aware of its operating context.
- Automated optimization is possible: When energy starts to become scarce the system again can be asked to optimize all three ports of

energy consumption to maximize its use whilst also allowing every load to be used as much as possible.

- When threat detection is active the system can strive to self-protection: By knowing its position and attitude the control structure can direct itself or the driver on a path away from threats which can lead it to safety and its destination.

All this is possible due to the dynamics of software feature interactions. By having different specialized algorithms used in a complementary fashion the simple rules of each one add up to create more complex behaviours. Having a quasi-organic controller is advantageous since one research objective is to have software that can be applied to different platforms not only to the one it was designed and initially tested on. The flexibility will be demonstrated in the test phase discussed in Chapter 5.

After describing in general terms the power supply and its accompanying control and supervisory logic it is time to pay attention to the numerical simulation used for the first phase of this research.
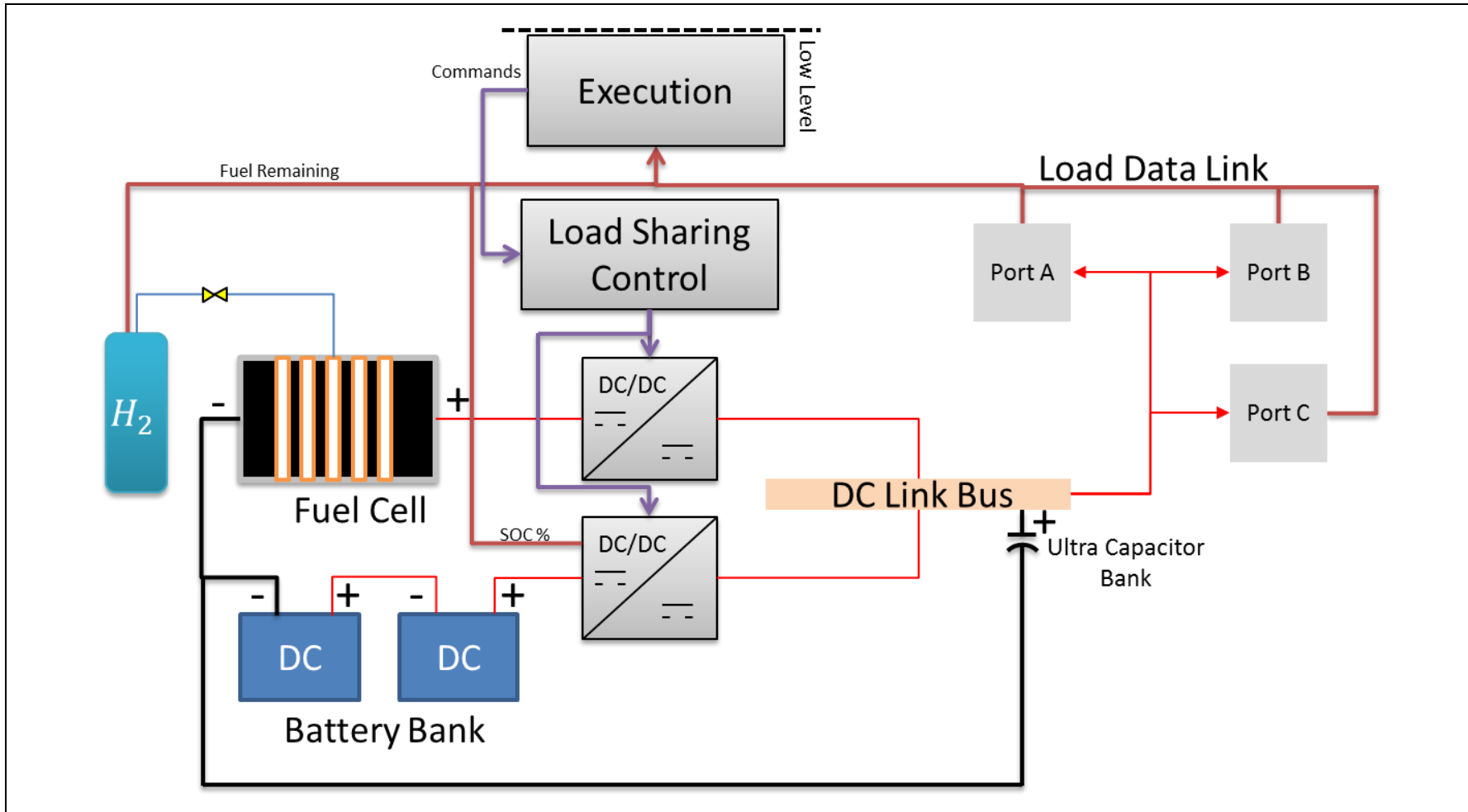
Figure 4-3 Low Level Layer/Hardware Interactions

77

5 Intelligent Control Structure

Chapter Summary:

As described in previous chapters the intelligent control system object of this research is divided into three different cooperative layers. Each one has its own purpose and capabilities. At the same time each layer has a degree of influence on the surrounding ones to create complex behaviours out of simple rules. This chapter will detail each layer and provide a summary of the overall system.

5.1 Introduction

As was described in general form in Chapter 4 the Intelligent Control Structure (ICS) object of this research is composed of a group of layers as shown in Figure 4-1. Each layer has its own individual functionality and purpose and shares information with the remaining ones. At the same time each layer is made up of several artificial intelligence algorithms which are used on tasks for which they are best suited. The motivation for this is that although several articles can be found in literature where a single type of methodology is used in different applications each algorithm will inherently be best suited for what it was conceived for (Gao 2008) (Hua 2011). Also, some layers have layers within themselves and that structure is to allow for different operating time horizons. For example, a budgetary algorithm will have a time horizon of the whole mission which could span hours or days, this is a slow algorithm as it updates less often. Meanwhile the power sharing logic needs to be fast as it commands the DC/DC converters to supply the vehicle. The reaction time is fast and its time horizon is in milliseconds or very short.

5.2 Low Level Layer

The Low Level Layer has been entrusted with carrying out the following tasks:

1. Use mission profile data, artificial or input by the operator, to monitor progress and predict beforehand if the vehicle has enough energy to carry it out whilst using the required loads and travelling the required distance.

2. Monitor energy availability in terms of what supplies are available on board the vehicle and how much energy each one is capable of providing for the mission.

3. Take into account energy supply dynamics, like Fuel Cell 0-100% output time, and capability to issue the corresponding commands to avoid shortages or inappropriate response.

To carry out these tasks the layer has been broken down into a matching number of functional blocks; each block using a specific algorithm in line with this research's philosophy. The functional breakdown is as follows:

1. **Graph Theory Tracker:** Used at the highest level to keep track of mission progress, forecast energy consumption and coordinate power generation between sources. Whilst reserving energy for mission critical systems (Felix 2013). It has a mission long time horizon and is the high level algorithm within this layer. A graph was selected for this task because its mathematical representation in matrices. This data structure makes it computationally efficient to have incredibly complex graphs described by a small number of matrices. Furthermore, a matrix is a dynamic object and can easily be modified to represent a new graph from one time step to the next. This last feature is of great importance for the mission tracking task required by the ICS.

2. State Machine Monitor: Monitor energy storage on-board and coordinate system wide operating mode including battery charging (Felix 2013). Medium speed and it occupies the medium level of the layer.

3. Fuzzy Energy Sharing Logic: Used to coordinate instantaneous power delivery to all loads which require it. It has one fuzzy set per operating mode and their output is modified by the algorithms higher up in the structure (Felix 2013). Due to its close interaction with the actual hardware it has high speed execution and occupies the lowest level of the layer. This fuzzy set is in charge of issueing the basic power split commands to be followed by the fuel cell and battery bank. It is the last, but still crucial, link in the intelligent energy management process. Fuzzy logic was choosen due to the flexibility and intuitive feel Mamdani FIS provide. This will be elaborated in more detail in Section 5.2.5.1.1. Figure 5-1 illustrates the multilayer control structure.
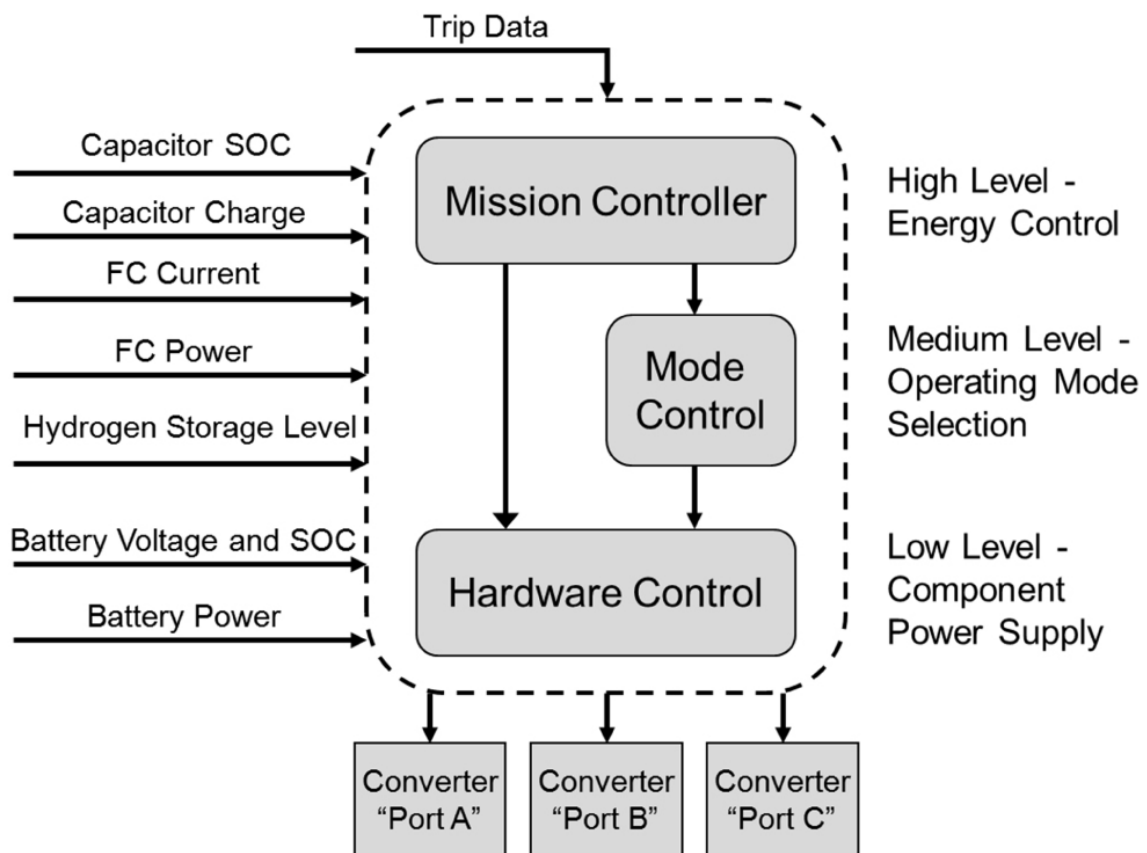
Figure 5-1 Internal Structure of the Low Level Layer

5.2.1 Mission Controller

The topmost algorithm makes up what is dubbed the Mission Controller.

As part of the pre-departure procedure, the operator must enter into the system a set of parameters which describe the mission. They are waypoints distance and power ratings of any mission payloads to be deployed during the mission.

In order to process this data the controller breaks it down and loads it into three matrices called Mission_Type, Mission_Data and Mission_Data_Type (Felix 2013). As mentioned before the heart of this level is a Graph Theory Tracker which needs data to be broken down into a specific format it can understand to then create an acyclical graph. The following trip description was can be used to exemplify how mission data is used by the graph tracker to populate the matrices. Considers a vehicle departing Depot A on a 16.28 km journey to a surveillance station where it will deploy a trailer mounted Centurion Phalanx anti-aircraft gun and remain there for one hour. Then it will proceed to Depot B a further 16.28 km away. (Felix 2013).Figure 5-2 is a graphical representation of the journey and a graph built from it. To apply standard graph notation nodes "V_x" are used to mark changes in mission stages and edges "e_y" represent each mission segment and its describing data.
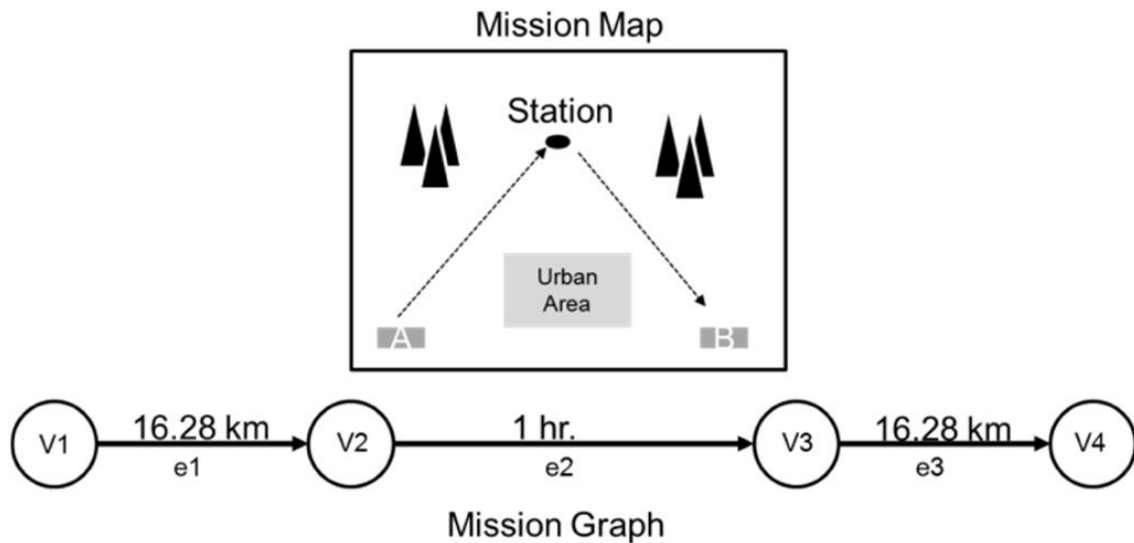
Figure 5-2 Mission Data Translated into Mission Graph. (Felix 2013)

How each of the mission matrices is used depends on what information it contains. Mission_Type is used to know if the vehicle is supposed to be moving, in stationary watch or idle. Mission_Data has the edge weight information or the mission parameter magnitude. Mission_Data_Type is used to convert each parameter from units more suitable for the operator into workable engineering units. The data in Mission_Data is expressed in kilometre, for distance, and hours, for watch and idle time. Mission_Data_Type indicates which conversion factor to use by using a single number (i.e. 1 for km and 2 for hrs). A final matrix is used to identify if any loads are critical for mission success. In case of scarcity these loads would be prioritized for energy supply. Presently the loads are grouped per ports as described in Chapter 1: Port A - Powertrain, Port B - Vehicle Systems (lighting) and Port C Mission Payload (vision system). The matrix used for this process is called the Criticality Matrix.

5.2.1.1 Travelling Node

To execute its tracking job the controller copies the mission graph and modifies it to include a new node. This "travelling" node is referred to in this way because it jumps from edge to edge in a walk along the graph. A walk in graph theory

terms is a set of nodes and edges that span the graph from beginning to end. When the nodes and edges which make up walk are unique then this walk can also be referred to as a path. Equation 5-1 shows the mathematical representation of the walk along the original mission graph. This walk fulfils the definition of a path.

$$\langle v_1, \{e_1\}, v_2, \{e_2\}, v_3, \{e_3\}, v_4 \rangle$$

5-1

An important rule in the creation of walks is that if the graph is of the directed kind the walk must follow the direction of the edge. Equation 5-1 satisfies this rule as well. When traversing through the mission graph, shown in Figure 5-2, each node is brought into the walk from left to right per the direction set by the edges and not in vice versa. Having made clear the basic graph theory concepts to be employed, the travelling node and its function can now be described in detail.

First of all, the purpose of it is to keep track of how much energy is actually spent during each mission phase and how much is still to be required according to the average consumption figures from the look-forward and look-backward forecasting algorithms. This forecast is done for each operating mode simultaneously. As a result the travelling node has a single incoming edge, called H for Historical, whose weight is the amount of Joules used so far during the present phase, and three outgoing edges, one per each operating mode (B for Battery Only, FC for Fuel Cell Only and FB for Fuel Cell/Battery Operation). The weight of each outgoing edge is the amount of energy still available for use on each operating mode (when the battery is being charged the mode used is FC). As the mission graph is an acyclical directed graph all nodes have both incoming and outgoing edges except for the ones located at the beginning and end. When the travelling node is inserted the mission graph is transformed into a multidigraph, or a graph where multiple directed paths exist between beginning and end. Figure 5-3 shows the resulting multidigraph after travelling node insertion at the initial phase.

83
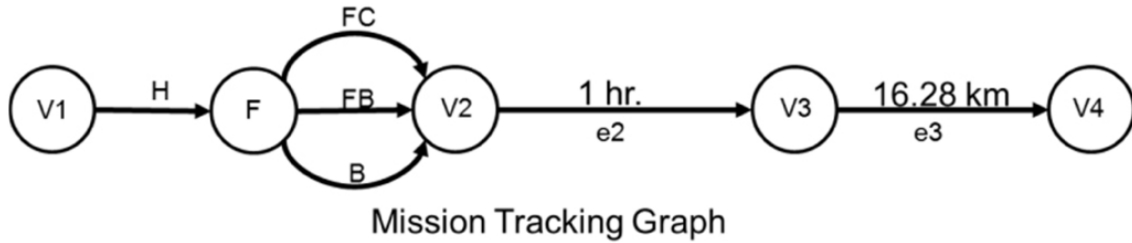
Figure 5-3 Mission Multidigraph for Energy Consumption Tracking (Felix 2013)

As drawn in Figure 5-3, there are now three possible ways to create a path along the graph, one for each operating mode. Equations 5-2 through 5-4 describe each path.

$$\langle v_1, \{H\}, F, \{FC\}, v_2, \{e_2\}, v_3, \{e_3\}, v_4 \rangle \qquad \textbf{5-2}$$

$$\langle v_1, \{H\}, F, \{FB\}, v_2, \{e_2\}, v_3 \{e_3\}, v_4 \rangle \qquad \textbf{5-3}$$

$$\langle v_1, \{H\}, F, \{B\}, v_2, \{e_2\}, v_3, \{e_3\}, v_4 \rangle \qquad \textbf{5-4}$$

Because of the multiplicity of paths two new matrices are needed which describe which node is the start or end of every edge; without them the walk generating algorithm would not be able to distinguish one path from the other. The new matrices are fittingly called Beginning and End matrices.

In order to select the active path a weight factor is assigned, which is the result of estimating an energy usage forecast using vehicle information and source usage statistics to forecast how much energy will need to come from each one from the present time until mission completion. This is not a straight forward calculation as it requires a series of computations to be done before hand. Firstly, two different percentages are calculated for both fuel cell and battery bank. This data indicates how much energy, historically, has come from each source along either mobile or stationary edges. Also, an average energy flow

figure is computed, in [J/s], for each source. This last piece of information is used in Equations 5-5 and 5-6 to estimate how long, in terms of time, each source will last before becoming empty. Equation 5-7 gives the combined estimate for the Fuel Cell/Battery mode of operation (Felix 2013).

$$Batt_{Duration} = \left(\frac{Batt\_Energy\_Flow}{Remaining\_Batt\_Energy}\right)^{-1} \qquad \textbf{5-5}$$

$$FC_{Duration} = \left(\frac{FC\_Energy\_Flow}{Remaining\_FC\_Energy}\right)^{-1} \qquad \textbf{5-6}$$

$$FB_{Duration} = Batt_{Duration} + FC_{Duration} \qquad \textbf{5-7}$$

Next, the final weight factor, called "action", is obtained from Equation 5-8 and has units of [J.s]. In this equation the character "X" stands for *FB*, *FC* or *Batt* according to each case.

$$X_{action} = X_{Duration}Forecasted\_Energy\_Usage \qquad \textbf{5-8}$$

In Equation 5-8 the rightmost parameter is the same for all cases, so out of three simultaneous computations the result with highest value is used to confirm the operating mode, and if this result is different from what lower level Mode Control has determined its decision is overridden by the higher level Mission Controller.

5.2.2 Mission Controller Energy Reserve

An important function of the mission controller is to set energy reserves within the battery and fuel cell supplies. By assigning an energy weight figure to each edge in every path, total energy consumption can be forecasted per supply and operating mode. This is done by continually assigning the active *H* edge the value of energy consumed in the present edge. *FC* receives the corresponding

share of fuel cell energy required, per the percentages computed in the previous section, taking into account the type of the present edge. For B the process is the same and FB uses the total figures. In the paths described in Equations 5-2 through 5-4 the future edges, those yet to be taken over by the travelling node together with FC, B or FB, per each case, are assigned energy weights again per the percentages applicable per edge type. Equations 5-9 through 5-12 show the calculation process for each type of edge; in them "y" stands for road, stationary or idle edge type and "n" is the edge number.

$$Edge\_Energy_y^n = Mission\_Data\_e_n * Historical\_Edge\_Energy_y \qquad \textbf{5-9}$$

$$FC_{weight} = Remaining\_Edge\_Energy * FC\_Percentage\_Type_y \qquad \textbf{5-10}$$

$$B_{weight} = Remaining\_Edge\_Energy * B\_Percentage\_Type_y \qquad \textbf{5-11}$$

$$FB_{weight} = Remaining\_Edge\_Energy * FB\_Percentage\_Type_y \qquad \textbf{5-12}$$

At the start of the mission Equation 5-9 can be applied to all the edges in front of node F in each path. This will give the total energy required per supply. As the mission progresses the weight of the edge immediately in front of node F will decrease over time until the segment is completed and a new one is taken over. When there is only one available energy source the total for the opposite path and for FB will be zero. To illustrate how all the previous Equations work together consider the following example based on the graph in Figure 5-2

1. Assume that historical data says the fuel cell supplies, on mobile edges, 75% of the required energy and 50% on stationary ones. Also this vehicle spends 6000 J/m when it's driven and 4500 J/s when it's in stationary watch.
2. Using mission and historical data in Equation 5-9 gives that e_1 has an energy weight of 97.68 MJ, e_2 has 16.2 MJ and e_3 a final 97.68 MJ.
3. Substituting the previous results in Equations 5-10 through 5-12 result in a require fuel cell reserve of 154.62 MJ and 56.94 MJ for the battery. The

combined reserve is 211.56 MJ which obviously is equal to the total of the original path from Equation 7-1.

4. As the mission progresses the weights of *FC*, *FB* and *B* decrease, but that of *H* will increase keeping the total constant along the mission*.

*_The Medium level layer will intervene when the total along the mission changes, but that will be discussed in Section 5.3._

5.2.3 Mission Controller Critical Energy Supply Limits

Once reserves have been created it is necessary to enforce them.

Firstly the overall reserve is divided amongst the mission edges according to their calculated requirements. Secondly, the Criticality Matrix, which will be discussed more in detail in Section 5.3.1.2.4, is used to flag which Port is critical for the current task and which is not. All critical Ports are assigned a fraction of the reserve according to its anticipated needs.

The process to divide and assign the reserves is as follows:

1. A figure called Not-To-Exceed, or *NTE*, is calculated using Equation 5-13. (Felix 2013)

$$NTE = \frac{\left(Remaining\_Energy - (1.10 Active_{Reserve})\right)}{Proportional\_Segment\_Use}$$ **5-13**

2. *NTE* is used to instantaneously determine how much energy is available for non-critical loads.

3. The *NTE* is then split amongst all edges proportionately per their share of the total energy consumption figure.

Figure 5-4 shows how *NTE* and the energy reserve behave during vehicle operation. The solid line shows the dynamically calculated reserve for the fuel cell source. As the mission progresses and the critical loads take up

their share of the reserve the reserve will decrease accordingly. Falling back on the financial metaphor, if you have a budget set as soon as you expend it the remaining budget will decrease.
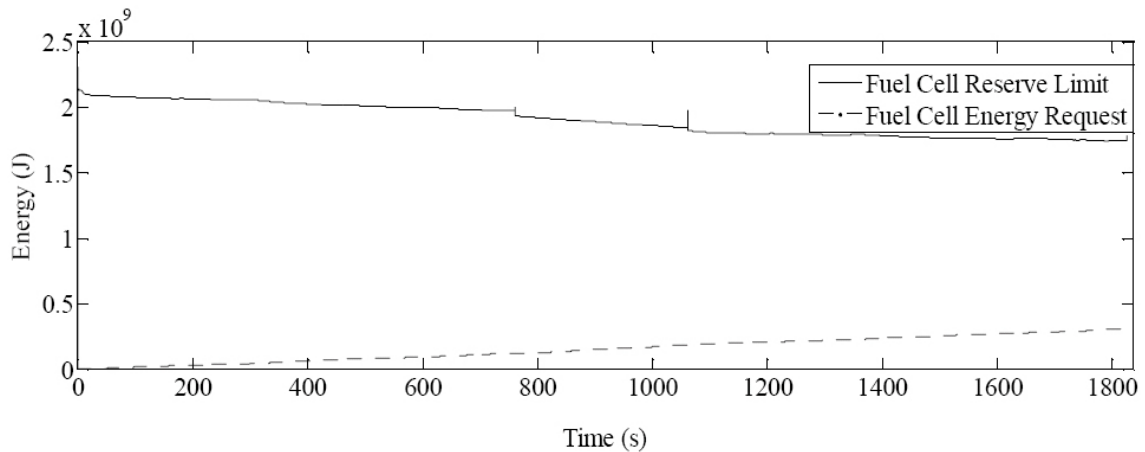
Figure 5-4 Energy Reserves vs. Energy Consumption (Felix 2013)

Should there be a case when actual energy consumption is higher than expected the active reserve is dynamically increased to accommodate for the critical loads resulting in a reduced *NTE*. If *NTE* runs out then all non-critical loads are sacrificed for the remainder of the mission, the procedure for this task will be discussed in Section 5.4.1.4. Figure 5-5 shows the system dynamically increasing the reserve. The trace in the figure is the result of intentionally entering the wrong load parameters for Port B loads. Therefore the forecast was too low and as the mission progressed the system had to continually increase the reserve.
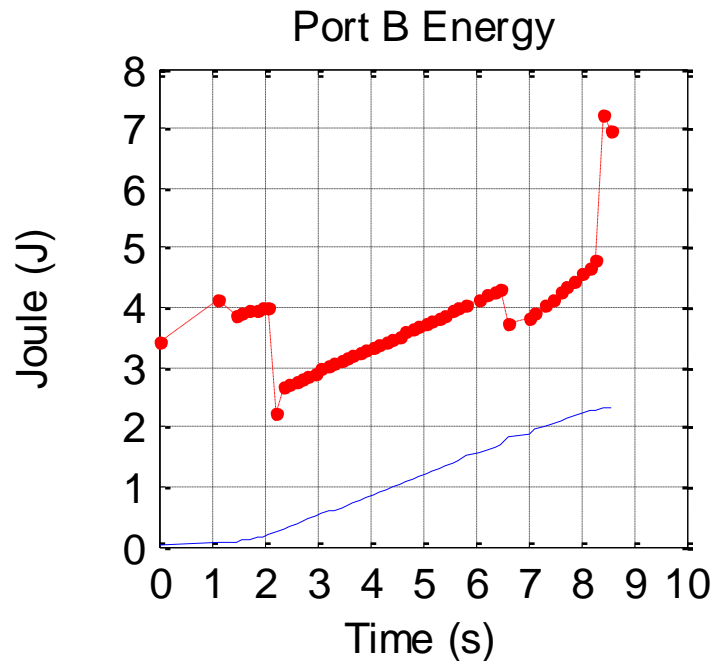
Figure 5-5 Dynamic Reserve Increase

The advantage of reserve setting procedure is that by using dynamical figures, which are managed by the medium level layer, each time the forecast for an edge type is updated the mission total is so as well. If the action factor from Equation 5-8, for the last available energy supply falls below one after an update the high level Behavioural layer will intervene to attempt to reconfigure the system in order to bring it back above one.

One final dynamic left to explore is that of the effect of criticality on how much energy is available for each load. As mentioned before, there exists a criticality matrix within the medium level layer which indicates to the system what load is critical during each mission segment. For example, a powertrain load will be critical when the vehicle is moving, so energy would be reserved for it, but whilst in silent stationary watch it would not be deemed critical and this load would then only have available what is left of *NTE*. Figure 5-6 shows how for each Port the energy reserve limits switched between *NTE* and Critical for the mission described in Figure 5-2. The middle section of the plot corresponds to the stationary segment and both extremities are mobile segments. At the top, on

the powertrain Port A plot, it is clear how when this load is not critical it is assigned a lower energy limit than on mobile edges.
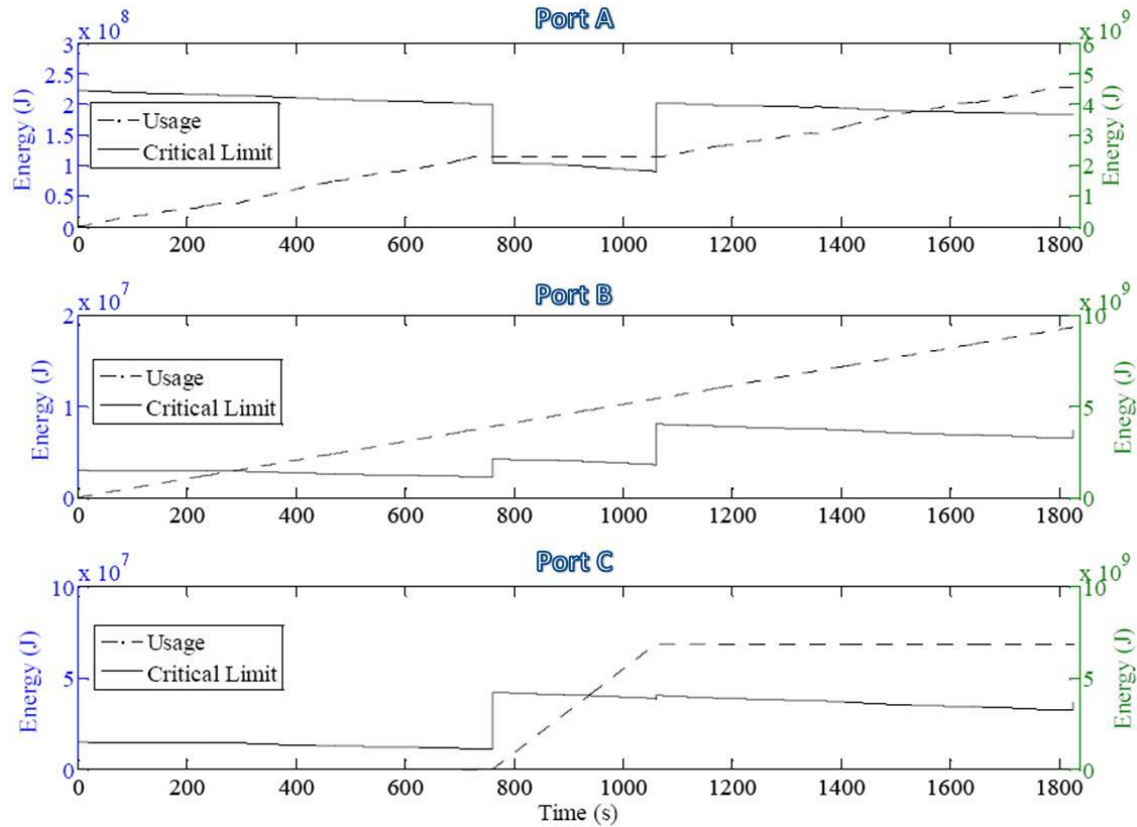
Figure 5-6 Energy Reserve Switching Over Time (Felix 2013)

One important behaviour to note in Figure 5-6 is evident in the plots belonging to Port B. This load is not critical during the first two mission stages, yet its energy limit seems to increase when the second phase of the mission starts. This is due to the fact that during the first stage of the process the energy consumption was less than expected so when node v_2 is reached the overall mission forecast is updated and reduced returning energy to NTE and the non-critical loads. This once more highlights the advantage of having dynamic updates along the mission.

5.2.4 Mode Control

As illustrated in Figure 5-1, on the Medium Level of the Low Level Layer sits the Mode Control logic. It's in charge of monitoring all available power supplies and determines:

A. Which supplies if any are available,
B. How much energy each one can still contribute with,
C. Determine the mode of operation where the highest level of energy will be available, and
D. Decide when the battery needs to be recharged by the fuel cell.

The mode of operation decision can be overridden by other functional blocks as has already been discussed. The algorithm used for mode control is a State Machine. These systems are best suited for this task as it involves the constant monitoring of logical thresholds whilst at the same time keeping track of the existing state of the system at the time a decision is made. Figure 5-7 shows the five possible states of the Mode Control machine.
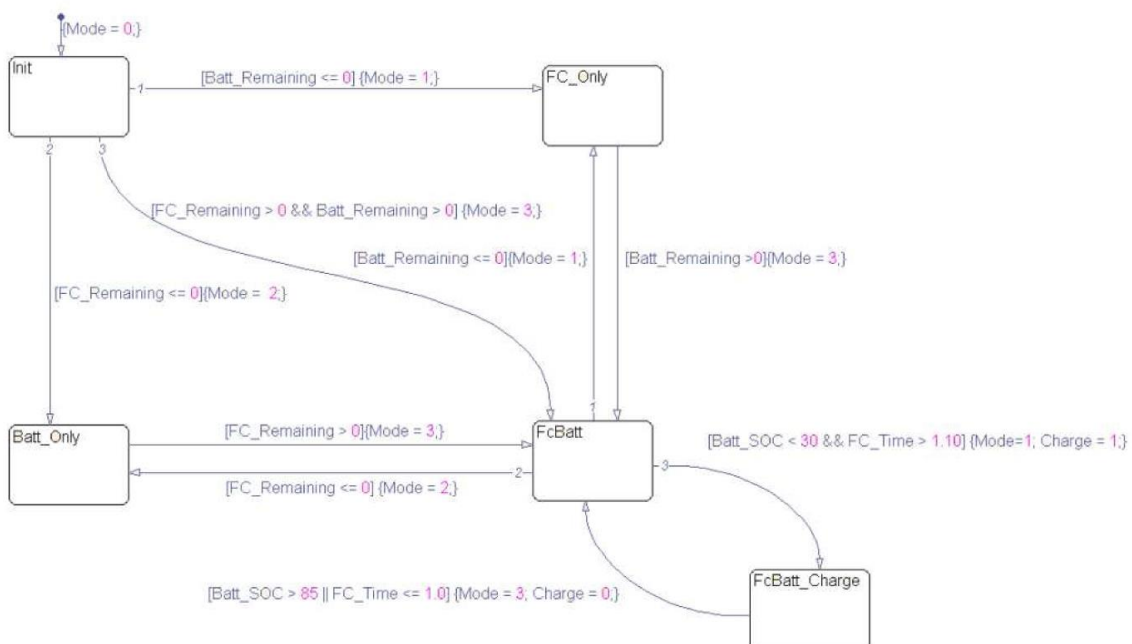
Figure 5-7 Mode Control State Machine

The machine is initialized at state zero, or "init", when it then reads energy source information and a mode is chosen. If not overridden then the higher level of the layer will obey this command when choosing a path along the multidigraph. There is one logic state considered which is not in turn mirrored by the multidigraph and that is FcBatt_Charge. When in FcBatt mode, if the battery SOC falls below 30% and the fuel cell has more energy than required to finish the mission it then deviates energy to charge the battery and carries on its shoulders all energy requests. Charging continues until either of two conditions is met, Battery SOC is above 85% or fuel cell action is below one. In the latter case the fuel cell has just enough energy to complete the mission and cannot spare anymore. When FcBatt_Charge mode is selected a FC_Only command is transmitted to "fool" the surrounding systems into believing there is no battery available and Mode Control modifies the mission parameter used by Mission Controller to add the battery energy requirement to the critical systems reserve. This way all energy expenditure is accounted for. It is important to note that the Mission Controller can only override Mode Control when it thinks a mode change will make it more likely that the mission can be completed given a set of energy sources. If Mode Control, which monitors energy availability, fools the Mission Controller into believing there is no energy to be had from a battery it is impossible for the latter to override the former in this regard.

5.2.4.1 Effects of Mode Selection

When a mode of operation is selected the information is read by not only the high level Mission Controller, but also by the low level Hardware Controller. This block houses a fuzzy logic engine which has different rule sets for each of the three basic operation modes. The hardware controller follows without question whatever command Mode Control issues to it.

When Fuel Cell Only mode the fuzzy Hardware Control directs all requested power to the Fuel Cell assuming it and the ultracapacitor bank will be able to

handle it. The same happens when in Battery Only mode. They dynamics of Fuel Cell/Battery mode will be elaborated on in the following section. If during operation one supply should run out or fail then Mode Control would relay this to the other levels in the layer by issuing the appropriate command.

5.2.5 Hardware Control

Hardware Control is the deepest level of the whole control structure and because of its direct interaction with the hardware it is the most dynamic one. All data processing, modelling and constructs result in the creation of real world effect, that of energy being dispensed and the vehicle being allowed to carry out its mission.

The core of the Hardware level of the Low Level Layer is a fuzzy logic controller with added selection logic which enables it to pick the right set of rules for the given mode command. In each of the three options energy is drawn from a supply in a more biased way than in other modes. Battery Only and Fuel Cell Only modes are self-explanatory, but Fuel Cell/Battery mode is more complex. When in the latter mode power requests are routed to the device with higher generation capabilities. The outputs of the fuzzy set are shown in Figure 5-8.
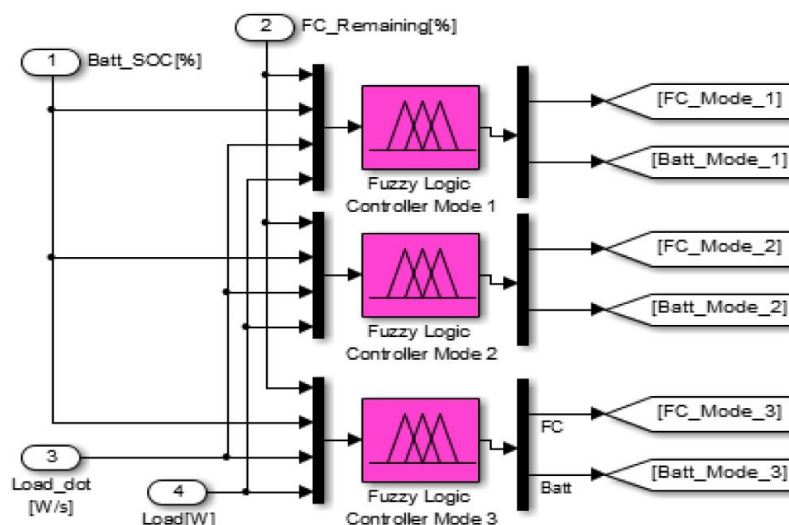
Figure 5-8 Hardware Control fuzzy set core (Felix 2013)

In full the responsibilities of the hardware controller are:

1. Provide a balanced fulfilment of the energy request by considering source dynamics and generation capabilities.
2. Provide the correct commands per the selected mode of operation.
3. Monitor, use and recharge the ultracapacitor bank.

5.2.5.1 Fuzzy Core Operation

The actual outputs of the core are percentage values. These percentages mean how much of the present request each supply must fulfil. They are then multiplied by the demanded value, to obtain the raw supply request, and fed through what is called the dynamic modifier stream. In here calculations made by Mission Controller and calibrated manufacturer specifications (i.e. fuel cell 0-100% reaction time, maximum battery discharge current, etc.) are considered.

One of the overall control structure design philosophies is clearly expressed in this level, and is that energy is considered to be a currency. Power, or expenditure request, can only be taken as the rate at which currency is generated, and there are up to two accounts from which to possibly withdraw it. Each source cannot instantaneously withdraw more than a certain amount like would be the case in a real world banking ATM. Should one of the accounts exceed its rate of withdraw limit (maximum power rating reached) the deficit is then charged from the second account until the demand is satisfied (Felix 2013).

Figure 5-8 shows that the inputs to the fuzzy core are Load, the load rate Load_dot, battery SOC percentage and fuel cell remaining fuel percentage.

5.2.5.1.1 Selection of Fuzzy Inference System

The system type used for the core of the fuzzy dynamic modifier chain was Mamdani. This is because it allows for a more intuitive way of crafting the output power command function for each energy supply. Remember that one of the input parameters is that of Load rate of change which is monitored to keep the fuel cell safe from spikes in demand. Although Sugeno action coefficients could be optimized for this task, through ANFIS for example, it was found that defuzzification process used in Mamdani (Mamdani 1981) gave a better feel of what the outcome would be for a given set of inputs. Figure 5-9 shows an example evaluation of the fuzzy rule set run in Matlab.
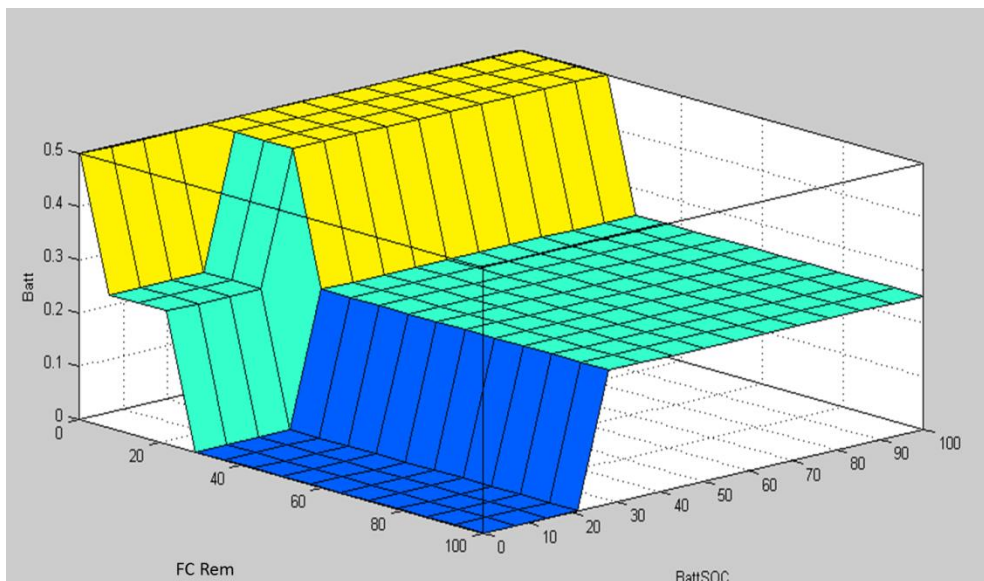
Figure 5-9 Fuzzy Rule Set Sample Surface Plot

Because the dynamic modifier chain sits at the bottom of an already complex low level layer, where three different algorithms reside, it was necessary for it to be optimized quickly and without adding even more optimization inner layers. A Mamdani FIS was then a useful tool to accomplish said goal. The type of

membership functions employed was trapezoidal for both input and outputs. This allowed for quicker fine tuning arising from simulation results. Figure 5-10 shows an example of the membership functions, in this case the one for the vehicle load power requirement input in operation mode 1.
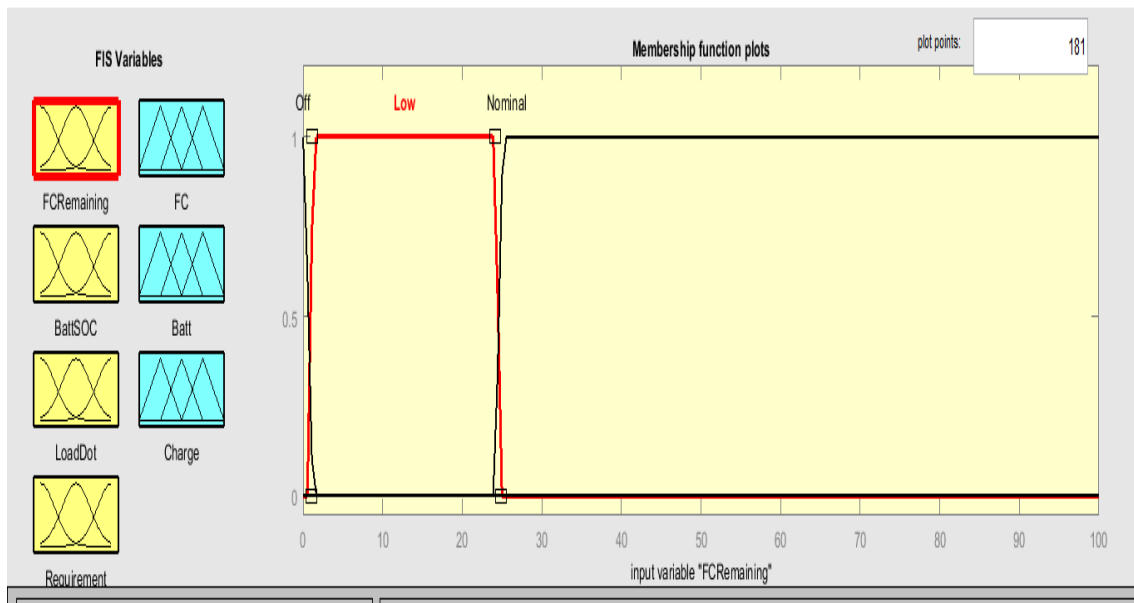
Figure 5-10 Vehicle Power Requirement Fuzzy Membership Function for Operating Mode 1

The Simulink model used to analyse the operation of the Low Level Layer, together with all the fuzzy logic rule sets is included in the accompanying media.

5.2.5.1.2 Fuzzy Core Load Input Estimation

Although Load is made up mainly of the vehicle's energy requests it also adds a parameter local to the Hardware Controller and that is the Ultra-Capacitor SOC. As mentioned before the fuzzy set takes into account the energy stored into the ultra-capacitor bank to satisfy system needs. Yet, this device needs to be recharged and that falls on the Hardware Controller. Therefore on top of whatever power requests are handed to it the modifying chain will add whatever

is necessary to keep the ultra-capacitor bank above 50% SOC. Load is then calculated using Equation 5-14 (Felix 2013).

$$Load = Cap_{recharge\_power} + \left(\sum Port_{power\_request} - Cap_{power} \right) \qquad \textbf{5-14}$$

The actual command sent to each individual power converter will therefore be slightly different than what the raw vehicle request was, as when the ultracapacitors need recharging an extra recharge_power figure will need to be added on top.

5.2.5.2 Dynamic Modifier Chain

The dynamic modifier chain performs the following tasks:

1. Guard the fuel cell against load driven reactant starvation,
2. Keep the battery bank operating within manufacturer limits,
3. Enforce energy reserves per supply,
4. Execute action factor derating.

To perform its first task the dynamic modifier chain follows the monetary analogy for the handling of on-board energy considered again an energy request as a currency withdrawal. As explained in Section 5.2.5.1 this withdrawal comes from either or both supplies, yet the commanded amount is an instantaneous mathematical calculation and the supplies are both chemical reactors which have inherent dynamics. Batteries and ultracapacitors can react almost instantly to any command which is within their capabilities, but the fuel cell cannot. This comes from the fact that for the hydrogen reaction described by Equations 2-1 and 2-2 to take place air has to be pulled into the fuel cell by a forced intake system. In the present there exist two options which are compressor driven or fan driven intakes. For this research the former option is being considered. As described by Equation 2-8 fuel cell stack voltage depends on reactant partial pressures which are driven in part by the compressor. This

ties power generation to flow dynamics which make the fuel cell the source with the slower reaction speed. To illustrate the effect of demand magnitudes versus fuel cell response consider Figure 5-11. The fuel cell power pack for the simulation is made up of two 150 kW fuel cells, which in turn are made up of two 75 kW stacks. Figure 5-11 shows the response to several current demand steps for one of the constituent 75 kW stacks.
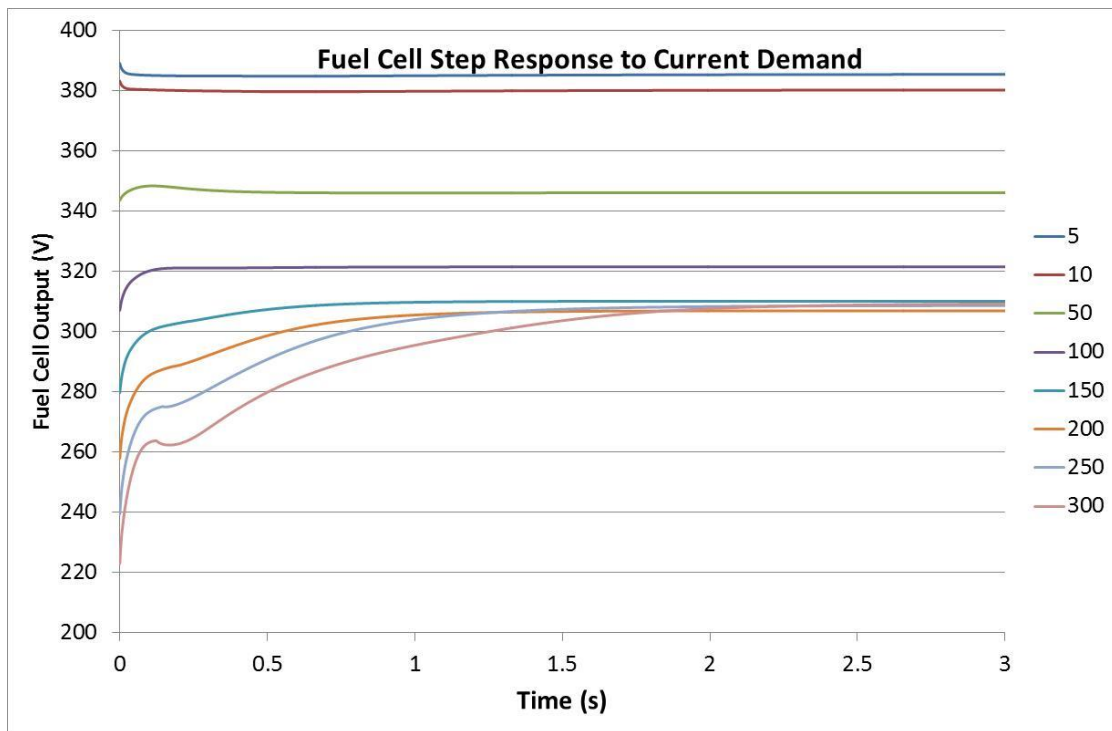
Figure 5-11 75 kW Fuel Cell Step Current Response

When a fuel cell is subjected to load changes the output voltage will drop in reaction to the losses described in Chapter 2, Equations 2-3 to 2-5, but if the change is too large and sudden voltage can drop below manufacturer minimums due to starvation. Figure 5-11 75 kW Fuel Cell Step Current Response shows that for currents of 150 amperes or over it takes the compressor almost two seconds to compensate and supply the required air for the reaction. Too many such episodes can permanently damage the fuel cell. Because of all this Hardware Control monitors the rate of change of the demand through input Load_dot with units of [W/s]. If Load_dot goes above a threshold

the excess load will be added to the battery´s account and withdrawn from there as much as possible while the compressor stabilizes then the excess is directed back to the fuel cell.

The Dynamic Modifier Chain is described in detail for both power supplies in the following equation chain. First is the chain for the Fuel Cell.

$$FC\_Cmd\_Raw = Power\_Rq\_Fuzzy * FC\_Mode \qquad \textbf{5-15}$$

$$Batt\_Cmd\_Raw = Power\_Rq\_Fuzzy * Batt\_Mode; \qquad \textbf{5-16}$$

In Equation 5-15, FC_Mode is the set percentage command output from the active fuzzy set. $Power\_Rq\_Fuzzy$ is equal to the result of Equation 5-14. Equation 5-16 is the equivalent for the battery pack. FC_Cmd_Raw and $Batt\_Cmd\_Raw$ are pre-compensation power commands or "raw" commands. After this initial calculation the chain needs to monitor if the request does not exceed the maximum battery discharge current. To this end the result of Equation 5-17 is the maximum power allowed to be drawn at present battery voltage which does not exceed manufacturer current limits. Vbatt stands for the instantaneous battery voltage, and $Max\_Batt\_Disch\_I$ is the calibratable manufacturer maximum discharge current parameter.

$$Act\_Batt\_Discharge\_Pwr = Max\_Batt\_Disch\_I * Vbatt \qquad \textbf{5-17}$$

To determine if the actual battery delivery is being limited to $Act\_Batt\_Discharge\_Pwr$, by the battery dynamic chain, this amount is added to the fuel cell command and then subtracted from the original Load command. If the result is other than zero that amount is automatically added to the fuel cell request per Equation 5-18

$$FC\_Pwr = FC\_Cmd\_Raw + (Load - (FC\_Cmd\_Raw + \\ Batt\_Energy\_Act)) \tag{5-18}$$

In Equation 5-18, *Batt_Energy_Act* is the battery power command after maximum discharge current limitation. Next, because the reserve energy is calculated in Joules, the power request is integrated over one time step to transform it into energy.

$$FC_{Energy} = \int_0^{Ts} FC_{Pwr}\,dt \tag{5-19}$$

Then FC_{Energy} is limited to the smallest of either the addition of the FC specific and Battery Exchange Energy or the remaining energy inside the hydrogen tank. The Battery Exchange Energy value comes from the battery dynamic chain and represents an energy amount which the battery could not supply due to scarcity. Figure 5-12 shows the Simulink diagram for the Energy Exchange and Limitation functionality.
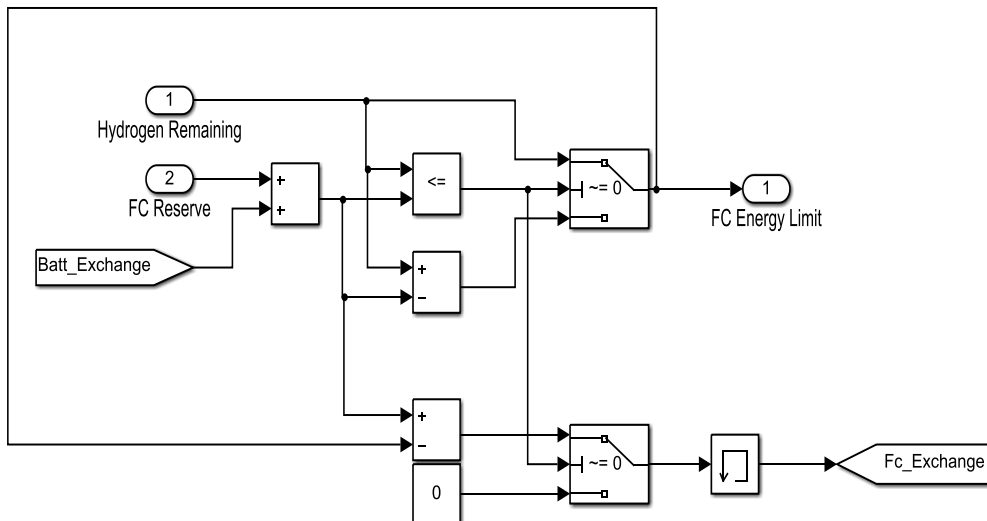
Figure 5-12 Fuel Cell Energy Exchange and Limitation Block

As mentioned the resulting limit is then applied to the Fuel Cell energy requirement. If there is a delta between the limited and unlimited values this amount is passed over to the battery. At first sight this second exchange might seem unnecessary, but it is carried out to cover for two cases. Firstly, since the energy exchanger block protects for reserve violations, the second exchange passes the amount to the battery to try and cover the shortfall. Secondly, if the remaining fuel cell supply is also smaller than both reserve and request at the same time, the second exchange again tries to cover for this. Figure 5-13 shows the Simulink block for this second phase of the chain, for both Battery, bottom part, and Fuel Cell, top part.
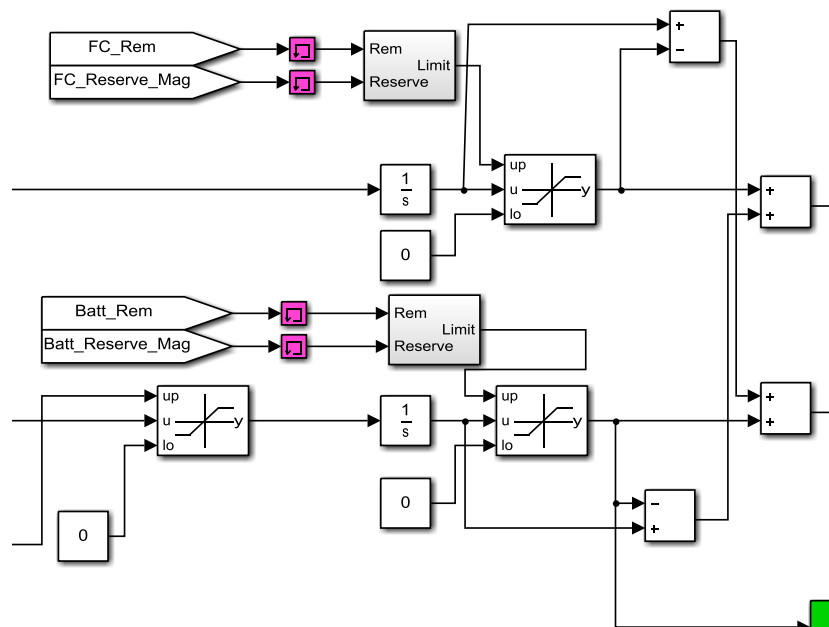
Figure 5-13 Reserve and Energy Limitation with Second Energy Exchange

The third and final phase of the dynamic modifier chain has to do with the action parameter defined in Equation 5-8. One of the objectives of the Mission Tracker is to try and achieve Action values greater than one, which means the vehicle will have enough energy to finish the mission. To achieve this if the present forecast for the mission results in an Action value smaller than one, the request

for both power supplies are further derated, or reduced, until Action reaches a value above 1.1.

The result of the previous process is then limited to positive values before being differentiated to obtain a power command which will then be limited again to the maximum power rating of the applicable source. Both limitations happen in the saturation blocks. As a final step the newly limited value is filtered to achieve a smoother signal.
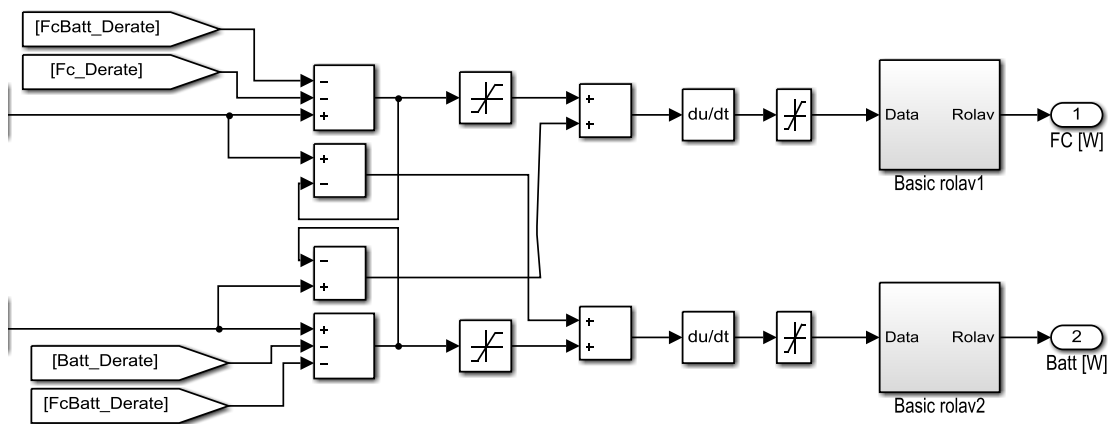
Figure 5-14 Dynamic Modifier Chain Final Phase

The previous paragraphs described the Fuel Cell Dynamic Modifier Chain. The Battery power command flows through an identical process. Both chains are shown in Figure 5-15.
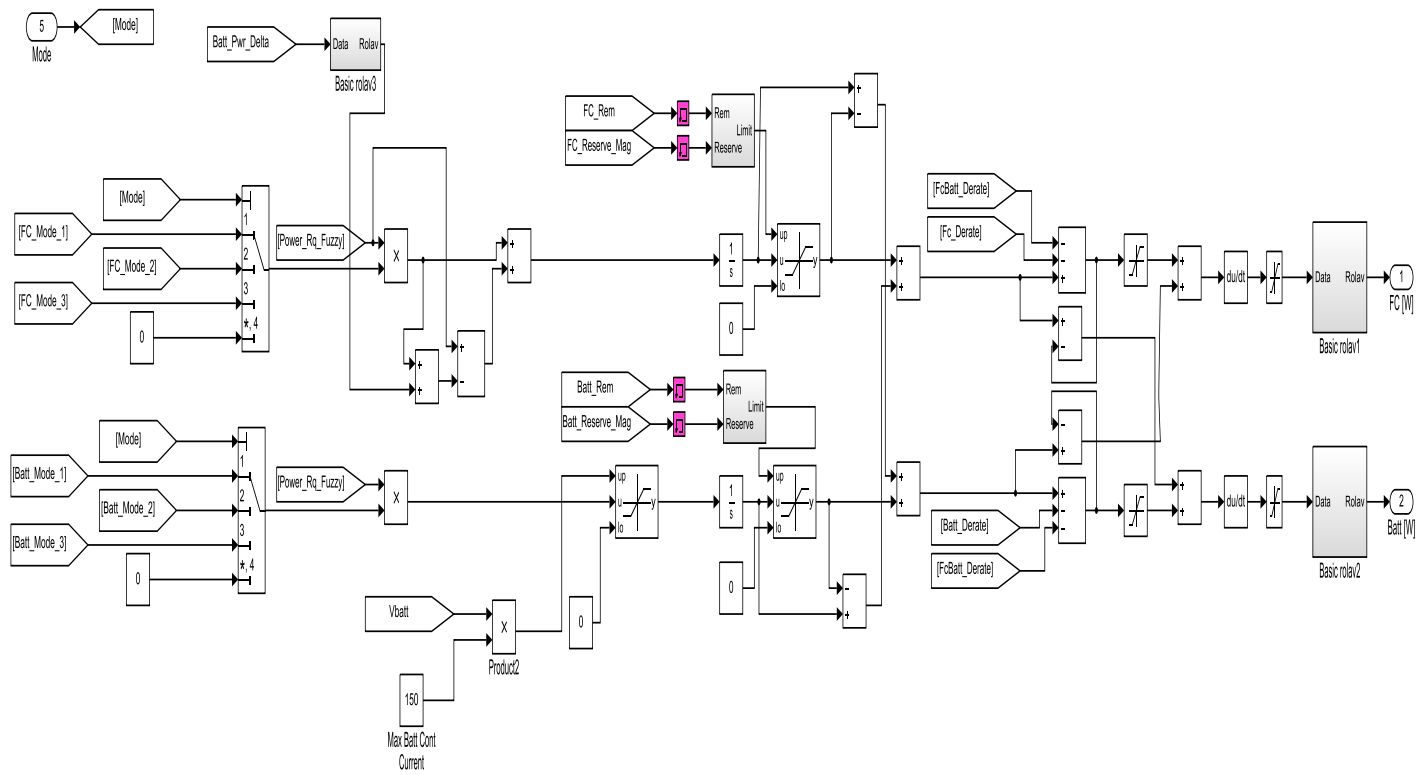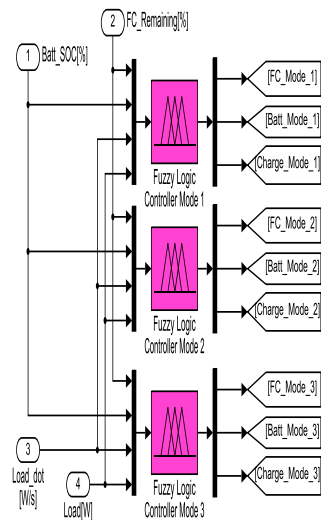
Figure 5-15 Full Dynamic Modifier Chain with Fuzzy Core

5.2.5.3 Power Converter Load Sharing

The final task of the Hardware Control module is to relay an energy delivery command to the two converters in front of each supply and to the capacitor isolation relay. Thanks to the Dynamic Modifier Chain fuel cell and battery commands are already limited and adapted to what each device can meet due to their inherent dynamics and characteristics. In the case of the ultracapacitor its current delivery is limited and reserved for high speed transient loads. To drive each converter a PWM signal is used together with a feedback signal to monitor energy delivery over time; through this mechanism each converter will duly carry on its share of the request. Figure 5-16 includes the circuit for this load sharing system.
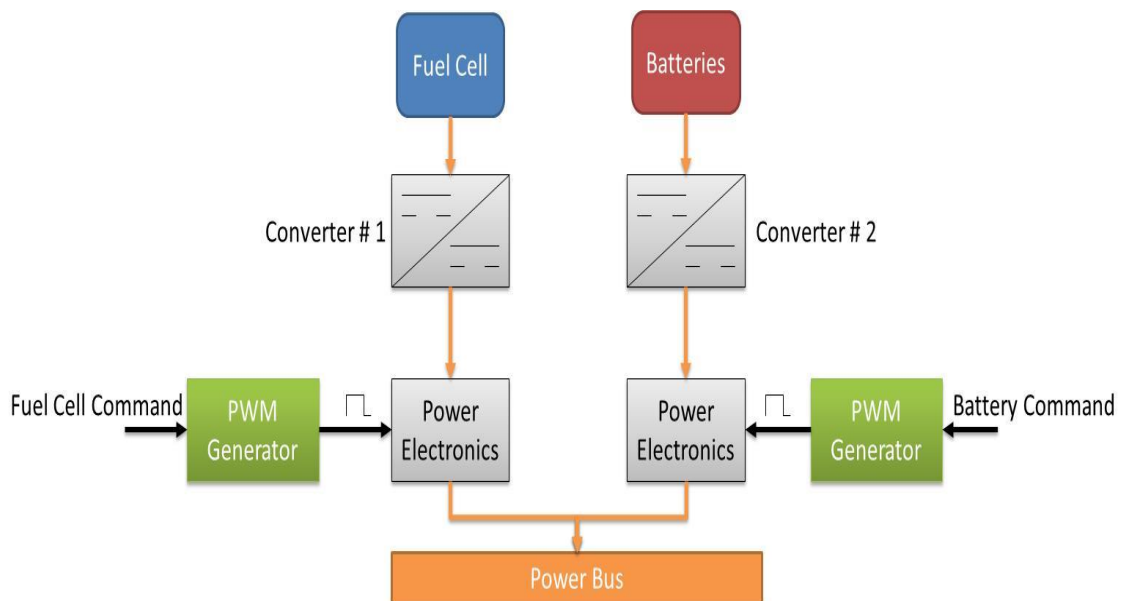
Figure 5-16 Load Sharing Circuit

5.3 Medium Level

The next level in the software structure has two responsibilities. Firstly, it uses vehicle historical energy usage information to predict how much energy will be spent over a given mission profile. Secondly, it uses this information, together with other vehicle inputs to arbitrate how much energy will be supplied to each different load subsystem to protect the reserves and ensure the fulfilment of the mission at hand. In doing so, if allowed by the user, the system can configure the vehicle electrical systems on its own.

5.3.1 Energy Forecasting System

The forecasting system the medium level layer is made up of a number of different algorithms which again process different information according to their own nature and goals. Because of a possible lack of external information the system has been conceived to be able to function without driver navigation and planning inputs, using the vehicle´s own history. Its tasks are as follows:

- If not provided one at the start of deployment, create an artificial mission profile based on historical data stored on board, and supply this profile to the low level graph engine.

- In hand with the previous task, maintain records of load system criticality to again create Criticality Matrix for the lower level layer and the Manage system of the medium level layer.

- Estimate average energy consumption for each system, or stakeholder, after the completion of each mission stage for use by the lower level graph engine and medium level layer Manage system. This is what is referred to as look-back energy forecast in this system.

- Create a look-forward energy consumption forecast based on instantaneous vehicle driving conditions and driver inputs.

All the information generated by this block which is used by other subsystems different from the Manage system is first received by the latter, processed and then sent out to other interested parties, per Figure 4-2.

As mention in the previous section the system has been conceived to be able to work with or without user navigational and mission information. The purpose of this is that in case external information cannot be trusted or provided for whatever reasons every function can carry on working as expected.

If the user does provide mission information prior to deployment the forecasting system creates a criticality matrix and passes the full information package to the lower level layer for its own ends. If not then the forecasting system creates the package using information stored on board which tells how the vehicle has been used since day one. This would constitute the worst case scenario and therefore require every one of the algorithms of the forecasting engine.

Figure 5-17 describes the flow of information inside each block of the forecasting system.

5.3.1.1 Mission Profile Data

Figure 5-2 shows how mission data is transformed into a mission graph. As explained in the previous sections the mission graph is defined by a group of matrices constructed from navigational information. This information is broken down to determine what the expected displacement or distance to be covered by the vehicle will be. For this system it is assumed a geospatial interpreter

breaks this information down and feeds the forecasting system a figure of how many miles or kilometres will need to be covered together with any silent watch period durations. When the user enters this data a software function stores it in a mission profile memory table. Table 5-1 shows the resulting table after a number of simulation runs.

Table 5-1 Mission Profile and Consumption Encoding (R. E. Felix Moreno 2014)

Profile Code	Times Used	Number of Energy Consuming Segments	Historic Energy Usage [J]	Number of Edges including Idle Edges
26	12	5	1374000000	5
11	5	4	1500000000	4
1	21	1	1080000000	2
10	9	4	1600000000	4
6	8	3	1300000000	4
13	15	4	1140000000	5
5	20	3	1200000000	4
124	2	7	800000000	7
78	1	7	600000000	7
45	8	6	1700000000	7

To enter the mission profile in to Table 5-1 each mission profile is coded in the following manner. For every mobile edge that edge is marked with a number one, watch or idle edges are marked with a zero. To calculate the numerical value resulting from the previous mission encoding a binary number is made up assigning the least significant bit to the initial edge value and progressing right along the mission encoding bits until the last edge is assigned to the most

significant bit. Consider the following example for a mission of four edges (mobile, stationary, mobile, and idle).
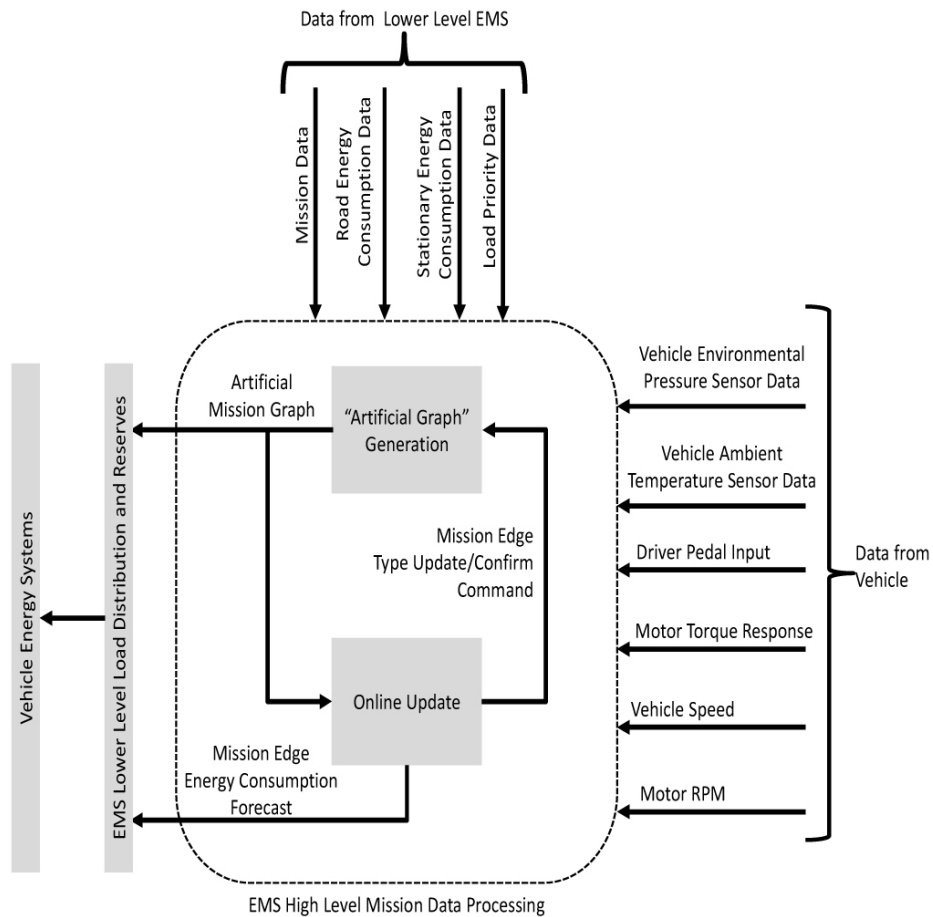
Figure 5-17 Forecasting System Architectural Diagram (R. E. Felix Moreno 2014)
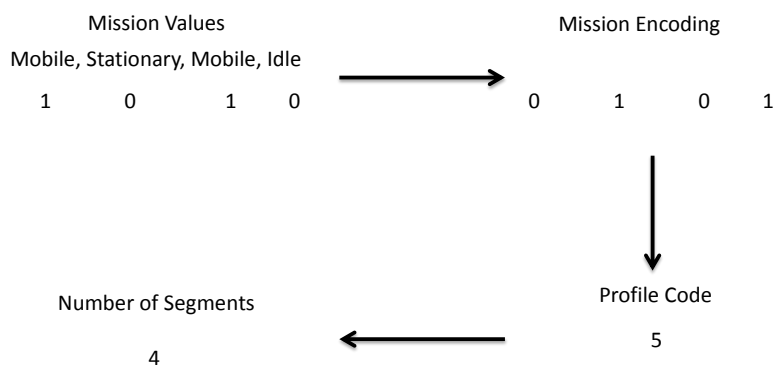
Figure 5-18 Mission Encoding Process

The first three steps of the four step mission encoding process have already been explained. The final step calculates and stores the number of edges present in the mission. This is done to avoid confusion between missions that could have the same encoding value, but different length. It can happen when two or more missions have a value of a given number. The shortest could have just enough bits to make up the value, and all the others can have a series of idle or stationary edges as the most significant bits. Consider the result from Figure 5-18. The final value is five, but there is an extra zero valued edge to left of the most significant bit with a value of one. The most significant zero will not add to the profile value, but to distinguish it from a mission with the same value, and only three edges of length, the number edges is used. Therefore codes with the same value and different length mean that after the most significant one-valued bit there are a number of zero-valued bits that make up the remainder of the mission. The last two pieces of vehicle usage information store in Table 5-1 are the number of times each profile has been used or observed and how much energy said profile has spent historically. The reason behind this type of encoding is that it takes very little memory space to store 255+ types of mission profiles.

5.3.1.2 Artificial Mission Profile Creation

The preceding section elaborates on how mission data is processed, encoded and stored when available from the user. For the opposite case, when the user has not provided any navigation information, a mission profile is created to allow the underlying lower level layer of the control structure to operate as intended. To fulfil the task of synthetizing this new mission profile a new system has been conceived dubbed the "Artificial Graph Generation" subsystem (R. E. Felix Moreno 2014), whose block diagram is shown in Figure 5-19 Artificial Graph Generation Subsystem Figure 5-19.
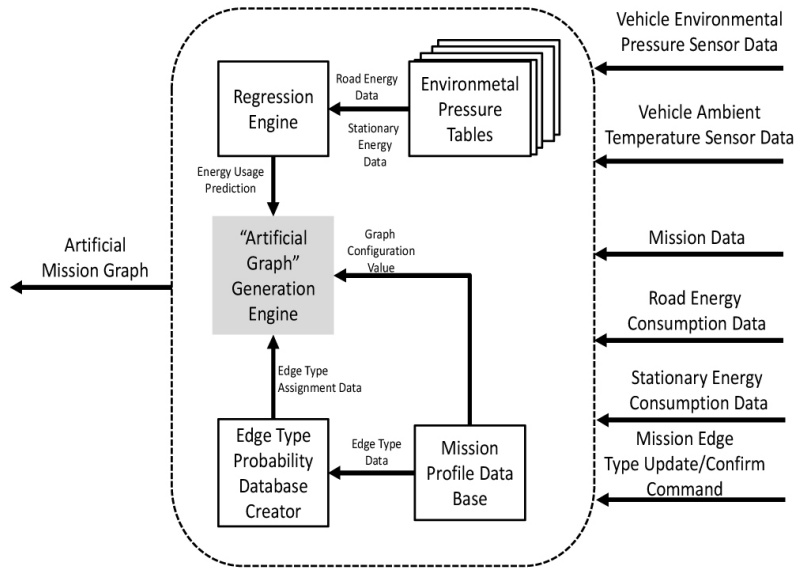
Figure 5-19 Artificial Graph Generation Subsystem (R. E. Felix Moreno 2014)

5.3.1.2.1 Environmental Pressure Tables

In order to create the artificial mission profile certain pieces of information must be acquired by the Artificial Graph Generation subsystem. Because PEM fuel cells require atmospheric air for the chemical reactions in Equations 2-1 and 2-2 its density has a big effect on the power generation capabilities of the fuel cell. One of the ways this is palpable is by the electrical load of the compressor which will vary for the same power output at different altitudes. The end effect is that the average energy consumption of the whole system will vary with altitude for the same usage profile. This parameter is needed by the low level layer and as such must be estimated by the medium layer until real world data of the current mission is captured. To estimate the average value, energy consumption is divided into two categories, one for mobile energy consumption and a second for stationary. Furthermore, the whole operating window of the vehicle, in terms of atmospheric pressure, is broken down into 5 kPa segments; starting a 108 kPa ending at 53 kPa. The data is further binned by profile code and tied to the average ambient temperature experienced when this code has been used. Table 5-2 shows the table resulting from a series of simulation runs (R. E. Felix Moreno 2014).

110

Table 5-2 103 kPa – 98 kPa Environmental Pressure Window Data (R. E. Felix Moreno 2014)

Profile Code	Ambient Temperature [°C]	Environmental Pressure [kPa]	Road Energy Usage [J/m]	Stationary Energy Usage [J/s]
26	1	98.01	6800	13000
11	36	101.00	6949	13803
1	11	97	7142	18715
10	37	101	6867	15045
6	16	100	6995	15092
13	7	103	7061	16397
5	3	100	6963	15073
124	18	98.50	7030	14524
78	27	99	6996	13563
45	28	100.50	6919	18756

The data entered in the energy usage columns is the output of a feedback rolling average. By having smaller environmental pressure tables, instead of a large master table, it is quicker for the system to determine if the vehicle has operated inside the present window or not. To obtain the average energy consumption figures, which will be in turn passed to the lower level layer, a linear regression-base machine learning algorithm is used.

5.3.1.2.2 Linear Regression

The objective of linear regression algorithms is to find coefficients that when placed inside an equation of the form "mx+b" will result in a function that closely fits a data set known as the training set. The linear equation is referred to as a hypothesis, $h_\theta(x)$ and is given in Equation 5-20, (Weisberg 1985), where x_1 is profile code, x_2 is ambient temperature and x_3 is environmental pressure and θ_x are the coefficients resulting from the learning process.

$$h_\theta(x) = \theta_0 + \theta_1 x_1 + \theta_2 x_2 + \theta_3 x_3 \qquad\qquad \textbf{5-20}$$

The reason behind the use of machine learning is that this type of algorithms are best suited for handling large amounts of data, and data describing features, for their calculations. This way as the vehicle accrues an ever larger number of missions the algorithm will be ready to handle the ever growing size of the data set. The way the system works is by taking a profile code, environmental pressure and ambient temperature as data while the average energy usage is the resulting output. This process is run twice to obtain an average for each one-valued edge (mobile) and another for zero-valued ones (stationary and idle).

In machine learning the automatic way to determine which coefficients are the best fit for the training data is to set a cost function, $J(\theta)$, given in Equation 5-21. In Equation 5-21 m is the number of training examples for the system.

$$J(\theta) = \frac{1}{2m} \sum_{i=1}^{m} (h_\theta(x^{(i)}) - y^{(i)})^2 \qquad\qquad \textbf{5-21}$$

The final step to complete the machine learning algorithm is the actual "learning". When the system receives a data set of the type provided where the data defining features (profile code, environmental pressure and ambient temperature) are entered with their result, mobile and stationary average energy consumption, it is said the system learns in a supervised manner. In essence it is given a problem and the answer to it. So far the system has the problem, the hypothesis, and the answers to past instances of it, the historical data. Gradient descent will now use this information to obtain the coefficients that will allow the system to compute an approximation of an answer to the problem with future unobserved data. These coefficients are obtained by minimizing the cost

function which is the measure of success. The smaller the output of the cost function means the data is fit better, so when the hypothesis is run using new data as its inputs the output will be a good approximation to the real answer. Gradient descent runs on the first derivative of the cost function until its minima is found using Equation 5-22. In Equation j is the index number of the θ coefficient from Equation 5-20, so that $j = 0 \dots 3$ in this case.

$$\theta_j := \theta_j - \alpha \frac{1}{m} \sum_{i=1}^{m} \left(h_\theta\left(x^{(i)}\right) - y^{(i)} \right) x^{(i)} \qquad \textbf{5-22}$$

The learning process is run multiple times until the cost function is less than a certain predefined threshold. Parameter α is the step size. Once learning is completed the system is ready predict the mobile and stationary energy consumption averages for a given new set of data.

5.3.1.2.3 Edge Type Prediction

Up to this point out of the data necessary to describe a mission the forecasting system has produced the average energy consumption figures for all edge types. The following step is to create the artificial mission profile itself.

The artificial mission profile is synthetized from data in Table 5-1. The profile generation function takes that data and partially reconstructs the applicable graph. It partially does so because it does not create the graph definition matrices, but instead it turns the base$_{10}$ value into binary and walks down it from left to right to determine the type and order of the edges in the profile. Figure 5-20 shows a selection of expanded profiles from Table 5-1 Mission Profile and Consumption Encoding Table 5-1
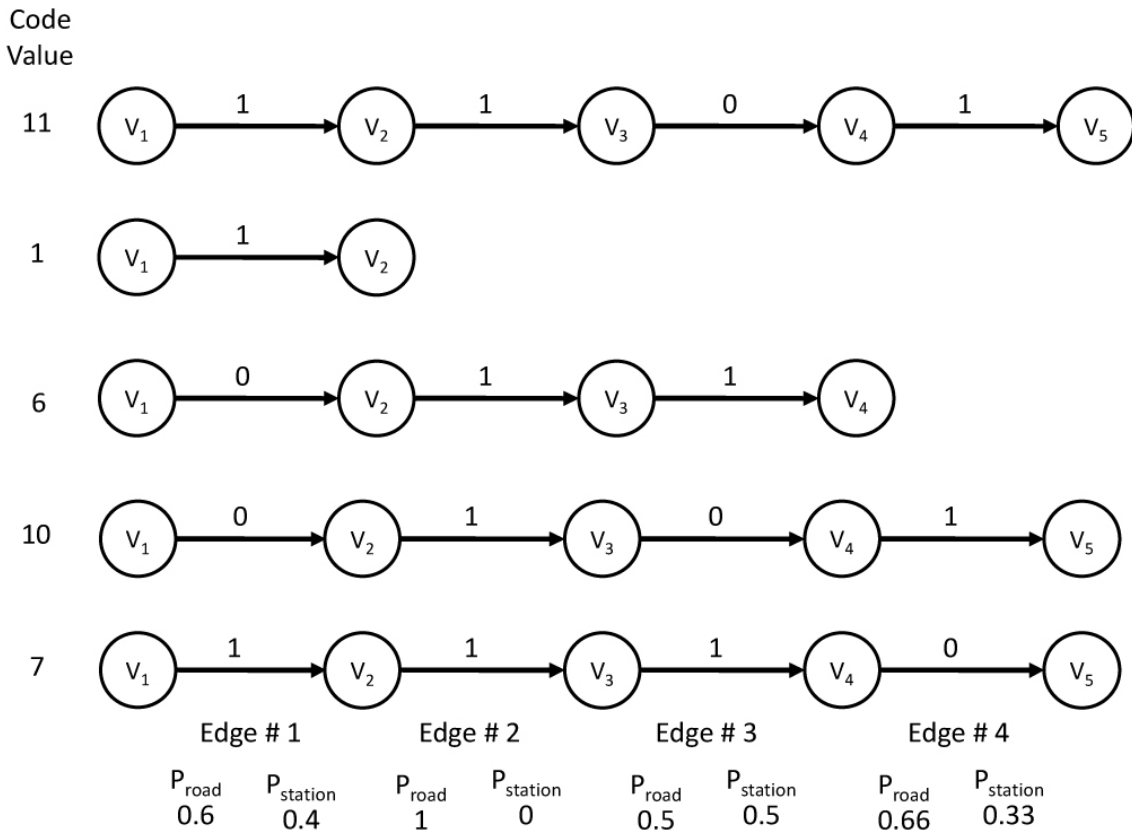
Figure 5-20 Edge type probability calculation for Markov process (R. E. Felix Moreno 2014)

When expanding a code into its partial graph the number of segments data is used to include the correct number edges regardless of their value. The next step is to calculate how likely it is that each edge in the walk is associated to any of the possible types. The bottom of Figure 5-20 shows the probabilities that each edge number belongs to one of the two types. Now there are two ways to try and build an artificial mission graph using the probabilities obtained in the previous step. One would be to use a binary tree and have two child nodes attached to the root, one for each edge type and assign the probability for that edge number to the corresponding edge leading to each child. The tree would be expanded until its depth matched the length of the largest mission profile. This would result in an unbalanced tree, as not all the codes would result in binary numbers of the same length. Then to build the artificial graph a tree search algorithm could go down the tree following the path set by the largest weights to the depth set by the profile code length mode (i.e. the most

common profile length). Although this process would unequivocally be successful there is a more computationally efficient way to achieve the same result and that would be to treat this data as a Markov process (Pearl 1988). Once again the aim is to use a more suitable algorithm for a specific task. The way a Markov process works is that by being given a probability table for a number of states it will provide the likelihood of the system moving from a given state to any of the possible states from time t to time t+1. In this case it would tell how likely it is that a given edge type is followed by the same or the opposite type when it progresses down the profile walk. Table 5-3 shows the probability table for the first edge of the artificial mission. It indicates that for Edge #1 of Figure 5-18, starting from stationary which is the default state or Edge # 0, it is more likely the next edge will be a Road or mobile one. Each Edge number has a similar table associated to it which is updated after every mission.

Table 5-3 Probabilities table for Markov process computations for Edge #1, Initial State fixed at Stationary (R. E. Felix Moreno 2014)

Edge #1	Road (t)	Stationary (t)
Road (t+1)	0	0.6
Stationary(t+1)	0	0.4

Using Markov processes the system can now determine which type of edge is more likely to follow the existing one, to calculate this it uses Equations 5-23 and 5-24 from (R. E. Felix Moreno 2014).

$$P_{road} = P_{Road(t) \cap Road(t+1)} * P_{Initial\ Road\ State} + P_{Stationary(t) \cap Road(t+1)} \\ * P_{InitialStationaryState}$$

$$\text{5-23}$$

$$P_{Stationary} = P_{Road(t) \cap Stationary(t+1)} * P_{Initial\ Road\ State} \\ + P_{Stationary(t) \cap Stationary(t+1)} * P_{InitialStationaryState}$$

$$\text{5-24}$$

The result of using Equations 5-23 and 5-24 simultaneously with the data from Table 5-3 results on Edge #1 being 60% likely to be a road edge, just as Figure 5-20 Edge type probability calculation for Markov process Figure 5-20 would suggest.

5.3.1.2.4 Electric Load or Port Prioritization

The next step in the artificial mission generation process is to create the load prioritization table or as it is known to the low level layer, the Load Criticality Matrix. It is by using this important matrix that loads will be assigned energy reserves in the supplies, so that each can fulfil its goals during the course of a mission. The way this matrix is built is by inserting a new row for each mission edge number, and three columns, one for each energy distribution Port (A, B or C). Along each row when on a given edge a priority or critical load will have a value of one in its cell or zero otherwise. Table 5-4 bears an example of a Criticality Matrix for a three-edge mission.

Table 5-4 Criticality Matrix Example

	Port A	Port B	Port C
Edge # 1	1	0	1
Edge # 2	1	1	0
Edge # 3	0	1	0

When the need arises for the system to create an artificial mission profile the Criticality Matrix must also be fashioned, again from historical information. To create the historical records, once more a binary number is composed from the bit content of each row and then translated into $base_{10}$. Table 5-5 shows the list of possible values obtained from the different possible configurations for the three different ports.

Table 5-5 Criticality Matrix Encoding (R. E. Felix Moreno 2014)

Configuration Value	Port A	Port B	Port C
0	X	X	X
1	1	0	0
2	0	1	0
3	1	1	0
4	0	0	1
5	1	0	1
6	0	1	1
7	X	X	X

Configuration values of zero or seven are ignored for artificial missions as prioritizing all or no loads would defeat the purpose of the system. To create the matrix itself, and because it is in essence the same process as the one required for the mission profile, a Markov process is again used to obtain the configuration values for the give mission length.

5.3.1.2.5 Mission Profile Creation

At this point the process to be followed for synthetizing the artificial mission profile can be summarized, from (R. E. Felix Moreno 2014):

1. Find the mission profile with highest historical energy consumption total in Table 5-1.
2. Use its segment number data to build the projected profile artificial graph.
3. Use Markov process to determine edge types for the whole length of the profile.

4. Use Markov process to obtain load priority configuration values.

5. Use linear regression to estimate projected average energy consumption values for road and stationary edges along the graph.

6. Relay information to underlying system as its initial conditions. The graph should be similar to the one in Figure 5-2.

7. Update online.

5.3.1.3 System Online Update

Up to this point the medium level layer is able to create an artificial mission profile based on historical information, yet it could be that the user does not follow it. To cover for this condition an online update system has been added to the layer to update the tables and therefore the artificial mission graph and all associated information. The algorithm works by monitoring vehicle speed, pedal position, electrical machine torque load and RPM. With this data it can then decide whether the present behaviour of the vehicle adheres to the prescribed mission profile or not. If it is the latter case the graph must be updated with the new information. In this manner the artificial mission graph is always grounded on the reality of the vehicle operating conditions.

As a first step the graph is updated by following the process described in Section 5.3.1.2.5. In the case of the average energy consumption the process is more complex, but it is so in an effort to provide the best information possible to the low level layer and every other interested party.

The average energy consumption is calculated in two manners. The first is executed every time the system estimates that an edge has been completed. It then divides the energy used during this edge by the distance travelled; this is what is called the "***look-back forecast***" because it is looking back in time. The

second one is done by comparing instantaneous actual vehicle information made comparing it to a library of driving patterns, or frames. These frames are made up of present Pedal, Load percentage, Motor RPM, energy consumption in the last second (i.e. watts) to create a "***look-forward forecast***", or LFF, because it will look forward in time working on historical information.

5.3.1.3.1 Look-forward Matrix Construction

Each frame is compared to an on-board database called the Pedal-Load combination database. If the frame is not found it is then entered into the database together with the distance travelled in the last second. The Load parameter is calculated using Equation 5-25, from (R. E. Felix Moreno 2014). The pedal value is obtained from normalizing the pedal input to a 0 − 100 % scale.

$$Load\ [\%] = \frac{Actual\ Torque}{Maximum\ Torque\ @\ RPM} * 100 \qquad \textbf{5-25}$$

Table 5-6 shows an extract of the database resulting from a series of Matlab simulation runs. The original table is 1634 rows in length.

The next step is to create or update two new matrices called the Node Incidence and Node Frequency matrices. In them each frame is treated as a node in a graph. Each node has associated to it incidence and frequency information to tell which frame has followed it in time and which one has done so more often. If the Pedal-Load Combination Database is of size (n x 6) then the node incidence and frequency matrices are of size (n x n). Figure 5-21 shows a plot of the maximum frequency count for each node and to what node that corresponds. This data is for the Node Frequency and Incidence matrices associated with the Pedal Load Combination Database whose extract is shown in Table 5-6.

119

Table 5-6 Extract of the Pedal-Load Combination Database from Matlab Simulation Runs

Node # (n$_x$)	Pedal [%]	Load [%]	RPM	Energy Cons. [J/m]	Distance Travelled [m]
1	1	1	3929	170	23
2	1	2	3960	718	23
3	2	3	4038	796	23
4	2	4	4101	646	24
5	3	5	4171	1030	24
6	5	7	3358	1000	19
7	5	8	3889	168	22
8	6	10	4459	1389	26
9	6	11	4420	2227	26
10	7	9	3451	1480	20
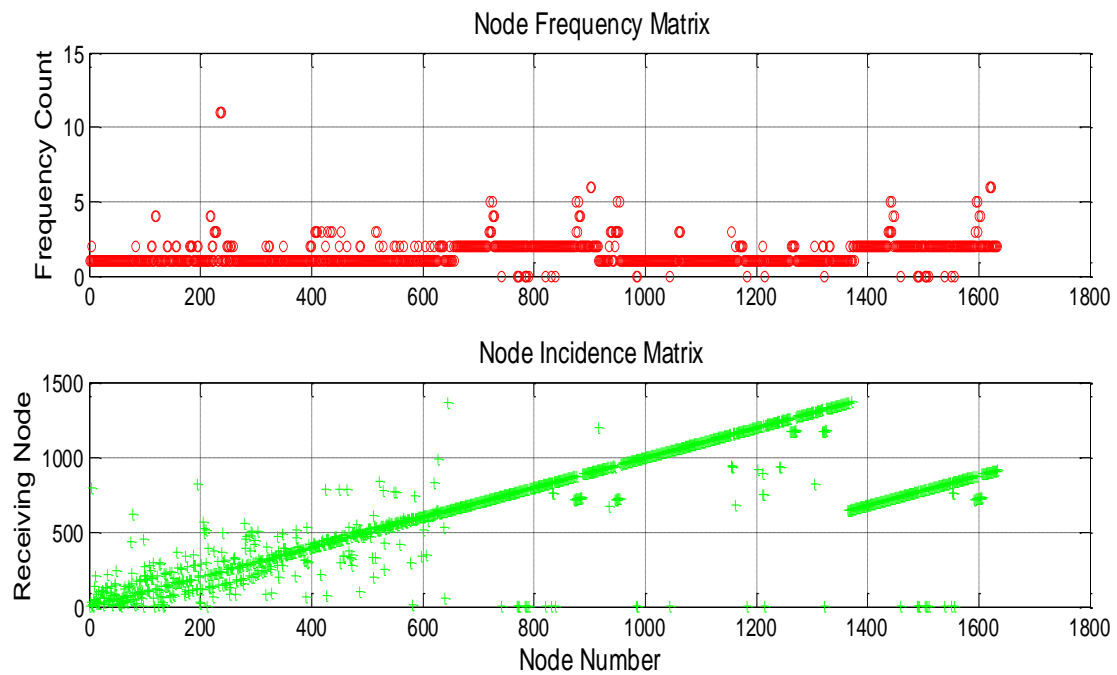
Figure 5-21 Plot of Maximum Values of Node Incidence and Frequency Matrices

To compute the average energy forecast the system groups the last ten frames in a matrix called the Pre_Node_Matrix. It then looks for each frame, one by one, in the database. If the present frame is found then the system takes the following one in the Pre_Node_Matrix to see if it is also in the database. If this is true then the incidence and frequency matrices are updated to show that the present frame is followed by the next frame in the Pre_Node_Matrix. If the present frame is not found in the database it is then concatenated at the end of it and the incidence and frequency matrices are updated as described before. If the following frame is not in the database then it is concatenated at the bottom and again the incidence and frequency matrices are update accordingly.

5.3.1.3.2 Look-forward Virtual Journey Forecast

In order to compute the LFF the system will employ what is referred here as a Virtual Journey subsystem. This system, as shown in Figure 5-22 receives the necessary information to create a new frame matrix and then uses it together with the matrices described in Section 5.3.1.3.1.
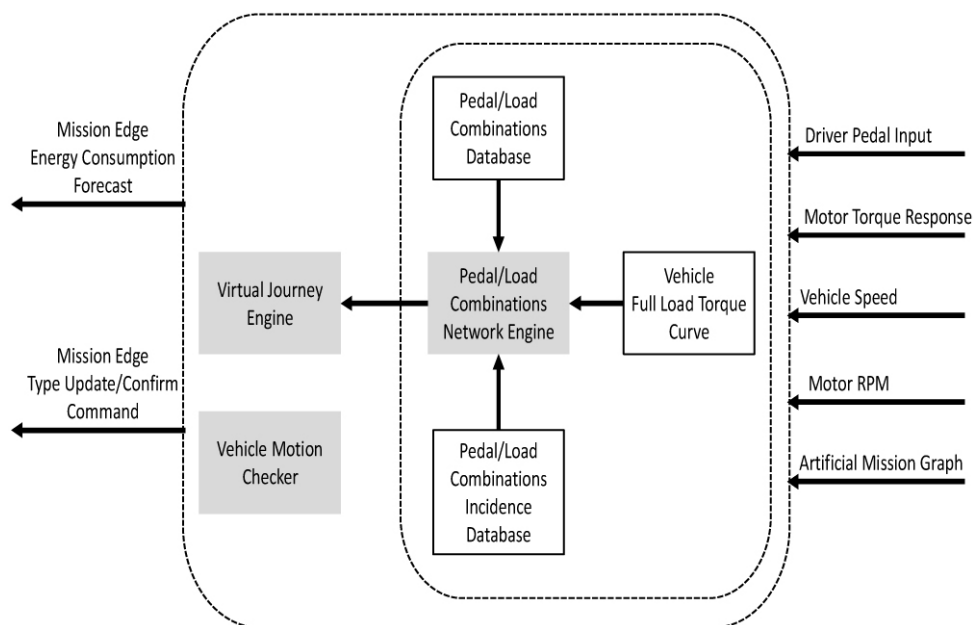
Figure 5-22 Virtual Journey Subsystem Block Diagram (R. E. Felix Moreno 2014)

The process is as follows:

1. Capture a set of ten frames and create the Pre_Node_Matrix.
2. Update matrices as described in Section 5.3.1.3.1.
3. Return to first frame and create a graph walk by selecting the node with the highest frequency count value as the next node in the walk.
4. Continue walking until either of two conditions is met: The sum of the distance values (column 6 of Pedal-Load Combination Database) is equal to the average trip distance for the vehicle, or a dead-end node is reached. A dead-end node is that which has never been followed by another node.
5. Multiple the values in the Energy Consumption column of each node in the walk by its corresponding Distance Travelled value.
6. Add the results from step 5 and divide by the walk´s accumulated distance travelled to obtain the [J/m] average for the virtual journey
7. Repeat the process for all ten frames in the Pre_Node_Matrix and run the results through a feedback rolling average filter.
8. Return the rolling average result as the LFF.

5.3.1.3.3 Virtual Journey Example

To further explain the virtual journey creation process, consider the sample Pedal-Load combination database graphically depicted by Figure 5-23.
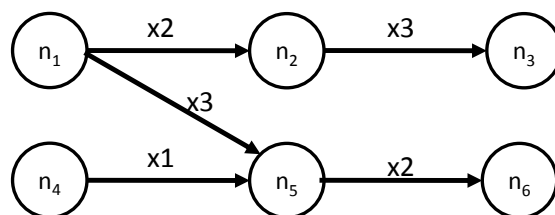
Figure 5-23 Example of a Pedal/Load combination network

122

The Pedal-Load combination database and frequency count matrices for the graph network are shown in Tables Table 5-7 and Table 5-8.

Table 5-7 Pedal-Load Combination Database for Example Network (R. E. Felix Moreno 2014)

Node # (n_x)	Pedal [%]	Load [%]	RPM	Energy Cons. [J]
1	70	100	3392	11911
2	75	100	3200	12750
3	80	100	3028	17193
4	65	75	2800	11847
5	82	81	1515	22705
6	66	82	3014	19249

Table 5-8 Node Frequency Count Matrix for Example Network (R. E. Felix Moreno 2014)

Node (n_x)	1	2	3	4	5	6
1	X	2	0	0	3	0
2	0	X	3	0	0	0
3	0	0	X	0	0	0
4	0	0	0	X	1	0
5	0	0	0	0	X	2
6	0	0	0	0	0	X

For the example assume the driver of the vehicle has input a sequence of frames, consisting of nodes 1, 4 and 5, which will now be processed by the system to create a virtual journey and obtain an average energy consumption figure.

As already explained the system takes the each frame and builds a journey starting from it and based on the incidence and frequency count matrices information. In this example the resulting journey for frame 1 is made up of nodes 1-5-6, for frame 4 is 4-5-6 and finally for frame 5 is 5-6. The reason why the journey from frame 5 is shorter is because it ran into a dead end node, node 6, sooner than the other two journeys.

After building the journey list the energy per meter is computed for each one and all the figures are then averaged. The final result will be used will be then passed on to the low level layer and to any other features that require it.

To determine how accurate the algorithm is, please refer to

Table 5-9 which includes the journeys for the example and the final result. In the last row you can see the actual average value for the input sequence. The important fact to stress is that with just a limited number of nodes the deviation of the forecast from the actual figure is 5.5 %. Obviously as more data is captured the forecast becomes even more accurate. But after all this is just an example. To illustrate the size and complexity of a full-fledged journey Figure 5-24 again shows an extract of the same database used to create Figure 5-21 and a virtual journey from a simulation run which employed it.

Table 5-9 Virtual Journey Table (R. E. Felix Moreno 2014)

Real Life Node Sequence	Virtual Journey for Node (n_x)	Avg. Energy [J/m]
1-4-5	(1) 1-5-6	2346.26
	(4) 4-5-6	2402.11
	(5) 5-6	1924.9
Virtual Journeys Avg.		2230.42
1-4-5 Sequence Avg.		2113.55
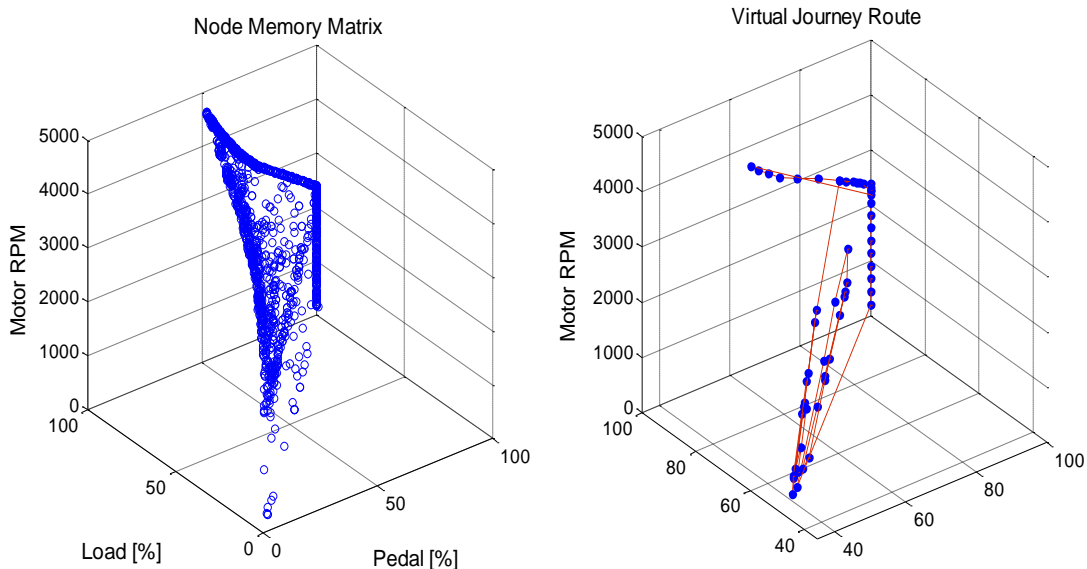
Figure 5-24 Virtual Journey and Pedal-Load Combination Database 3D plot

At this point the medium level layer has fulfilled one of its two main functions, and that if to provide the "look-back" and "look-forward" forecasts. Before this information is cascaded out of the layer it must first go through the second functional block of the medium layer and that is the Manage system.

5.3.2 Manage System

The purpose of the Manage system is to use the information originating from the lower level layer and the forecasting system, in the medium level layer, to enforce the load configuration and restrictions set by the high level layer's Configurator system.

The Manage system is broken into three sub modules which are Budget Update, Average Update and Load Activation Manager. To efficiently be able to estimate how much energy will be spent by each energy port a separate data storage scheme was created which employs Object Oriented Programming. This programming doctrine employs dynamic memory allocation and addressing to create identical and independent data structures. Inside these structures can be not only variables of a predetermined type, but also software functions, called methods, which can work with external and internal data to produce a desired output.

In this type programming an object can be conceived to hold specific data, like device voltage or stored energy, and have a specific behaviour, through its methods, to mimic a real life device. When defining a type of object, with variables and methods, one is said to be creating a "Class". Within the Manage system the defined Classes are:

- Low_Level: An object of this class holds information about how energy is to be held in reserved for every port, specific load, and critical/non-critical systems. By storing this information such and object data transfer between layers is more efficient.
- Pt: This class holds the energy budget, on time, average consumption, vehicle speed mode and energy consumption data for the powertrain.

- SJB: In here is contained the same information that for a Pt object together with device specific data for the vehicle lighting system. This object handles ON/OFF loads.
- Vision: Vision is a copy of the SJB class, but with added specifics for configurable type loads of the vehicle vision system.

All of the previous classes of objects contain the methods required for initializing and updating all the data variables inside them. The objects are created and initialized by the top level Behaviour layer and handed down the control structure.

5.3.2.1 Average Update

The first software feature of the Manage system is charged with computing and storing the device specific average energy consumption value. This is done exclusively for non-powertrain loads. The feature receives a port class object, like SJB or Vision, and works out for all active loads what their average energy consumption is. Then it stores the updated value inside the object and returns it. The pseudo code for this feature is as follows:

Average_Update (object, Load_ON_Indicator, On_Fly_Data, dT) {

If Load_ON_Indicator = ON   %Is the Load ON?

%Keep track of how long the object has been on by using data from the On_Fly_Data structure

On_Fly_Data.Load_ON_Time = On_Fly_Data.Load_ON_Time + dT;

%Pull Average data for all of the device´s loads from the object by using Get_Avg method

New_Load_Average = Get_Avg(object);

%Pull accumulated energy usage information for the specific load from the object using the Get_Load_Energy_Usage method

Specific_Load_Energy_Usage = Get_Load_Energy_Usage(object);

%Compute a new load specific average consumption figure

$$New\_Load\_Average.Specific\_Load = (Specific\_Load\_Energy\_Usage) / (On\_Fly\_Data.Load\_ON\_Time)$$

%Store new Average information in the object using the Set_Avg method

object = Set_Avg(New_Load_Average, object);

%Exit function

Return(object); }

It can be appreciated that by using Object Oriented Programming the whole operation of the Manage system, which could deal with an unknown number of devices, is more easily read, understood and data flows more consistently. Also by using classes the code becomes generic and applicable to any device which uses the same type of object. Once more the design philosophy of the project is followed by using a specific methodology for what its best intended.

5.3.2.2 Load Activation Manager

This feature sits at the heart of the Manage system. Its task is to take the objects for all devices and:

- For ON/OFF loads, authorize which one can be turned on at any given time.
- For CONFIGURABLE loads, determine how many "Transient" events each one has left in its energy budget.
- Keep track of how much ON time each load has left.
- Update subsystem and device specific energy reserves.
- Keep track of how much energy is yet to be spent on the active Mission Graph edge for each subsystem.
- Update critical load energy reserves for the low level layer.

The previous list mentions that the Load Activation Manager only works with ON/OFF and Configurable loads. This is due to the fact that continuous loads like the powertrain are dealt with by the high level Behaviour layer. The reason behind it is that such loads are critical for vehicle operation and are also involved with directly with mission performance and execution.

Going back to the Load Activation Manager´s handling of ON/OFF loads, these are the most simple of all load types. They need only be tracked in how long each has been on and how much energy they are actually consuming. When their allotted On Time in the current Mission Graph edge is spent the load is simply turned off.

For the case of Configurable Loads please consider Figure 5-25 which graphically depicts the different parameters employed in their management.

$$E = \int\limits_{0}^{t} P \ dt$$
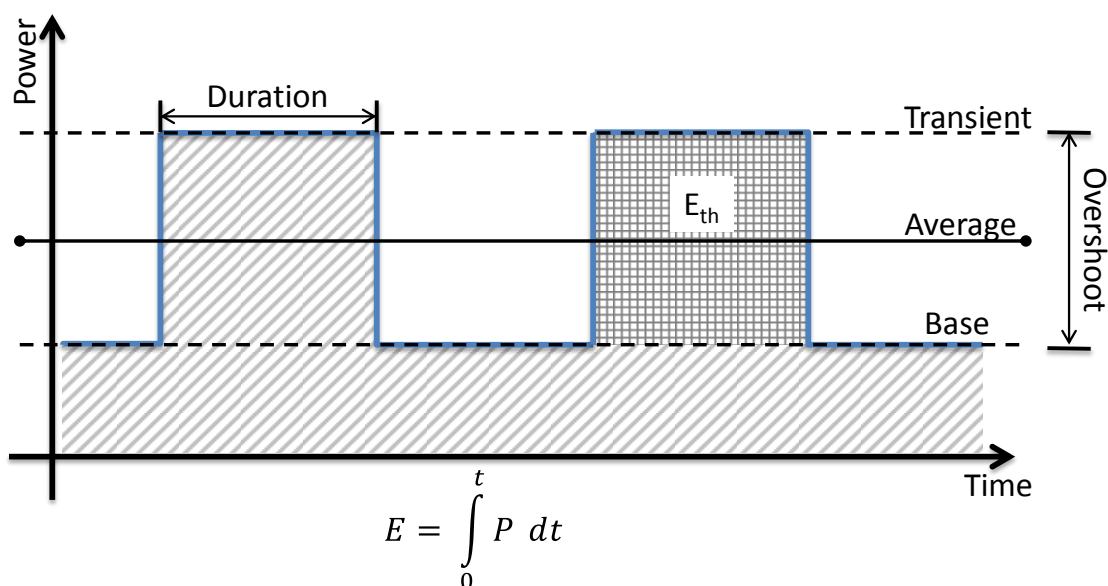
Figure 5-25 Configurable Loads Energy Estimation Diagram

One of the main characteristics of configurable loads is that they can have many different modes of operation, any of which can be used at any given time. Thus the number of parameters needed to describe their energy usage profile is larger. As a specimen, consider the load described by Figure 5-25. It has three possible operational states: Off, On/Base and On/Transient.

On/Base operational state is taken to be the default and most common. On/Transient is a secondary, but also typical operational state which takes a different amount of energy. Finally, Off is self-explanatory. The average energy consumption is the result of dividing the accumulated energy usage, E, by the On-Time of the load. By knowing these three pieces of information the Load_Activation_Manager can then process whether the load is authorized or not to operate. To do so it will carry out the following computations:

131

1. Recover the duration of the current Mission Graph edge from the lower level layer.

$$Time\_Segment = Edge\_Duration_x \qquad [s] \qquad \textbf{5-26}$$

2. Estimate Overshoot power

$$Overshoot = Transient - Base \qquad [W] \qquad \textbf{5-27}$$

3. Work out how much energy the load needs to operate at base

$$E_{min} = Base * Duration \qquad [J] \qquad \textbf{5-28}$$

4. Work out how much energy is taken up by a single transient event

$$E_{th} = Overshoot * Duration \qquad [J] \qquad \textbf{5-29}$$

5. Since the device´s energy budget is decided by the high level Behaviour layer based on average consumption, work out how much energy is available for transients

$$E_{Trans} = (Average * Time\_Segment) - E_{min} \qquad [J] \qquad \textbf{5-30}$$

6. Determine how many transients could be executed within the given budget.

$$Trans\_Count = {E_{Trans}}/{E_{th}} \qquad \textbf{5-31}$$

7. Create a tentative budget for the given edge, based on the energy required for operation in base and the computed number of transients.

$$E_{Load} = (E_{Th} * N_{Trans}) + (Tran\_Count - N_{Trans}) * E_{Th} + E_{min} \qquad [J] \qquad \textbf{5-32}$$

$$N_{Trans} = floor(Trans\_Count) \qquad \textbf{5-33}$$

In the first term of Equation 5-32 the energy required to run an integer number of transients is considered, computed in Equation 5-33. Next, by it computes how much energy is required for incomplete transient events to finally add what energy is need to run in base. This budget E_{Load} is then compared to the one set for the actual edge by the high level layer, $Edge\_Budget_x$, to verify the latter is not exceeded. If so, the load is either shut off to protect the reserves, or the load is set as non-critical and assigned to that energy pool to allow it to be used. Figure 5-26 shows the flow diagram for this decision.
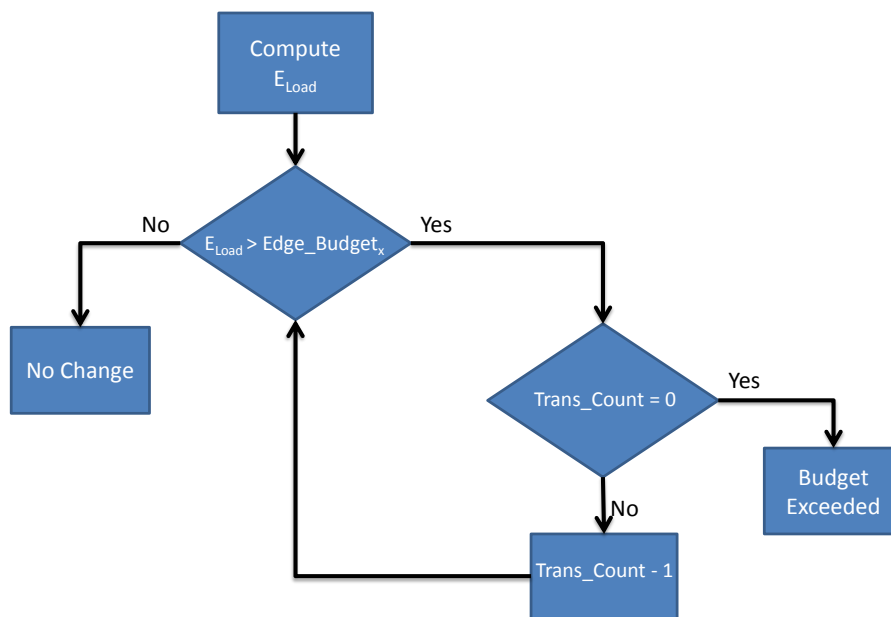
Figure 5-26 Configurable Loads Decision Flow

It is important to note that the Load Activation Manager is constantly updating, so if the transient event last longer than expected the available energy budget would be reduced proportionally. Thus when the feature is executed in the next time step the number of available transients would be affected by the abnormal duration of the last one automatically, since it depends on actual available energy.

At this point both types of loads have had their average information updated and stored in objects, and being given or denied permission to be turned on. As a last step the budget for each load port and device must be updated to keep the reserves true per the vehicle´s operation.

5.3.2.3 Budget Update

To keep the mission's energy budget up to date this software feature will use instantaneous load consumption, vehicle distance travelled and mission elapsed time information. The following pseudo code describes the operation of this feature:

Budget_Update(object, vehicle_status, low_level_data, current_parameters) {

%Capture current operational data in local variables

Distance_Travelled = current_parameters.Distance_Travelled;

Elapsed_Time = current_parameters.Elapsed_Time;

%Pull average data for device loads from object using Get_Avg method

Retrieved_Avg = Get_Avg(object);

Load_Average = Retrieved_Avg.Load_Average;

%Is the current edge a road edge?

If edge_type = road_edge

    *New_Budget = low_level_data.distance_remaning / Avg_speed * Load_Average;*

%Is the current edge a watch edge?

Elseif edge_type = watch_edge

    *New_Budget = low_level_data.time_remaining * Load_Average;*

%Is the current edge an idle edge?

Elseif edge_type = idle_edge

    *New_Budget = low_level_data.time_remaining * Load_Average;*

end

%Update load reserve using Set_Load_Reserve method and using New_Budget as the new reserve limit for this edge

    Object = Set_Load_Reserve(New_Budget, object);

    Return(Object);   }

5.3.2.4 Summary

By running these three steps of the Manage system it can be guaranteed that the overall management structure is always fed energy usage information which is current and correct for the existing vehicle operation conditions and mission. Also the reserves are kept up to date which is of paramount importance for the low level layer. Finally, budgetary information is maintained per load port and device which is in turn monitored by the high level Behaviour layer for energy usage arbitration and

5.4 High Level

The last piece of the Intelligent Control Structure is the high level Behaviour layer. It is charged with the long time horizon tasks and with monitoring information generated by the underlying levels. Because of it deals with decision which affect the vehicle in the long run it is the slower of all layers, but the one whose decisions affect the system as a whole.

It is divided into three major task blocks.

1. **Threat Avoidance:** It uses sensor data to determine if the vehicle is under threat from outside agents. If allowed, the internal Navigator system attempts to navigate the vehicle away from the threat, but closer to the vehicle´s goal at the same time. Threat avoidance has the authority to independently shut down loads if it means more energy will be available for the vehicle to remain safe.

2. **Continuous Load Management:** As the mid-level layer uses the Load Activation Manager to handle interruptible and configurable loads and enforce their budget, Continuous Load Management does likewise with the non-interruptible loads, like the powertrain. One more task it performs is monitoring the low level layer fuzzy modifier chain to rebalance the power commands should the fuel cell become too hot for safe operation.

3. **Configurator:** This last block has the fundamental task of initializing the objects used by the mid-level layer. Parsing mission information to determine what energy is required by each load on every graph edge. Finally it determines the optimum budget and configuration parameters for all three types of loads, such as Interruptible load ON/OFF times and when the vehicle should lower/increase its speed for better efficiency.

Figure 5-27 shows the internal breakdown of the high level layer functional blocks.
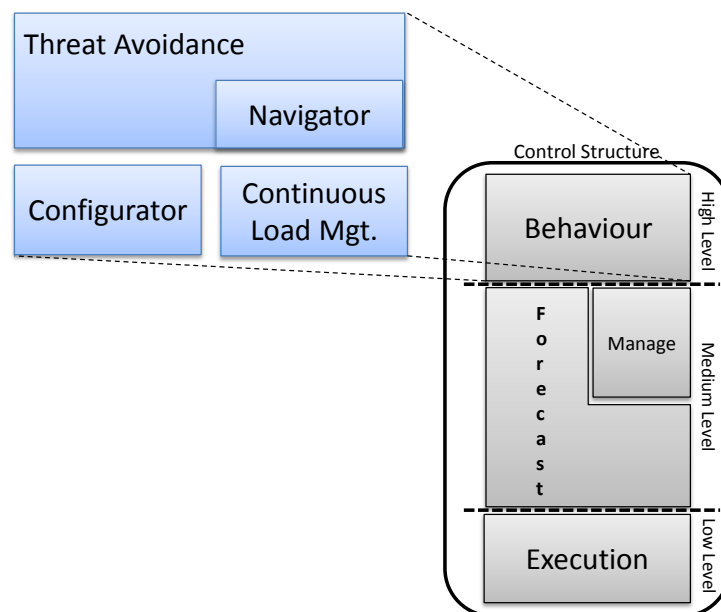
Figure 5-27 High Level Layer Breakdown

5.4.1 Configurator

The first of the block´s functions is to configure the vehicle´s loads and set up a budget based on artificial or user provided mission information.

First, in order to configure the vehicle and determine a budget for the whole mission the Configurator employs a concept which is called subsystem "personality". This concept was thought of to allow for each subsystem to be able to have a "dialogue" with the Configurator to stand up for its own interests. Basically, it is meant to present an initial budget proposal to the configurator, make sure the budget allows it have energy in every edge where it has loads identified as critical. Also, it must communicate to the Configurator if there is a discrepancy between the "personality´s" budget and the Configurator´s. If the low level layer informs the Configurator that it does not have enough energy to fulfil the budget then the "personality" is restricted to operational limits which can coexist with the available on board energy. The following section describes this interactive dialogue and how the configurator sets the system up for operation.

5.4.1.1 Configurator Initialization – Personality Interaction

As a first step the high level layer looks for Mission Information. If it is not preset (i.e. provided by the user) then it triggers the Artificial Graph Generator, within the Medium Level layer, once a mission graph is available the interactive dialogue happens as follows:

1. Configurator turns mission data into budgetary targets. This is done by walking down the acyclic directed mission graph and creating a nominal and transient sum of each load´s power ratings marked as critical. Equations 5-34 through 5-37 are used to estimate the total budget for the mission in nominal and transient terms.

$$Load_y^{overshoot} = Load_y^{Transient} - Load_y^{Nominal} \qquad [W] \qquad \textbf{5-34}$$

$$Budget_{nominal} = \sum_{e_1}^{e_x} Load_y^{nominal} * Criticality_{x,y} \qquad [W] \qquad \textbf{5-35}$$

$$Budget_{Transient} = \sum_{e_1}^{e_x} Load_y^{overshoot} * Criticality_{x,y} \qquad [W] \qquad \textbf{5-36}$$

$$PerEdgeBudget_{(x,1)} = \sum_{1}^{y} Load\_Nominal_y * Edge\_Duration \qquad [J] \qquad \textbf{5-37}$$

$$PerEdgeBudget_{(x,2)} = \sum_{1}^{y} Load\_Overshoot_y * Edge\_Duration \qquad [J] \qquad \textbf{5-38}$$

In the previous equations "x" stands for edge number and "y" is the load number within each edge. Equations 5-35 and 5-36 provide the total power required by the loads. In order to know how much energy will be required both per edge total nominal and transient power ratings are then multiplied by the projected edge duration time.

2. The previous process is repeated to have per edge budgets for every power consumption port, A through C. In Equations 5-39 through 5-41 "z" stands for port identifier (A, B or C).

$$Load_y^{overshoot} = Load_y^{Transient} - Load_y^{Nominal} \qquad [W] \qquad \textbf{5-39}$$

$$Port_{(z,x)nominal} = \sum_{e_1}^{e_x} Load_y^{nominal} * Criticality_{x,y} \qquad [W] \qquad \textbf{5-40}$$

$$Port_{(z,x),Transient} = \sum_{e_1}^{e_x} Load_y^{overshoot} * Criticality_{x,y} \qquad [W] \qquad \textbf{5-41}$$

3. Next is the first actual dialogue between the Configurator and the "personalities".

    a. If the subsystem has not critical loads in the mission, the dialogue is cut short and the budget for critical reserve for the subsystem is zero.

    b. Otherwise, the subsystem using internal load statistics drafts a budget for the loads it has been told are critical. Using mission duration information it returns a per edge energy budget, in Joules, to the Configurator together with a status flag regarding a comparison between Configurator and internal budgets. The status flag can have one of three values: -1 for "not enough energy in budget", 0 for "enough energy in budget" and 1 for "too much energy".

4. Configurator then queries the low level layer for available on board energy information. With this information it estimates if its own budget can be satisfied by the on board supplies.

    a. If the budget is enough, Configurator then agrees with the budget proposed by every personality and a "confirmation" message is sent to each one.

b. If the budget is not enough Configurator estimates based on the original requirements how much of the available energy will go to each subsystem. If in the original requirement a load received 50% of the budget, in the reworked budget it will receive 50% of what is available. Then Configurator sends an "update" message to each personality together with how much energy is available to each one.

c. Upon reception of an update or confirmation message each personality uses linear programming simplex method to determine the ON/OFF time or in the case of configurable loads the Edge_Duration parameter.

The definition of the linear problem is as follows:

$$\min_{x} f^{T}x \ such\ that\ \{ \begin{array}{l} Ax \leq B \\ lb \leq x \leq up \end{array} \qquad \textbf{5-42}$$

Where f is the vector of power ratings for every load in each subsystem per edge, therefore its dimensions are (1,$edge\_number * y$), and y is the number of loads in the system. A is the matrix of load power ratings and activation flags. B is the vector of edge energy budgets and limit edge time duration in seconds. x is the resulting vector of allowed on times/edge durations of the same dimensions as f. lb is the vector of lower bounds whilst up is the vector of upper bounds for x. Because the Configurator requires that x be minimal at the time of the computations f is taken as its negative. Figure 5-28 shows how both A and B match with each other.
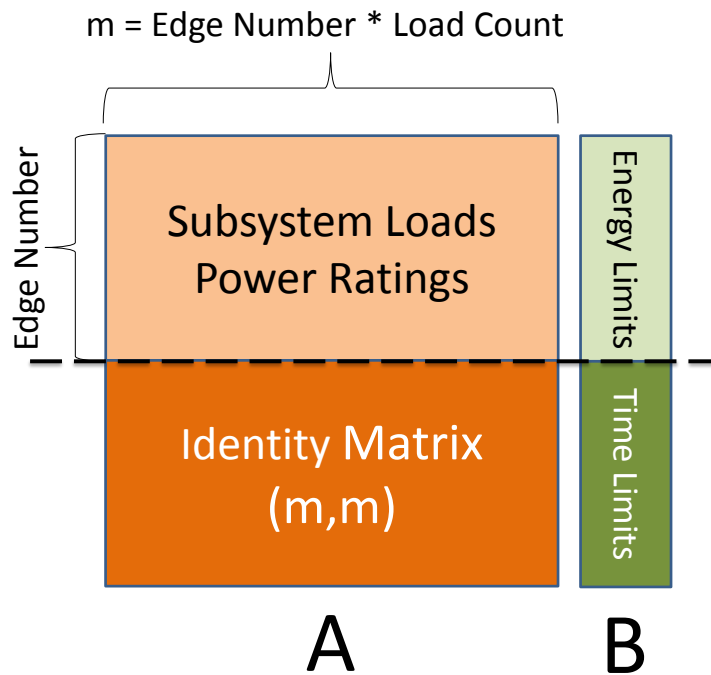
Figure 5-28 A matrix and B vector matching

The reason why both A and B are subdivided in the described manner is to obtain both a set of on times that are limited by the edge duration and available energy for each load per edge. It is important to mention that only critical loads are considered for this calculation. To reflect this non-critical loads are set to zero in the upper part of A. Once this process is complete the dialogue between the personalities and the Configurator moves on to its next stage.

5.4.1.2 Initial Average Consumption Figures for Low Level Layer

As mentioned in Section 5.2 the low level layer requires an initial average energy consumption figure to start its calculations. This parameter is computed by the Configurator based on the result of its dialogue with the personalities. As explained in Section 5.4.1.1 the personalities provide a budget to the Configurator. Whether the result of an update or a confirmation message the end budget is the looked at in detail to obtain how much energy is estimated to

be spent on each one of the three types of edges (mobile, stationary or idle). This is done walking down the mission graph. The parameters H_{or} and H_{os}, which store the Joules per metre and Joules per second figures respectively, are computed per Equations 5-43 and 5-44.

$$if\ edge\ type = \text{road}: H_{or,pre} = \sum_{e_1}^{e_x} \frac{Budget_{x,system}}{Distance} \qquad \text{[J/m]} \qquad \textbf{5-43}$$

$$if\ edge\ type \neq road: H_{os,pre} = \sum_{e_1}^{e_x} \frac{Budget_{x,system}}{Time} \qquad \text{[J/s]} \qquad \textbf{5-44}$$

As such $H_{or,pre}$ and $H_{os,pre}$ hold sum of the Joule per metre or Joule per second figures for the whole mission. To obtain a single final average this values are processed further per Equations 5-45 and 5-46.

$$H_{or} = {H_{or,pre}} \big/ {\#\ of\ road\ edges} \qquad \text{[J/m]} \qquad \textbf{5-45}$$

$$H_{os} = {H_{os,pre}} \big/ {\#\ of\ non-road\ edges} \qquad \text{[J/s]} \qquad \textbf{5-46}$$

5.4.1.3 Object Creation

Next Configurator will create the memory objects used by the medium and low level layers. There are two types of objects which are created. The first is the subsystem object, which is used by the medium level layer in the Manage System, and the second is a low level object. The latter is used to pass information back and forth between the high and low level layers.

To initialize a subsystem type object Configurator calls four base methods and two helper methods.

Table 5-10 Subsystem Type Object Method Calls

Base Methods:
Set_Budget(subsystem_name, subsystem_personality.Energy_Per_Edge);
Set_Energy_Edge(subsystem_name, subsystem_personality.Energy_Per_Edge);
Set_Avg(subsystem_name, subsystem_personality.Avg);
Set_Edge_On_Time(subsystem_name, subsystem_personality.Edge_On_Time);
Secondary Methods:
Set_Load$_x$_On_Time(subsystem_name, subsystem_personality.Load$_x$_ON_Times);
Set_Load$_x$_Energy_Use(subsystem_name, 0);

Set_Budget method stores the sum of the energy per edge estimates to have a total budget figure stored in the object. Set_Energy method stores the energy per edge structure intact. Set_Avg method stores the average consumption figure from the personality into the object. Set_Edge_On_Time stores the full edge estimated duration in the object. In the secondary methods Set_Load$_x$_On_Time stores the negotiated ON/OFF or Edge_Duration times for each individual load in the subsystem. Set_Load$_x$_Energy_Use is initialized with zero as no energy has been spent yet. Later this method is used to keep track of how much energy the load has used out of its allocate budget.

The second type of object is the Low_Level kind. It has one base method and one secondary method. Their respective calls are shown in Table 5-11.

Table 5-11 Low Level Type Object Method Calls

Base Method:
Set_Load$_x$_Reserve(lowlevel, subsystem_personality_data.Load$_x$_Energy_per_Edge);
Secondary Method:
Create_Reserve(lowlevel, vehicle.on_board_energy, 1);

Set_Load$_x$_Reserve sets inside the low level type object an initial energy reserve based on the sum of the load´s energy per edge budget provided by the subsystem personality. The Create_Reserve secondary method takes all the reserves already inside the object and adds them together to create the full mission critical loads reserve. To determine if there is any energy left for non-critical uses it employs Equation 5-47.

$$Non\ Critical\ Reserve = \frac{On\_Board\_Energy\ -\ Critical\ Reserve}{\#\ of\ Edges} \quad [J] \quad \textbf{5-47}$$

By using Equation 5-47 as energy forecasts and expenditure are updated the non-critical reserve is kept current and evenly distributed in all remaining edges.

5.4.1.4 Configurator Load Killer

One of the purposes for the creation of the memory objects, outside of data communication and record keeping, is to avoid having to run the configurator on every time step of the mission. This is due to the fact that some of its processes can be quite time consuming. Though there is one instance that could trigger a configurator re-run and that is a change of operating mode in the low level layer. If one power supply fails triggering a sudden and abrupt reduction in on-board energy, the Configurator would kick in and run the Load Killer Sequence.

In the sudden event of energy supply failure Configurator will start to cut loads in Ports B and Port C (configurable and interruptible loads) to try and keep continuous loads active for as long as possible. The navigator subsystem of the high level layer would try to optimize the continuous loads for the same end.

The Load Killer Sequence starts by looking at the preset priority table and starts to cut loads off by a preset index. A high index value means that load will be left without power sooner than others.

Table 5-12 Load Killer Priority Table

Port		Criticality	Priority Index
All ports		0	100
C High Power	Interruptible	1	90
C		1	80
B High Power	Configurable	1	70
B		1	60
A Non-Propulsion	Continuous	1	30
A		1	0

By having the lowest possible index, continuous propulsion related load will always be left on to try and get the vehicle to its planned destination.

The parameter used to trigger the Load Killer is the applicable duration parameter, from Equations 5-5 to 5-7, for the selected operating mode. If X_{action} is less than one and the low level layer operating mode is *FC_Only* or *Batt_Only*. The load killer will then start cutting loads off until it has either gone through the whole table or X_{action} has returned to a value higher than one, meaning the systems forecasts it has enough energy to complete the mission. By following the priority table, should the *NTE* limit set by the low level layer run out Load Killer will then cut off all non-critical loads at once. At that time X_{action} should remain above one, but if not then Load Killer will continue to go down the table until only critical continuous loads remain.

5.4.2 Continuous Load Management

The tasks entrusted to this feature are continuous load budget enforcement and optimization, Fuel cell thermal protection and signalling to the Navigator when it needs to start a more aggressive path planning strategy.

5.4.2.1 Budget Enforcement

In terms of how the budget is being observed by continuous loads the methodology could be said to be backwards from what the Load Activation Manager, from Section 5.3.2.2, as it not about shutting down the continuous load when power runs out. Instead all other loads are sacrificed in an effort to make sure the vehicle can keep this energy port supplied at all times following mission parameters. This feature then expands on what is done by the

Configurator though instead of shutting down a load it forces it to operate in its most efficient manner. At first such an idea sound logical, and would be expected that all loads operate at their best point at all times, yet that is rarely the case in real life. In the specific case of the powertrain, the point of highest efficiency could not be what is currently being commanded or programmed into the mission profile. Figure 5-29 shows a calculated data, based on measurements taken from one of the DC motors employed on the test platform described in Chapter 6; it shows how the point of best efficiency does not coincide with the point for peak power. Figure 5-30 show how it does not coincides with peak torque either, yet this point would be where the budget can be made to last longer as most of it is actually creating propulsive effort for the vehicle.
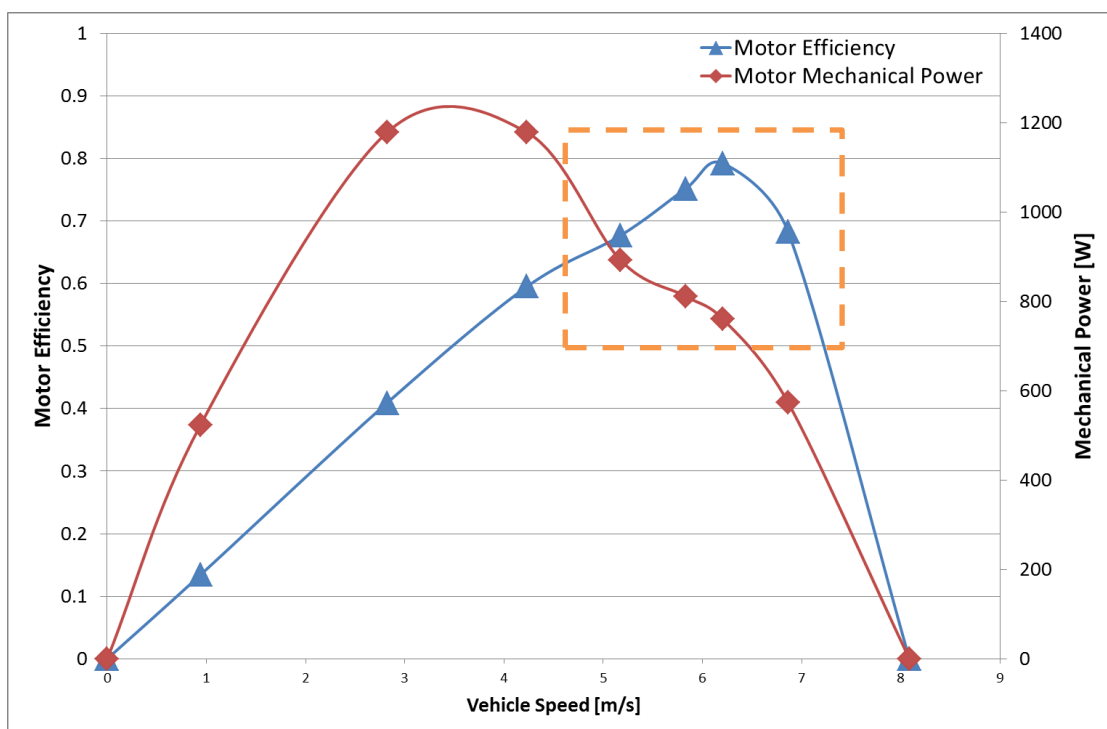
Figure 5-29 DC Motor Efficiency vs. Mechanical Power
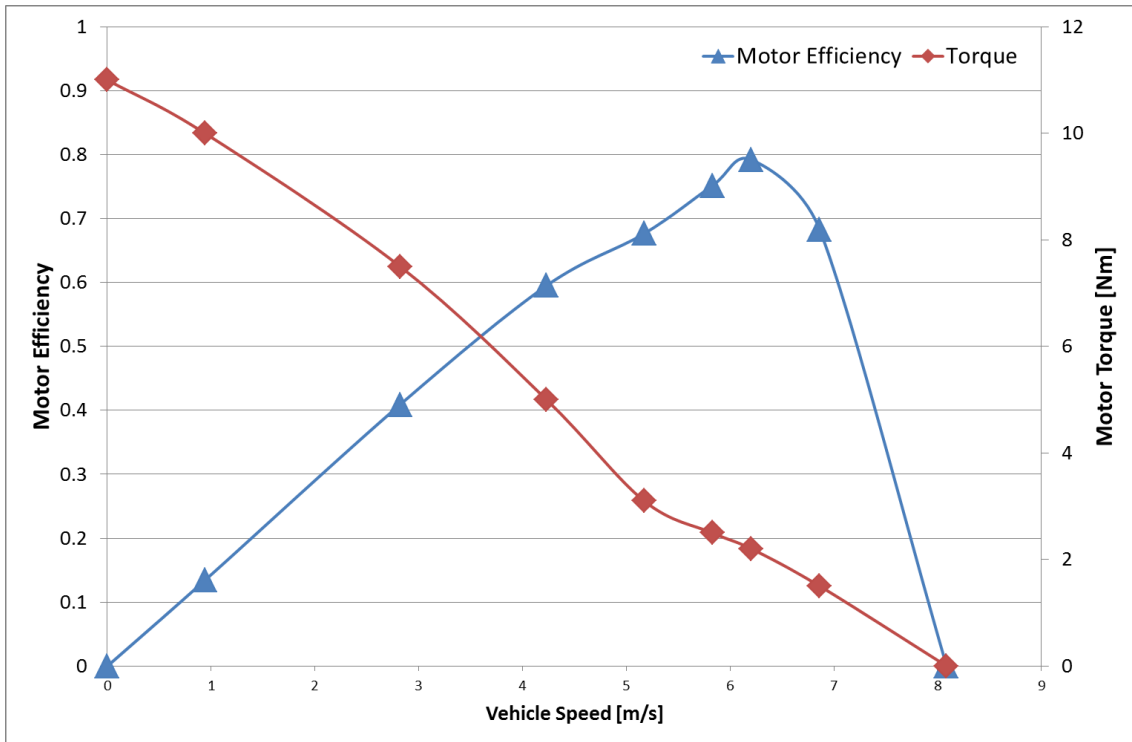
Figure 5-30 Motor Efficiency vs. Motor Torque

In case then of energy shortage the Navigator would be asked to increase vehicle speed to a point inside the dashed box in Figure 5-29. These set of points are form a trade-off between speed, rate of energy consumption (i.e. power) and efficiency. When inside the box the vehicle might be operating at a high speed, but is also operating at its best. It could be feasible for the software to demand a fixed point at all times, yet real world terrain varies so it is necessary, and more realistic, to operate inside a given window. Obviously such speeds might not be friendly with a surveillance profile and will therefore be reserved for energy shortage situations where the vehicle must abort the mission and head to its pre-programmed destination. In this case the Navigator will be advised to set the best course possible forward. Figure 5-31 shows the process steps and information flow for the speed optimization task of the continuous load manager.
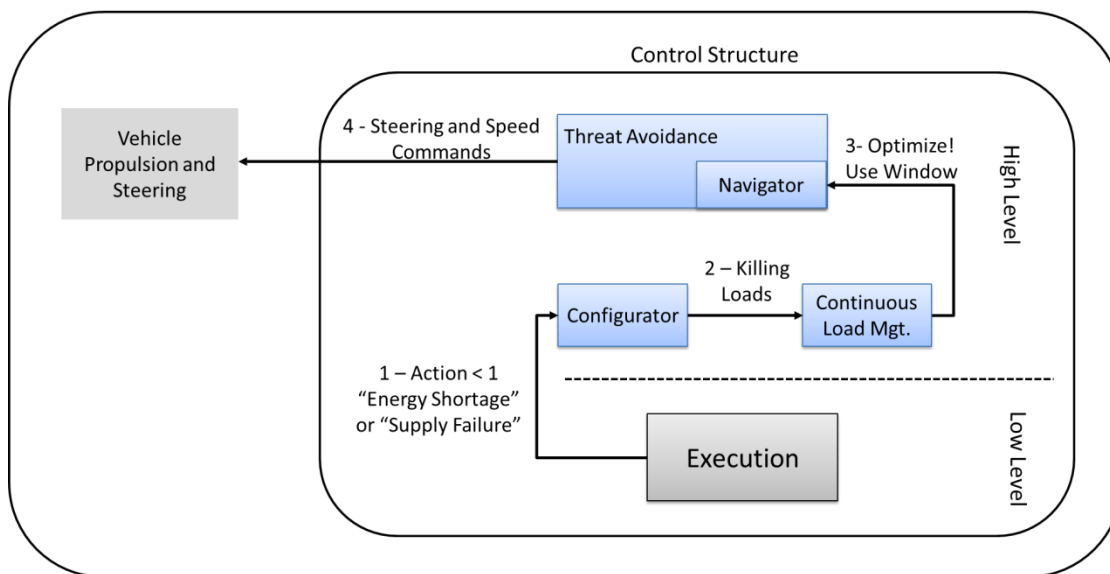
Figure 5-31 Continuous Load Management - Speed Optimization Information Flow

5.4.2.2 Fuel Cell Protection

FCEVs generally have both batteries and fuel cells as power supplies; obviously the main one being the fuel cell chemical reactor. As mentioned in Chapter 2, fuel cells require both fuel and oxygen, obtained from atmospheric air, to generate the electric current used for powering all the on-board systems. For all its benefits, like quick fuel recharge time and low operating temperature, a fuel cell needs to be monitored and protected from excessive power demands which could damage it by causing either an over temperature or oxygen depletion. In the former case the power demand exceeds the capabilities of the cooling system hence raising the operating temperature of the stack which damages it. In the latter case the air supply system cannot cope with the current demand and there is not enough oxygen to react with hydrogen ions causing hydrogen to flow out of the cathode, so instead of having the reaction described by Equation 2-2 the end result is the reaction described by Equation 5-48.
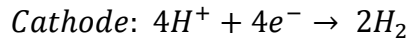
$$Cathode: 4H^+ + 4e^- \rightarrow 2H_2 \qquad\qquad \textbf{5-48}$$

This type of starvation is referred to as "oxidant" starvation and its effects are a drop in fuel cell electrical potential, which can cause irreversible damage to the cell, and a flow of hydrogen gas through the exhaust system into the atmosphere. The electrical compressor is in charge of pumping pressurized air into the cathode manifold for it to then feed through into the flow channels. The amount of air the compressor can supply is dependent on not only its mechanical capabilities, but also the temperature and availability of atmospheric air. When a vehicle travels at high altitudes air density decreases making it harder for the compressor to keep air mass supply and cathode pressure high enough for the stack to maintain a given power output. Also this effect is made worse by the presence of high ambient temperatures (above 25 °C) where not only air density drops even more, but also heat rejection by the cooling system becomes less efficient. In any given system an internal controller would protect the fuel cell on its own by clipping the request to a safe power output level, yet this would create a delta between desired power and actual power. Since the whole control structure is about making sure critical loads are always fed allowing a delta to exist would defeat its purpose, therefore the structure includes its own fuel cell protection algorithm which detects the delta and attempts to redirect it to the battery.

Inside the high level layer there is a calibratable map which stores fuel cell brake power output information as a function of altitude and ambient temperature, both parameters are normally monitored by motor vehicles today. In Figure 5-32 a map for a modelled 3 kW water-etylene-glycol cooled pressurized fuel cell, built using the information from Chapter 2 and 9Appendix B, shows the effect of both air density and ambient temperature on fuel cell output.
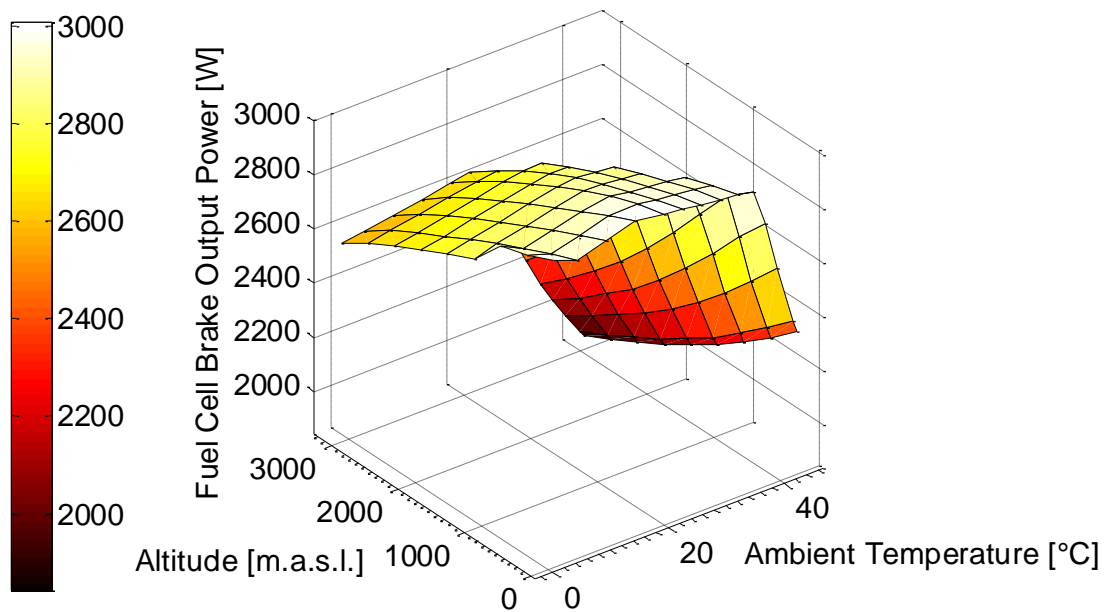
Figure 5-32 Fuel Cell Protection Map

For a constant altitude as ambient temperature increases power has to be limited more aggressively since the cooling system cannot dissipate the same amount of energy, and also it requires more power in itself to work both coolant pump and fan. When considering a constant temperature power peaks at the compressor´s peak efficiency and then drops anywhere else. The mechanism for fuel cell protection is depicted in Figure 5-33. The process works as follows:

1. A powertrain model estimates its energy requirement and sums it with instantaneous measurements from vehicle loads.
2. The fuzzy dynamic modifier chain provides a power split ratio for each available supply.
3. The result of step one is multiplied per Equations 5-49 and 5-50.

$$Fuel\ Cell\ Power = Estimated\ Vehicle\ Power * Fuel\ Cell\ Ratio \qquad \textbf{5-49}$$

$$Battery\ Power = Estimated\ Vehicle\ Power * Battery\ Ratio \qquad \textbf{5-50}$$

4. The output of Equation 5-49 is fed into the power limitation map feature and a delta is calculated. The delta could be zero if the desired power does not reach the map´s limit or a higher map limited value as applicable.

5. A new battery command is computed using the output of the fuzzy dynamic modifier chain, from Figure 5-14, and the power limited delta.

$$Modified\_Battery\ Power\ Cmd = Batt\_Cmd + Fuel\_Cell\_Delta \qquad \textbf{5-51}$$
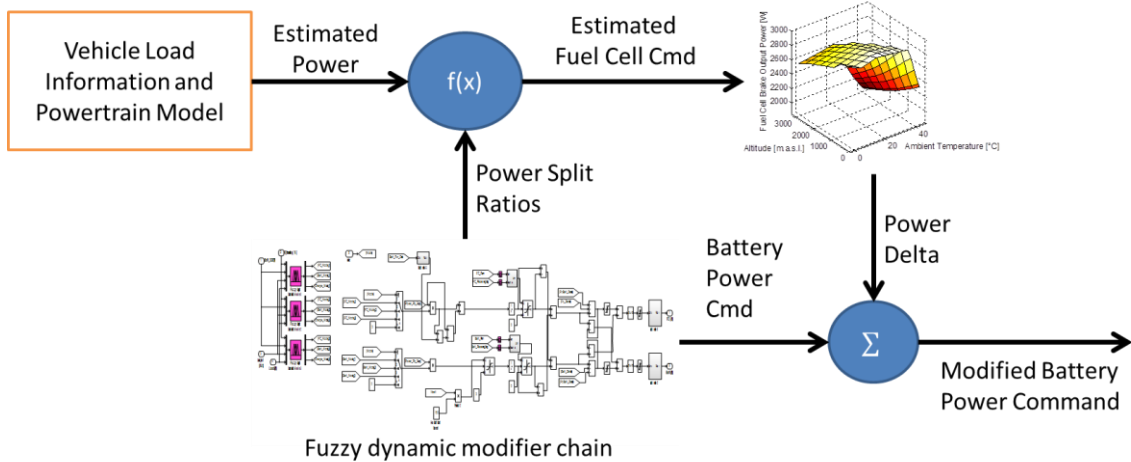
Figure 5-33 Fuel Cell Protection Information Flow

This system is active regardless of operating mode. When in Battery Only mode the delta would always be zero, since the power split ratio for the fuel cell would be zero. In Fuel Cell Only mode the delta would inevitably be absorbed by the powertrain in the form of a slower response as not all the desired energy would be delivered.

5.4.3 Threat Avoidance

The last and one of the most influential blocks of the control structure is Threat Avoidance. In itself has the capability to override the commands of the Configurator Load Killer, work in tandem with the Continuous Load Manager and by doing so indirectly influence the operation of all lower layers

As its name implies this block is in charge of avoiding threats to the vehicle, but since the platform in question would be involved in security related missions the threats are not objects around the vehicle, but other vehicles which could be targeting the platform in some way. In order to avoid these possible threats the block is divided into two major subsystems: Threat detection and tracking and Navigation.

5.4.3.1 General Description of Operation

Since the focus of this research is not object tracking, which can be expanded into a project in its own right, it is assumed the vehicle is equipped with a sensor array capable of detecting and discriminating a given threat inside a three dimensional space. It is at this point where the control structure comes in. It takes a given target position, assigns it a column in a threat matrix and begins maintaining a track of its (x,y,z) coordinates over time. It also estimates the distance to target together with its position in the vehicle´s coordinate frame. This last calculation is made to help determine a plausible escape trajectory. If allowed by the user the system then steers the vehicle away from the threat, but at the same time attempts to keep a trajectory in direction of its intended end destination. The following sections will expand on each of the previous tasks.

5.4.3.2 Threat Identification and Storage

As already described the system is assumed to receive the position of the threat from a detection system. As a first step it is determined whether the Threat-To-Vehicle distance, or TTV, is shorter than a given predefined limit called the Distance Between Objects, or DBO. This distance is computed using Equation 5-53

$$TTV = \sqrt{(x_{veh} - x_{th})^2 + (z_{veh} - z_{th})^2 + (y_{veh} - y_{th})^2} \quad [m] \quad 5\text{-}52 \quad .$$

Figure 5-34 shows the axis convention used by the system.

$$TTV = \sqrt{(x_{veh} - x_{th})^2 + (z_{veh} - z_{th})^2 + (y_{veh} - y_{th})^2} \quad [m] \quad 5\text{-}52$$
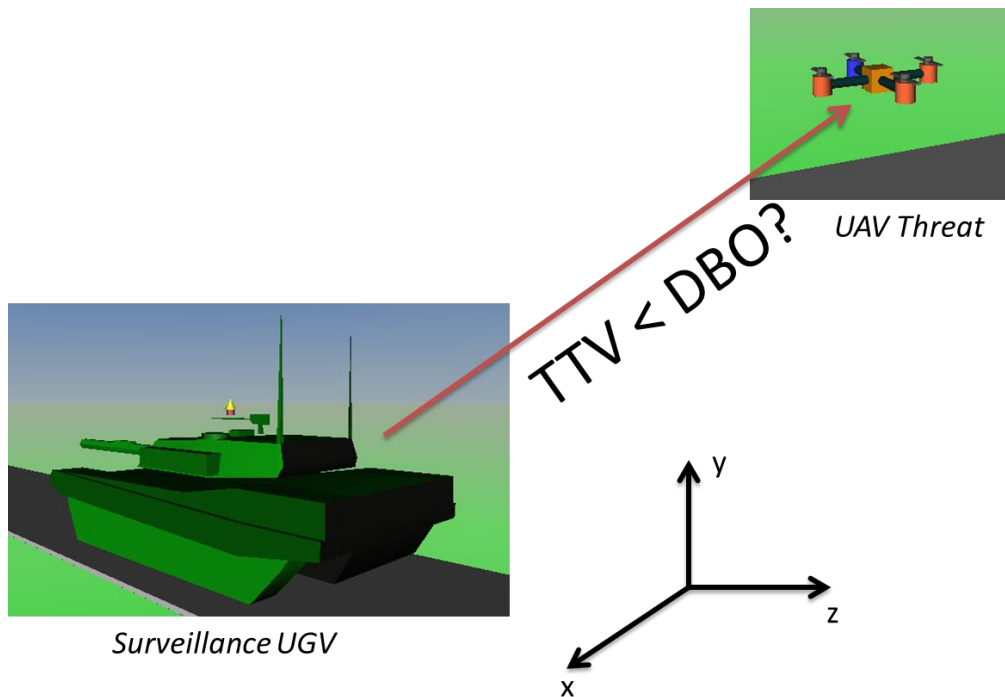
Figure 5-34 Threat Avoidance Axis Convention

The position updates for each detected object are tracked in a tracking Matrix and used to compute its position relative to the vehicle´s own coordinate frame. If *TTV* is smaller than the preset *DBO* an escape trajectory creation algorithm is activated.

5.4.3.3 Escape Trajectory

Once the relative position of the threat has been determined, a simple computation is made to determine an escape trajectory. Because this research is interested in the dynamics between decision making agents (i.e. each structure layer) the escape trajectory is calculated in a geometric way taking into account only instantaneous threat position. The guideline to follow for creating an escape trajectory is to look for the vector which will represent the quickest route to keep the threat out of the *DBO* threshold, as shown in Figure 5-35.
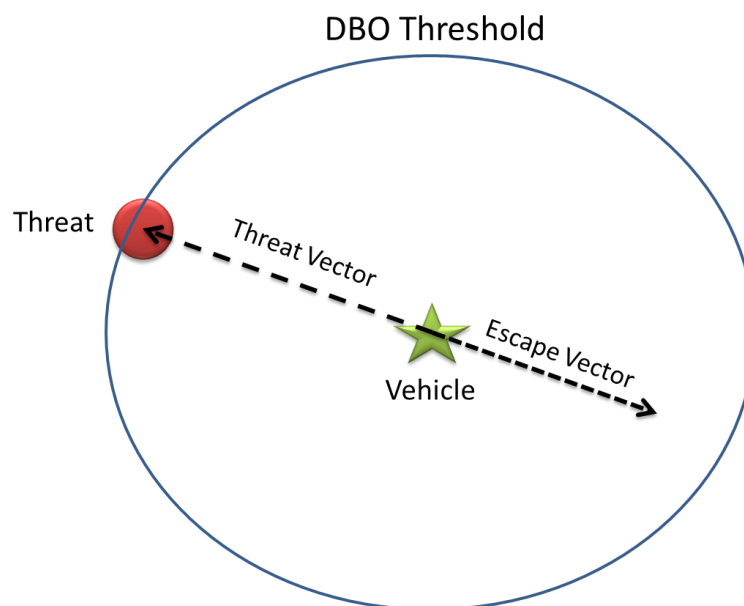
Figure 5-35 Graphical Representation of the Escape Vector Creation Logic

It is this basic escape trajectory which will later be modified to take into consideration the distance to destination. To compute the Threat Vector the following process is used:

1 – Obtain the z-x plane distance:

$$Distance_{zx} = \sqrt{Local_x{}^2 + Local_z{}^2} \qquad \text{[m]} \qquad \textbf{5-53}$$

$Local_x$ and $Local_z$ stand for the distance in the vehicle´s own coordinate frame from the origin (the vehicle) to the threat, which is the same as the TTV.

2 – Compute the angle in the z-x plane:

$$Bearing_{zx} = \sin^{-1}\left({Local_x}\big/{Distance_{zx}}\right) \qquad \text{[rad]} \qquad \textbf{5-54}$$

3 – The same is done for the z-y plane:

$$Distance_{zy} = \sqrt{Local_y{}^2 + Local_z{}^2} \qquad \text{[m]} \qquad \textbf{5-55}$$

$$Bearing_{zy} = \sin^{-1}\left({Local_y}\big/{Distance_{zy}}\right) \qquad \text{[rad]} \qquad \textbf{5-56}$$

To create the escape vector both threat vector angles, or bearings, are inverted by 180° and together with the $Distance_{zy}$ and $Distance_{zx}$ are used to craft the new vector; for instance, if the threat coordinates are (10, 35, -20), the escape vector would be (-10, -35, 20). It would be easy to think that the vector could be inverted by multiplying by minus one, then what is the meaning of all this? The point is that the bearing angles are required for they will become the steering command. In the case of a ground vehicle, the inverted Bearing$_{zx}$ will be used as target heading and as such the vehicle must be steered to meet this objective. If the platform is a UAV or submersible then both $Bearing_{zx}$ and $Bearing_{zy}$ can be used as yaw and pitch angles respectively.

5.4.4 Navigator

Once the Escape Vector is set, all would be fine except for the possibility that such a heading could lead away from the vehicle´s preset destination, meaning that when the threat were to finally be outside the *DBO* threshold the vehicle could be too far from its destination to actually reach it with its allotted energy. To compensate for this a Navigator block is included in the Behavioral system.

The Navigator is in charge of translating the bearing angles into steering angles, to pass on the Continuous Load Manager Budget Enforcement speed command and also to compensate the steering angles to keep the trajectory closer to the preset destination. The latter is achieved by a cost function where the system can be calibrated by weights to either favour the escape vector or the home vector (the vector pointing towards the destination) when setting the final steering angles. The process to determine this angle bias towards the preset destination is called Home Vector Bias, or HVB.

The HVB is a three step process. First, the Home Vector must be crafted together with its bearing angles and that is done in the same manner as for the Escape Vector. Instead of using the *TTV* for the distance parameter in Equation 5-53 the distance to home is used. $Local_y$ and $Local_x$, in Equations 5-54 and 5-56 are the corresponding coordinates of the preset destination in the vehicle´s coordinate frame. Second, the angle between the Escape and Home Vectors is computed using Equation 5-57.

$$InterVector\ Angle = \cos^{-1}\left(\frac{\widehat{EV} \cdot \widehat{HV}}{\|\widehat{EV}\| \cdot \|\widehat{HV}\|}\right) \quad [rad] \qquad \textbf{5-57}$$

In the previous Equation EV stands for Escape Vector and HV stands for Home Vector. Up to this point the computed data would paint a geometric picture as shown in Figure 5-36 where α is the Home Vector angle, β is the Escape Vector angle and θ is the Intervector angle.
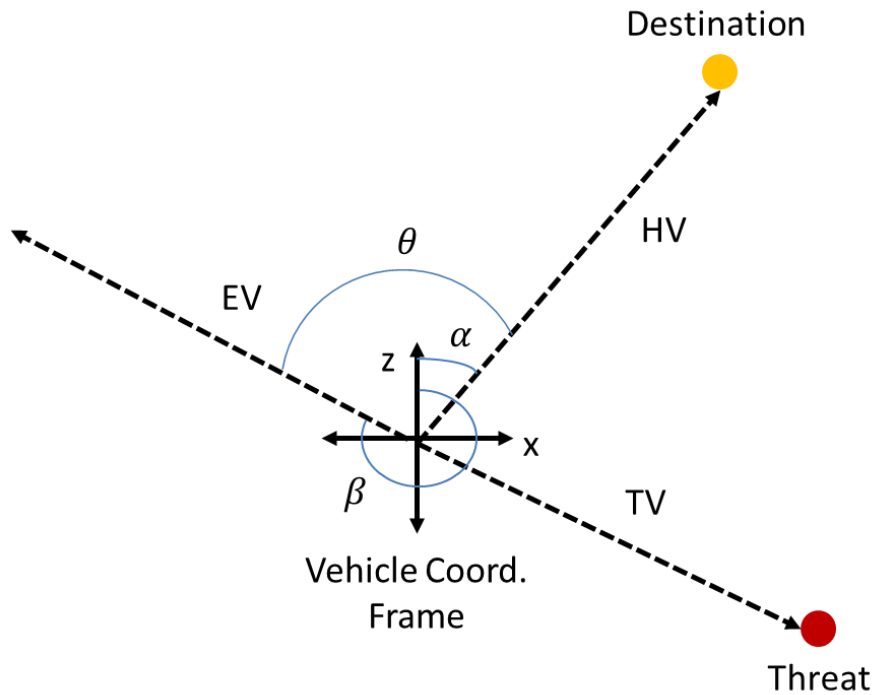
Figure 5-36 Home Vector, Escape Vector and InterVector Angles

The third step is to create the actual bias. There are two options. If $\beta > \alpha$ the bearing angle for the compromise vector will be calculated with Equation 5-58

$$Bearing_{comp} = \alpha + W\theta \qquad \text{[rad]} \qquad \textbf{5-58}$$

If $\alpha > \beta$, then

$$Bearing_{comp} = \alpha - W\theta \qquad \text{[rad]} \qquad \textbf{5-59}$$

W is the calibratable bias weight. Its value ranges from 0 to 1. For larger values of W the compromise vector will approach the Escape Vector until they both have the same bearing. As W approaches zero it will eventually match the bearing of the Escape Vector. The final compromise escape vector would resemble Figure 5-37.
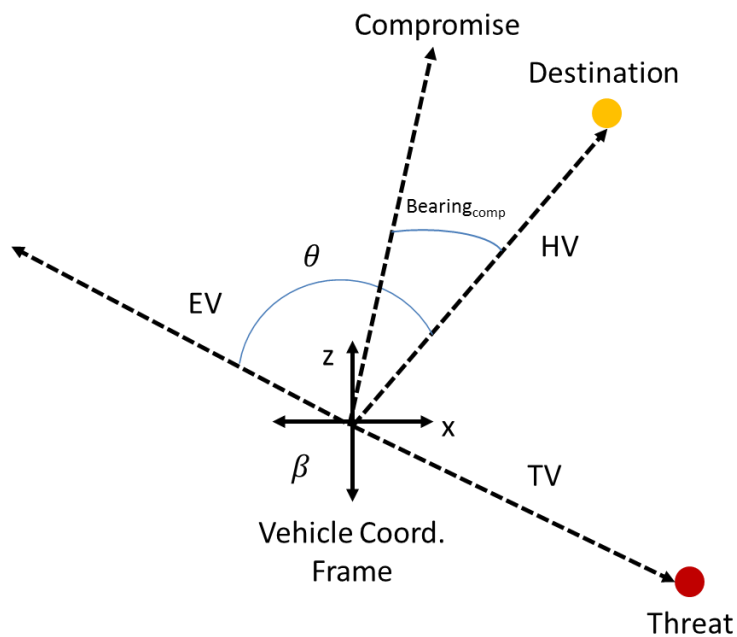
Figure 5-37 Home Vector Bias Result Example

5.5 Intelligent Control Structure Summary

Before moving on to the following chapter, which describes the physical test platform designed to try out the Intelligent Control Structure software on a real life vehicle it is worthwhile making a parenthesis to discuss the general operation of the algorithms presented in this chapter.

Firstly, there was the low level layer where energy levels are monitored, the higher layers are informed of what power generation infrastructure is present and finally the mission progress is tracked. This layer is fairly complex. Three different algorithms work in tandem to manage reserve, supply and energy expenditure information. Without it this data all forecasts coming from the medium level layer would be impossible. It also works as a microcosm of the complete control structure. Each algorithm has a different time horizon. The shortest belongs with the Fuzzy logic dynamic modifier chain engine, which is by the way the only continuous algorithm in the system (meaning its output is smooth and analogue in nature compared to, for example, the state machine which can abruptly go from one integer value to another). The Mission Controller has a time horizon which spans the entirety of the vehicle´s deployment, something only the high level layer can rival.

Secondly, the medium level layer, whilst depending on the low level layer for information, has its own crucial role to play. The forecasts it calculates provide a better understanding of how energy is being spent. This helps fine tune the workings of the low level layer where reserves will ultimately be better designed to meet actual operating conditions. Furthermore, the Manage system plays an important part in managing the configurable and interruptible loads and in keeping their budgets in line with the reserves. Again, the importance of the low level layer echoes higher up. This layer also adds value to the complete system by sharing information with both the other layers, like the subsystem load power ratings used by the Configurator in its dialogue with the system personalities or the updated average energy consumption figures for the Mission Controller.

Thirdly, the High Level Layer gives a final level of intelligence to the control structure and that is its initial awareness of the vehicle´s surroundings, the relation between its current position and the objective destination, obtained when available from the low level layer´s mission data. How its speed can affect the rate at which energy is spent. Also the Configurator dialogue sequence

proves how the control structure is capable of self-management. The Home Vector Bias also shows that energy consumption aware trajectory planning is possible.

Finally, although Figure 4-1 shows a very clean cut software control stack of three layers the reality is somewhat different where boundaries between layers are a little blurry. The top level layer can affect the low level one by means of the Fuel Cell protection scheme and it can also meddle into how the medium level layer controls its loads by using Load Killer commands. On the other hand it can itself be influenced by the low level layer when an Action command triggers the Continuous Load Manager to issue a vehicle speed command.
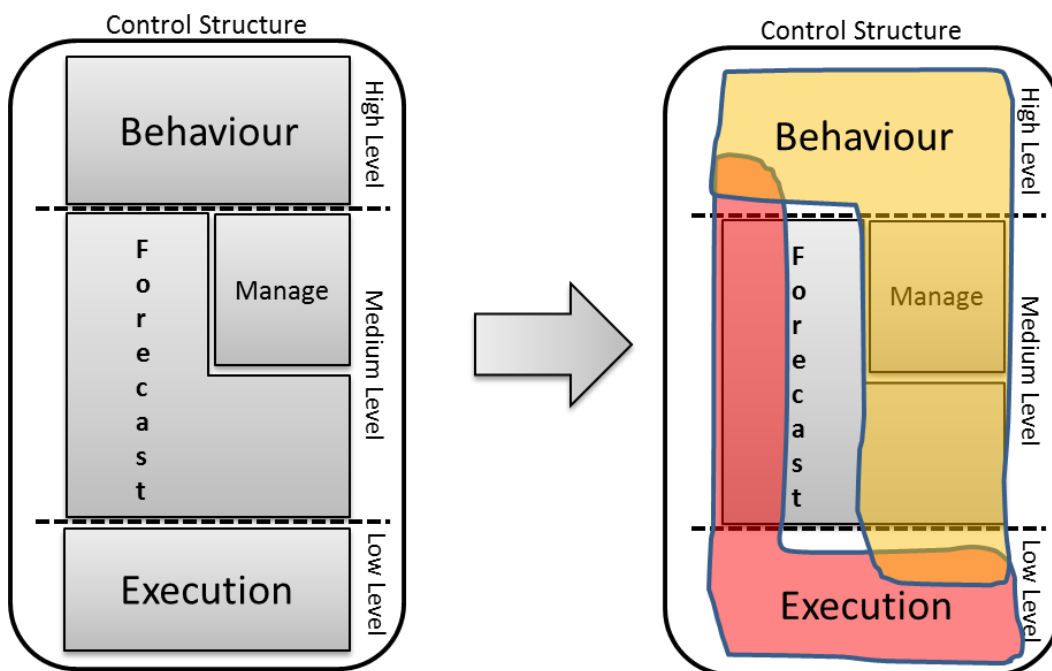
Figure 5-38 Theoretical vs. Actual Layer Influence Areas

In the end, no feature stands alone as they are all interconnected which is one of the organic characteristic traits object of this work.

6 Testing Platform

Chapter Summary:

Numerical simulations have been proven to be useful for predicting the behaviour of a system described by equations. Yet, all models have limitations which are clearly defined in its assumptions. To fully assess the capability of the proposed intelligent concept a physical test system has been devised which will introduce real life noise and variability into the system´s operation. The chapter will elaborate on the virtual reality/hardware platform and its capabilities.

6.1 Introduction

Chapter 5 described in detail the Intelligent Control Structure algorithms used to control an electric vehicle placing in front and foremost energy expenditure efficiency. Yet in the realm of software everything can be fully monitored and controlled given the right resources and testing environment. A software which results of this type of endeavour, even after being thoroughly tested and analysed, might still fail when reality and all its implacable unknowns are added to the mix.

With the intention of proving that the Intelligent Control Structure is robust a prototype vehicle running the algorithms was placed in a bespoke dynamometer test bed. Both components, vehicle and test bed, will prove that what works in a cybernetic realm might need some adjustments or adaptions to do so in real life. Let us then proceed forward and describe the test system concept, how it was translated into a realizable design and lastly how the actual test system operates.

6.2 Test platform concept

To meet its objective of training both the ICS and the unmanned vehicle operator the test platform must meet a list of targets:

1. Must work with a skid steered vehicle. This means that the four vehicle wheels will be controlled in pairs, left and right, with wheels within each pair spinning at the same speed and in the same direction, clockwise or counter clockwise.

2. Must be able to be operated remotely.
3. Must provide real-time data back to the command station.
4. The command station software must be able to operate with or without the dynamometer being active.
5. Two vehicles, of different domains, must run the ICS independently from each other within the test rig. These vehicles can be either real or simulated.
6. The power system of the prototype vehicle must include an ultracapacitor bank and at least one power converter, to implement the ICS software´s commands.

Figure 6-1 shows a high level conceptual diagram of the test bed.
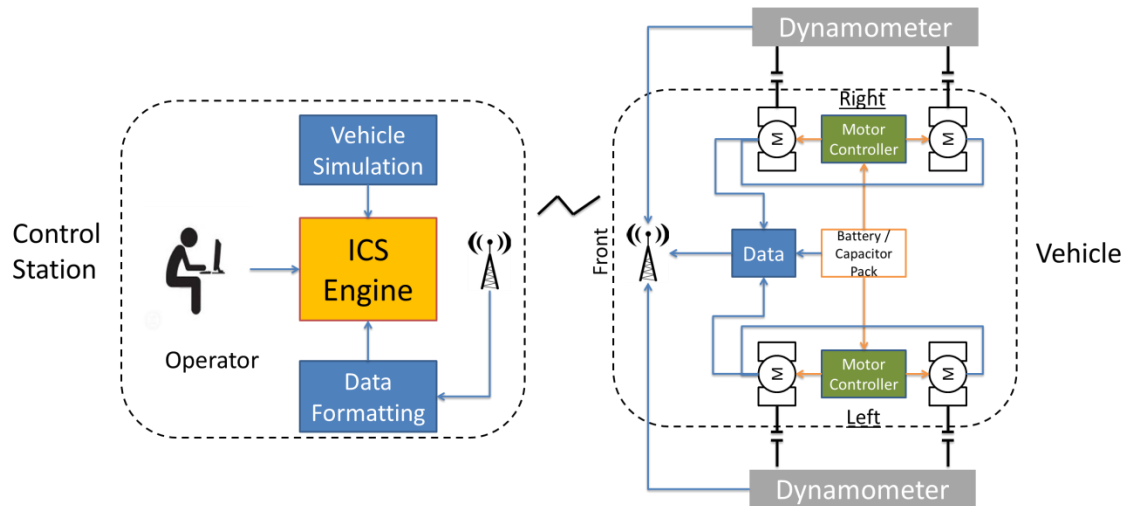
Figure 6-1 Dynamometer Test Bed Conceptual Diagram

6.3 Test platform design

For the test platform design to meet the concept´s objectives it first needed to consider not only the research needs, but also the constraints imposed on it by the physical characteristics of the complex components used. Starting with powertrain and dynamometer motor torque and power, then dynamometer gear ratios and braking mechanisms, after that power converter capabilities, battery capacity ratings, ultracapacitor energy storage, and safety, finally controller communication protocols and interface with Matlab.

Based on the direction set by the concept and the characteristics of the real life components the design was thus divided into three functional blocks, and was done so that tests could be performed and simulations run without all system blocks present if needed.

Block 1:

- Matlab m-script running the Intelligent Control Structure software on two different vehicles; one vehicle is a UGV and the second one a UAV the intention being to prove that the software can operate on any electrically powered platform. The UAV is simulated, but in the case of the UGV it can employ a vehicle model or real-time data coming from the dynamometer.

- Simulink 3D graphical engine which animates and displays on-screen vehicle navigation, mission status and energy consumption information.

- Human-Machine-Interface layer. Since the system must not only be useful for training the ICS, but also would be UGV operators there must be an input method for user commands.

- Matlab to Test Controller Communications layer.

Block 2:

- Software interface layer between test rig and Block 1. Proving yet another tenet of the research philosophy that of the software being able to run on any electrically powered vehicle. The only requirement is a need for a software interface layer which translates the software´s commands into signals that can be used to drive the rig´s hardware. This block is divided into three execution streams, programmed in National Instruments LabView, where the first is used to drive continuous loads and the dynamometer. The second is responsible for the interruptible and configurable loads and the third is in charge of "clean up" after a test run. This "clean up" routine basically resets the system and takes it back into a safe state from where tests can be run.

- Block 2 code is run in an embedded controller. In this case a Compact Field Point 2020 array.

Block 3:

- It is divided into two parallel systems, vehicle and dynamometer, which run on the same controller.

- The vehicle is a skid steered UGV. It has four permanent magnet DC motors, driving one wheel each, for a total of 3kW of propulsion power at twenty four volts. It has all the necessary hardware to regulate the speed of the motors per pair. Although it has the hardware to broadcast a video signal back to an operator, its interruptible and configurable loads are represented by four LED set, two per load type, for the sake of simplicity.

- The dynamometer is a 1.5kW system with four friction band brakes. It has two permanent magnet DC motors, one per side, which are connected to the vehicle wheels via a gearing system. These motors can be used to brake or push the vehicle in a dynamic fashion following commands from Block 1. The friction brakes can be manually set create a constant road resistance for the case when no dynamic braking is wanted, or if the test requires it.

Figure 6-2 shows the detailed diagram of the test bed hardware design, whilst Figure 6-3 through Figure 6-8 show pictures of the actual test rig.
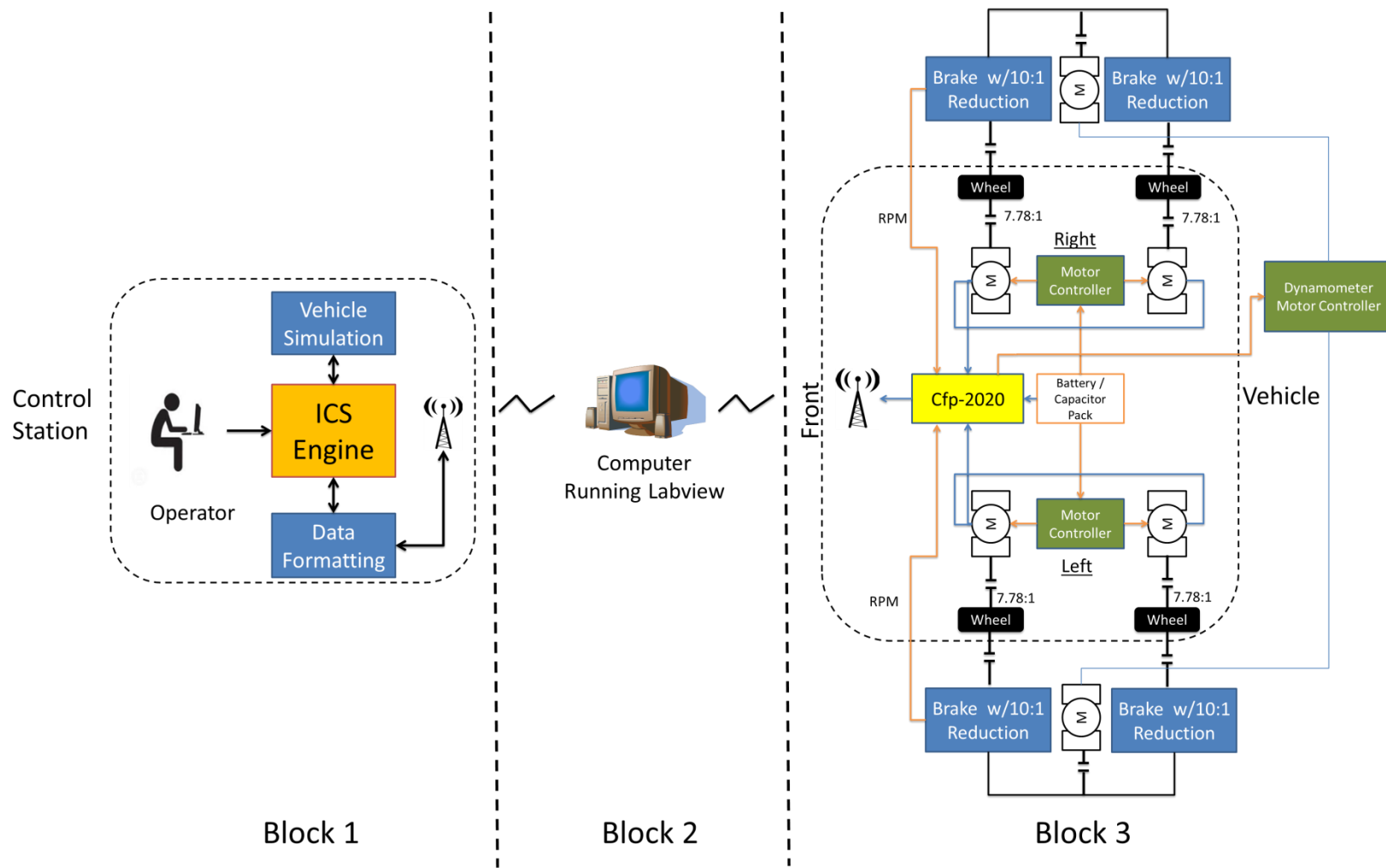
Figure 6-2 Dynamometer Test Bed Design Diagram

168
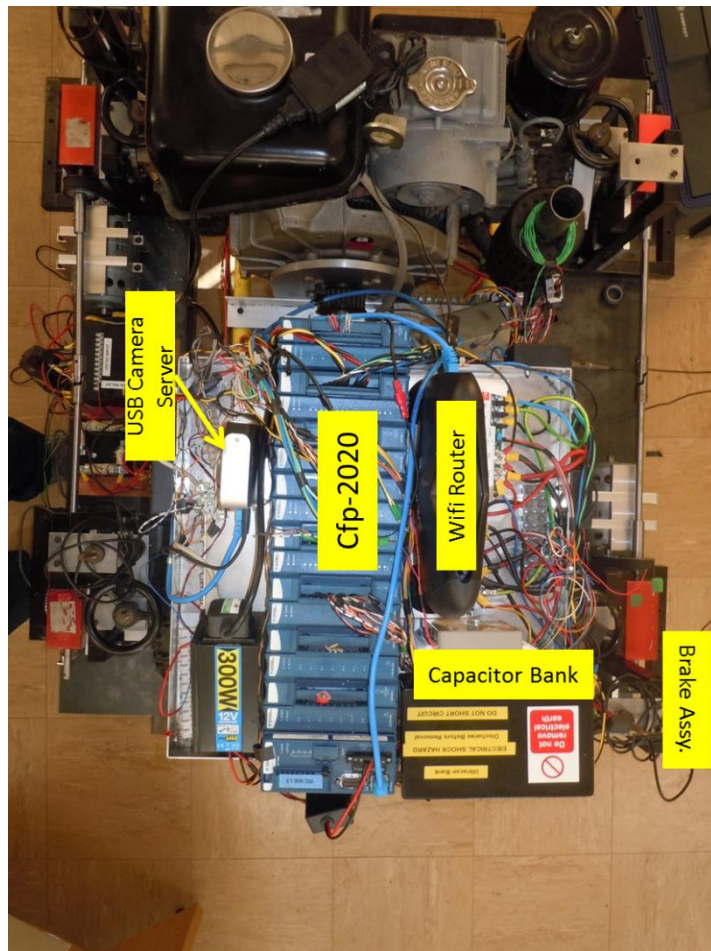
Figure 6-3 Top Level View of Test Platform
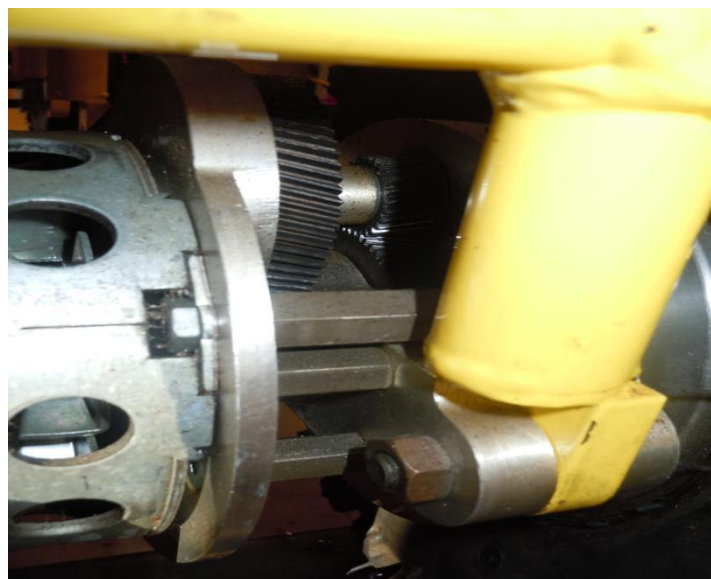
Figure 6-4 Traction Motor 7.78:1 Gear Reduction

169
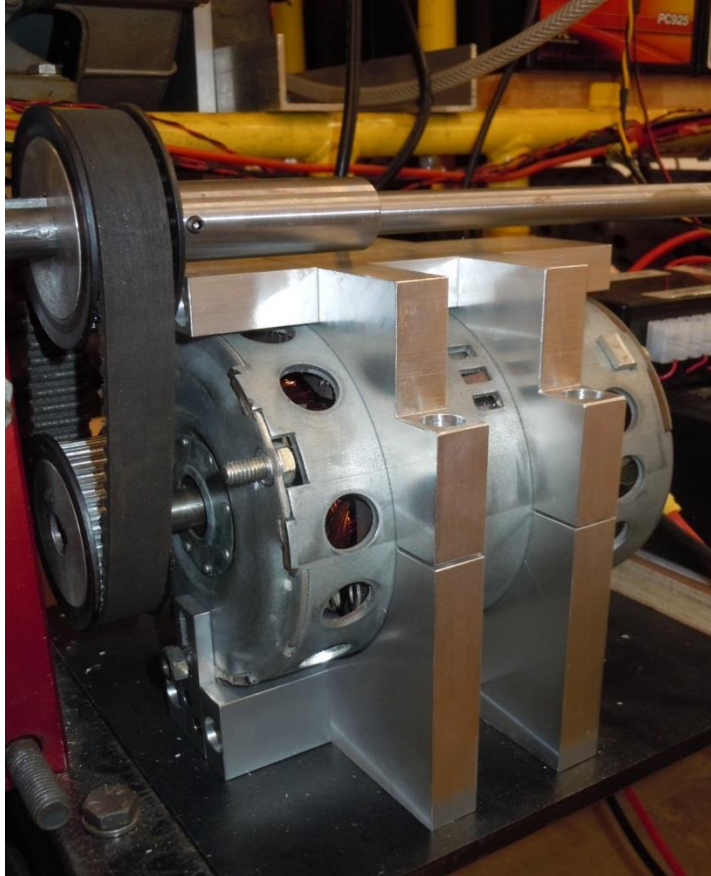
Figure 6-5 Dynamometer Brake Motor

Traction Motor

Friction Brake

10:1 Reduction
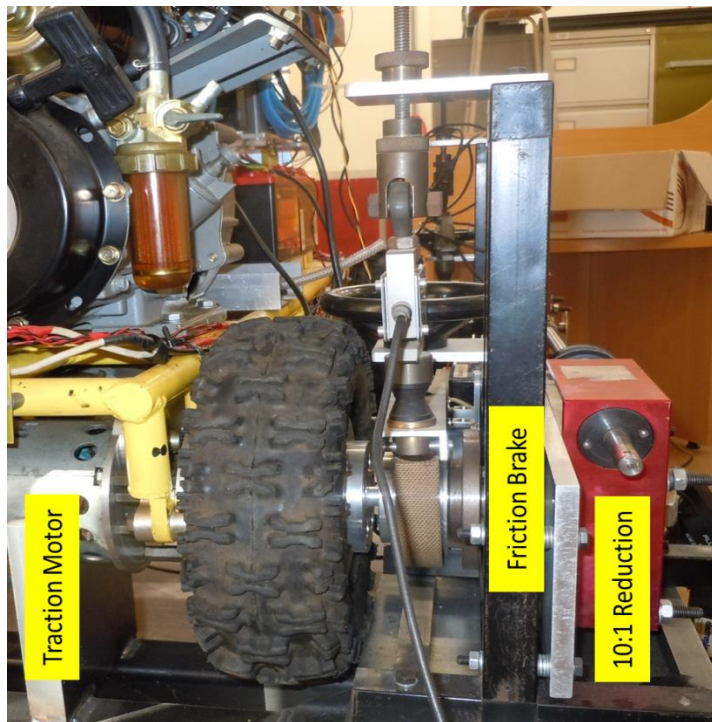
Figure 6-6 Traction Motor - Dynamometer Coupling
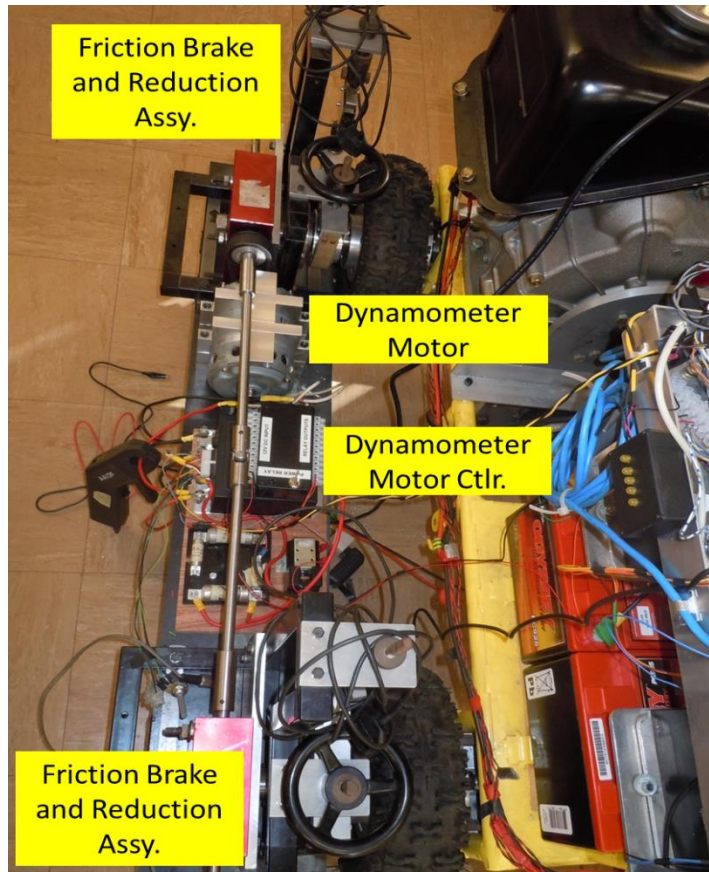
Figure 6-7 Left Dynamometer Top View
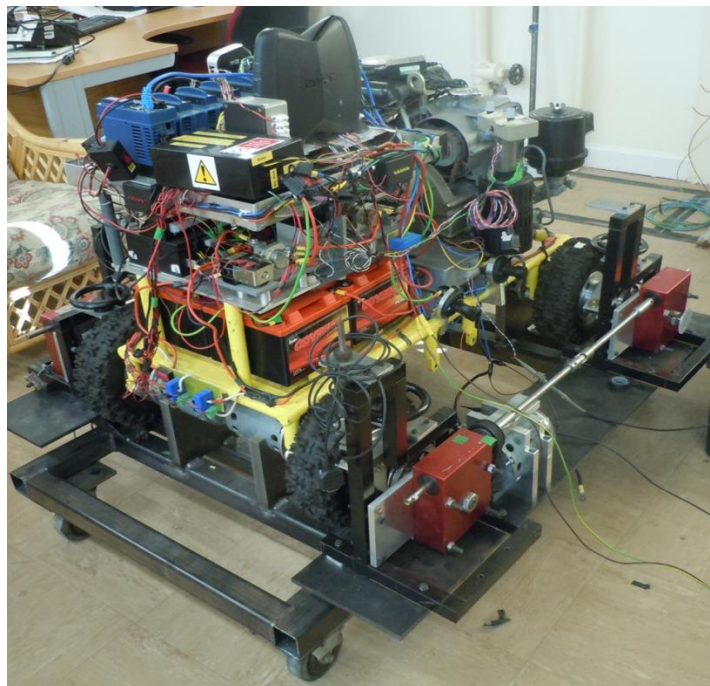
Figure 6-8 Isometric View of a UGV in the Chassis Dynamometer

The LabView software used in the system can be consulted in the attached media disc.

6.3.1 Virtual Reality Simulation Design

In order to demonstrate that the ICS software can operate in any type of electrically powered platform the simulation includes two different vehicles. First an UGV and second an UAV.

6.3.1.1 UGV Simulation

The simulated UGV is a 4x4 skid steered vehicle which included in its model the characteristics of the real UGV mounted in the dynamometer, listed as Vehicle 3: UGV in the List of Symbols.
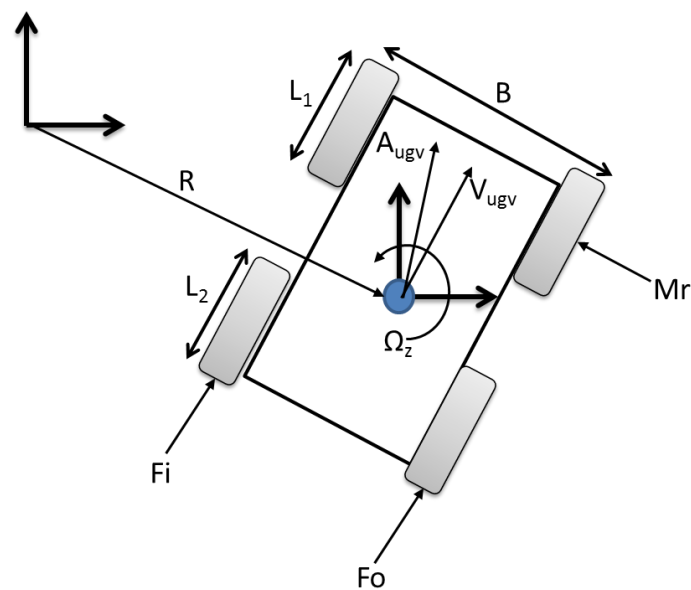
Figure 6-9 Skid Steer Model Diagram

The vehicle model described in Section 3.4.5 is augmented to account for the skid steering dynamics. Based on the forces, moments and angles described by Figure 6-9 the new components of the ground vehicle model are enunciated by the following set of equations, from (Wong 2001).

$$M_r = \frac{\mu_t W L_{Tot}}{4} \qquad \text{[Nm]} \qquad \textbf{6-1}$$

Where,

M_r is the moment of lateral resistance, in [Nm],

μ_t is the coefficient of adhesion of rubber on asphalt,

W is the UGV weight, and

L_{Tot} is the contact length for each side of the vehicle, in [m].

$$\gamma_m = 1.04 + 0.0025 \, i_{Tot}^2 \qquad \textbf{6-2}$$

Where,

γ_m is the inertia mass factor, and

i_{Tot} is the traction motor gear ratio.

Next are the equations which describe the forces generated by the propulsion system on each side of the vehicle during turn to the left (Wong 2001).

$$F_o = F_r + \frac{M_r}{B} \qquad\qquad [\text{N}] \qquad\qquad \textbf{6-3}$$

$$F_i = F_l - \frac{M_r}{B} \qquad\qquad [\text{N}] \qquad\qquad \textbf{6-4}$$

Where,

F_o is the force on the "outer" side of the vehicle during the manoeuvre, in [N],

F_i is the force on the "inner" side of the vehicle during the manoeuvre, in [N],

F_r is the force generated by the right hand side propulsion system, in [N],

F_l is the force generated by the left hand side propulsion system, in [N], and

B is the vehicle tread, or distance between wheel centres, in [m].

When the turn is to the right, the F_r and F_l values are interchanged in Equations 6-3 and 6-4. Next the turn radius R can be computed (Wong 2001).

$$R = \frac{B}{2} \left(\frac{r_d \omega_o + r_d \omega_i}{r_d \omega_o - r_d w_i} \right) \qquad\qquad [\text{m}] \qquad\qquad \textbf{6-5}$$

Where,

R is the turn radius, in [m],

r_d is the wheel radius, in [m],

ω_o is the rotational speed of the outer side wheels, in [rad/s], and

ω_i is the rotational speed of the inner side wheels, in [rad/s].

With the turn radius the yaw velocity can be obtained (Wong 2001).

$$\Omega_z = \frac{r_d \omega_o + r_d \omega_i}{2R} \qquad \text{[rad/s]} \qquad \textbf{6-6}$$

Again, taking as an example the case for a left turn the actual vehicle rotation in degrees is obtained from the following equation (Wong 2001).

$$Veh_{Rot} = \frac{180 \Omega_z \Delta_t}{\pi} \qquad \text{[degrees]} \qquad \textbf{6-7}$$

Where,

Veh_{Rot} is the vehicle rotation since the last time step, in [degrees], and

Δ_t in the simulation time step, in [s].

For the opposite case, of a right turn, Veh_{Rot} is obtained from Equation 6-8

$$Veh_{Rot} = -\frac{180 \Omega_z \Delta_t}{\pi} \qquad \text{[degrees]} \qquad \textbf{6-8}$$

The direction of the velocity vector is then computed using Veh_{Rot} in converted into radians/s and put through a rotation matrix.

$$\hat{V}_{UGV} = \begin{bmatrix} \cos \beta & 0 & \sin \beta \\ 0 & 1 & 0 \\ -\sin \beta & 0 & \cos \beta \end{bmatrix} \begin{bmatrix} 0 \\ 0 \\ V_{spd} \end{bmatrix} \qquad \text{[m/s]} \qquad \textbf{6-9}$$

Where

β is the accumulated rotation angle since the start of the test, in [rad/s], and

V_{spd} is the total vehicle speed, in [m/s].

6.3.1.2 UAV Simulation

For the second vehicle case, that of the UAV, the vehicle is defined based on the works of Harandi, *et al.* (Farshid Jafari Harandi 2010). The model is of a 6 degrees of freedom quadrotor aerial vehicle. This is due to the recent popularity of this type of platform, and because it can hover in place which gives it additional flexibility when defining surveillance mission profiles.

First the vertical lift force and torques generated by the four motors need to be computed, following the reference frame from (Farshid Jafari Harandi 2010) in Figure 6-10.
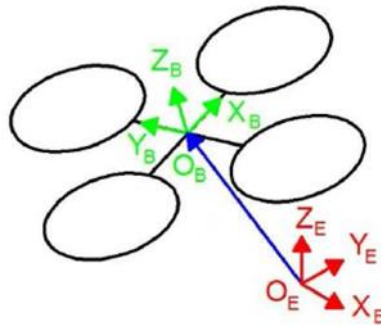
Figure 6-10 Quadrotor Model Reference Frame (Farshid Jafari Harandi 2010)

$$U_1 = b \left(\Omega_1{}^2 + \Omega_2{}^2 + \Omega_3{}^2 + \Omega_4{}^2 \right) \qquad \text{[N]} \qquad \textbf{6-10}$$

Where (Farshid Jafari Harandi 2010)

U_1 is the vertical force, in [N],

b is the thrust factor, in [Ns^2], and

Ω_n is the speed of the n-th motor where n = [1,2,3,4], in [rad/s].

$$U_2 = bl \left(-\Omega_2{}^2 + \Omega_4{}^2 \right) \qquad \text{[Nm]} \qquad \textbf{6-11}$$

Where (Farshid Jafari Harandi 2010)

U_2 is the body roll torque, in [Nm], and

l is the distance between the body and propeller centres, in [m].

$$U_3 = bl \left(\Omega_1{}^2 - \Omega_3{}^2 \right) \qquad \text{[Nm]} \qquad \textbf{6-12}$$

Where (Farshid Jafari Harandi 2010)

U_3 is the pitch torque, in [Nm].

$$U_4 = d \left(-\Omega_1{}^2 + \Omega_2{}^2 - \Omega_3{}^2 + \Omega_4{}^2 \right) \qquad \text{[Nm]} \qquad \textbf{6-13}$$

Where (Farshid Jafari Harandi 2010)

U_4 is the yaw torque, in [Nm], and

d is the drag factor, in [Nms^2].

At this point the indicated lift force and torques have been calculated, but to determine the brake forces which act on the vehicle the aerodynamic losses need to be subtracted. These are obtained from the following equation chain. The first quantity to be found is the propeller angle of attack (Martínez Martínez 2007).

$$\alpha = \tan^{-1}\left(\frac{V_z}{V_x}\right) \qquad \text{[rad]} \qquad \textbf{6-14}$$

Where

α is the propeller angle of attack, in [rad],

V_z is the UAV speed on the Z-axis, in [m/s], and

V_x is the UAV speed on the X-axis, in [m/s].

Now the aerodynamic drag of is worked out (Martínez Martínez 2007)

$$Cd_{uav} = 0.05 + 0.7\alpha \qquad \qquad \textbf{6-15}$$

Before finding the actual drags in all three axes, the equivalent propeller area in each one is obtained (Martínez Martínez 2007).

$$A_x = (L_b \sin\theta)L_b \qquad \qquad \text{[m}^2\text{]} \quad \textbf{6-16}$$

$$A_y = (L_b \sin\phi)L_b \qquad \qquad \text{[m}^2\text{]} \quad \textbf{6-17}$$

$$A_{yaw} = \begin{bmatrix} \cos\theta & -\sin\theta & 0 \\ \sin\theta & \cos\theta & 0 \\ 0 & 0 & 1 \end{bmatrix}\begin{bmatrix} 1 & 0 & 0 \\ 0 & \cos(-\phi) & -\sin(-\phi) \\ 0 & \sin(-\phi) & \cos(-\phi) \end{bmatrix} \quad \text{[rad]} \quad \textbf{6-18}$$

$$\hat{A}_{yaw} = A_{yaw} \begin{bmatrix} L_b \\ L_b \\ 0 \end{bmatrix} \qquad\qquad \text{[m]} \qquad \textbf{6-19}$$

$$A_z = \hat{A}_{yaw}(1)\hat{A}_{yaw}(2) \qquad\qquad \text{[m}^2\text{]} \qquad \textbf{6-20}$$

Where

A_x is the propeller area in the X axis direction, in [m^2],

A_y is the propeller area in the Y axis direction, in [m^2],

A_{yaw} is the matrix used to calculated propeller shadow projection on the yaw plane,

$\hat{A}_{yaw}$ is the vector which describes the propeller´s shadow projection on the yaw plane,

A_z is the propeller area on the Z axis direction, in [m^2], and

ϕ, θ and ψ are the roll, pitch and yaw angles respectively.

With the previous data the propeller drag forces along each axis is calculated (Martínez Martínez 2007).

$$X_{drag} = 0.5Cd_{uav}A_x\rho_{air}X_{spd}{}^2 \qquad \text{[N]} \qquad \textbf{6-21}$$

$$Y_{drag} = 0.5Cd_{uav}A_y\rho_{air}Y_{spd}{}^2 \qquad \text{[N]} \qquad \textbf{6-22}$$

$$Z_{drag} = 0.5Cd_{uav}A_z\rho_{air}Z_{spd}{}^2 \qquad \text{[N]} \qquad \textbf{6-23}$$

Where

X_{drag} is the propeller drag force in the x axis direction, in [N],

Y_{drag} is the propeller drag force in the y axis direction, in [N],

Z_{drag} is the propeller drag forc in the z axis direction, in [N], and

ρ_{air} is the air density around the vehicle, in [kg/m³].

With the indicated force and torques together with drag forces the quadcopter´s inertial accelerations of can be worked out (Martínez Martínez 2007).

$$\ddot{X}_{uav} = \frac{(\sin\phi \sin\psi + \cos\phi \sin\theta \cos\psi)U_1 - X_{drag}}{m} \quad [\text{m/s}^2] \quad \textbf{6-24}$$

$$\ddot{Y}_{uav} = \frac{(-\sin\phi \cos\psi + \cos\phi \sin\theta \sin\psi)U_1 - Y_{drag}}{m} \quad [\text{m/s}^2] \quad \textbf{6-25}$$

$$\ddot{Z}_{uav} = \frac{-g + \left((\cos\phi \cos\theta)U_1 - Z_{drag}\right)}{m} \quad [\text{m/s}^2] \quad \textbf{6-26}$$

Where

m is the quadrotor´s mass, in [kg], and

$\ddot{X}_{uav}, \ddot{Y}_{uav}$ and $\ddot{Z}_{uav}$ are the inertial acceleration along each axis, in [m/s²].

To fully understand the quadcopter´s pose in 3D space not only do we need the force and acceleration vectors, but also the vehicle´s orientation. Therefore roll, pitch and yaw accelerations originating from forces must be calculated (Martínez Martínez 2007).

$$\ddot{\phi} = \dot{\theta}\dot{\psi}\left(\frac{I_{yy} - I_{zz}}{I_{xx}}\right) + \frac{U_2}{I_{xx}} \qquad \text{[rad/s}^2\text{]} \quad \textbf{6-27}$$

$$\ddot{\theta} = \dot{\phi}\dot{\psi}\left(\frac{I_{zz} - I_{xx}}{I_{yy}}\right) + \frac{U_3}{I_{yy}} \qquad \text{[rad/s}^2\text{]} \quad \textbf{6-28}$$

$$\ddot{\psi} = \dot{\phi}\dot{\theta}\left(\frac{I_{xx} - I_{yy}}{I_{zz}}\right) + \frac{U_4}{I_{zz}} \qquad \text{[rad/s}^2\text{]} \quad \textbf{6-29}$$

Where

I_{zz}, I_{xx} and I_{yy} are the body moments of inertial around each axis respectively, in [Nms^2], and

$\ddot{\phi}, \ddot{\theta},$ and $\ddot{\psi}$ are the roll, pitch and yaw angles accelerations, in [rad/s^2]

Finally, the last parameter needed to simulate the quadcopter is its speed vector. This is obtained from the inertial accelerations computed before, and is given by the following equation.

$$V_{uav} = \begin{bmatrix} \dot{X}_{uav} \\ \dot{Y}_{uav} \\ \dot{Z}_{uav} \end{bmatrix} \qquad \text{[m/s]} \quad \textbf{6-30}$$

With Equation 6-30 both models are now complete and ready for insertion within the 3D virtual realm where they will act according to their own instance of the ICS and/or user commands.

6.3.1.3 Virtual Reality Environment

Using Matlab´s Simulink 3D toolbox a virtual world, or realm, was created where the two vehicles can operate and if needed interact with each other.
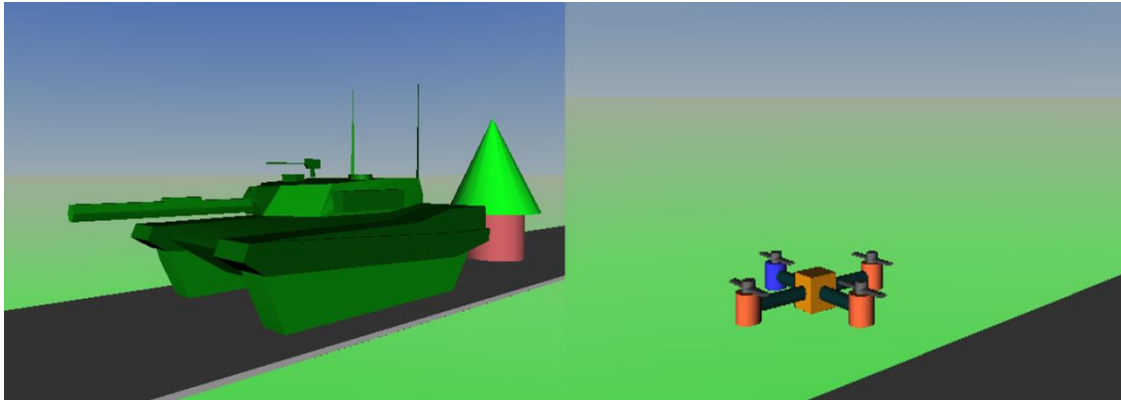
Figure 6-11 UGV and UAV inside Virtual Realm

Inside this virtual realm each vehicle will operate per the predefined mission profile, ICS outputs and if applicable per its user´s commands. Also, somewhere inside the realm there is a beacon, similar to the one shown behind the UGV in Figure 6-11 which is its home destination for use with the ICS behaviour layer.

While the test or simulation is running Matlab shows a set of screens where mission and vehicle data is provided for mission progress monitoring and for UGV operator navigation.

The main screen, shown in Figure 6-12, is divided into two sections. On the left are the UGV scopes and navigation window and on the right the ones corresponding to the UAV.
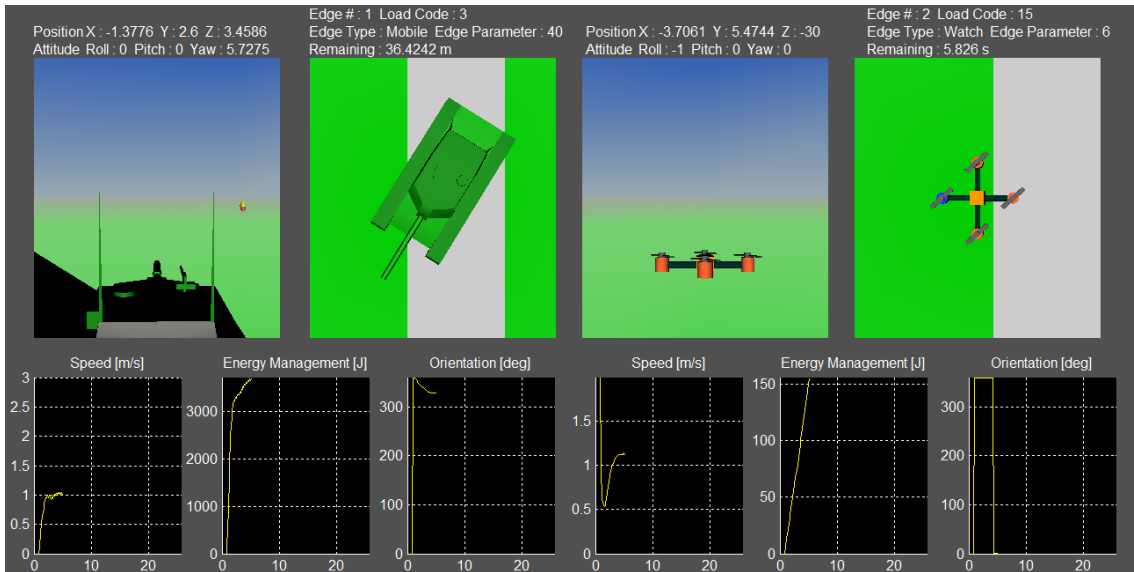
Figure 6-12 Main Operator Window

At the top of each section the user can see the vehicle´s coordinates, pose, and detailed mission data such as actual edge number and interruptible load activation code. On the lower part of the window are three scopes for each vehicle. These show vehicle speed, accumulated energy expenditure and vehicle orientation reference against the scene´s true north. In the middle section are the navigation windows with two views per vehicle, top and view from behind.

Although initially the intention was for only the UGV to be capable of being operated by a human user, in the end both platforms can be controlled via a joystick. This allows for both instances of the ICS to learn from either automated or real command inputs. The joystick controls are shown in Figure 6-13 , and the function of each button is described in Table 6-1.

183

Figure 6-13 VR realm user control pad

Table 6-1 VR realm user control pad button functions

Button	Function
Button 1	UGV Forward
Button 2	No Use
Button 3	UGV Backward
Button 4	UGV Stop
Button 5	UGV Left side low speed
Button 6	UGV Right side low speed
Button 7	UGV Left side high speed
Button 8	UGV Right side high speed
Cross pad (Up/Down)	UAV Pitch (forward/backward)
Cross pad (Left/Right)	UAV Roll (left/right)
Left joystick	No use
Right joystick (front/back)	UAV Altitude (up/down)
Right joystick (left/right)	UAV Yaw (left/right)

As the vehicles move inside the VR realm their propulsion system and load simulations create power demands for the ICS. For the specific case of the UGV, when the dynamometer is active the VR sends speed and load activation commands to the test rig and instead of using simulated power consumption data it uses the real world data which it receives from the rig.

Also, both vehicles have a threat monitoring system, shown in Figure 6-14, used in conjunction with the ICS behaviour layer.
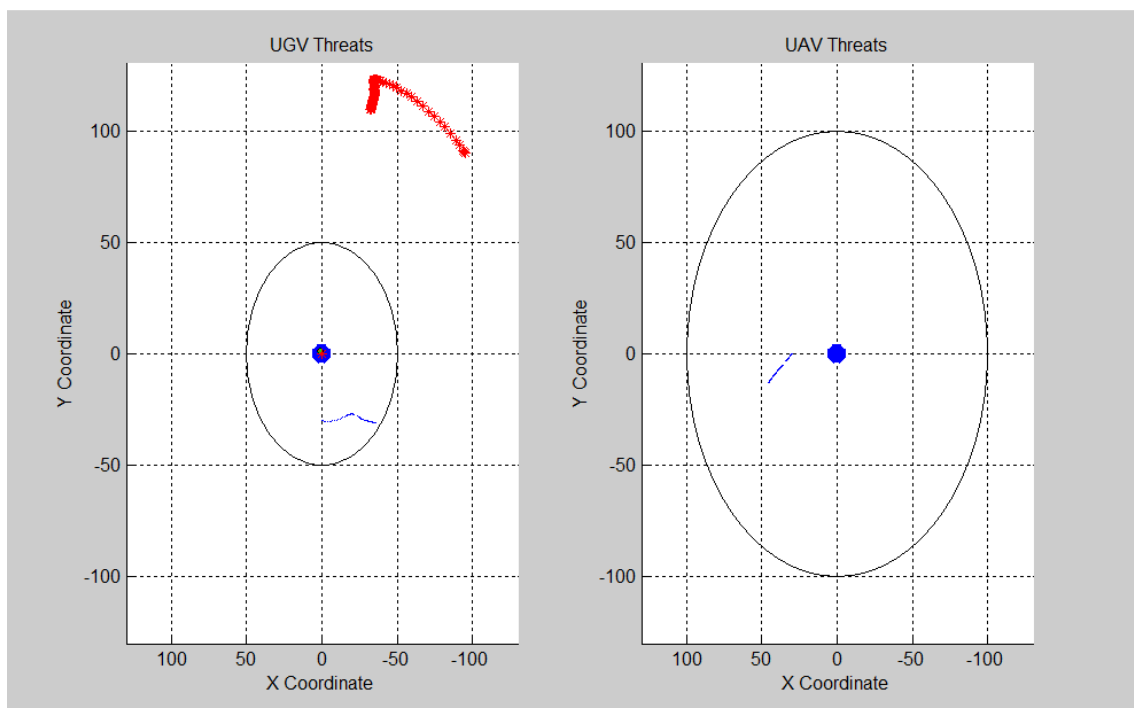
Figure 6-14 VR Realm Threat Monitoring System

On the left hand side the UGV scope tracks the position of both the home beacon and UAV relative to the UGV. The thick spiky track belongs to the home beacon whilst the thin one is for the UAV. On the right hand side the UAV scope tracks only the UGV shown in the thin track. The appearance of an oval in any scope indicates there is a threat near the vehicle. When the threat is far away the oval disappears. This oval is the graphical representation of the *DBO* threshold.

6.3.1.4 UGV vs. UAV implementation of the ICS

As already illustrated by Figure 4-3, the ICS operates on top of the physical powertrain layer. This gives it the flexibility of being able to be used on any type of electrically powered vehicle. By simulating both the UAV and UGV together running the ICS this concept has been proven to be true. The flexible implementation capability came about from the usually ignored fact that all motor vehicles on every domain (marine, ground and aerial) move about in three dimensional space. The difference lies on how each one interacts with the medium and how it can control all six degrees of freedom which describe a vehicles movement. Aerial vehicles have control over all six degrees, where surface marine and ground vehicles can only control yaw directly and roll or pitch through interacting with their environment. A submarine would also be able to control most of the degrees of freedom, albeit in a more restrained manner than an airplane. Thanks to this fact the High level layer can work on all vehicles if given the right navigational contraints.

6.4 Dynamometer Mapping

As mentioned in previous sections the dynamometer test bed has two types of road loads. The first is the fixed load provided by a friction band brake whilst the second is the dynamic load which comes from a set of DC motors. The former kind of load can be used to simulate a given rolling resistance and can be set individually for each wheel. The latter kind of load is useful to simulate slopes in the terrain. Because it is controlled electronically the dynamometer can provide variable and dynamic changes in terrain gradient. It does so by creating either a drag, in the case of positive slopes, or boosting the vehicle´s propulsion system, in the case of negative slopes. To fully exploit the potential of the dynamic loading system a dynamometer map must be created to find out what its capabilities are.
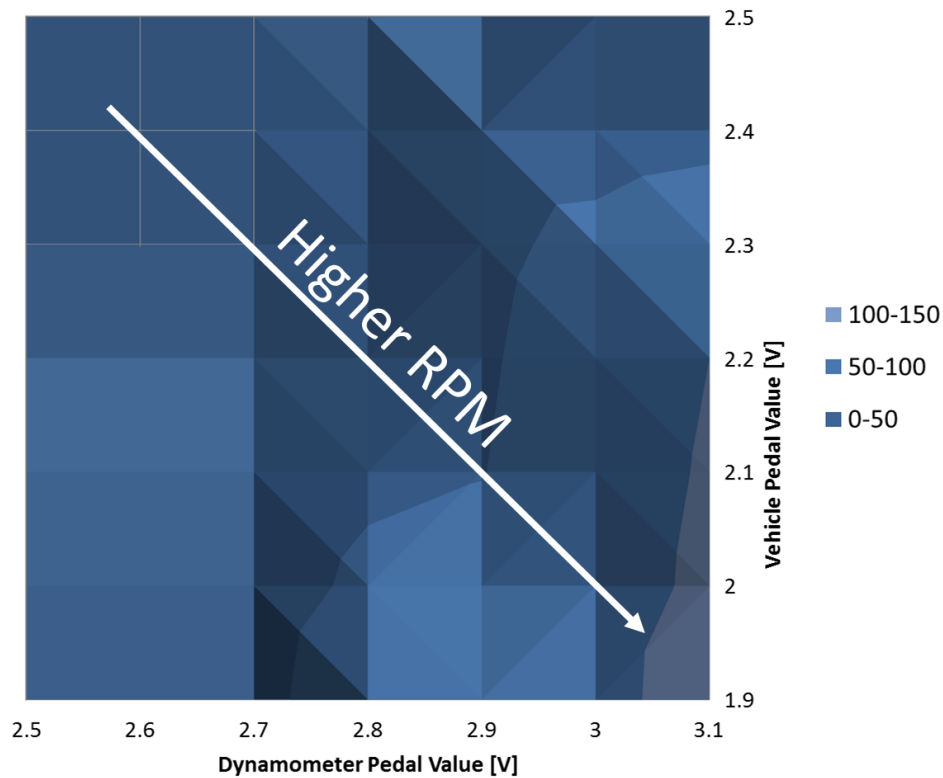
Figure 6-15 Vehicle Wheel RPM for different dynamometer and vehicle pedal combinations

Figure 6-15 shows the effect of dynamometer loading on vehicle wheel speed. As the UGV pedal input is higher, signified by a lower pedal voltage, the torque output of the powertrain is higher therefore the wheel speed rises. Yet, if the dynamometer is at idle (i.e. dynamometer pedal voltage of 2.5 volts) the final speed is between 0 and 50 RPM because the drivetrain is being loaded on by the dynamometer mechanics. If the dynamometer starts to provide its own power the final (i.e. the dynamometer pedal voltage increases) the resulting wheel speed for the same vehicle pedal value is higher as the drag from the dynamometer mechanical components is less, and less until the dynamometer is actually pushing the vehicle forward. This last effect is what creates the gravity assistance effect experienced whilst driving downhill. To illustrate how this dynamic loading affects the outcome of a given drive cycle please consider

the following plots obtained from running the first eighty seconds of the FTP-75 cycle under different dynamometer loads.
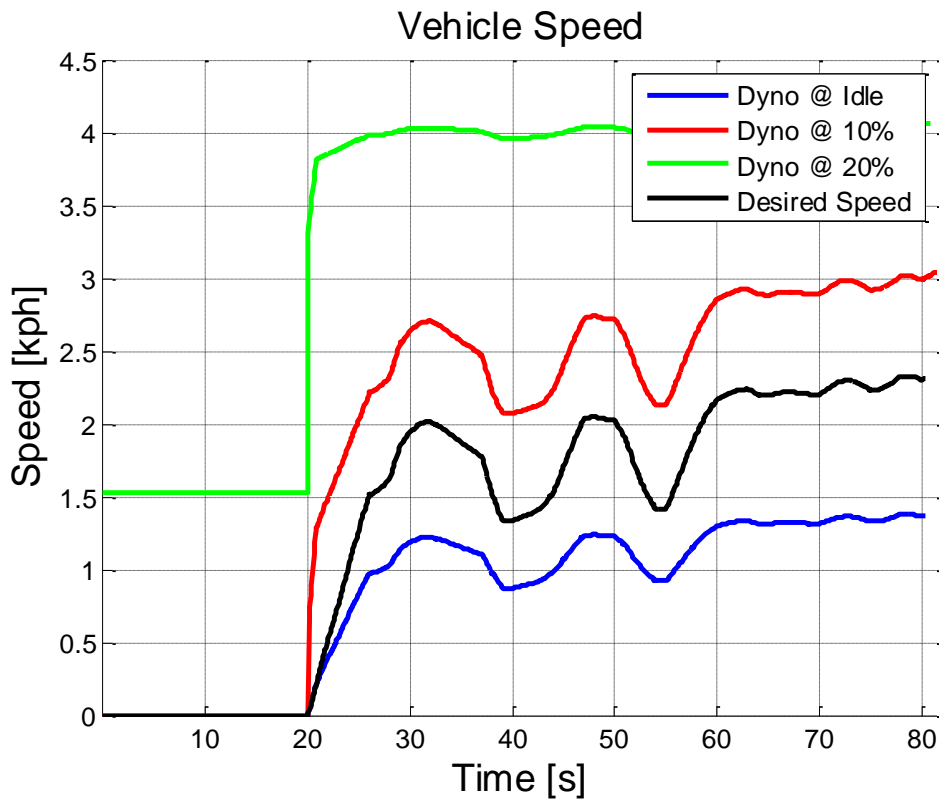
Figure 6-16 FTP-75 Vehicle Speed Under Different Dynamometer Load Regimes

In Figure 6-16 vehicle speed magnitude has been scaled down to fit the capabilities of the prototype UGV. The resulting drive cycle is shown as the black trace, or second from the bottom. When at idle, dynamometer loading creates a braking effect on the vehicle´s powertrain decreasing the maximum vehicle speed by one metre per second. At 10% assistance, in pedal input value scale, maximum vehicle speed has recovered what was lost and added an extra 0.6 metres per second. At 20% assistance the shape of the required speed profile is all but lost as the dynamometer is clearly pushing the vehicle forward to a point where it overpowered it shown by speed step input of 1.5 metres per second when the drive cycle, and hence the vehicle pedal input, is zero. Once the vehicle tries to launch both dynamometer and powertrain torque add up shooting the vehicle forward almost erasing the drive cycle´s trace.
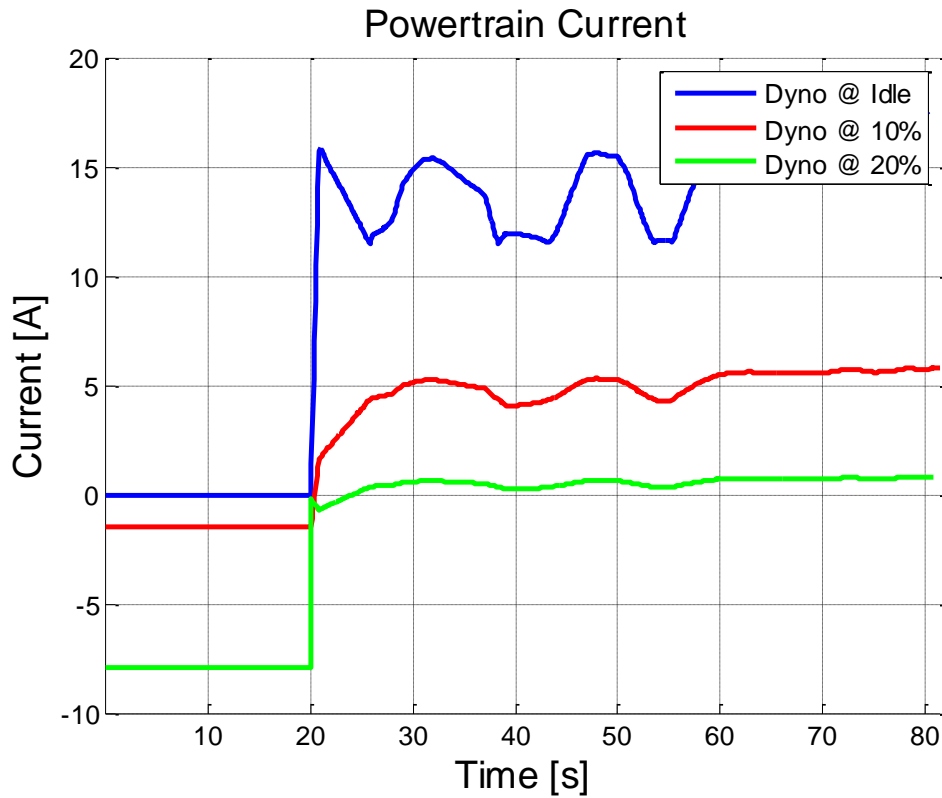
Figure 6-17 Powertrain Current Profile Under Different Dynamometer Load Regimes

Another area where the effect of dynamometer loading is visible is in the powertrain current consumption, shown in Figure 6-17. At dynamometer idle current consumption is highest due to the additional mechanical drag, but as dynamometer assistance increases the vehicle even starts to regenerate current. By using powertrain motor manufacturer data the torque can be estimated.
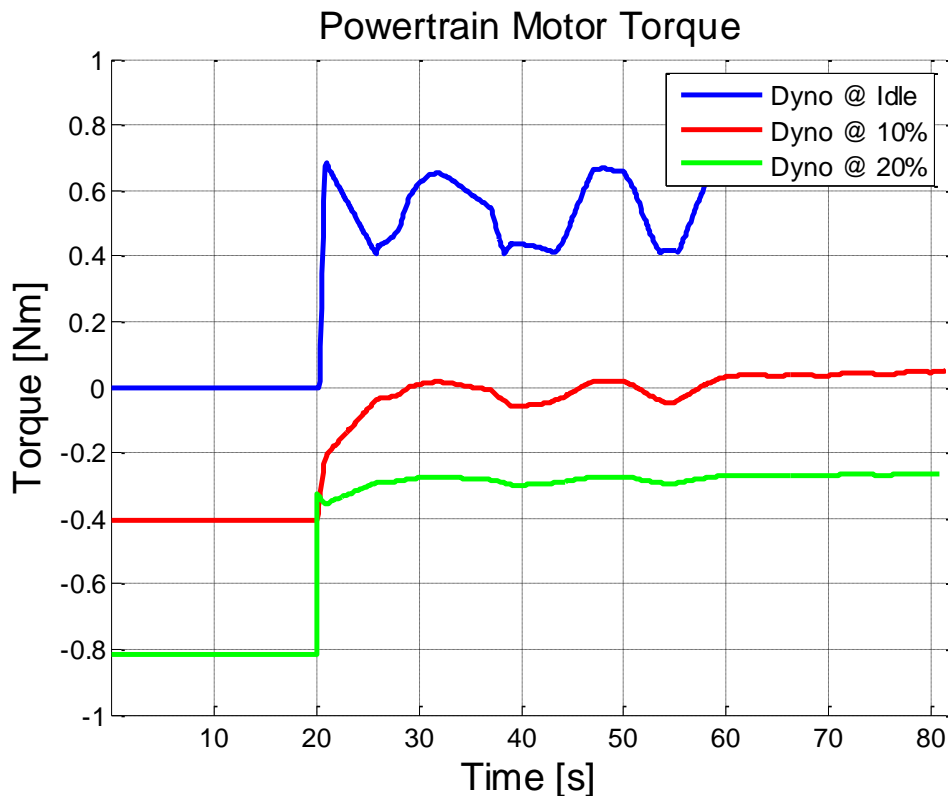
Figure 6-18 Powertrain Motor Torque Under Different Dynamometer Loading Regimes

Figure 6-18 shows how estimated powertrain motor torque falls as dynamometer assistance increases. At 10% dynamometer pedal input powertrain motor current consumption is approximately five amperes. This is close to the no load current specified by the manufacturer which matches the estimated torque which oscillates around zero. At 20% dynamometer assistance powertrain motor current is almost zero meaning the dynamometer has absorbed, or paid for, all the powertrain motor inherent losses which create the no load current.

After this analysis of dynamometer-vehicle interaction it is clear that the test bed can fulfil its purpose and is ready for use. The relevant section within the Discussion of Results chapter will elaborate on the impact real world data has on ICS learning. There the FTP-75 results used in the previous figures will be elaborated on from the ICS perspective.

6.5 Power Converter Load Sharing Failure

During the final stage of the dynamometer´s construction an accidental short circuit happened across one of the Power Field Effect Transistors used for the power controlling the sharing functionality between the DC-DC converters. Although the transistor itself was replaced the data channel within the National Instruments cFP CTR-502 control module was irreparably damaged. This prevented the testing of the power sharing functionality, product of the fuzzy dynamic modifier chain in real life. Yet all was not lost as the vehicle then operated in Battery Only Mode which by being an expected operating mode allowed for the remaining functionality to be tried out regardless.

7 Discussion of results

Chapter Summary:

After the numerical model was completed and the test platform was mapped the ICS was tested at all levels. The results obtained proved that both systems can meet their purpose. This chapter will describe the numerical results obtained and then discuss how the test system was used to tie both the virtual reality simulation and the real world components of the prototype vehicle.

7.1 Low Level Layer Simulation Results

The low level layer of the ICS was tested in a vehicle model derived as described in Chapter 3, so there was no skid steering. The mission profile used for the simulation was that of Figure 5-2, but different only in that the stationary segment was made shorter for computer processing sake. To compensate for the reduced watch time, the simulated power consumption of the mission payload, a Centurion anti-aircraft gun, along with the regular vehicle systems is increased proportionally to keep total energy consumption for that phase equal versus the original, longer, mission profile. The road edge phase is simulated by means of a Highway Fuel Economy Test cycle trace repeated for the second road segment. This standalone simulation of the low level layer was carried out with a more power hungry vehicle whose architecture is described by *Vehicle 1 (SV)* to insure that the operation of the low level layer was more demanding. This vehicle uses a set of Permanent Magnet Synchronous Machines (PMSM) which as described in (R. J. Felix Moreno 2012) provides good acceleration and better fuel consumption than a single PMSM in vehicles of this size and powertrain type. Mission payload power was obtained from manufacturer specifications and the on-board system load regime was estimated based on the work of Filipi.(Filipi 2004).

The system simulation was run through the already mentioned mission profile: Two HWFET driving segments separated by a power hungry watch phase. The power demand trace from the vehicle, equipped with the loads from *Vehicle 1 (SV)* is depicted in Figure 7-1. In the figure, the watch phase is discernible by the long steady power trace in the middle section of the plots. By comparing the top and middle plots it can easily be agreed that all power requests are met by the supply system, but by looking closer at the power supply plot a dark fringe can be appreciated. This "fringe" is created by supply oscillations which happened due to the demand hitting its reserve limit. To avoid these fringes is that the system was upgraded with the dynamic reserve increase and Load Killer features discussed in Sections 5.2.3 and 5.4.1.4 respectively.
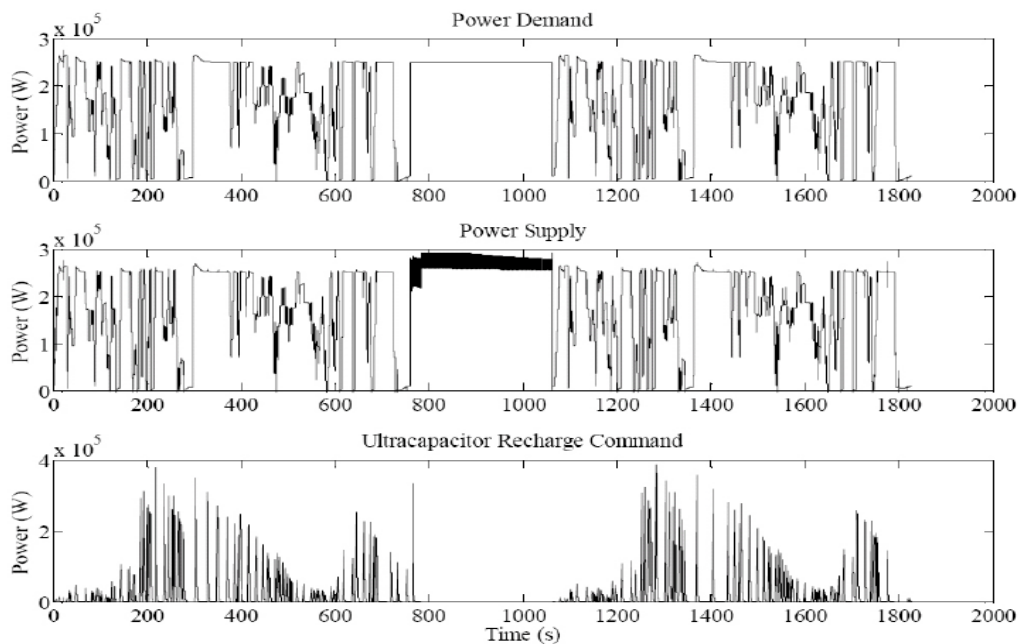
Figure 7-1 Low Level Layer Simulation Run Power Demands (Felix 2013)

Also, in the bottom plot of Figure 7-1 is the plot of the ultracapacitor recharge commands. When the dynamic modifier chain was discussed it was mentioned that the need to recharge this component was considered in the final power delivery command to the supply systems. This recharge command appears in the form of spikes as it is a quick short term request which if satisfied

immediately does not result in an aggressive energy delivery gradient that could damage the fuel cell or battery. The system as it is does react instantly to the recharge request and fulfils it without hesitation.
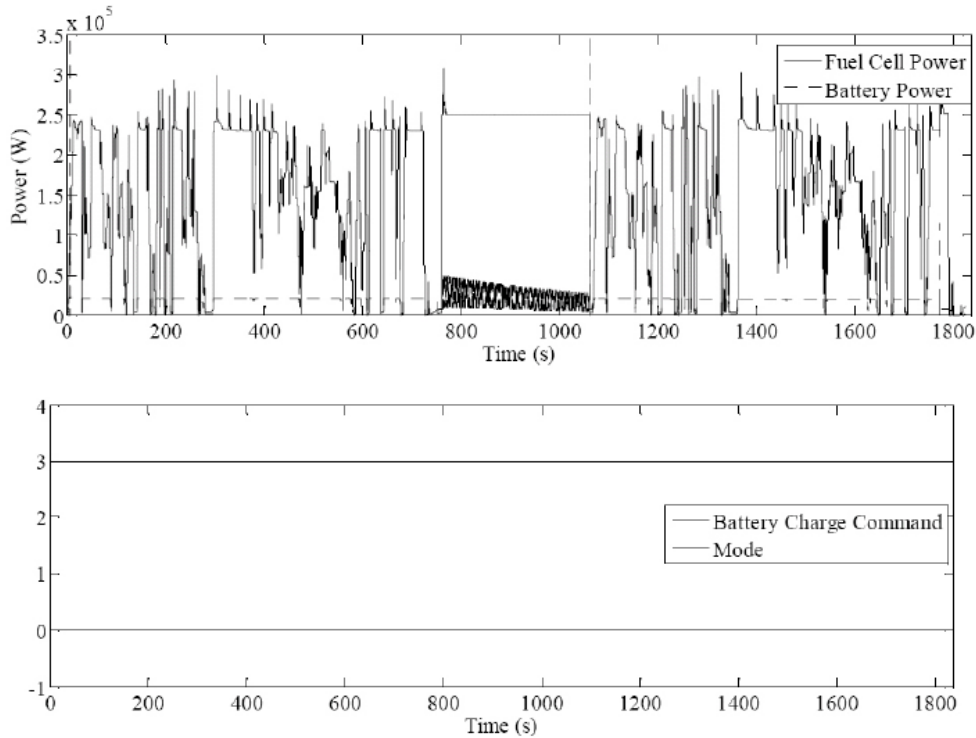
Figure 7-2 Low Level Layer Fuel Cell/Battery Power Split and Mode Selection (Felix 2013)

Another feature of the Low Level Layer was that of protecting the fuel cell from quick demand changes. That was achieved again through the dynamic modifier chain. The top plot in Figure 7-2 shows how the quick switching experienced during the watch phase, where the demand hit its reserve, was channelled to the battery command. The latter being a faster reaction supply is better suited for this type of energy delivery gradients and at the same time the fuel cell is protected from demand driven reactant starvation and oscillations. The operation of the mode controller is shown in the bottom plot of Figure 7-2. In it the mode selection value is three, Fuel Cell/Battery mode, and since the battery SOC never reached the preset threshold the battery charge command remains at zero. So far the working order of two of the low level layer components has

been verified. The only remaining one is that of the Mission Controller. To do this, please consider Figure 7-3.
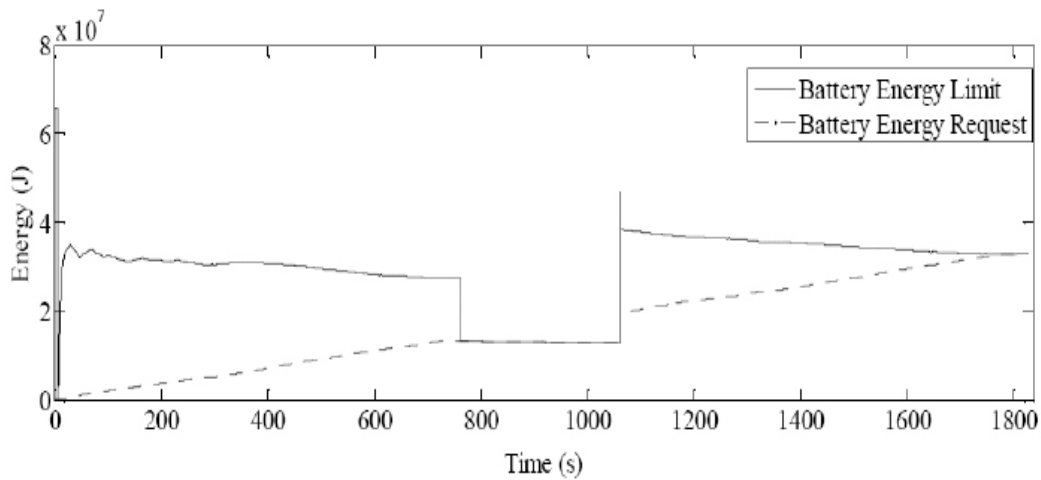
Figure 7-3 Mission Controller Criticality Switching (Felix 2013)

The fringe and rapid switching observed in previous plots have their origin in a collision of battery energy limitation and energy requests. When the simulation reaches the watch edge, the average data used to estimate is that of Joules per Second. So far the layer has used the Joules per metre figure applicable to mobile edges and has updated it to a higher value at the end of the first mobile edge. This can be observed by the higher energy reserve limit which appears at the beginning of the second mobile edge. The update was done by the "look back" forecast only because this simulation was performed without the medium level layer "look forward" forecast system, so when the mission payloads demanded more power than expected the request hit the reserve, but nobody adjusted for this. Had this simulation been run with the medium level layer the "look forward" forecast would have adjusted the reserve set by the Mission Controller to match the instantaneous energy consumption. Regardless, the Mission Controller performed its duty of updating the mission graph as progress was made and even reassessed the total energy required by the future road edge by means of the "look back" forecast. This shows that on its own, even with the reserve/request collision the system acted well within its parameters

195

and capabilities. The existence of the medium level layer only enhanced and upgraded the system´s performance as will be discussed in the next section.

7.2 Medium Level Layer Simulation Results

To test and validate the performance and working order of the Medium Level Layer systems, and match it with what was obtained from the simulation run of the low level layer, it was trained using the Highway Fuel Economy Test as well. Unfortunately, as shown in Figure 3-9 this cycle is very straight forward in terms of forecasting. The trace is somewhat stable with not many aggressive changes which make predicting future energy needs easier. To complement the training of the "look forward" forecasting engine it was then run through an FTP-75 cycle since the speed trace for it has a higher degree of variation. This second cycle also includes a group of idle periods which can create dead end nodes, so it is useful as well to test the robustness of the algorithm against them. Finally, following established machine learning practices, the trained system is now exposed to real world speed data gathered from a test vehicle (8,850 kg. GVW) driven in city traffic and highway conditions. Figure 7-4 shows the aforementioned real world vehicle speed trace.

It is quite clear by now that the cycle complexity has increased on each simulation run. The first training run was a more stable continuous trace, followed by a more cycle with more transient conditions which included idle periods. This last real world speed trace is totally random as is the result of unplanned driving in an ever changing environment as would be the case when the ICS is included in an actual vehicular platform.
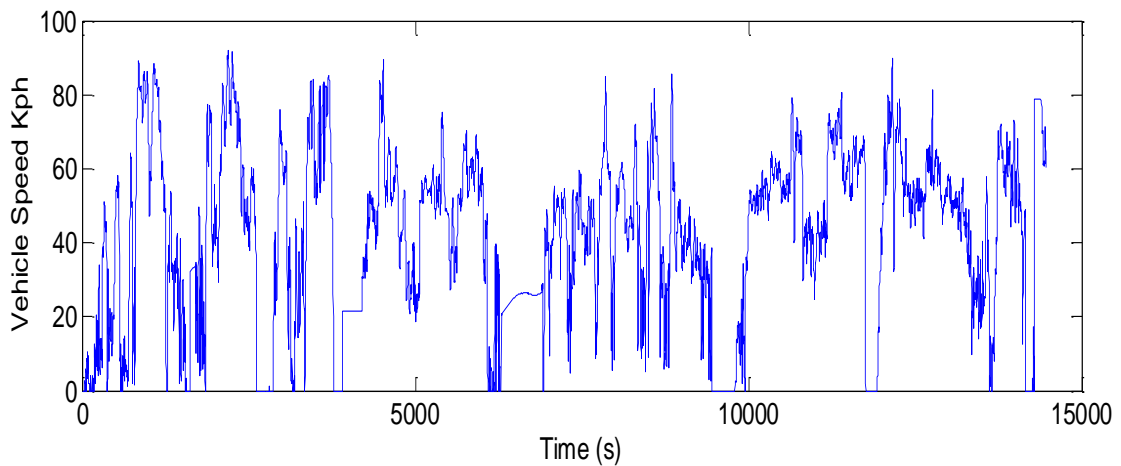
Figure 7-4 Real World Vehicle Speed Trace

So, how did the "look forward" and "look backward" averages compare in performance at the end of the day? Table 7-1 shows the comparison between the two types of forecasts. These results were obtained from simulation runs using *Vehicle 2 (MDV).* This vehicle is a heavier platform which uses twice as many PMSMs. This illustrates how the same software has so far been shown to operate two different vehicles with different powertrain configurations.

Table 7-1 Forecasting Result Comparison (R. E. Felix Moreno 2014)

Cycle	"Look Backward" Average [J/m]	"Look Forward" Average [J/m]	Variation [%]
HWFET	7.04e+03	6.74+03	4.26
FTP – 75	8.92e+03	8.80e+03	1.35
Road Data	9.30e+03	9.02e+03	3.01

The "look backward" average figure included in Table 7-1 is the final average calculated at the end of the cycle, so in essence is the actual Joule per metre figure as is it computed using the total energy spent over the complete cycle distance. The "look forward" figure is the average of the algorithm´s results over the complete cycle. It can be seen that as the forecasting engine training progressed its accuracy was better and when exposed to the real world data it remained under the initial training error of 4.26%. So, why use the "look forward" forecast? In this ICS the "look back" forecast is updated at the end of

197

the mobile edge this exposes it, as already discussed, to reserve/request collisions. This type of forecast is useful though when run at the end of a stage as it uses the resulting actual expenditure and distance travelled data for the updates. On the other hand in production vehicles fuel consumption and range estimations are run using similar algorithms, but on instantaneous data. Every manufacturer has its own proprietary algorithm, but the most common implementation is that of a rolling average. The system takes fuel flow data uses its estimated energy content and divides it by the distance travelled since the last calculation to obtain the joule per metre figure. It then applies a rolling average to this result to filter out noise. There are some drawbacks to this approach as it is also sensitive to idle periods where the distance travelled is zero. Then the result would tend to infinity, but is clipped to a sensible value. Figure 7-5 shows the graphical comparison between the two approaches
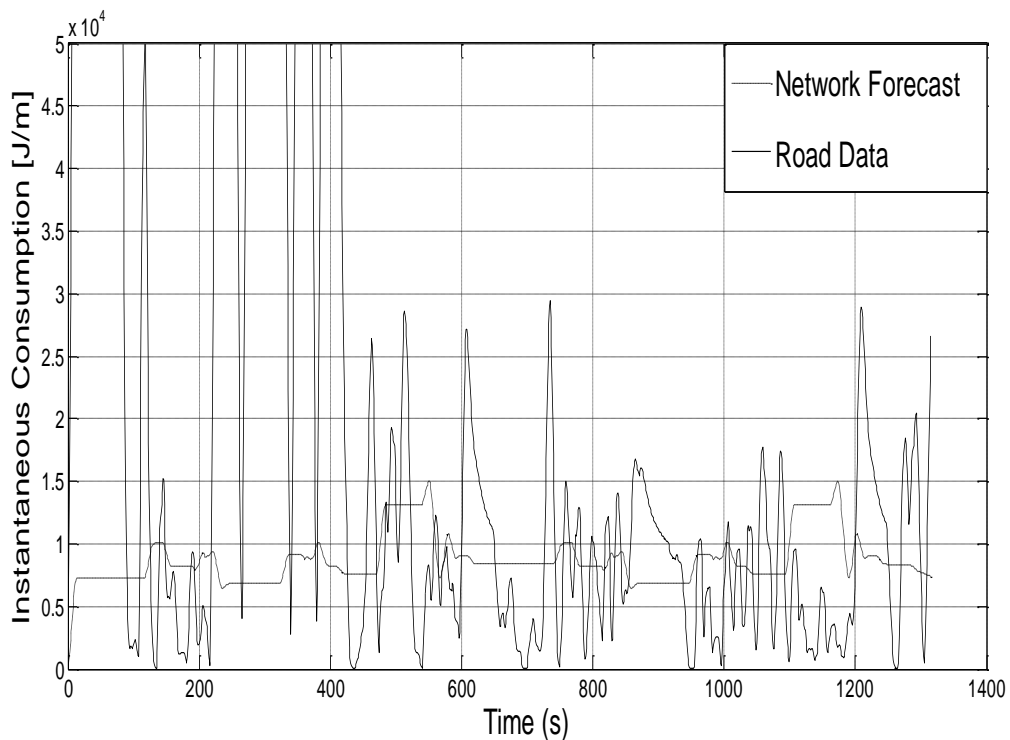
Figure 7-5 Rolling Average Look Back vs. Node Network Look Forward (R. E. Felix Moreno 2014)

198

The solid line shows the result of the rolling average algorithm. It is clear how the reading has a greater variance and to be used for range and energy consumption forecast it would need additional filtering. The dashed line is the result of the Medium Level Layer "look forward" forecasting engine. The reading is more stable and more suitable to be used by the other ICS layers without further post processing. Its accuracy, as already illustrated, is around 95% and it has the advantage of enabling the only reserve update. Also of note is that the rolling average approach, because of the way it is calculated, is heavily tied to both driver input and distance travelled giving high Joule per metre results when the vehicle is either under heavy loads or stationary. The medium level layer graph node network approach is more biased towards driver input having high values only where there is a high power demand. Figure 7-6 shows how energy consumption is at a maximum at the points of maximum vehicle speed (i.e. high power demand points), and no spikes appear during idle periods.
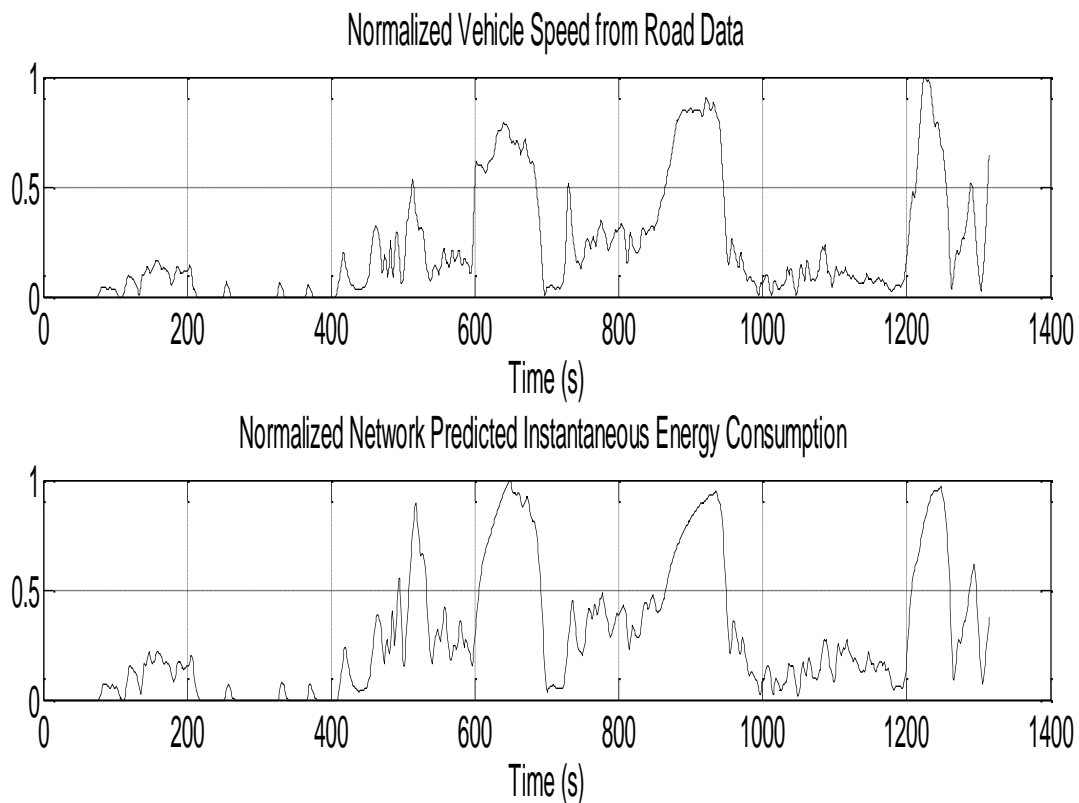
Figure 7-6 Driver Demand and Energy Consumption Prediction (R. E. Felix Moreno 2014)

In this very simple manner it can be proved that the medium level layer works as intended as the "look forward" forecast needs every other underlying system in the layer working properly to do itself.

7.3 High Level Layer Simulation Results

The first feature to test in the High Level Layer is the Configurator. The object of the simulation is to verify if the personalities dialogue is actually rendering a limited budget for the loads determined to be critical for a given mission profile. For the simulation the mission profile is as follows:

Table 7-2 Configurator Test Mission Profile

Number of Edges	4
Type of Edges	Mobile-Watch-Mobile-Idle (1,2,1,3)
Node Parameters	Mobile 1: 40 metres Watch : 6 seconds Mobile 2: 4 metres Idle: 30 seconds
Critical Loads	Mobile 1: Powertrain, Lights 1, IR and RGB Camera Watch: Lights 1 and 2, Thermal Imager, RGB Camera Mobile 2: Powertrain, RGB Camera, Lights 1, Idle: None
Estimated Total Required Energy	120.4 kJ
Available Energy	100.22 kJ

The available on-board energy was intentionally set to be lower than the requirement to force the Configurator to negotiate with the personalities. In an ideal world, following the preset vehicle speed all interruptible (lights) and configurable (vision system) loads should be ON for the entire duration of the mission. Unfortunately, the energy shortage will force the ICS to limit the energy expenditure of each load. Table 7-3 set out the original and resulting negotiated budget for each load type.

Table 7-3 Original vs. Negotiated Budgets

Load Type	Original Budget per Edge [J]	Negotiated Budget per Edge [J]
Lights	[8.256,2.064,0.8256,0]	[5.608,0.175,0.056,0]
Vision	[5.856e+02,1.723e+03,34.560,0]	[3.978e+02,1.463e+02,2.347,0]
Powertrain	[9.60e+04,12000,9.600e+03,0]	[6.52e+04,1.01e+03,6.52e+02,0]

The negotiated budget does not cover the requirement of the continuous loads; therefore the Load Killer must come in, together with the Continuous load manager.

When there is not enough energy for mission completion and a threat is near, the continuous load manager will command the vehicle to maximum electrical efficiency motor speed. The purpose of this is to have the vehicle move away from the threat as fast as possible whilst using as little energy as possible. Figure 7-7 shows a comparison between two threat avoidance strategies. The blue line shows the higher initial energy consumption of the continuous load manager commanded speed, versus the lower threat avoidance command from the behaviour module.
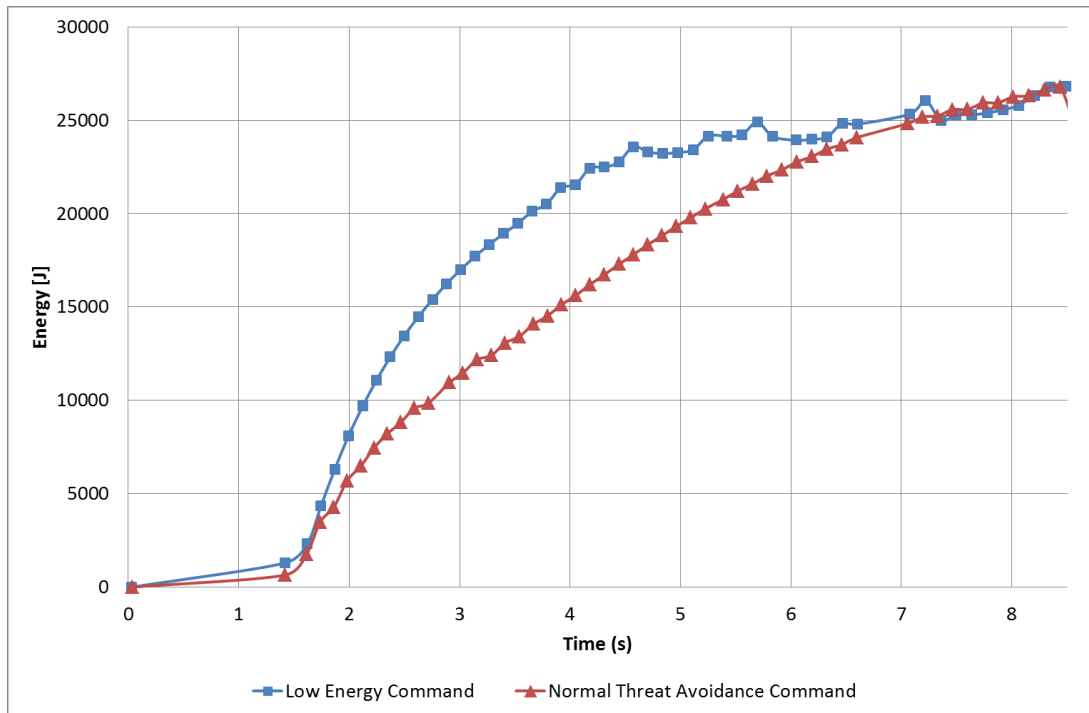
Figure 7-7 Energy Consumption Comparison Between Threat Avoidance Strategies

By also looking at Figure 7-8 it can be easily determined how the continuous load manager has gotten the vehicle to cover a greater distance by spending almost the same amount of energy. It is important to remember that when energy is scarce the vehicle should hurry back to base regardless of any pending mission objective to keep extra resources from being spent on recovering it from the field.

These results validate the working order of the Continuous load manager. Now let's look at how the behaviour layer works to keep the vehicle away from threat, but keeping its home beacon trajectory as short as possible per the weight in Equations 5-58 and 5-59.
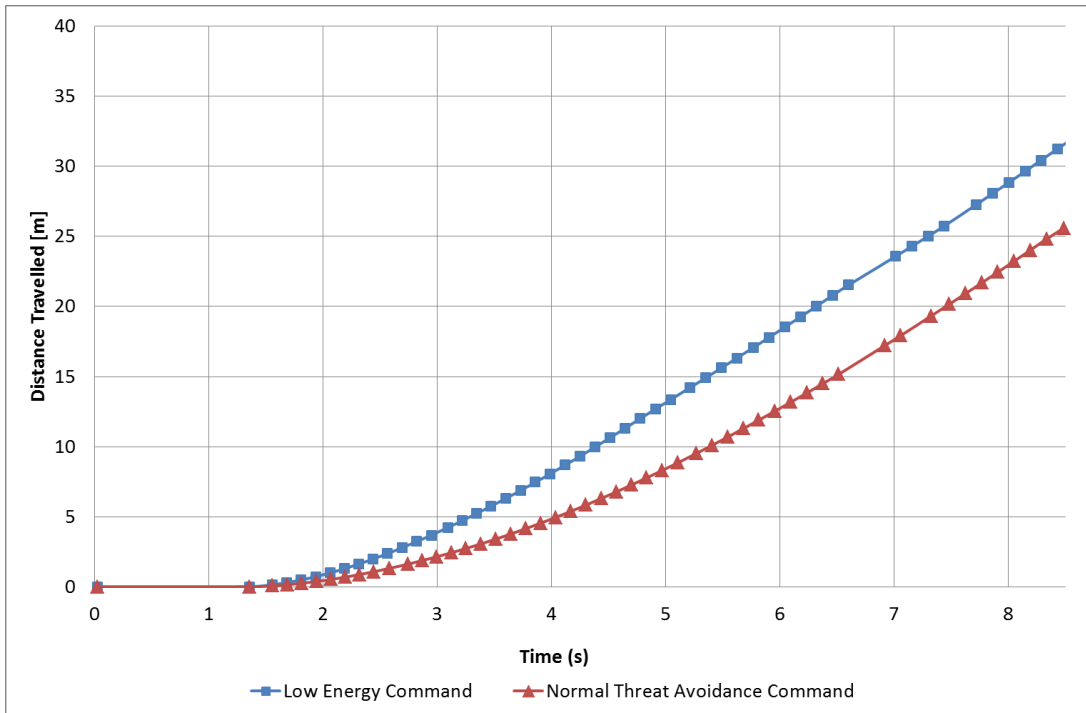
Figure 7-8 Comparison of Travelled Distances for Each Threat Avoidance Strategy

When the weight parameter **W** is positive or even zero the vehicle will try to avoid the threat and stay on course towards the home beacon. A larger weight value will bias the vehicle's navigation to a more direct route towards the home beacon. On the opposite end, a negative value will prioritize threat avoidance over home beacon proximity. Figure 7-9 throughFigure 7-12 show the resulting trajectories followed for the indicated weight factor values.
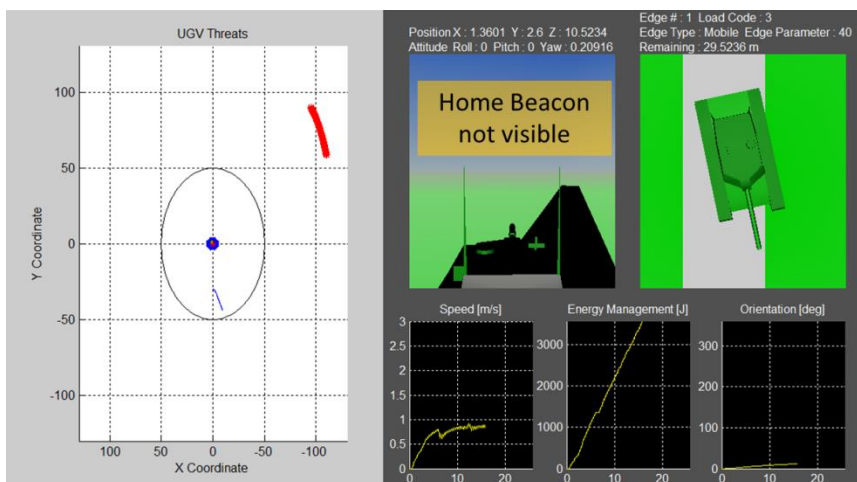
Figure 7-9 Home Beacon Bias Not Active

The results for a weight value of 0.25, shown in Figure 7-10, are the most balanced ones. The red coarse trace on the scope screen, belonging to the home beacon, together with the thin blue trace, belonging to the UAV threat, show a similarly biased displacement. This means the vehicle is trying to get away from the threat at much as it is looking to arrive at the home beacon.
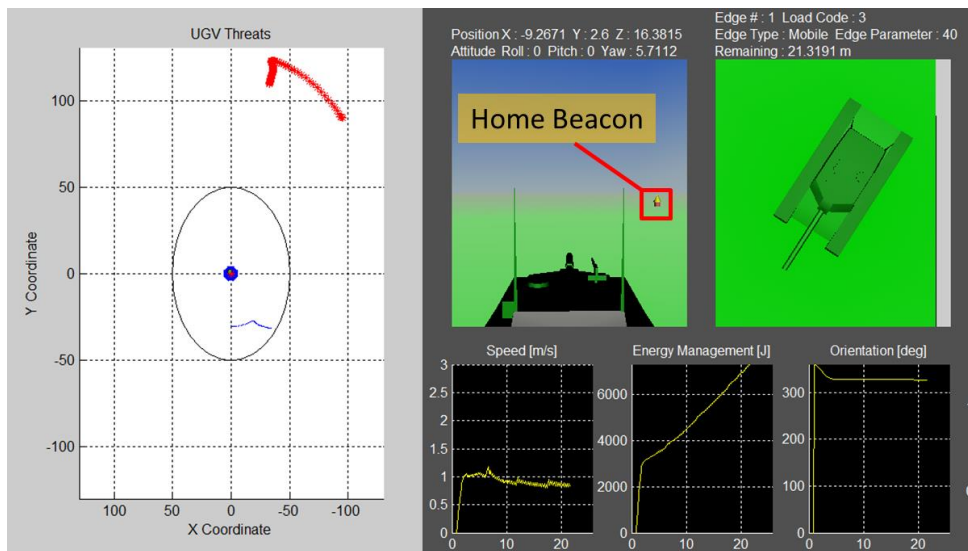
Figure 7-10 Home Beacon Bias - Weight 0.25

Whereas a value of 0.75 shows, in Figure 7-11 , the vehicle travelling on an almost straight line towards the home beacon creating an almost horizontal, and longer, threat trace.
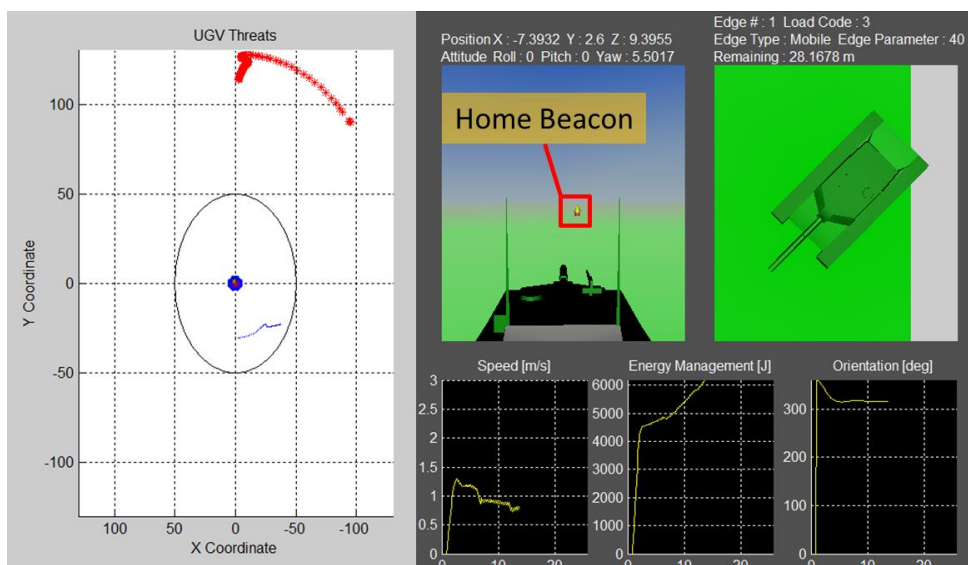
Figure 7-11 Home Beacon Bias - Weight 0.75

The negative weight value, of -0.25, in Figure 7-12, results in an almost vertical threat trace, meaning the UGV was most worried with avoiding it than getting closer to the home beacon.
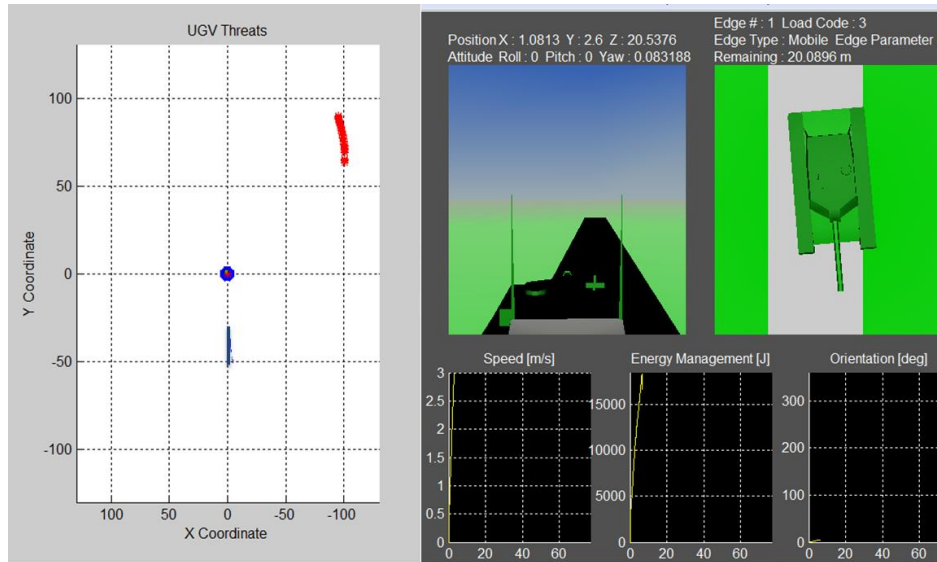
Figure 7-12 Home Beacon Bias - Weight -0.25

These results validate the working order of the Behaviour module by showing it being totally adjustable and efficient in fulfilling its navigational task.

7.4 Testing Platform Results

To evaluate the working order of the test rig three tests were run. Some of the results obtained were included in Figure 6-16 through Figure 6-18, in Section 6.4 when the capabilities of the test system were initially discussed. Taking a deeper dive into the results the following can be established.

1. The test rig is fully capable of being controlled remotely.
2. The Load activation manager can fully control interruptible loads.
3. Through the means of the control pad a would-be operator can issue commands to the UGV with very little training.
4. Both instances of the ICS, on the UGV and UAV, operate with no problem. This is shown by Figure 7-13 which shows reserve management plots for all three energy consumption port of each platform.
5. From the start the creation and design of the test rig fed back to the ICS lower layer by driving hardware and reality driven changes into its conceptual design. One example of this was the power sharing commands illustrated in Figure 4-3, which came about when it became necessary to deal with real power converters over conceptual ones.
6. Finally, the undeniable differences in the physical layer of the powertrain between real life UGV and simulated UAV further demonstrated how the ICS operation is not affected by them as it sits on top of the physical layer of each vehicle.
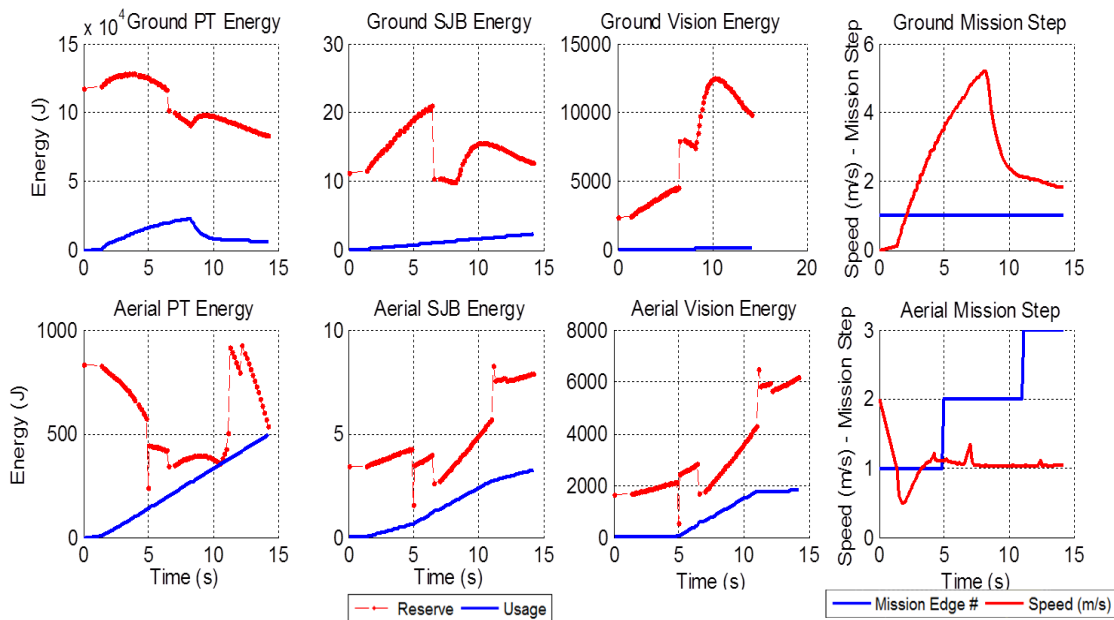
Figure 7-13 Usage vs. Reserve plot for UAV and UGV

7.4.1 Driver training

One of the objectives of the test rig was to create a training platform for would be UGV operators. To this end the VR simulation world and supporting data screens where put into good effect.

The main screen includes navigational coordinates data from a simulated GPS input. It also displays vehicle orientation and overall energy expenditure, so the driver can be aware of the status of the vehicle. It also includes mission progress information and interruptible load configuration data.

By using a video game related control pad the learning curve for its use is reduced as would be users are familiar with the controller and the function of each button, lever or pad. Figure 7-15 shows how an untrained person can quickly issue basic commands to the vehicle. More detailed instruction can be achieved over time.

Figure 7-14 Popular Videogame Console Control Pad and VR Environment Control Pad

Figure 7-15 Untrained Operator with Control Pad

7.4.2 Preset Drive Cycle Testing

The three physical tests performed in the laboratory where done using a preset laboratory drive cycle, the FTP-75. Because its duration is of more than 3600 seconds all three tests were set to run until 80 seconds as they were meant for test rig validation and providing data for ICS training inside a very constrained time window.

Another consideration is that the drive cycle is meant for full size commercially available ground vehicles, so the trace's top speed exceeds ninety kilometres per hour which a UGV like the one employed cannot reach. Therefore the whole speed trace was scaled down to match five kilometres per hour top UGV speed. Figure 7-16 shows the comparison between the original and scaled down traces.
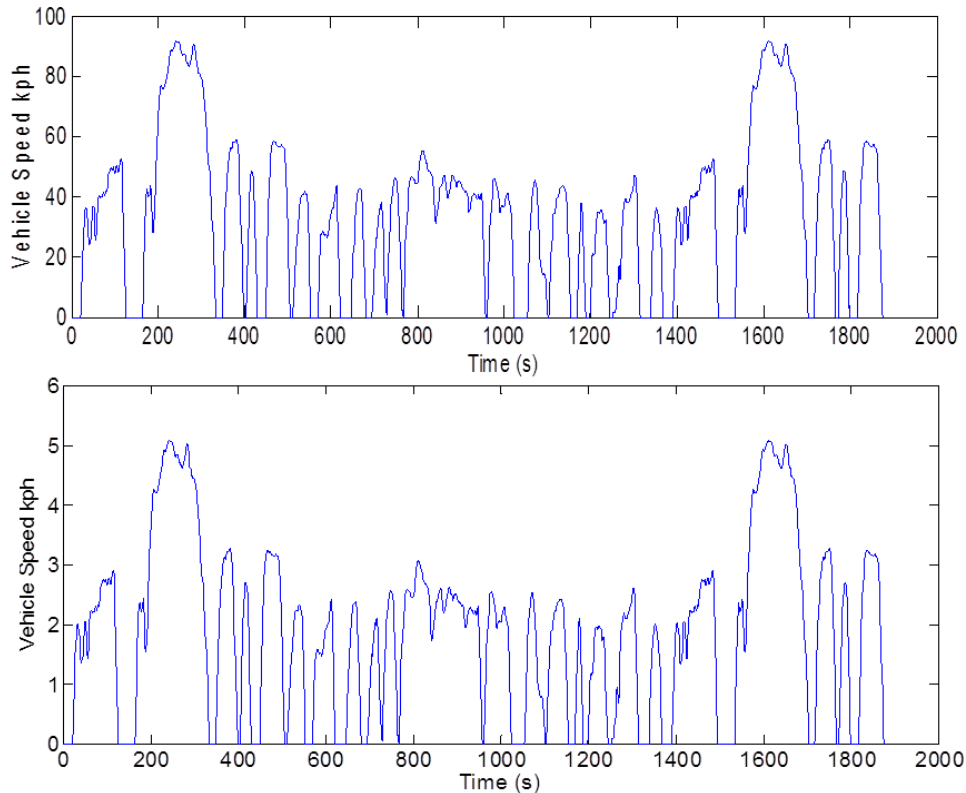
Figure 7-16 Comparison Between Scaled and Original FTP-75 Drive Cycle Trace

7.4.3 ICS learning

Whilst running the tests the ICS medium layer had the opportunity to learn unknown driving patterns during each run. Although the target trace was the same one must remember that each test was run using different dynamometer loading regimes. Thanks to this, the data in the frames entered into the database were different every time. The frame includes pedal, RPM, energy used and distance travelled data. Figure 7-17 shows how the resulting vehicle speed and power consumption traces are unique on each run, therefore all the resulting frames will be so too.
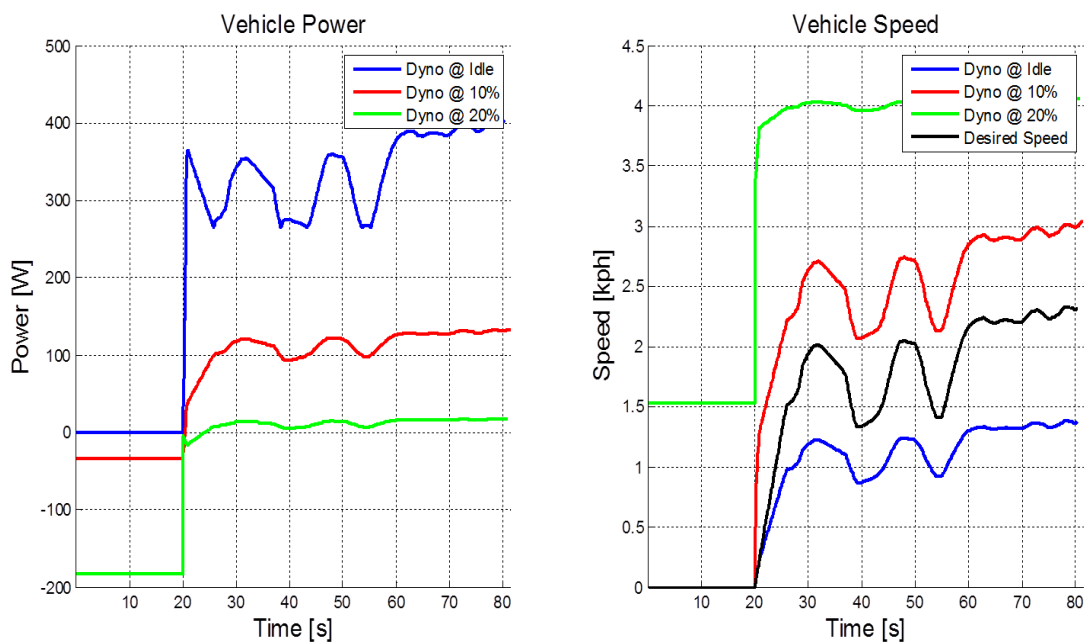
Figure 7-17 Power and Speed Plot for Different Dynamometer Load Regimes

The resulting data base will then be enriched as shown in the 3D plots in Figure.
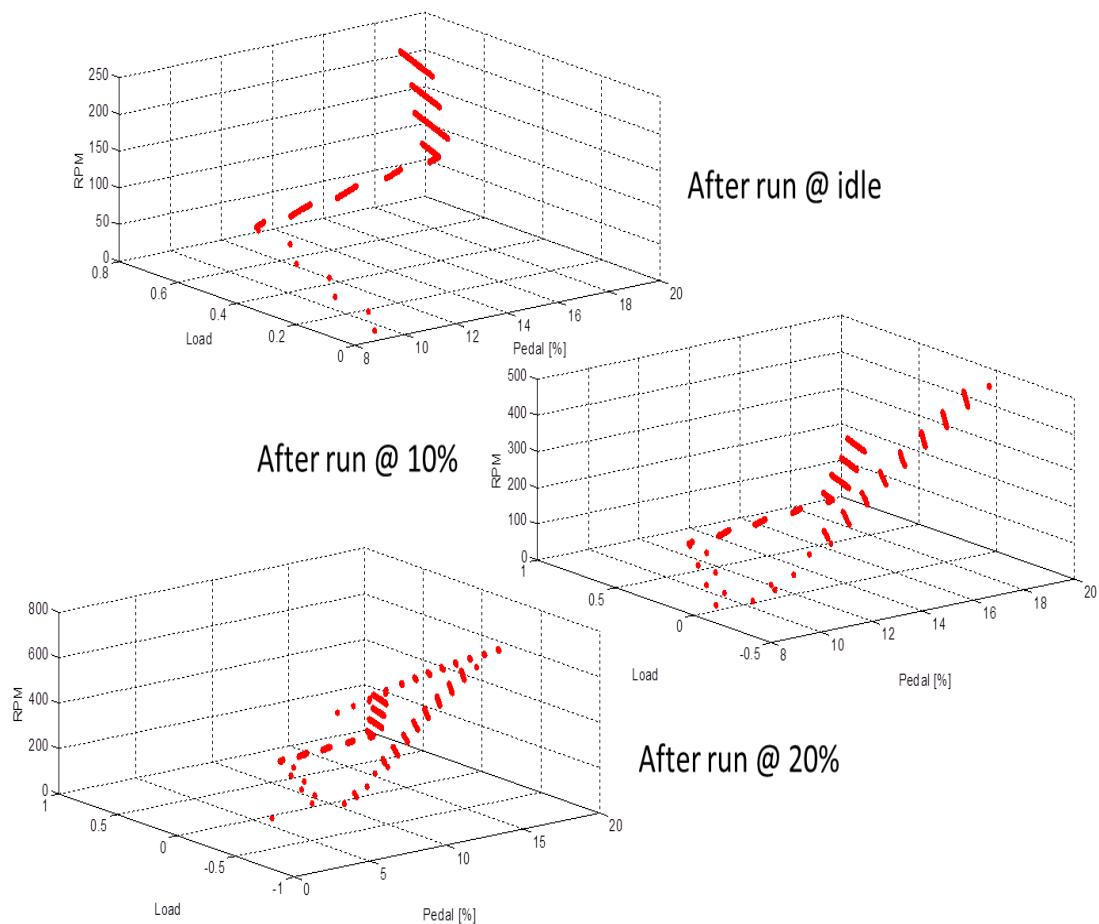
Figure 7-18 Node Matrix Growth after Three Dynamometer Runs

By quickly looking at the axis of the three plots, it is obvious how for the same range of pedal percentages (0%-20%) the breadth of RPM and Load combinations has grown. Not only are there positive loads, meaning positive torques, but also negative ones therefore the matrix is richer as it now considers the possibility of regeneration conditions. The example database matrix from Figure 5-24 was created running simulations with laboratory drive cycles which are taken to be on level roads. The test rig has now enriched the node matrix creation process with conditions not found before and by varying the dynamometer load or applying the fixed friction brake the database will receive more varied and realistic frames. The rig has then fulfilled its purpose of allowing the ICS to learn from a more diverse and powerful set of possible

driving conditions beyond unexpected driver commands into also unknown roads topography and surface conditions.

7.4.4 Road Conditions Simulation

The final aspect of the test rig's objectives was to be able to simulate different terrains. Although the limited test time available was not enough to fully exploit its terramechanics capabilities, again the dynamic tests performed were enough to demonstrate how it can, by modifying a single parameter, emulate three different kinds of slopes. An idle dynamometer can emulate either an uphill climb or even a load being towed. By increasing dynamometer load two different downhill conditions were created. This can easily be expanded to create vehicle coasting for current regeneration purposes. The traces in Figure 7-19 show how vehicle speed becomes more dependent on dynamometer loading as it increases until it very much controls it as would be the case of a steep downhill descent.
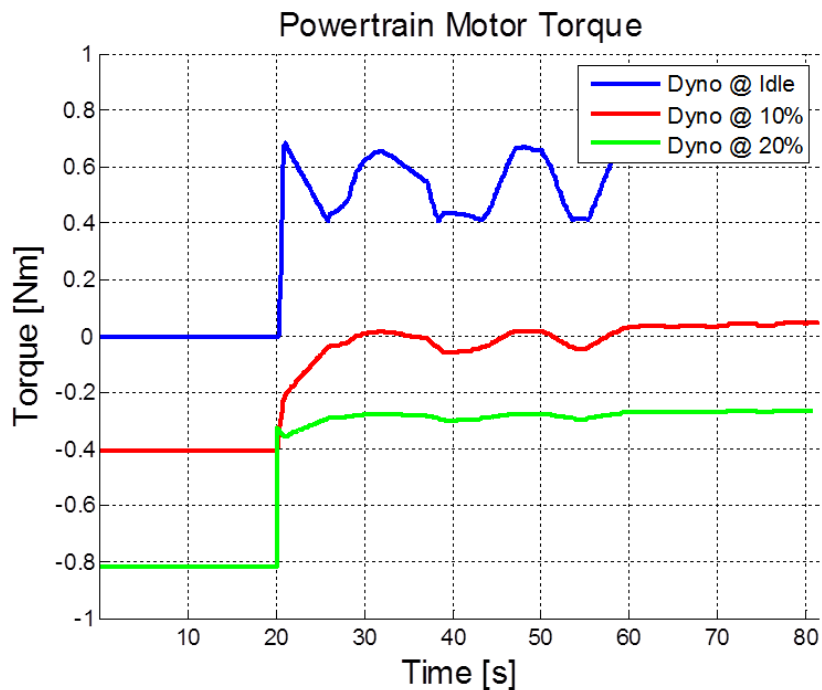
Figure 7-19 Powertrain Torque Under Different Dynamometer Load Regimes

In these test runs the vehicle was driven in a straight line against the same loading on each side of the powertrain. It is possible thanks to having two separate dynamometer motors to emulate different road forces on each set of wheels. This way the left could be made to spin faster than the right side to emulate a spin or skid on the way down a hill. In summary both sides of the dynamometer can be set to different road conditions if needed. The amount of road type combinations then becomes incredibly large.

7.4.5 Summary

To close this chapter it is worth while making a quick summary of what was gained by mounting the ICS on a real life platform and how that process enriched this research endeavour.

By exercising the ICS in the VR simulation environment and then mounting it in the test system the operation of the whole architecture was validated. As already discussed in Chapter 5 the diverse nature of all the different continuous and discontinuous algorithms opened the door to prior unexpected interactions and dynamics. Still the system has proven to work in a uniform manner exhibiting the organic computing characteristics expected. The ICS can configure and attempts to protect the vehicle through the high level layer; it can diagnose its energy supplies through the low level layer. It is conscious, albeit in a limited manner, of its surroundings and operating context and finally thanks to both the medium and high level layers it automatically manages its load system to optimize the use and distribution of the available on-boar energy. The test rig results only supports this argument by allowing two instances of the ICS to exist in two different electrically powered platforms also proving that another research premise has been fulfilled, that of the algorithms being able to control any type of electric vehicle regardless of the domain where it operates. Also the test rig provides more varied driving conditions which are useful for better ICS training.

8 Impact Analysis and Conclusions

Chapter Summary:

This final chapter is divided into four sections. Through them the merits of this research will be reasoned by pointing out its advantages, disadvantages, further work inspired by the results and close out by drawing conclusions.

8.1 Advantages

It would be improper to presume that all excellent with the resulting test and simulation outcomes described in the previous chapter. Yet, it is fair to recognize that which is positive and can qualify as an advance in the area. Therefore in the following paragraphs the advantages resulting from the research described in the present thesis will be discussed at length.

First, it is standard practice that software features be self-contained for ease of coding, diagnosis and maintenance. Yet this approach where functionality is abstract and depends on parallel and some cases concurrent software features, like the top level layer interactions with lower layers, the behaviours exhibited by the vehicle in both test environments, virtual and real, are more according to the way an average person thinks. Not very often does it happen that a decision is made without several flags being turned on in a person's head about extra and sometimes unexpected information and conditions. Does one walk down a dark alley? The answer to the question will depend not only on the subject´s capability to walk, as would be decided by a software only interested in functional efficiency, but on factors as is the city safe? Have there being reports of ill events around this part of town? This kind of ingrained situational and informational awareness is what was imbued in the ICS to make it more

conscious of its own limitations and the challenges it faces during the course of a mission. The advantages of the proposed energy management system are precisely that. The vehicle operates not only aware of how much energy and torque it has at its disposal, but it is capable of an internal dialogue of sorts which make it capable of making better use of the resources at its disposal.

On the test side of the research, the design and realization of the test platform concept has resulted in a powerful and versatile tool for vehicle dynamic and control system studies and research. The simulation environment allows for the creation of whatever test scenario comes to mind. Thanks to the software and its division between Matlab and LabView not only can a researcher test new intelligent algorithms, in the former language, but also new ways to control the physical hardware in view of whatever information is passed down to LabView. In essence anyone can create a virtual world as complex or simple as necessary and have the hardware behave as needed per the vehicular concept under test. This flexible platform has great capabilities and opens up possibilities to further research in the areas of terramechanics simulation, skid steer control, power and energy management and so on.

8.2 Disadvantages

As already said, it would be not be correct to imply that everything is nice and perfect. The present approach does present a downside. This mainly comes in the degree of complexity an abstract software system like this brings with it. Software performance and response analysis becomes more complicated as a given vehicle performance aspect takes longer to dissect due to the many feature and layer interactions. What makes the system so capable is also what can make any modifications or upgrades a complex affair. Although this can provide for another avenue for research, that of diagnosis of embedded organic software, it can also present a hurdle when the intention is only to prove out a new simple concept. The speed at which new features or concepts can be

included will depend directly on the experience of the programmer and his/her knowledge of the state of the ICS.

The test bed also has its drawbacks. It can only test vehicles of a certain size and dimensions. Also it cannot test hybrid concepts where internal combustion engines are involved as it does not contemplate an emissions control system. This in terms of pure electric or fuel cell vehicles does not present a problem, but today hybrid platforms abound and not being able to test on them can represent a considerable limitation.

8.3 Further work

The simulations considered that the vehicle had some sort of tracking system which provided threat and vehicle position. This data came in with no latency or noise which to the purposes of the ICS concept research was enough. Yet in the future analysis of how the vehicle reacts to tracking and position system problems could prove interesting.

Another avenue of work is that of vehicle autonomous behaviour. The high level layer already has the structure to allow for further work on this area. How would the vehicle react to two differences in terrain? Would it choose the shortest path or maybe one that could be longer, but safer in terms of the presence of threats? What about the most energy efficient? Could it make a compound decision where the road chosen is a mix of any of the above? If so why and how?

The test rig today allows for skid testing per side, meaning one set of conditions can apply to the left or right side or even both. What could happen if the number

of motors where increased to four and tyre by tyre conditions could be tailored? This represents an amazing avenue of vehicle dynamics research with a test platform for real world validation outside of the simulation realm.

8.4 Conclusions

After all which has been written and done, it can be said without risk that the area of intelligent energy management for electric surveillance vehicles is a deep and interesting one. At the start of the project the goals were known and thanks to previous experience there was a clear notion of what could be achieved. Yet, during the course of this research the work took unanticipated paths which resulted in a learning experience much richer that initially thought.

The Intelligent Control Structure presented risks and did not come about before prompting a few runs into dead ends or even some backtracking. Many intelligent algorithms were analysed to carry out the tasks considered. For example, initially genetic algorithms were tested in lieu of the linear programming system for the Configurator's dialogue function. Support Vector Machines and even Graph Cuts were also candidates for the "look forward" forecaster before the node matrix system was conceived on a late night during a congress. To create a final design of the test rig many ideas ended up inside the bin as cost, software and even safety constraints set up an envelope within where the platform would be born.

In technical terms the Intelligent Control Structure and its test platform met their objectives. How is this so?

- The vehicle can configure itself to increase the powertrain's available energy and therefore increase range.

- It can protect the fuel cell against damaging power demands. Also, the fuel cell model succesfuly incorporated provisions for environmental conditions like ambient temperature, altitude and humidity.

- It can diagnose its power supply system and reconfigure itself accordingly.

- The ICS can cope with three different kinds of load systems during any programmable mission profile or even in the absence of one. In the latter case the system will craft an artificial mission profile and carry on with the mission. In both modes of operation no GPS systems were considered.

- The vehicle can navigate under threat and do so in an energy expenditure aware manner, this sets it apart from systems which focus only on operational energy efficiency, and places it in a shelf of abstract complex systems.

- The test rig designed for the ICS met its target. It can be used by inexperienced users. It can test the same software in any kind of electrically powered platform in different domains (air, ground, etc.) and in the case of ground can also prove in the real world domain by existing within a prototype vehicle.

- The vehicles equipped with the ICS, ground and aerial, can operate aware of their surroundings and configure their loads and supplies accordingly.

- All together makes for a complex and sometimes too elaborate system, but which has created a tool for further research into the intelligent systems and energy management arenas.

The knowledge created or applied was published in journals both for ground and aerial vehicles further proving the applicability and versatility of the research. It can surely be said that the author has grown through having his ideas, knowledge and resolve be tested, so from any point of view it can be

proposed that this PhD research has been successful in the academic and personal aspects.

9 Publication History

Felix Moreno, Rodrigo, John T. Economou and Prof. K. Knowles, "Driverless Vehicles and LIDAR: Evaluation of Possible Security Threats on the Open Road." To be presented at SAE World Congress and Exhibition 2015.

Felix, Rodrigo, John Economou, and Kevin Knowles."UAS Behaviour and Consistency Monitoring System for Countering Cyber Security Threats.". SAE Technical Paper 2014-01-2131. Presented at SAE 2014 Aerospace Systems and Technology Conference in September 2014.

Felix Moreno, R., Economou, J., and Knowles, K., "Energy Management System for Electrified Tactical Mobility Platforms," SAE Technical Paper 2014-01-1911, 2014. Presented at SAE World Congress 2014 , doi:10.4271/2014-01-1911.

Felix, R., Economou, J., and Knowles, K., "Control System for a PEM Fuel Cell Powered Heavy Duty Tactical Mobility Truck with Auxiliary Power Generation Capabilities," *SAE Int. J. Alt. Power.* 2(3):413-427, 2013, doi:10.4271/2013-01-2472

Felix Moreno, Rodrigo, John T. Economou, D. Bray and Prof. K. Knowles "Modelling and simulation of a fuel cell powered electric drivetrain for wide body passenger aircraft." Proceedings of the Institution of Mechanical Engineers Part G Journal of Aerospace Engineering. 02/2013.

Felix Moreno, Rodrigo, John T. Economou and Prof. K. Knowles "Modelling and simulation of a fuel cell powered medium duty vehicle platform" IMECHE Sustainable Vehicle Technologies: Driving the Green Agenda, Gaydon, Warwickshire, U.K. 11/2012.

REFERENCES

Agency, Energy Intelligence. «"U.S. Gasoline and Diesel Retail Prices", .» 2011.

Agency, Environmental Protection. *Dynamometer Drive Schedules.* 2008. http://www.epa.gov/nvfel/testing/dynamometer.htm (último acceso: 5 de November de 2012).

Ali Almansoori, Hui Liu, Ali Elkamel and Michael Fowler. «Analysis of Hydrogen Economy for Hydrogen Fuel Cell Vehicles in Ontario.» *Proceedings of the 2012 International Conference on Industrial Engineering and Operations Management.* Istanbul, Turkey, 2012.

Aono, Thoshihiro and Takehijo Kowatari. «Throttle-Control Algorithm for Improving Engine Response Based on Air-Intake Model and Throttle-Response Model.» *IEEE Transactions on Industrial Electronics* 53, nº 3 (June 2006).

Auer, Juergen and Schneuwly, Adrian. «Ultracapacitors drive new efficiencies for powertrains.» *Advanced Automotive Electronics Conference 2006.* 2006.

Ballard Power Systems Inc. «FCvelocity-HD6 product data sheet.» Burnaby British Columbia, 2011.

Banco de México. *"Informe Anual 2009".* Mexico City: Banco de México, 2010.

Banco de México. *"Informe Anual 2010".* Mexico City: Banco de México, 2011.

Banco de México. *"Informe Anual".* Mexico City: Banco de Mexico, 2012.

Barbir, Frano. *PEM Fuel Cells. Theory and Practice.* Elsevier Academic Press, 2005.

British Petroleum. «"BP Statistical Review of World Energy".» 2010.

British Petroleum. «BP Statistical Review of World Energy.» June 2014.

Callaghan, Anissa Dehamna and Lisa. «Military and Fuel Cell Adoption.» *Cleantech Magazine*, September de 2010.

Centro de Estudios de las Finanzas Públicas - Cámara de Diputados. *"Indicadores de la Iniciativa de Ley de Ingresos de la Federación 2014".* México City: Cámara de Diputados, 2014.

Chan, C.C. «The State of the Art of Electric, Hybrid and Fuel Cell Vehicles.» *Proceedings of the IEEE* 95, nº 4 (Abril 2007).

Chan, C.C., Alain Bouscayrol and Keyu Chen. «Electric, Hybrid and Fuel-Cell Vehicles: Architectures and Modeling.» *IEEE Transactions on Vehicular Technology* 59, nº 2 (2010).

Comision Federal de Electricidad. *Energía renovable en CFE.* 15 de September de 2012. http://www.cfe.gob.mx/ConoceCFE/Desarrollo_Sustentable/energiarenovable/Paginas/EnergiarenovableenCFE.aspx (último acceso: 26 de September de 2014).

Crothers, Brooke. *"With Toyota in its rearview mirro, GM talks fuel-cell cars".* 28 de June de 2014. http://www.cnet.com/uk/news/with-toyota-in-its-rear-view-mirror-gm-talks-fuel-cell-car-technology/ (último acceso: 29 de September de 2014).

—. «Toyota to launch first hydrogen fuel-cell vehicle for about $70K.» *CNET.* 25 de June de 2014. http://www.cnet.com/news/toyota-to-launch-first-hydrogen-fuel-cell-vehicle-for-about-70k/ (último acceso: 29 de September de 2014).

Cunningham, J.M., M.A. Moore and D.J. Friedman. «Requirements for a Flexible and Realistic Air Supply Model for Incorporation into a Fuel Cell Vehicle (FCV) System Simulation.» *SAE Paper 1999-01-2912.* Society of Automotive Engineers, 1999.

Diesel Net. *European Stationary Cycle (ESC).* 2000. http://www.dieselnet.com/standards/cycles/esc.php (último acceso: 4 de November de 2012).

Dubin, Mark Wm. *How the Brain Works.* Malden, U.S.A.: Blackwell Science, 2002.

E. Y. Ng, P. W. Johnson and S. Watkins. «An Analytical Study on Heat Transfer Performance of Radiators with Non-Uniform Airflow Distribution.» *IMECHE Journal of Automotive Engineering* 219 Part D (August, 2005).

El Universal. *Montoya aseguró que Chávez regala la renta petrolera a otros países.* 15 de Agosto de 2012. http://www.eluniversal.com/nacional-y-politica/elecciones-2012/120815/montoya-aseguro-que-chavez-regala-la-renta-petrolera-a-otros-paises (último acceso: 25 de September de 2014).

Erdinc, O. and M. Uzunoglu. «Recent Trends in PEM Fuel Cell-powered hybrid systems: Investigation of application areas, design architectures and energy management approaches.» *Renewable and Sustainable Energy Reviews*, nº 14 (2010): 2874–2884.

Estados Unidos Mexicanos- Presidencia de la República. «LEY PARA EL APROVECHAMIENTO DE ENERGÍAS RENOVABLES Y EL FINANCIAMIENTO DE LA TRANSICIÓN ENERGÉTICA.» *Diario Oficial de la Federación.* Mexico City: Oficina de la Presidencia, 28 de November de 2008.

European Comission. «PRESS RELEASE - Fuel Cells and Hydrogen 2 Joint Undertaking (FCH 2 JU) under Horizon 2020: launch of activities and first calls.» *EU support for research on fuel cells and hydrogen.* 9 de July de 2014. http://www.fch-ju.eu/sites/default/files/Press%20Release%20FCH%202%20JU%20final.pdf (último acceso: 29 de September de 2014).

European Comission, Directorate-General for Research Cooperation | Energy. «"European funded research on Hydrogen and Fuel Cells: Review, Assessment, Future Outlook".» 2008.

Farshid Jafari Harandi, Vahid Khorani and Alireza Mohammad Shahri. «Modelling, Simulation and Implementation of a Quadrotor.» *RoboCup Iran 2010 Symposium.* Tehran, Iran, 2010.

Felix Moreno, R., Economou, J., and Knowles, K.,. «Energy Management System for Electrified Tactical Mobility Platforms.» *SAE World Congress and Exhibition.* Detroit. U.S.A.: Society of Automotive Engineers, 2014.

Felix Moreno, Rodrigo, John T. Economou and Prof. K. Knowles. «"Modelling and simulation of a fuel cell powered medium duty vehicle platform" .» *IMECHE Sustainable Vehicle Technologies: Driving the Green Agenda.* Gaydon, Warwickshire, U.K.: Institution of Mechanical Engineers, 2012.

Felix Moreno, Rodrigo, John T. Economou, Derek Bray and Prof. Kevin Knowles. «"Modelling and simulation of a fuel cell powered electric drivetrain for wide body passenger aircraft.".» *Proceedings of the Institution of Mechanical Engineers Part G Journal of Aerospace Engineering*, 2013.

Felix, R., Economou, J., and Knowles, K. «Control System for a PEM Fuel Cell Powered Heavy Duty Tactical Mobility Truck with Auxiliary Power Generation Capabilities.» *SAE Int. J. Alt. Power* 2, nº 3 (2013).

Filipi, Z., Louca, L., Stefanopoulou, A., Pukrushpan, J. et al.,. «Fuel Cell APU for Silent Watch and Mild Electrification of a Medium Tactical Truck,.» *SAE Technical Paper 2004-01-1477.* SAE, 2004.

Fraas, Arthur and M. Necati Ozisik. *Heat Exchanger Design.* John Wiley & Sons, 1965.

Gao, Dawei, Jin Zhenhua, and Lu Qingchun. «Energy management strategy based on fuzzy logic for a fuel cell hybrid bus.» *Journal of Power Sources* 185, nº 1 (2008): 311-317.

GBTimes. *Taliban destroys Nato fuel supply in Afghanistan .* 15 de July de 2014. http://gbtimes.com/world/taliban-destroys-nato-fuel-supply-afghanistan (último acceso: 29 de September de 2014).

Genta, Giancarlo. *Motor Vehicle Dynamics.* Singapore: World Scientific Publishing, 1997.

Gou, Bei. K. N. Woon and B. Diong. *Fuel Cells: Modeling, Control, and Applications.* CRC Press, 2010.

Government of Canada. «Fuel Cells and Hydrogen - Government Programs and Regulations.» 27 de November de 2013. http://www.nrcan.gc.ca/energy/alternative-fuels/fuel-facts/hydrogen-fuelcells/3569 (último acceso: 25 de September de 2014).

Green GT. *Green GT H2 Technical Data Sheet .* Le Mont-sur-Lausanne, Switzerland, 2012.

Greimel, Hans. «Toyota says cost of fuel cells will plunge by 2015.» Automotive News. 7 de March de 2011. http://www.autonews.com/apps/pbcs.dll/article?AID=/20110307/OEM06/303079980/1186 (último acceso: 24 de March de 2011).

Hua, Jianfeng, Lu Languang, Ouyang Minggao, Li Jianqiu, and Xu Liangfei. «Proton exchange membrane fuel cell system diagnosis based on the signed directed graph method.» *Journal of Power Sources* 196, nº 14 (2011): 5881-5888.

Hyundai Motor Company. *2015 Hyundai Tucson Fuel Cell Vehicle.* 2014. https://www.hyundaiusa.com/tucsonfuelcell (último acceso: 29 de September de 2014).

I. Zamora, San Martín, J.I., García, J., Asensio, F.J., Oñederra, O., San Martín, J.J., and Aperribay, V. «PEM Fuel Cells in Applications of Urban Public Transport.» *International Conference on Renewable Energies and Power Quality.* 2011.

IHS Jane's. *Military-Industrial Company BTR-90 (GAZ-5923) armoured personnel carrier.* 2014.

INFONAVIT. «Ahorro y Cuido el Medio Ambiente.» 23 de July de 2014. http://portal.infonavit.org.mx/wps/wcm/connect/infonavit/trabajadores/saber+para+decidir/cuido_mi_casa/ahorro+y+cuido+el+medio+ambiente (último acceso: 25 de September de 2014).

Instituto Nacional de Ecología. « "Inventario Nacional de Emisiones de México, 1999".» 2006.

Instituto Nacional de Estadística y Geografía. *Registro de Vehículos de Motor en Servicio.* 2009.

Just-Auto. «"GERMANY: Hydrogen Infrastructure Ready Says GM".» 7 de December de 2010. http://qube.just-auto.com/article/germany-hydrogen-infrastructure-ready-says-gm (último acceso: 7 de December de 2012).

—. «SOUTH KOREA: Government announces cash injection to boost green vehicles.» 7 de December de 2010. http://qube.just-auto.com/article/south-korea-government-announces-cash-injection-boost-green-vehicles (último acceso: 7 de December de 2012).

—. «SOUTH KOREA: Hyundai sets production date for fuel cell vehicle.» 21 de December de 2010. http://qube.just-auto.com/article/south-korea-hyundai-sets-production-date-fuel-cell-vehicle (último acceso: 7 de December de 2012).

Khalig, Alireza and Li Zhihao. «Battery, Ultracapacitor, Fuel Cell, and Hybrid Energy Storage Systems for Electric, Hybrid Electric, Fuel Cell, and Plug-In Hybrid Electric Vehicles: State of the Art.» *IEEE Transactions on Vehicular Technology* 59, nº 6 (2010).

KJ Magnetics. *KJ Magnetics.* s.f. http://www.kjmagnetics.com/ (último acceso: 5 de November de 2012).

Krishnan, R. *Permanent Magnet Synchronous and Brushless DC Motor Drives.* CRC Press, 2010.

M.A. Hannan, F.A. Azidin and A. Mohamed. «Multi-Sources Model and Control Algorithm of an Energy Management System for Light Electric Vehicles.» *Energy Conversion and Management.* 2012. 123-130.

Mamdani, E.H. «A fuzzy rule-based method of controlling dynamic processes.» *20th IEEE Conference on Decision and Control including the Symposium on Adaptive Processes.* 1981. 1098-1103.

Manoj Pudukudy, Zahira Yaakob, Masita Mohammad, Binitha Narayanan, Kamaruzzaman Sopian. «Renewable Hydrogen Economy in Asia – Opportunities and Challenges: An Overview.» *RenewableandSustainableEnergyReviews*, 2014: 743-757.

Martínez Martínez, Vicente. *Modelling of the Flight Dynamics of a Quadrotor Helicopter.* MSc. Thesis, Cranfield University, 2007.

McEachern, Sam. *General Motors Highlights Its Hydrogen Fuel Cell Technology And Clean Energy Patents.* 17 de June de 2014. http://gmauthority.com/blog/2014/06/general-motors-highlights-its-hydrogen-fuel-cell-technology-and-clean-energy-patents/ (último acceso: 29 de September de 2014).

MEGlobal. *Ethylene Glycol – Product Guide.* 2008.

Meier, Konrad. «Hydrogen production with sea water electrolysis using Norwegian.» *International Journal of Environmental Engineering*, May 2014.

Murphey, Yi Lu, Jungme Park, Leonidas Kiliaris, Ming L. Kuang, M. Abdul Masrur, Anthony Phillips and Qing Wang. «Intelligent Hybrid Vehicle Power Control - Part II: Online Intelligent Energy Management.» *IEEE Transactions on Vehicular Technology.* January 2013. 69-79.

Murphey, Yi Lu, Jungme Park, Zhihang Chen, Ming L. Kuang, M. Abdul Masrur and Anthony Phillips. «Intelligent Hybrid Vehicle Power Control - Part I: Machine Learning of Optimal Vehicle Power.» *IEEE Transactions on Vehicular Technology.* October 2012. 3519-3530.

Noticias 24. *Maduro critica que "la derecha" diga que Venezuela le regala petróleo a Cuba: "Lo que nos regalamos mutuamente es amor.* 10 de March de 2014. http://www.noticias24.com/venezuela/noticia/227151/maduro-critica-que-la-derecha-diga-que-venezuela-le-regala-petroleo-a-cuba-lo-que-nos-regalamos-mutuamente-es-amor/ (último acceso: 25 de September de 2014).

NSERC Hydrogen Canada. «NSERC Hydrogen Canada.» 2014. http://www.h2can.ca/ (último acceso: 25 de September de 2014).

Organisation for Economic Co-operation and Development. *Country Statistical Profiles 2010.* 2010.

Park, Jungme, Zhihang Chen, Leonidas Kiliaris, Ming L. Kuang, Abdul Masrur, Anthony Phillips and Yi Lu Murphey. «Intelligent Vehicle Power Control Based on Machine Learning of Optimal Control Parameters and Prediction of Road Type and Traffic Congestion.» *IEEE Transactions on Vehicular Technology.* November 2009. 4741-4756.

Pearl, Judea. *Probabilistic Reasoning in Intelligent Systems: Networks of Plausible Inference.* San Francisco, CA, U.S.A.: Morgan Kaufmann Publishers Inc., 1988.

Performance Trucks Website. *Performance Trucks Website.* s.f. http://m.performancetrucks.net (último acceso: 5 de November de 2012).

Petróleos Mexicanos. «"Indicadores Petroleros".» 2011.

Petroleos Mexicanos. «Indicadores Petroleros.» 2014.

Pillay, Praganasan and R. Krishnan. «Modelling of Permanent Magnet Motor Drives.» *IEEE Transactions On Industrial Electronics* 35, nº 4 (1988).

PressTV. *Taliban attack NATO fuel tankers in east Afghanistan.* 16 de September de 2014. http://www.presstv.ir/detail/2014/09/16/378927/nato-tankers-attacked-in-afghanistan/ (último acceso: 29 de September de 2014).

Pukrushpan, Jay T., Anna G. Stephanopoulou and Huei Peng. *Control of Fuel Cell Power Systems. Principles, Modeling, Analysis and Feedback Design.* Springer-Verlag, 2004.

Qi Li, Weirong Chen, Yankun Li, Shukui Liu, Jin Huang. «Energy Management Strategy for Fuel Cell/Battery/Ultracapacitor Hybrid Vehicle Based on Fuzzy Logic.» *International Journal of Electrical Power & Energy Systems 43. No 1.* 2012. 514-525.

REUTERS. *UK gas prices at four-month high on tight supply, Ukraine concerns.* 2 de September de 2014. http://uk.reuters.com/article/2014/09/02/uk-britain-gas-prices-idUKKBN0GX1B720140902 (último acceso: 24 de September de 2014).

Rose, Robert. «Fuel Cells: Civilian and Military Applications.» *Fuel Cells 2000.* 2 de May de 2008. http://www.fuelcells.org/uploads/rosemilitary.pdf (último acceso: 29 de September de 2014).

RT. *Taliban attack leaves 37 burned-out NATO fuel trucks in Afghanistan.* 19 de June de 2014. http://rt.com/news/167016-nato-convoy-attacked-afghanistan/ (último acceso: 29 de September de 2014).

Smith, Martin. *Clearing the air about the hydrogen economy.* 26 de September de 2013. http://www.rsc.org/chemistryworld/2013/09/hydrogen-economy-fuel-cell-energy (último acceso: 25 de September de 2014).

Spiegel, Colleen. *PEM Fuel Cell Modeling and Simulation Using Matlab.* London: Academic Press, 2008.

Strategic Defence Intelligence. *Russia develops and tests Krymsk robotic armoured personnel carrier.* 31 de July de 2013. http://www.strategicdefenceintelligence.com/article/5nHXweGEzo/2013/07/31/russia_develops_and_tests_krymsk_robotic_armoured_personnel_/ (último acceso: 29 de September de 2014).

Tamor, Michael. «Simplified Fuel Cell System Modelling.» Ford Motor Company, Dearborn, Michigan, 1997.

The Guardian. «UK renewable energy subsidies capped at £200m a year.» 24 de July de 2014. http://www.theguardian.com/environment/2014/jul/24/uk-renewable-energy-subsidies-capped-at-200m-a-year (último acceso: 25 de September de 2014).

—. *Ukraine tensions driving up UK fuel prices.* 29 de Abril de 2014. http://www.theguardian.com/money/2014/apr/29/uk-fuel-prices-rise-as-ukraine-tensions-continue (último acceso: 24 de September de 2014).

Thompson, Maj. David. *Convoy Security Shortfalls.* Monograph, Fort Leavenworth: School of Advanced Military Studies, 2012.

Tremblay, O., Dessaint, L.-A. «Experimental Validation of a Battery Dynamic Model for EV Applications.» *World Electric Vehicle Journal* 3 (May, 2009).

U.S. Energy Information Administration. *Gasoline and Diesel Fuel Update.* 22 de September de 2014. http://www.eia.gov/petroleum/gasdiesel/ (último acceso: 24 de September de 2014).

—. «Japan.» 31 de July de 2014. http://www.eia.gov/countries/cab.cfm?fips=ja (último acceso: 25 de September de 2014).

—. «South Korea.» 1 de April de 2014. http://www.eia.gov/countries/cab.cfm?fips=KS (último acceso: 25 de September de 2014).

—. «Venezuela.» June de 2014. http://www.eia.gov/countries/cab.cfm?fips=ve (último acceso: 25 de September de 2014).

U.S. Environmental Protection Agency. « "Inventory of U.S. greenhouse gas emissions and sinks: 1990 – 2009".» 2011.

U.S.A. Government. «Title 40, Chapter I, Subchapter C, Part 86 .» *Code of Federal Regulations.* Vols. Title 40, Part 86. 1333. U.S.A. Government, 26 de September de 2014.

USA Today. «Ethanol pumping up food prices.» 14 de February de 2011. http://usatoday30.usatoday.com/money/industries/food/2011-02-09-corn-low_N.htm (último acceso: 25 de September de 2014).

Veziroglu, Ayfer and Rosario Macario. «Fuel cell vehicles: State of the art with economic and environmental concerns.» *International Journal of Hydrogen Energy*, nº 36 (2011): 25-43.

Weisberg, Sanford. *Applied Linear Regression.* New York: John Wiley & Sons, 1985.

Wissam Dib, Alexandre Chasse, Philippe Moulin, Antonio Sciarretta and Gilles Corde. «Optimal Energy Management for an Electric Vehicle in Eco-Driving Applications.» *Control Engineering Practice.* 2014. 298-307.

Wong, Jo Yung. *Theory of ground vehicles.* John Wiley & Sons, 2001.

World Energy Council. *World Energy Resources: 2013 Survey.* London: World Energy Council, 2013.

Yu, Hai, Finn Tseng and Ryan McGee. «Driving Pattern Identification for EV Range Estimation.» *Electric Vehicle Conference (IEVC), 2012 IEEE International.* IEEE, 2012.

Zhang, Chen and Ardalan Vahidi. «Route Preview in Energy Management of Plug-in Hybrid Vehicles.» *IEEE Transactions on Control Systems Technology.* March 2012.

APPENDICES

Appendix A Permanent Magnet Synchronous Machine Model

One of the main electrical machine options for electrical powertrains, the Permanent Magnet Synchronous Machine (PMSM) can be designed for compact build and high power density (Krishnan 2010), (I. Zamora 2011). The results obtained from the first simulations have indicated this technology to be a good option either as a standalone high torque machine or as part of a combined drive package together with an induction machine (Felix Moreno 2012). In the latter option the PMSM is of a reduced torque capacity intended for torque boosting when the main induction machine is not enough to meet the required torque command.

The following sections will describe the equations used to describe the motor model employed within the numerical simulations scenarios discussed in Chapter 7. The basic model will only be modified in its parameters to meet the different requirements of each one of the different powertrain architectures under analysis.

A.1 Permanent Magnet

At the core of the Permanent Magnet Synchronous Machine (PMSM) lies the permanent magnet (PM). The characteristics of this component (demagnetization, energy flux, material, etc.) will define the behaviour and performance of the machine and vehicle as a whole. The first part of the model is based on the equations and principles discussed by R. Krishnan in Chapter 1 of (Krishnan 2010).

As described in (Krishnan 2010) the magnets in these machines are made of specific materials which retain magnetism. Each individual one is described by the two components of its magnetic flux density. Firstly, intrinsic flux density, B_i, is determined by the specific characteristics of the material when in an applied field during magnetization. Secondly, the flux component due to excitation, B_h, is proportional to the magnetic field intensity, H, to which the magnet is subjected. This latter component is relatively small when compared against B_i. Finally, the total flux density in the magnet is given by

$$B_m = B_i + B_h \qquad [T] \qquad \textbf{A-1}$$

Figure 5-1 shows the flux density for the magnets used on the model. The magnet is based on a Neodymium magnet. The line in the plot details the demagnetization characteristics of the material. B_r is the remnant flux density, in layman terms is the magnetism level to which the magnet returns after the excitation field of the coils is removed. H_c is the coercive force required to bring the normal flux density to zero. The magnet in this model is assumed to be of Neodymium N-52, which has good magnetism recovery after the stator field is removed. Lower grade materials like Alnico-5 return to a considerably lower B_r when the field is removed resulting a degradation of the machine´s performance.
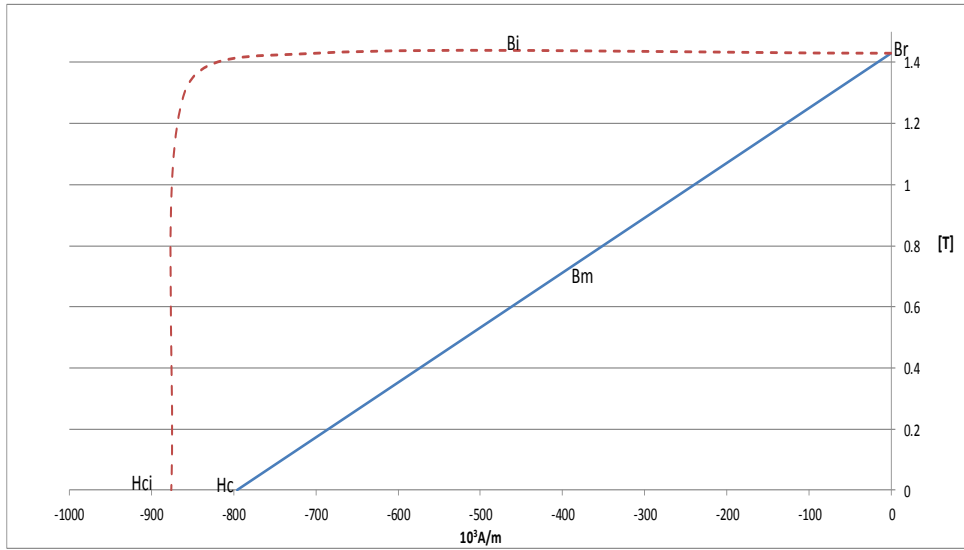
Figure A-1 Neodymium N52 Magnetic Flux Densities [ndfeb website]

To obtain the desired 1000 Nm+ torque the model considered a vertical stack of 2 magnets per pole, based on the N52. This was motivated by initial simulation results which showed that one magnet would result in constant operation near the magnetization region (B_m < 0.0). In this manner B_r it is assumed would increase from 1.43 T to 2.0 T. The remnant flux density does not increase linearly (B_r x 2) as the field of each underlying magnet would have to travel through the other members of the stack. For an approximate figure to be calculated a loss factor of 21% (KJ Magnetics s.f.) was considered per magnet layer in the stack (i.e. the field of the magnet at the bottom would be losing 21% flux intensity by the time it reached the top of the stack).

Once the magnet has been defined, the next step is to calculate the operating point on the B_m line. The first step is to calculate the "no load" flux line. This will give the operating point when no external field is being applied.

$$B_o = \frac{B_r}{1 + \mu_{rm} \dfrac{l_g}{l_m} \dfrac{A_m}{A_g} \dfrac{1}{k}} \qquad [T] \qquad \textbf{A-2}$$

Where:

B_o is the "no load" flux density, in [T],

μ_{rm} is the relative permeability of the magnet,

l_g and lm are the air and magnet gaps, in [A]

A_m and A_g are the magnet and air gap cross sectional areas, in [m^2]

k is the inverse leakage factor.

Figure A-2 shows the normal flux density and no load lines for the combined two magnets stack.
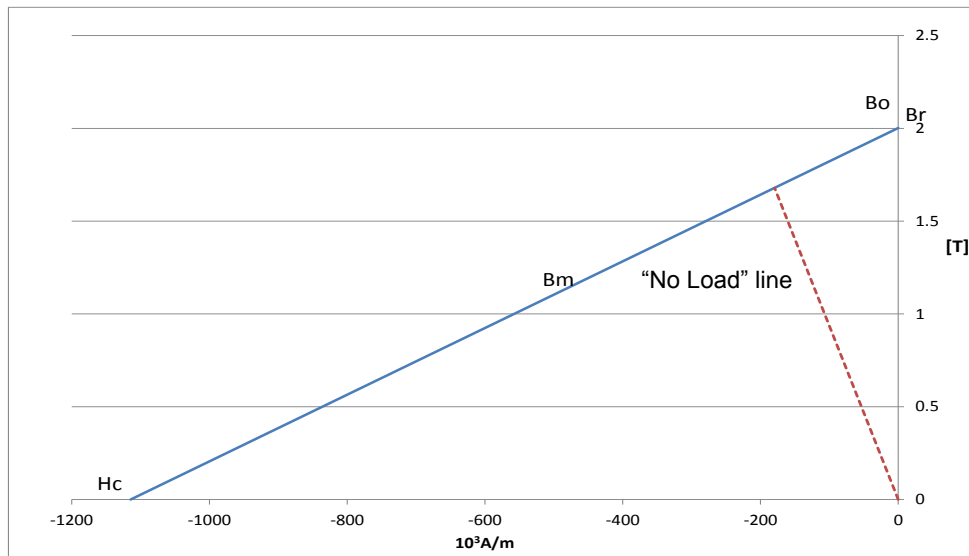
Figure A-2 Magnets Stack Flux Density with "no load" line for model´s specific motor

For this simulation, the specific geometry and magnet configuration determines the $\boldsymbol{B_o}$ point and the "no load line". The magnet would then always operate left of this line.

Now the operating B_m point can be computed using Equation A-3

$$B_m = \frac{1}{1 + \mu_{rm}\frac{lg}{lm}\frac{Am}{Ag}\frac{1}{k}}[B_r + \mu_o\mu_{rm}\frac{T_{ph}I}{l_m}] \qquad \text{[T]} \qquad \textbf{A-3}$$

New terms introduced in this equation are:

μ_o, permeability of air,

T_{ph}, Conductor wire turns per phase, and

I, Stator phase current, in [A].

The significance of the rightmost term of Equation A-3 arises also from the motor's characteristics and operating conditions.

$$F_e = T_{ph}I \qquad \text{[AT]} \qquad \textbf{A-4}$$

$$H_e = \frac{F_e}{l_m} \qquad \text{[A/m]} \qquad \textbf{A-5}$$

F_e is the external source mmf, AT.

H_e is external field intensity, A/m.

So far the magnet and its operating point have been defined in terms of the simulated motor´s design and operating conditions.

A.2 Electromagnetic Power

To determine the operating point of the magnet and hence the required operating phase current for the stator, consider Equation A-6.

$$P_a = \frac{3}{2} E_m I_m \sin \delta \qquad \text{[W]} \qquad \textbf{A-6}$$

Where:

P_a is the air gap power, in [W]

E_m is peak-induced emf, in [V]

I_m is the peak phase current, in [A]

δ is the torque angle, in [rad]

In this formula it is apparent how the power of the machine is directly proportional to current flow, and that by altering the torque angle (the angle through which the stator current leads the rotor flux) the output of the machine can be controlled. This will prove important further on when power and emf are discussed.

A.3 Electromotive Force (EMF)

The thickness of the magnet (also referred to as magnet length, $\boldsymbol{l_m}$), its arc and operating $\boldsymbol{B_m}$ are motor specific components that not only set every design apart from all the others, but also directly affect the power capability of the machine through the peak-induced emf.

Consider the following chain of equations. Firstly, assuming that the peak fundamental flux in the machine is produced by the magnet,

$$\emptyset_{ml} = \frac{B_{ml}DL}{\left(\frac{P}{2}\right)} \qquad\qquad \text{[Wb]} \qquad \textbf{A-7}$$

D is the inner stator diameter, in [m]

L is the stator lamination stack length, in [m], and

P is the number of poles.

$\boldsymbol{B_{ml}}$ is the peak of the fundamental magnet flux density, in T, computed from

$$B_{ml} = \frac{4}{\pi} B_m \sin\beta \qquad\qquad \text{[T]} \qquad \textbf{A-8}$$

β is the half the magnet arc, in rad/s

From Equations A-7 and A-8 it is clear how the peak flux density depends on the construction of the machine and magnet arrangements. Equation A-7 shows that care should be taken when deciding how many poles the machine will have as the peak fundamental flux will be adversely affected.

The computation of the peak induced emf takes all these machine design dependant parameters directly into account, allowing for an analysis of the effects that a given change on a specific part of the motor will have in the overall behaviour of the system. Peak induced emf is given by

$$E_m = 2\pi f_s (T_{ph} k_w) \emptyset_{ml} \qquad\qquad \text{[V]} \qquad \textbf{A-9}$$

f_s is the stator supply frequency, in Hertz.

k_w is the fundamental winding factor.

The winding factor, $\boldsymbol{k_w}$, considers the different possible construction variations of the rotor and stator.

$$k_w = k_d k_p k_{sk} \qquad\qquad \textbf{A-10}$$

$\boldsymbol{K_d}$, distribution factor, results from the way each phase winding is distributed under one pole. $\boldsymbol{K_p}$, pitch factor, results from the angle of separation between wire conductors in a given phase. $\boldsymbol{K_{sk}}$, skewing factor, comes from the way stator laminations are skewed by a given angle from one end of the machine to the other. For the case of this simulation work the final $\boldsymbol{k_w}$ factor is taken to be 0.9.

A.4 Electromagnetic Torque

At this point, all necessary equations required to calculate the power output of the machine, in terms of its design and construction, have been defined. Yet one final equation must be introduced to establish a relationship between torque and machine speed. PMSMs are synchronous machines therefore do not rely on slip as induction machines do, so the specific speed of the machine is directly proportional to the frequency of the stator electrical supply as shown in Equation A-11.

$$f_s = \frac{PN_{sp}}{120} \qquad \text{[Hz]} \qquad \textbf{A-11}$$

N_{sp} is the speed in revolutions per minute.

An important fact in this equation is the contradictory effect which the number of poles in the machine exerts on its performance. As shown in Equation A-7 a higher number of poles will have a negative effect on the peak fundamental flux, reducing air gap power, while a higher number of them are required to reach higher speeds. This is the main driving factor for the utilization of a 2 magnets stack as a single magnet did not provide the necessary flux to reach the required speeds whilst producing the necessary torque for the simulated vehicle platform. Finally, electromagnetic torque is described by

$$T_e = \frac{P_a}{\omega_m} \qquad \text{[Nm]} \qquad \textbf{A-12}$$

where ω_m is the mechanical speed in [rad/s.]

A.5 Three-phase currents

Once all equations for the elements on the right-hand side of Equation A-6 have been defined, it can then be solved for I_m, which is the peak phase current. The computed value is used in Equations A-13 through A-15 to determine the direct and quadrature axis currents. The following sections are based on what is discussed in Chapters 3 and 4 of (Krishnan 2010).

$$i_{as} = i_s \sin(\omega_r t + \delta)$$ [A] **A-13**

$$i_{bs} = i_s \sin(\omega_r t + \delta - \frac{2\pi}{3})$$ [A] **A-14**

$$i_{cs} = i_s \sin(\omega_r t + \delta + \frac{2\pi}{3})$$ [A] **A-15**

i_s is the source current, or $\frac{I_m}{\sqrt{2}}$, in [A],

ω_r is the rotor´s electrical speed, or $\omega_m * P_p$, in [rad/s].

i_{as}, i_{bs} and i_{cs} are the three phase currents (a,b and c) in the stator windings, hence the "s" subscript.

A.6 Direct and Quadrature Axis

A very common tool used in modelling and understanding PMSM machines is the two axis system known as DQ-axes reference frame. The name comes from the direct and quadrature axes faced by the flux field as the rotor moves. The direct axis is defined as the axis of field flow when a stator winding is facing a rotor magnet. On the other hand, quadrature axis is the case when the winding is facing the iron core of the rotor. By using this system the observer is "placed" on the rotor so instead of solving a problem where the system is rotating the equations are transformed, through Park´s transform, into a stationary or DC problem. To this end consider Equation A-16.

$$\begin{bmatrix} i_{qs}^r \\ i_{ds}^r \\ i_0 \end{bmatrix} = \frac{2}{3} \begin{bmatrix} \cos\theta_r & \cos\left(\theta_r - \frac{2\pi}{3}\right) & \cos\left(\theta_r + \frac{2\pi}{3}\right) \\ \sin\theta_r & \sin\left(\theta_r - \frac{2\pi}{3}\right) & \sin\left(\theta_r + \frac{2\pi}{3}\right) \\ \frac{1}{2} & \frac{1}{2} & \frac{1}{2} \end{bmatrix} \begin{bmatrix} i_{as} \\ i_{bs} \\ i_{cs} \end{bmatrix}$$ [A] **A-16**

i_{qs}^r and i_{ds}^r are the stator d- and q- axes currents in the rotor´s reference frame. i_0 represents any imbalance in the three-phase currents. If the currents are balanced ($i_{as}+i_{bs}+i_{cs} = 0$) i_0 will be zero. θ_r is the rotor position, in [rad].

A.7 d and q-Axes Inductances

To correctly employ the two phase conversion each rotor axis must have an inductance that matches the stator windings on the given axis. By combining the expressions for calculating the corresponding flux, flux density, mmf and cross-section per pole the individual two-phase system inductances can be computed.

$$L_d = 1.125\pi\mu_o \left(\frac{T_{ph}}{P}\right)^2 \frac{DL}{g_d} \qquad \text{[H]} \qquad \textbf{A-17}$$

$$L_q = 1.125\pi\mu_o \left(\frac{T_{ph}}{P}\right)^2 \frac{DL}{l_g} \qquad \text{[H]} \qquad \textbf{A-18}$$

L_d and L_q are the respective axis inductances and the expressions to obtain them are practically identical. The key difference resides on the effective air gaps, g_d and g_q. In the case of the direct axis the effective air gap comes from another equation, not mentioned in this report, which considers the influence of the tooth and slot widths of the stator core. The quadrature axis effective air gap is considered to be equal to the machine air gap as the axis by definition does not include the magnet; the substitution has already been made in Equation A-18.

A.8 Resistive Losses

Every time current is carried by a conductor there will be associated losses due to the specific resistivity of the material from which the windings are made of. In the case of PMSMs this losses are computed from the number of turns per phase, T_{ph}, the specific characteristics of the material and average conductor length l_c.

$$R_s = \rho \frac{l_c}{a_c} (2T_{ph}) \qquad [\Omega] \qquad \textbf{A-19}$$

ρ is the resistivity of the material, in [Ωm],

l_c is the average length of a stator phase conductor or half of a winding turn, in [m],

a_c is the cross sectional area of the armature conductors, in [m^2].

The power lost to the machine´s winding, for a three phase machine, is easily computed using the rms phase current.

$$P_{sc} = 3I_s^2 R_s \qquad [W] \qquad \textbf{A-20}$$

A.9 d- and q-axes Voltage

The final steps to complete the model are to find out the operating voltages of the machine itself. Firstly, since the equations to determine the d- and q-currents have already been defined consider the following expression, using the

dynamic motor model described in Chapter 3 of (Krishnan 2010) and the model described in (Pillay 1988).

$$v_{qs}^r = i_{qs}^r(t)R_s + L_q\frac{di_{qs}^r(t)}{dt} + L_d\omega_r i_{ds}^r(t) + \omega_r\lambda_{af} \qquad \text{[V]} \qquad \text{A-21}$$

$$v_{ds}^r = i_{ds}^r(t)R_s + L_d\frac{di_{ds}^r(t)}{dt} - L_q\omega_r i_{qs}^r(t) \qquad \text{[V]} \qquad \text{A-22}$$

The only new term in these equations is λ_{af}, the armature flux linkage created by rotor magnets, in [V-s]. This parameter is obtained from Equation A-23

$$\lambda_{af} = \frac{T_e}{\frac{3}{2}\frac{P}{2}i_{qs}^r} - (L_d - L_q)i_{ds}^r \qquad \text{[V-s]} \qquad \text{A-23}$$

A.10 Three-phase Voltages and Stator Peak Voltage

Using the inverse Park transform the phase voltages can be determined.

$$\begin{bmatrix} v_{as} \\ v_{bs} \\ v_{cs} \end{bmatrix} = \begin{bmatrix} \cos(\theta_r) & \sin(\theta_r) & 1 \\ \cos\left(\theta_r - \frac{2\pi}{3}\right) & \sin\left(\theta_r - \frac{2\pi}{3}\right) & 1 \\ \cos\left(\theta_r + \frac{2\pi}{3}\right) & \sin\left(\theta_r + \frac{2\pi}{3}\right) & 1 \end{bmatrix} \begin{bmatrix} v_{qs}^r \\ v_{ds}^r \\ v_0 \end{bmatrix} \qquad \text{[V]} \qquad \text{A-24}$$

Lastly, to obtain the peak DC-Link supply voltage at the stator windings the rotor reference frame d-q voltages must be transformed into their stator counter parts. This is done by applying the following inverse transformation; please note that the stator voltages do not carry the "r" superscript.

$$\begin{bmatrix} v_{qs}^r \\ v_{ds}^r \end{bmatrix} = \begin{bmatrix} \cos(\omega_r t) & -\sin(\omega_r t) \\ \sin(\omega_r t) & \cos(\omega_r t) \end{bmatrix} \begin{bmatrix} V_m \sin(\omega_r t + \delta) \\ V_m \sin(\omega_r t + \delta) \end{bmatrix}$$

$$= \begin{bmatrix} V_m \sin(\delta) \\ V_m \cos(\delta) \end{bmatrix} \qquad \text{[V]} \qquad \textbf{A-25}$$

V_m is the peak stator voltage for the sinusoid supply. In the present simulation the motor is operating with a constant torque angle of 90°, the result of which is a direct axis current of approximately zero amperes. Because of the previous facts the peak supply voltage is computed from the quadrature axis equation.

$$V_m = \frac{v_{qs}^r}{\sin(\delta)} \qquad \text{[V]} \qquad \textbf{A-26}$$

A.11 Torque Vs. Speed Curve

At this point the model includes the necessary equations to describe the machine in enough detail while providing an estimate of its torque generation capabilities. For the calculation of the break torque, some additional mechanical losses must be taken into account.

$$T_e = T_{load} + J\frac{d\omega_m}{dt} + B\omega_r \qquad \text{[Nm]} \qquad \textbf{A-27}$$

J is the load and machine combined moment of inertia, in [kg/m^2]

B is the friction coefficient of the load of the machine,

T_{load} is the desired torque that the machine must supply, in [Nm].

Electromagnetic torque is externally limited to protect the machine and power system, per the curve below. This limited torque, T_{lim}, is later used for the vehicle dynamic calculations.
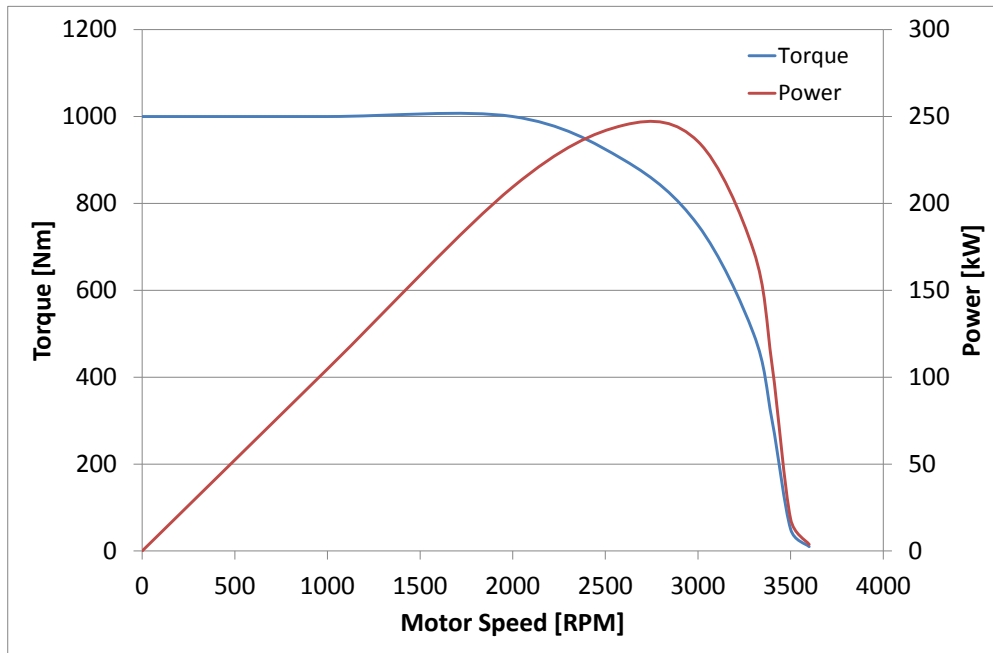
Figure A-3 Permanent Magnet Synchronous Machine Torque Curve

Appendix B Cooling System

All devices modelled to be equipped on the vehicle are inherently inefficient. This fact means that a portion of the electrical power provided by hydrogen fuel will be lost mainly as heat. In the case of the electrical bus DC-DC converters a flat 9.0% inefficiency is considered during any power transfer. For simplicity, heat generated from the electrical machines is only considered to come from electrical conduction losses, P_{sc}, whereas heat generated from the hydrogen chemical reaction is detailed in the following sections.

The cooling system is composed two cooling loops as detailed in Figure B-1.
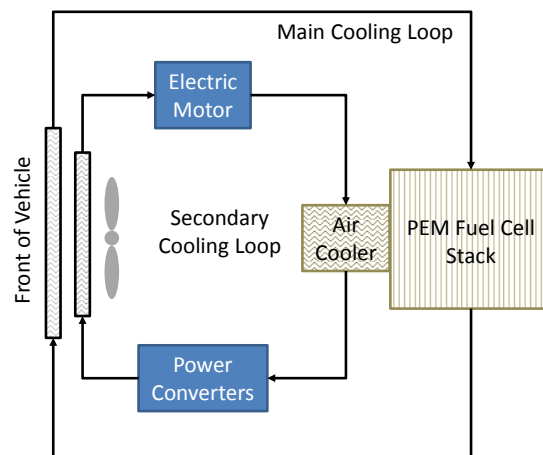
Figure B-1 Simplified Diagram of the Cooling System

B.1 Fuel Cell Stack Heat Management

Due to the lack of manufacturer data regarding the construction and operation of the internal cooling system for a fuel cell stack, the best approach was deemed to be as proposed by (Gou 2010).

$$\dot{Q}_{stack} = C_t \frac{dT_s}{dt} = P_{tot} - P_{elec} - \dot{Q}_{cool} - \dot{Q}_{loss} \quad \text{[J/s]} \qquad \textbf{B-1}$$

Where

$\dot{Q}_{stack}$ is the rate of heat absorption by the stack, in [J/s],

C_t is the thermal capacitance, in [J/°C],

P_{tot} is the total power released by the anode chemical reaction, in [W],

P_{elec} is the power consumed by the electrical load, in [W],

$\dot{Q}_{cool}$ is the flow rate of heat being removed by the cooling system, in [J/s],

$\dot{Q}_{loss}$ is the flow rate of heat lost through the stack´s surface, in [J/s].

Each component of equation B-2 can be quickly determined.

$$P_{tot} = \frac{N_{cell} I_{fc}}{2F} \Delta H \qquad\qquad \text{[W]} \qquad \textbf{B-2}$$

Where

ΔH is the enthalpy of combustion for hydrogen equal to 285.5 kJ/mol,

N_{cell} is the number of fuel cells in the stack,

I_{fc} is the stack current, in [A],

F is Faraday´s constant [96,485 C/mol].

Both cooling loops are considered to use a mixture of Water and Ethylene–Glycol (WEG) at 50% concentration. As mentioned before, in absence of detailed manufacturer information a simplified way of calculating the rate of coolant heat removal is given by first principles

$$\dot{Q}_{cool} = \dot{m}_{WEG} c_p \Delta T_s \qquad \text{[J/s]} \qquad \textbf{B-3}$$

Where

$\dot{m}_{WEG}$ is the mass flow rate of coolant fluid, in [kg/s],

c_p is the specific heat capacity of water, in [J/kg.K],

ΔT_s is the temperature delta across the heat exchanger, in [°K].

The heat loss through the stack´s surface is given by the following equation

$$Q_{loss} = hA_{stack}(T_s - T_{amb}) = \frac{T_s - T_{amb}}{R_t} \qquad \text{[J/s]} \qquad \textbf{B-4}$$

Where

hA_{stack} is the heat transfer coefficient, in [W/°K],

T_s is the stack temperature, in [°K],

T_{amb} is the ambient temperature, in [°K], and

R_t the thermal resistance of the stack, given in [°K/W]

Finally, P_{elec} is simply calculated by the product of stack voltage and current.

B.2 Base Radiator Model

Probably the most important component of each cooling loop is the radiator. In this case both radiators are cross flow, forced convection, water-to-air radiators with both fluids unmixed. Each takes the hot fluid coming from the components connected downstream and cools it to a set temperature in order to keep the system from thermal failure.

The following sections will describe the system of equations necessary to model a radiator as the one mentioned above. It will initially rely on (E. Y. Ng August, 2005) for the geometric equations and for some of the criteria used to calculate the heat transfer coefficients, but then will use well known thermodynamic equations (Fraas 1965) to calculate the outlet temperatures of the fluids.

B.3 Radiator Geometry

Applying the same method explained in (E. Y. Ng August, 2005) to determine heat transfer and fluid flow areas the radiator can be defined by the following parameters:

Core height, B_h in [m],

Core width, B_w in [m],

Core thickness, B_t in [m],

Number of coolant tube rows in the core thickness direction, N_r,

Number of coolant tubes per row, N_{ct},

Number of fin profiles on the core height direction, N_p,

Number of fins per metre in the core width direction, N_f,

Louvre pitch, L_p in [m],

Louvre length, L_l in [m],

Fin thickness, F_t in [m],

Fin height, F_h in [m],

Fin pitch, F_p in [m],

Fin end radius, R_f in [m],

Angle of fin, α_f in [deg],

Coolant tube length, Y_l in [m],

Coolant tube cross-section length, Y_{cl} in [m],

Coolant tube cross-section width, Y_{cw} in [m],

Coolant tube thickness, Y_t in [m],

Coolant tube pitch, Y_p in [m],

Coolant tube end radius, R_t in [m].

The equations to calculate the different heat transfer areas (E. Y. Ng August, 2005) are as follows:

Fin length, F_l,

$$F_l = \pi R_f + \frac{F_h - 2R_f}{\cos \alpha_r} \qquad \text{[m]} \qquad \textbf{B-5}$$

Radiator core frontal area, $A_{fr,r}$

$$A_{fr,r} = B_h B_w \qquad [\text{m}^2] \qquad \textbf{B-6}$$

Frontal area of coolant tubes, $A_{fr,t}$

$$A_{fr,t} = Y_{cl} Y_l N_{ct} \qquad [\text{m}^2] \qquad \textbf{B-7}$$

Total fin frontal heat transfer area, $A_{fr,f}$

$$A_{fr,f} = F_t F_l (N_f Y_l) N_p \qquad [\text{m}^2] \qquad \textbf{B-8}$$

Total Fin Heat Transfer Area, A_f

$$A_f = 2 B_t F_l (N_f Y_l) N_p \qquad [\text{m}^2] \qquad \textbf{B-9}$$

Total heat transfer area, air side, A_a

$$A_a = A_f + 2 N_{ct} Y_l N_r [(Y_{cl} - 2R_t) + (2\pi R_t)] \qquad [\text{m}^2] \qquad \textbf{B-10}$$

Total heat transfer area on coolant side, A_c

$$A_c = [2\pi (R_t - Y_t) + 2(Y_{cl} - 2R_t)] Y_l N_{ct} N_r \qquad [\text{m}^2] \qquad \textbf{B-11}$$

Total air pass area, $A_{p,a}$

$$A_{p,a} = A_{fr,r} - A_{fr,f} - A_{fr,t} \qquad [m^2] \qquad \textbf{B-12}$$

Total coolant pass area, $A_{p,c}$

$$A_{p,c} = [\pi(R_t - Y_t)^2 + (Y_{cw} - 2Y_t)(Y_{cl} - 2R_t)]N_{ct}N_r \qquad [m^2] \qquad \textbf{B-13}$$

B.4 Radiator Air Heat Transfer Coefficient

From (E. Y. Ng August, 2005) the Colburn modulus can be estimated for louvered fin surfaces with at Reynold´s number between 100 and 4000.

$$j = 0.249 Re^{-0.42} L_h^{0.33} \left(\frac{L_l}{F_h}\right)^{1.1} F_h^{0.26} \qquad \textbf{B-14}$$

The previous holds true for Louvre form ratios of $0.62 < \left(\frac{L_l}{F_h}\right) < 0.93$.

Before the transfer coefficient can be estimated a number of parameters need to be established; first the characteristics of the inlet air need to be determined.

Density:

$$\rho = \frac{MP}{RT} \qquad [kg/m^3] \qquad \textbf{B-15}$$

Where

M is the molar mass of dry air, in [kg/mol],

P is the ambient pressure, in [Pa],

R is the ideal gas constant (8.3144621 [J/(mol.°K)]), and

T is the ambient temperature, in [°K].

Dynamic Viscosity:

$$\mu = \mu_o \frac{T_o + C}{T + C} \left(\frac{T}{T_o}\right)^{\frac{3}{2}}$$ [Pa.s] **B-16**

Where

μ_o is the reference viscosity, in [Pa.s]

T_o is the reference temperature, in [°K]

C is Sutherland´s constant for gaseous materials, C_{air} = 120 [°K].

For a cross flow heat exchanger the air heat transfer coefficient can be estimated using the following equation:

$$j = StPr^{\frac{2}{3}}$$ **B-17**

Where

St is Stanton´s number, and

Pr is Prandtl number.

These coefficients are given by

$$Pr = \frac{\mu c_p}{K} \qquad \text{B-18}$$

Where µ is the dynamic viscosity of air, c_p is the specific heat capacity of the fluid [J/(kg.ºK)] and K is the thermal conductivity [W/(m.ºK)]. For gases this coefficient should have a value between 0.7 and 1.0.

$$St = \frac{h_a}{G c_p} \qquad \text{B-19}$$

G is the maximum mass flow rate flux [kg/(s.m^2)] and h_a is the convection heat transfer coefficient of air [W/(m^2.ºK)].

$$G = \frac{\dot{m}_a}{A_c} \qquad \text{B-20}$$

A_c is the smallest cross-sectional area of the air passage [m²] and $\dot{m}_a$ is the mass flow of air [kg/s]. With the previous result now Reynold´s number can be computed.

$$Re = \frac{D_h G}{\mu} \qquad \qquad \textbf{B-21}$$

D_h is the hydraulic diameter of the air passage given by

$$D_h = \frac{\sin(2\alpha_f) F_l{}^2}{2} \qquad \qquad \text{[m]} \qquad \textbf{B-22}$$

Substituting Equation B-21 in B-14, using the result together with Equations B-13 through B-16 and B-18 through B-22 into B-17 and solving for h_a gives the equation for the convective heat transfer coefficient.

$$h_a = jGc_p Pr^{0.64} \qquad \qquad \text{[W/(m².°K)]} \qquad \textbf{B-23}$$

B.5 Radiator Coolant Heat Transfer Coefficient

A similar process to what was followed for the air side convective heat transfer coefficient can be followed for the coolant side. Firstly, per (E. Y. Ng August, 2005), consider the following set of equations to calculate Nusselt´s number depending on the coolant´s flow regime. All parameters with a "c" subscript refer to coolant flow conditions.

Laminar flow (2,300 > Re_c)

$$Nu = 3.66 + \frac{0.0668 \left(\frac{D_{h,c}}{Y_l}\right) Re_c Pr_c}{1 + 0.04 \left[\left(\frac{D_{h,c}}{Y_l}\right) Re_c Pr_c\right]^{\frac{2}{3}}}$$ **B-24**

Transition flow (10,000 >= Re_c >= 2,300)

$$Nu = \frac{\left(\frac{f}{8}\right)(Re_c - 1000)Pr_c}{1 + 12.7^2 \sqrt{\frac{f}{8}} \left(Pr_c^{\frac{2}{3}} - 1\right)}$$ **B-25**

Turbulent flow (Re_c > 10,000)

$$Nu = \frac{\left(\frac{f}{8}\right) Re_c Pr_c}{1.07 + 12.7^2 \sqrt{\frac{f}{8}} \left(Pr_c^{\frac{2}{3}} - 1\right)}$$ **B-26**

Where f is friction factor for isothermal flows inside smooth tubes given by

$$f = [0.79 \ln(Re_c) - 1.64]^{-2}$$ **B-27**

and $D_{h,c}$ is the hydraulic diameter of the coolant pipes in the radiator core.

$$D_{h,c} = D_e = \frac{4\pi r^2}{2\pi r}$$ [m] **B-28**

D_e is the equivalent diameter for an elliptical pipe, such as the ones considered in this model for the core.

$$D_e = 1.55 \frac{A^{0.625}}{P^{0.2}}$$ [m] **B-29**

A is the pipe cross-section and P is the wetted perimeter.

$$A = \frac{\pi(Y_{cw} - 2Y_t)(Y_{cl} - 2Y_t)}{4}$$ [m^2] **B-30**

$$P = 2\pi \left(\frac{1}{2} \left(\left(\frac{(Y_{cw} - 2Y_t)}{2} \right)^2 + \left(\frac{(Y_{cl} - 2Y_t)}{2} \right)^2 \right) \right)^2$$ [m] **B-31**

Re_c is calculated using Equation B-21, but using the applicable data for the coolant (G_c, $D_{h,c}$ and μ_c). In order to calculate the heat transfer coefficient for the coolant side, consider the following equation

$$Nu = \frac{h_c D_{h,c}}{K_c}$$ **B-32**

Where K is the thermal conductivity [W/(m.°K)] of WEG at 50% concentration. This parameter can be estimated using a manufacturer provided curve fit equations based on test data (MEGlobal 2008).

$$K_f = 0.23951 + 8.9758 \times 10^{-5}T - 1.3975 \times 10^{-6}T^2 \qquad \textbf{B-33}$$

$$K_c = K_f \times 1.7307 \qquad\qquad [W/(m.°K)] \qquad \textbf{B-34}$$

T is the coolant temperature in °C. The last piece of data required for the calculation is the Prandtl number, Pr_c. This is done using Equation B-18, but using coolant data as inputs (c_{pc}, K_c, μ_c). The heat transfer coefficient is then obtained by solving Equation B-32 for h_c.

B.6 Exit Temperature Estimation

To obtain the heat transferred between coolant and air through the radiator the ε-NTU method was employed. Since the model is a numerical engine, utilizing LMTD was not suitable as many drive cycles include idle running phases. In these instances air flow is minimal or close to zero creating occurrences of numerical inconsistencies when using logarithmic expressions. It is suggested in (E. Y. Ng August, 2005) that to properly estimate the heat resistance of both air and coolant side first some thought is given to fin efficiency in terms of how much heat is transferred versus the theoretical maximum. The proposed equation for a straight fin of uniform cross-section is as follows

$$\eta_f = \frac{\tanh(mL)}{mL} \qquad \textbf{B-35}$$

Where m is a fin efficiency parameter which depends on the heat transfer coefficient for the air side. L is the effective fin length [m].

$$m = \sqrt{\frac{2h_a}{KF_t}}$$ **B-36**

$$L = \frac{F_h}{2}$$ [m] **B-37**

Because radiators are finned-tube arrays, the total surface efficiency is introduced to account for weighed mean of the complete core.

$$\eta_o = 1 - \frac{A_f}{A_a}(1 - \eta_f)$$ **B-38**

The overall heat transfer resistance does not consider fouling nor wall conduction; this last term is eliminated assuming it is negligible from the core being made from a low resistance material such as aluminium or copper.

$$\frac{1}{UA_{fr,r}} = \frac{1}{\eta_o h_a A_a} + \frac{1}{h_c A_c}$$ **B-39**

As it is widely known the ε-NTU method is a measure of how much is being transferred and how efficient the exchanger is. The first step is to calculate each heat capacity rate, C_x, for the coolant and air sides.

$$\dot{C}_a = (A_a \rho_a V_a)c_{p,a}$$ [J/(s.°K)] **B-40**

$$\dot{C}_c = (A_c \rho_c V_c) c_{p,c} \qquad\qquad \text{[J/(s.°K)]} \qquad \textbf{B-41}$$

$$V_c = \frac{\dot{m}_c}{A_c \rho_c} \qquad\qquad \text{[m/s]} \qquad \textbf{B-42}$$

Where V_a and V_c are the flow speeds of air and coolant [m/s] respectively. The former is calculated using Equation B-55 explained later on. Using the previous three equations the heat capacity rate is

$$\dot{C}_r = \frac{\dot{C}_{min}}{\dot{C}_{max}} \qquad\qquad \textbf{B-43}$$

$$\dot{C}_{min} = \min(\dot{C}_a, \dot{C}_c) \qquad\qquad \text{[J/(s.°K)]} \qquad \textbf{B-44}$$

$$\dot{C}_{max} = \max(\dot{C}_a, \dot{C}_c) \qquad\qquad \text{[J/(s.°K)]} \qquad \textbf{B-45}$$

The number of transfer units, NTU, and the exchanger efficiency, ε, depend on both the heat capacity rate and transfer resistance.

$$NTU = \frac{UA_{fr,r}}{\dot{C}_{min}} \qquad\qquad \textbf{B-46}$$

$$\varepsilon = 1 - exp\left[\frac{e^{-NTU^{0.78}C_r} - 1}{NTU^{-0.22}C_r}\right] \qquad\qquad \textbf{B-47}$$

To determine each temperature delta (how much the temperature of each fluid rises or falls) the maximum and actual heat transfer rates must be obtained.

$$\dot{Q}_{max} = \dot{C}_{min}\left(T_{c,in} - T_{a,in}\right) \qquad\qquad \text{[J/s]} \qquad \textbf{B-48}$$

$$\dot{Q}_{actual} = \varepsilon . \dot{Q}_{max} \qquad\qquad \text{[J/s]} \qquad \textbf{B-49}$$

Finally, the radiator outlet temperatures for each fluid are

$$T_{air,out} = T_{a,in} + \frac{\dot{Q}_{actual}}{\dot{C}_a} \qquad\qquad \text{[}^\circ\text{K]} \qquad \textbf{B-50}$$

$$T_{coolant,out} = T_{c,in} + \frac{\dot{Q}_{actual}}{\dot{C}_c} \qquad\qquad \text{[}^\circ\text{K]} \qquad \textbf{B-51}$$

B.7 Secondary Cooling Loop

Beside the fuel cell stack are a number of components which require cooling. These are all the electrical bus power converters, powertrain electrical machine, or machines, and power converters for the cooling system´s own ancillary items (fan and coolant pumps). To keep these components within their operating envelopes a smaller radiator is used, which is placed behind the main loop radiator so as to share in the forced airflow created by the fan, as illustrated by Figure B-1. The model this component uses is the same base radiator model developed for the main loop, but with different parameters to fit the new smaller size.

B.8 Coolant Pumps and Fan

With the intention of calculating the mass flow rate of air that enters the radiator´s fin channels consider

$$\dot{m}_{grill} = V_{air} A_{grill} \rho_a \qquad\qquad \text{[kg/s]} \qquad \textbf{B-52}$$

A_{grill} is the area of the grill channels, obtained from published data [0.2693 m^2] through which air can flow into the under-hood area. V_{air} is the speed of air entering the grill channels; usually this is the speed of the vehicle in [m/s]. It is assumed that there are no air leaks around the radiator shroud. Now, normal airflow caused by vehicle motion can be augmented by the cooling fan. For simplicity, the final airflow considered to enter the radiator is calculated as

$$\dot{m}_a = \dot{m}_{grill} + \dot{m}_{fan} \qquad [kg/s] \qquad \textbf{B-53}$$

Using manufacturer data for variable speed electric cooling fans used on medium duty trucks the air flow rate, $\dot{m}_{fan,max}$, can be set to 4.955 [m^3/s] (Performance Trucks Website s.f.).

$$\dot{m}_{fan} = Fan_{spd}\, \rho_a\, \dot{m}_{fan,max} \qquad [kg/s] \qquad \textbf{B-54}$$

Fan_{spd} is a factor used to estimate the airflow depending on fan speed. It has values from 0 to 1, depending on what percentage of the maximum RPM possible is used. Now that the mass air flow is know the speed of air can be calculated.

$$V_a = \frac{\dot{m}_a}{A_a \rho_a} \qquad [m/s] \qquad \textbf{B-55}$$

For the case of the coolant pump, lack of a commercially available pump that can reach the required flow levels in excess of 230 lpm a new pump is modelled as three individual pumps in parallel. Each one is capable of supplying 115 lpm, so as the system´s flow requirement increases they are activated gradually until all are working together. This was done with the intention of not only modelling the flow dynamics, but also to calculate the electrical power required to drive

each system. Both the main and secondary cooling loops have the same pumping system. The dynamic response of the pumping system was modelled as an array of transfer function and a look-up table. The reason for this was firstly to closely model the delay in the response for the coolant pumps, and also to include heat rejection requirements from manufacturer data (Ballard Power Systems Inc 2011).
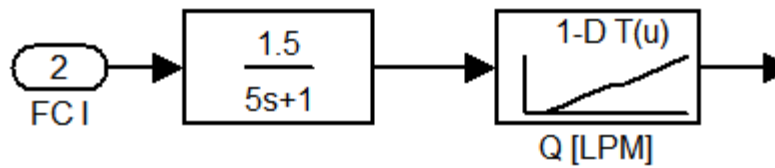
Figure B-2 Coolant Pumping System Control

The system using data from (Gou 2010) is assumed to have a gain of 1.5 and time constant of 5s. That control value enters a manufacturer data fed look-up table.

Table B-1 Load Based Coolant Flow Requirements (Ballard Power Systems Inc 2011)

Fuel Cell Current [A]	Coolant Flow, Q [LPM]
15	40
40	45
75	77
100	125
150	148
175	165
200	187.5
270	260

B.9 Simplified Heat Exchangers

All components which are connected to the cooling loops are kept in operating temperature ranges thanks to heat exchangers. They remove thermal energy from power converters, charge coolers and electrical machinery. To simplify the system each heat exchanger is modelled per first principles.

$$\dot{Q}_{hx} = \dot{m}_{coolant} c_{p,c} \Delta T \qquad \text{[J/s]} \qquad \textbf{B-56}$$

$\dot{Q}_{hx}$ is rate at which heat is being generated by each device, in [J/s]. The mass flow rate of coolant, $\dot{m}_{coolant}$ in [kg/s], is common to all devices in the loop and ΔT is the temperature rise for the coolant, in [^{o}K]. The exit temperature of the flow is the addition of the inlet temperature, which is the outlet temperature for the nearest upstream device, and ΔT. This result is externally limited to be no higher than the device´s own temperature.

Appendix C Test Platform Information

This appendix includes wiring harness interconnection information for the Compact Field Point Equipment in the test platform. It also includes wiring diagrams and TCP/IP Message details for the Matlab/LabView communications.

Table C-1 Digital Output Module DO-410 Wiring Table # 1

DO-410 @ 7					
Channel #	Vout	Vsup	COM	Use	Colour
0	1	17	2,18	Front LED	White/Black
1	3	19	4,20	Right LED	Green
2	5	21	6,22	Left LED	Yellow
3	7	23	8,24	Rear LED	Blue
4	9	25	10,26	N.U.	
5	11	27	12,28	N.U.	
6	13	29	14,30	N.U.	
7	15	31	16,32	N.U.	

Table C-2 Digital Output Module DO-410 Wiring Table # 2

DO-410 @ 6					
Channel #	Vout	Vsup	COM	Use	Colour
0	1	17	2,18	F.C. Conv On	White
1	3	19	4,20	Batt. Conv On	Blue
2	5	21	6,22	Cap Bank On	Orange
3	7	23	8,24	24V Realy On	White/Green Tape
4	9	25	10,26	N.U.	
5	11	27	12,28	N.U.	
6	13	29	14,30	N.U.	
7	15	31	16,32	N.U.	

Table C-3 CFP-2020 Module Data

CFP-2020	
IP Adress	192.168.1.3
LED	Meaning
A	N.U.
B	Program Running
C	Powertrain Frame Received
D	Load Frame Received

Table C-4 Counter Module CTR-502 Wiring Table

CTR-502 @ 4						
Count Input						
Channel #	Vin	Colour	Vsup	COM	Colour	Use
0	1	White/Black	17	18	Black	RPM Right
1	2		17	18		Internal Count Source to RPM Right
2	3	Orange/Black	19	20	White/Blue	RPM Left
3	4		19	20		Internal Count Source to RPM Left
4	5		21	22		N.U.
5	6		21	22		N.U.
6	7		23	24		N.U.
7	8		23	24		N.U.
Gate Input						
0	9		25	26		Gate for Count Input #1
1	10		25	26		N.U.
2	11		27	28		Gate for Count Input #2
3	12		27	28		N.U.

Open Collector Output						
0	13		29	30		Internal to RPM Right
1	14		29	30		Internal to RPM Left
2	15	Thick Blue	31	32	Thick Light Green	Load Sharing 1
3	16	Thick Yellow	31	32	Thick Light Green	Load Sharing 2
Open Collector Output is Inverse Logic						

Table C-5 Analogue Input Module AI-110 Wiring Table

AI-110 @ 3							
Channel #	Vin	Colour	Iin	Vsup	COM	Colour	Use
0	1	Orange/Black	2	17	18	White/Blue	Motor I1
1	3	White/Blue	4	19	20	Orange/Black	PWM 3
2	5	Orange/Red	6	21	22	White/Black	Motor I2
3	7	White/Black	8	23	24	Orange/Red	PWM 4
4	9	Orange	10	25	26	White	Motor I3
5	11	White	12	27	28	Orange	Voltage L
6	13	Orange/Green	14	29	30	Grey	Motor I4
7	15	Grey	16	31	32	Orange/Green	Voltage R

Table C-6 Analogue Input/Output Module AIO-610 Wiring Table

AIO610 @ 5							
Input Channels							
Channel #	Vin	Colour	Iin	Vsup	COM	Colour	Use
0	1	White	2	17	18	Black	Left Pedal Out
1	3	Dirty White	4	19	20	Purple	Cap Bank Voltage
2	5	Yellow	6	21	22	Blue	Right Pedal Out
3	7	Orange	8	23	24	Grey	Ctrl. Batt. Voltage
Output Channels							
0	9	Orange/Black		25	10,26	Black	Left Pedal Out
1	11	White/Black		27	12,28	Orange/Green	Right Pedal Out
2	13	Thick Yellow		29	14,30	Thick Black	Dyno Pedal
3	15			31	16,32		N.U.

Table C-7 Logic Table for Control Pad UGV TCP/IP Messages - Forward

Direction	Right Slow	Right Fast	Left Slow	Left Fast	Message I.D [Hex].
Forward = 0					
Stop	0	0	0	0	30
Forward = 1					
75% Left	0	0	0	1	31
25% Left	0	0	1	0	32
------	0	0	1	1	X
75% Right	0	1	0	0	34
75% Right 75% Left	0	1	0	1	35
75% Right 25% Left	0	1	1	0	36
------	0	1	1	1	X
25% Right	1	0	0	0	38
25% Right 75% Left	1	0	0	1	39
25% Right 25% Left	1	0	1	0	40

Table C-8 Logic Table for Control Pad UGV TCP/IP Messages - Backward

Direction	Right Slow	Right Fast	Left Slow	Left Fast	Message I.D [Hex].
Backward = 1					
75% Left	0	0	0	1	61
25% Left	0	0	1	0	62
------	0	0	1	1	X
75% Right	0	1	0	0	64
75% Right 75% Left	0	1	0	1	65
75% Right 25% Left	0	1	1	0	66
------	0	1	1	1	X
25% Right	1	0	0	0	68
25% Right 75% Left	1	0	0	1	69
25% Right 25% Left	1	0	1	0	70

Table C-9 Load Sharing Box Connections

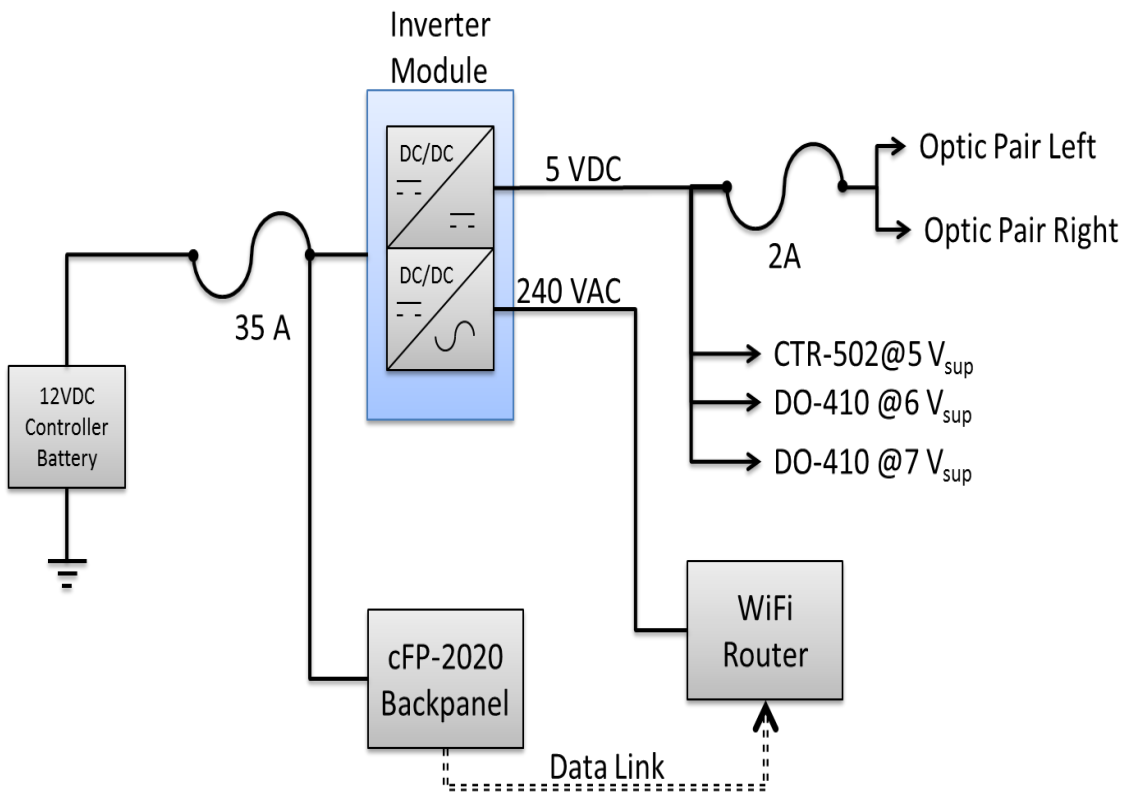| Functional Label	Destination
0V	GND
5V	24 Volt Relay Output
PWM4	CTR-502@4 Output 2
PMW5	CTR-502@4 Output 3

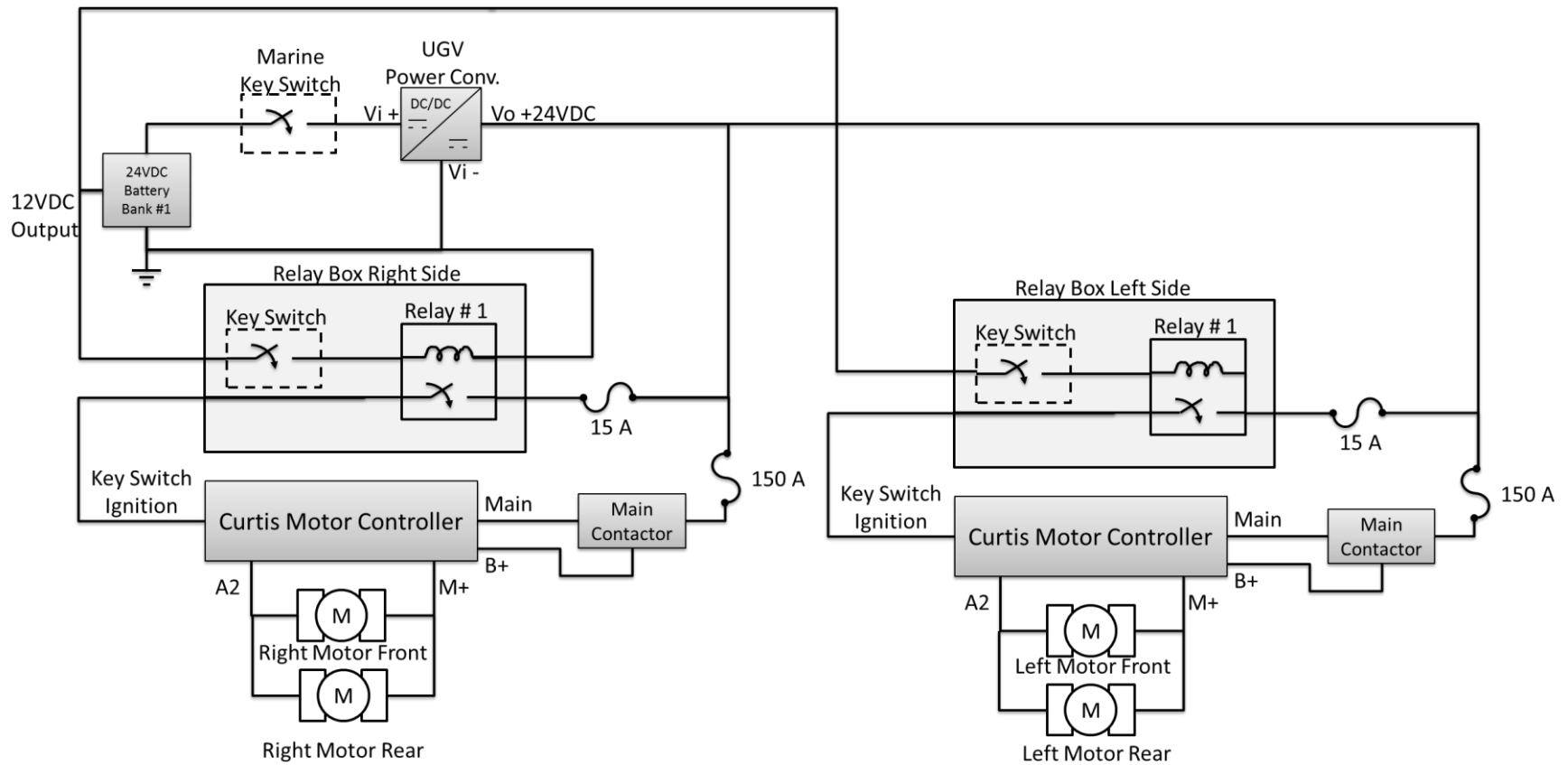**Figure C-1 UGV 12V Power Supply and Data Link Connection Block Diagram**

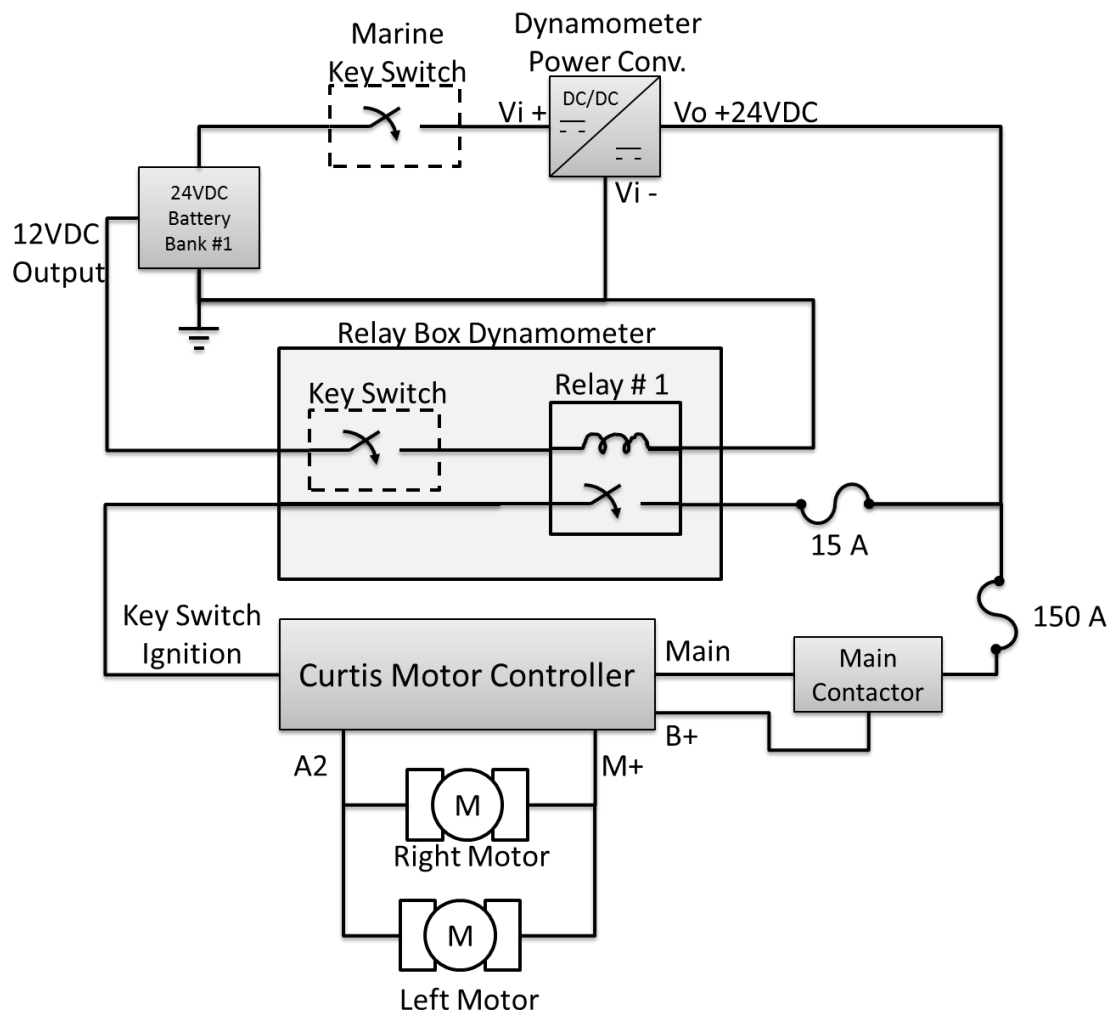**Figure C-2 UGV 12/24 VDC Power Supply Connection Block Diagram**

Figure C-3 Dynamometer 12/24 VDC Power Supply Connection Block Diagram

Appendix D Software Code Chart

❑Animate:
+Port_A_E_Limiting
+Avg_Updates_A
+UGV vehicle dynamics
+UAV vehicle dynamics
+VR World Animation

❑Scheduler:
+Load_Activation_Manager
+Avg_Updates_BC
+Budget_Update

❑Low_Level:
+Object Data Retrival
+FC_Monitor (**Fuel cell protection
+Battery_Monitor
+State_Machine
+Fuzzy Evaluation
+Modifier Chain
+Mission Tracking Graph
+Reserve Creation

❑Test Cycle Execution:
+Test_Cycle_Reader
+Cycle_Speed_Cmd
+Dyno_Cycle_Speed_Cmd

❑ICS:
+Global_Variable_Init_Ground
+Labview_Connection
+Mission_Vector_Coding
+Recover_Applicable_Ambient_RO
LAV
+TCP_Comms_No_Reception
+Data_To_Read_Fcn
+Update_Graph_Generator_Data
+Store_Applicable_ROLAV_Vector

❑Behaviour:
+Threat_Scope
+World_Object_Matrix
+Radar_UGV
+Tracker_Update
+Update_Threat_Scope
+Behaviour_Module
+Escape_Navigation

❑Behaviour_Module:
+Threat_Attitude_Estimation
+Threat_Avoidance_Angles

❑Software Function
+ Software Subfunction
➢ Conceptual Grouping of
Software Subfunctions

❑Configurator_Init_Routine:
+Criticality_Assignment
+Mission_Budget
+Subsystem_Budget

❑ Configurator_Main_V12:
+System_Init
+Power_Supply_Init
+Configurator_Init_Routine
+Low_Level
+Load_Killer
+Continuous_Load_Management

❑Configurator:
+Configurator_Main_V12

➢ Personalities Features
+Budget
+Update
+Confirm
+ON_OFF (**Linear
Programming)

➢ Personalities Dialogue
+Send_Message
+SJB
+Vision
+Pt

❑System_Init:
+Configurator_Reset
+Configurator_Init

➢ Graph Generation:
+Parser
+Energy_Memory_Processing_f
+Pseudo_Parser